



Towards the Noise Reduction of Synthetic Jet Actuators Using Lobed Orifices

A Thesis

By

Jonne Jeyalingam

April 2018

Submitted in partial fulfilment of the requirements for the degree of

Doctor of Philosophy

Awarded by

Brunel University

College of Engineering, Design and Physical Sciences, Brunel University London

© Jonne Jeyalingam, 2018. All rights reserved. No part of this document may be reproduced without written permission of the copyright holder.

ABSTRACT

With increasing strain on the civil aviation industry to meet strict targets to reduce the adverse effects aviation has on the environment by 2050, significant advances in aircraft design and research are required. Aerodynamic improvements have been a focus for several decades now, however, current and future civil transport aircraft are based on traditional designs originating from the 1950s. Optimisation of aircraft external geometry for aerodynamic gain is reaching maturity and is becoming increasingly non-cost-effective.

New advances in sensor and actuator technology has allowed for the development of active flow control (AFC) devices that have shown promising results in laboratory and even full-scale flight conditions, as seen by the joint NASA-Boeing ecoDemonstrator. One such device is the synthetic jet actuator (SJA), that synthesises periodic jets without the requirement for external air supply, while adding momentum to the surrounding flow. For this reason, SJAs are also referred to as zero-net-mass-flux actuators. There exists extensive work on the use of these devices for flow control applications in a laboratory setting.

One of the key issues that remains unresolved, hindering successful aircraft application to-date, is the actuator self-noise generated. The noise level of SJAs can be so severe that they were rejected for application on the ecoDemonstrator in favour of a higher authority, quieter AFC device. SJAs were only considered for use in emergency situations on aircraft. Furthermore, the actuators were also not permitted to operate simultaneously at full power, which may severely limit scope for flow control on aircraft. Other applications that would benefit from SJAs include heat transfer for cooling in electronic devices. Studies in this field identify the same problem with noise levels of up to 73 dB reported.

It is clear that work towards the self-noise reduction of SJAs is required to harness the full potential of this actuator technology. In the work presented, passive and active noise control measures in the form of lobed orifices and antiphase operation of two jets, respectively, on the noise reduction of SJAs are

investigated. Noise sources of synthetic jet actuators include mechanical (diaphragm) and jet induced noise, where the focus of this work is on the latter type. Tests were conducted in quiescent conditions using jet velocity measurements, acoustic measurements, and flow visualisation.

Tests were carried out using a single chamber SJA with variable cavity height and both circular and lobed orifices. These tests helped identify a SJA self-noise generation mechanism when using a circular orifice. This mechanism is characterised by a constant frequency behaviour visible in acoustic spectra for a specific jet Reynolds number range of $600 < Re_j < 750$ and Strouhal number range of $0.22 < St < 0.50$. The geometries of the lobed orifices used in this work differ in lobe count and penetration. It was shown that a broadband noise reduction is possible with such orifices, with a maximum noise reduction of 14 dB at particular frequencies. The results indicate that a high number of lobes and penetration are preferred for noise reduction, however, at the expense of quickly dissipating downstream jet velocity. Flow visualisation reveals that this adverse effect is caused by enhanced mixing of lobed jets with ambient air that leads to earlier and more aggressive breakup of flow structures.

A double chamber SJA is also used to demonstrate the noise attenuation through the antiphase operation of two cavities, caused by the interference pattern of the sound field of each source. The maximum reduction measured using this actuator configuration is 14 dB, depending on directivity.

ACKNOWLEDGMENTS

First, I would like to express my sincere gratitude to my supervisor, Dr. Mark Jabbal, for his continual support, patience and guidance that made this project possible.

Besides my supervisor, I would like to thank Dr. Tze Pei Chong and Dr. Jan Wissink for their insightful comments and encouragement. I would also like to thank the EPSRC and Brunel University for providing the funding for this PhD and the RAeS for its travel grants that made it possible to present this work at international conferences.

This work could not have been possible without the technical support and expertise provided for the experimental work and manufacture of test components. For this I would like to thank Kevin Robinson, Paul Yates, Philip Mackenzie, Gerald Edwardson, Michael Lateo and also Tom Buss from the University of Nottingham.

I am grateful for the company and support from fellow students and friends – Franck, Raghav, Laith, Auris, Philip, Yasir, Lincoln, Farzad, Oliver and many others.

Finally, I am eternally grateful to my family and Sowmiya for their tremendous support and encouragement throughout the last few years.

TABLE OF CONTENTS

CHAPTER	PAGE
ABSTRACT	i
ACKNOWLEDGMENTS	iii
TABLE OF CONTENTS	iv
LIST OF TABLES	ix
LIST OF FIGURES	x
Nomenclature	1
1 Introduction	3
1.1 Rationale for Research.....	3
1.1.1 Current state of the civil aviation industry.....	3
1.1.2 Potential of active flow control.....	5
1.1.3 Self-noise of synthetic jet actuators	7
1.2 Aim and Objectives	9
1.3 Methodology Overview.....	10
1.4 Publications and Conferences	12
1.5 Organisation of the Thesis.....	14
2 Literature Review	16
2.1 A Brief History of Flow Control.....	16
2.1.1 Flow separation on wings and its implications	16
2.1.2 Traditional flow control.....	17
2.1.3 Passive flow control.....	19
2.1.4 Active flow control actuator.....	20
2.2 Synthetic Jet Actuators.....	25

2.2.1	Comparison between continuous jets and synthetic jets in quiescent conditions.....	25
2.2.2	Comparison between continuous jets and synthetic jets in crossflow ..	26
2.2.3	Development of synthetic jet actuators.....	29
2.2.4	Operation of synthetic jet actuators.....	30
2.2.4.1	Formation of synthetic jets.....	30
2.2.4.2	Importance of actuation frequency.....	35
2.2.5	Design of synthetic jet actuators.....	36
2.2.5.1	Cavity	36
2.2.5.2	Orifice.....	38
2.2.5.3	Actuation method.....	41
2.3	Synthetic Jet Actuator Noise.....	42
2.3.1	Noise of active flow control devices.....	42
2.3.2	SJA noise sources.....	43
2.3.3	Jet noise and Lighthill's analogy of aerodynamic sound	45
2.3.4	Hole tone	47
2.3.5	Effect of orifice shape on noise	48
2.3.5.1	Asymmetric orifices	48
2.3.5.2	Lobed orifices.....	50
2.3.6	Effect of active noise control on SJA noise	52
2.3.7	Current SJA self-noise reduction techniques	53
2.3.7.1	Enclosures	54
2.3.7.2	Operating conditions.....	55
2.3.7.3	Orifice geometry.....	55
2.4	Chapter Summary.....	56
3	Synthetic Jet Actuator Design	58

3.1	Original Synthetic Jet Actuator.....	58
3.1.1	Design and preliminary tests.....	58
3.1.2	Geometric discrepancies.....	60
3.1.3	Diaphragm clamping.....	61
3.2	New Synthetic Jet Actuator	64
3.2.1	Diaphragm selection.....	65
3.2.2	Single chamber synthetic jet actuator	67
3.2.3	Double chamber synthetic jet actuator.....	69
3.2.4	Orifice design.....	70
3.2.5	Manufacture.....	72
3.3	Chapter Summary.....	73
4	Methodology	75
4.1	Jet Velocity Measurements.....	75
4.1.1	Hotwire setup.....	75
4.1.2	Hotwire calibration	78
4.2	Diaphragm Deflection Measurements.....	79
4.2.1	Displacement.....	79
4.2.2	Mode shape	80
4.3	Acoustic Measurements	82
4.3.1	Anechoic chamber.....	82
4.3.2	Microphone selection.....	83
4.3.3	Microphone setup	83
4.3.4	Acoustic measurement metrics.....	85
4.4	Flow Visualisation.....	85
4.4.1	Dye flow setup	85
4.4.2	Schlieren visualisation.....	88

5 Jet Flow and Acoustic Characteristics of Piezoelectric-driven SJA in Quiescent Conditions	91
5.1 Jet Flow Parameters	91
5.1.1 Circular Orifice SJA	91
5.1.1.1 Test conditions	91
5.1.1.2 Effect of actuator configuration on frequency response	92
5.1.1.3 Effect of cavity height on frequency response	93
5.1.2 Lobed Orifice SJA	96
5.1.2.1 Frequency response	96
5.1.2.2 Velocity profiles	100
5.1.2.3 Streamwise development	104
5.1.2.4 Jet spreading	106
5.2 Acoustic Characteristics	112
5.2.1 SJA noise reduction using double chamber antiphase operation	112
5.2.2 SJA noise reduction using lobed orifices	115
5.3 Jet Flow Visualisation	119
5.3.1 Test conditions	119
5.3.2 Flow structure streamwise propagation	119
5.3.3 Jet axis-switching	122
5.3.4 Lobed vortex ring dynamics	125
5.4 Summary	127
6 Jet Flow and Aeroacoustic Characteristics of Electromagnetic-driven SJA in Quiescent Conditions	130
6.1 Circular Orifice SJA	130
6.1.1 Test conditions	131
6.1.2 Acoustic response	134

6.1.3	Strouhal number dependence.....	137
6.1.4	Reynolds number dependence	139
6.1.5	Stroke length dependence.....	140
6.1.6	Velocity spectra and Schlieren visualisation.....	141
6.1.7	Effect of cavity height on the acoustic and velocity response	148
6.1.8	Effect of orifice height on the acoustic and velocity response	152
6.2	SJA Self-Noise Reduction Using Lobed Orifices.....	155
6.2.1	Frequency response.....	155
6.2.2	Acoustic response	155
6.2.3	Effect of non-dimensional jet flow parameters	159
6.2.4	Flow structures of lobed and circular jets.....	163
6.3	Summary.....	167
7	Conclusions and recommendations	169
7.1	Conclusions.....	169
7.2	Recommendations for Future Work.....	174
	References	176

LIST OF TABLES

TABLE	PAGE
Table 1. Summary of active flow control actuators (Cattafesta & Sheplak, 2008)	22
Table 2. Noise reduction methods employed for SJAs	54
Table 3. Quality factor for circular orifices in the double chamber SJA	64
Table 4. SJA dimensions scaled on peak velocity optimised design (Crowther & Gomes, 2008).....	66
Table 5. Key eigenfrequencies and mode shapes of PZT diaphragm obtained from eigenfrequency analysis	67
Table 6. SJA geometric parameters	91
Table 7. Value of lobe penetration, P, for the different orifice shapes	106
Table 8. SJA operating and jet flow parameters.....	119
Table 9. Test conditions.....	132

LIST OF FIGURES

FIGURE	PAGE
Figure 1.1. Boeing 787 (top) and F-35B (bottom) engine/nozzle with chevrons for noise reduction.....	5
Figure 1.2. Boeing 757 ecoDemonstator tail section with sweeping jet actuators installed.....	7
Figure 1.3. Typical Synthetic Jet Actuator geometry.....	8
Figure 2.1. Flow separation and reversal of flow on a slope (Mukut et al. 2014)	17
Figure 2.2. Flat plate using microblowing through (a) permeable wall (Kornilov & Boiko, 2012) and (b) permeable sections interlaced with impermeable ones (Kornilov & Boiko, 2014).....	19
Figure 2.3. Schematic of plasma actuator (Matsunuma & Segawa, 2012)	24
Figure 2.4. Fluorescent dye visualisation of (a) a synthetic jet and (b) an equivalent continuous jet with lines marking the apparent mean boundary of the dye flow (Cater & Soria, 2002).....	26
Figure 2.5. Variation of (a) lift coefficient, C_L , and (b) drag coefficient, C_D against angle of attack with and without SJAs (Tang, Salunkhe, Zheng, Du, & Wu, 2014)	29
Figure 2.6. Application of SJA on aircraft (left) and typical configuration of a SJA (right)	30
Figure 2.7. Vortex roll-up dyed in the mid-plane at the outlet edge (Auerbach, 1987).....	31
Figure 2.8. Exit velocity profiles of synthetic jets at phase of maximum blowing for (a) $d = 5$ mm and different Stokes numbers; and (b) $d = 5$ and 0.5 mm with $S = 8.9$ and $L = 1.6$ (Zhong, et al., 2007).....	34
Figure 2.9. Vortex roll-up of synthetic jets issuing from orifice with $d = 5$ mm using particle tracing. Data was taken using PIV, where phases shown are arbitrary, (a) $S = 7$, $L = 2.9$, $Re_L = 71$; (b) $S = 12$, $L = 1.4$, $Re_L = 52$; (c) $S = 22$, $L = 3$, $Re_L = 756$ (Zhong, et al., 2007)	35

Figure 2.10. SJA frequency response with the Helmholtz and diaphragm resonance shown for (a) uncoupled and (b) coupled system (Gomes et al. 2006)	36
Figure 2.11. Arrangement of inclined opposite SJA array (Jabbal et al. 2012)	37
Figure 2.12. Effect of cavity height: (a) phase angle and (b) jet velocity (Jain et al. 2011)	38
Figure 2.13. flow through a cylindrical orifice with constant diameter and increasing height: (a) separated flow, (b) marginally reattached flow and (c) fully reattached flow (Gomes et al. 2006)	40
Figure 2.14. A micro SJA with square orifice dimensions of 0.6 x 0.6 x 0.2 mm using PZT ceramic wafer bonded to monocrystalline silicon wafer using epoxy resin at low temperature (Wang et al. 2015) (Wang, Ma, Deng, Qu, & Luo, 2015).	42
Figure 2.15. Transitional conventional jet (Van Dyke, 1982)	45
Figure 2.16. (a) linear variation of hole tone frequency with jet velocity and (b) flow visualisation showing the vortex shedding from continuous jet during the tone generation (von Gierke, 1947)	48
Figure 2.17. Schematic showing (a) deformation and axis-switching of low aspect ratio elliptic vortex ring and (b) deformation, axis switching and splitting of high aspect ratio vortex ring (Husain & Hussain, 1999)	49
Figure 2.18. LIF flow visualisation results using a lobed nozzle at varying downstream distances (Hu, Saga, Kobayashi, & Taniguchi, 2000)	51
Figure 2.19. Sound field for two opposite but equally large sources with varying separation distance between sources (a) $h = \lambda/4$, (b) $h = \lambda/2$, (c) $h = \lambda$ and (d) $h = 2\lambda$ (Moeser, 2009)	53
Figure 2.20. SJA noise reduction scheme using an enclosure with muffler attached (Arik, 2007)	54
Figure 2.21. Summary of acoustic results in a 3 in x 3 in x 3 in enclosure (Arik, 2007)	55
Figure 3.1. PZT diaphragm dimensions (27 mm)	59
Figure 3.2. Double chamber SJA assembly (top) and lobed orifice geometry (bottom) (Kykkotis, 2014)	59

Figure 3.3. Close-up (x 20) of 3D printed orifices (a) circular, (b) high amplitude 6-lobed and (c) low amplitude 6-lobed orifice (Kykkotis, 2014).....	60
Figure 3.4. Schematic of clamped (green) and unclamped (red) edge of diaphragm.....	61
Figure 3.5. Circular orifice velocity response of the double chamber SJA with varying torque applied to the bolts (a) 0.35 Nm, (b) 0.55 Nm and (c) 0.75 Nm (dashed line marks the diaphragm resonance).....	63
Figure 3.6. PZT diaphragm dimensions (50 mm).....	66
Figure 3.7. Single chamber SJA layout.....	68
Figure 3.8. Double chamber SJA layout.....	69
Figure 3.9. Orifice designs: (a) circular, (b) low amplitude 6-lobed, (c) high amplitude 6-lobed and (d) 4-lobed orifice with dimensions shown below.....	71
Figure 3.10. Close-up of (a) low amplitude 6-lobed, (b) high amplitude 6-lobed, (c) 4-lobed orifice and (d) all SJA components.....	73
Figure 4.1. SJA hotwire test rig setup with schematic of traverse system (right)	76
Figure 4.2. Hot wire anemometry test setup.....	77
Figure 4.3. Microtrak 3 system setup on benchtop test rig.....	79
Figure 4.4. Dantec Q-400 DIC system setup (top) and close-up of stochastic speckle pattern on the diaphragm (bottom).....	81
Figure 4.5. Schematic of Brunel University London anechoic chamber facility ...	82
Figure 4.6. SJA acoustic measurement setup: microphone placed at grazing incident to jet.....	84
Figure 4.7. SJA geometry for dye flow visualisation (Conibear, 2016).....	86
Figure 4.8. Dye flow visualisation setup.....	87
Figure 4.9. Schlieren flow visualisation test setup.....	90
Figure 5.1. Comparison of single and double chamber actuator frequency response.....	92
Figure 5.2. Single chamber, circular orifice SJA frequency response as a function of cavity height.....	94
Figure 5.3. Instantaneous exit centreline velocity response at the first mechanical resonance mode, where (a) shows the SJA output cycle at the actuation frequency where the peak velocity, U_{peak} , is obtained (325 Hz) and (b) shows the	

peak output at the corresponding actuation frequency for each cavity (275 – 325 Hz)	95
Figure 5.4. Orifice designs with the same effective diameter and area: (a) circular, (b) low amplitude 6-lobed, (c) high amplitude 6-lobed and (d) 4-lobed orifice...	96
Figure 5.5. Frequency response of SJA as a function of orifice shape (a) H = 1.2 mm, (b) H = 3 mm, (c) H = 4 mm, (d) H = 5 mm, (e) H = 6 mm, (f) H = 8 mm, where the red lines mark the constant resonant frequencies in the response and blue lines mark the changing resonant frequency.....	99
Figure 5.6. Diaphragm resonance frequencies and mode shapes from simulation (COMSOL; top) and experiment (DIC; bottom)	100
Figure 5.7. Velocity profiles with H = 1.2 mm, S = 43 & Re _j = 938 of (a) circular, (b) low amplitude 6-lobed, (c) high amplitude 6-lobed and (d) 4-lobed orifices measured along the major axis, where x/d = 0 represents the centre of the orifice.....	102
Figure 5.8. Velocity profiles with H = 1.2 mm, S = 23 & Re _j = 449 of (a) circular, (b) low amplitude 6-lobed, (c) high amplitude 6-lobed and (d) 4-lobed orifices measured along the major axis	104
Figure 5.9. Reduction of jet centreline velocity with streamwise distance from the orifice.....	105
Figure 5.10. Schlieren visualisation of the mean flow with corresponding velocity profiles, S = 23 & Re _j = 449, for (a) circular, (b) low amplitude 6-lobed, (c) high amplitude 6-lobed and (d) 4-lobed orifices, taken along the major axis (red dash lines).....	109
Figure 5.11. Power Spectral Density (PSD) as a function of spanwise location across the orifice at f _a = 325 Hz for (a) exit, (b) y=5d, (c) y=10d and (d) y=15d streamwise locations	111
Figure 5.12. (a) Double chamber SJA velocity response, (b) directive noise plot of far field noise measurements for f _a = 925 Hz	113
Figure 5.13. Acoustic spectra at different directive positions around the actuator	114
Figure 5.14. Acoustic response of the PZT diaphragm at the two system resonant frequencies.....	115

Figure 5.15. Single Chamber SJA acoustic spectra at $f_a = 325$ Hz and $f_a = 1225$ Hz as a function of orifice shape: (a) circular, (b) low amplitude 6-lobed, (c) high amplitude 6-lobed and (d) 4-lobed orifice	116
Figure 5.16. Acoustic spectra of Δ SPL as a function of frequency (a) C-L6, (b) C-H6 and (c) C-4L	118
Figure 5.17. Side view of dye flow visualisation for the matched L case ($Re_j = 134$, $L = 5.4$): (a) circular, (b) low amplitude 6-lobed, (c) high amplitude 6-lobed and (d) 4-lobed orifice taken at the same phase in the cycle	121
Figure 5.18. Side view of dye flow visualisation for the matched Re_j case ($Re_j = 1152$, $L = 23$): (a) circular, (b) low amplitude 6-lobed, (c) high amplitude 6-lobed and (d) 4-lobed orifice taken at the same phase in the cycle	122
Figure 5.19. Close up view of the orifice exit plane showing jet formation for the (a) high amplitude 6-lobed, (b) 4-lobed and (c) low amplitude 6-lobed orifice. Dash outlines marks axis switching.....	124
Figure 5.20. 4-Lobed jet development, $L = 11.5$, $S = 17.7$ & $Re_j = 576$	126
Figure 5.21. Illustration showing 4-lobed jet formation and vortex dynamics..	127
Figure 6.1. Comparison of PZT diaphragm noise ($f_a = 325$ Hz) to stretched Latex membrane (diaphragm) noise ($f_a = 60$ Hz) clamped in SJA	131
Figure 6.2. (a) SJA frequency response as a function of cavity height, H, for Case 2 and (b) diaphragm peak-to-peak displacement for different test cases.....	133
Figure 6.3. Frequency response of SJA (a) jet centreline velocities vs. actuation frequency for $h = 4.2$ mm (solid line) and $h = 2.5$ mm (dashed line)	134
Figure 6.4. Acoustic response for $h = 4.2$ mm and $H = 1.2$ mm (a) Case 1, (b) Case 2 and (c) Case 3, where f_1 and f_2 mark the two dominant constant frequency lines and f_{St} marks a constant Strouhal number behaviour in the spectra.....	136
Figure 6.5. Jet Strouhal number as a function of jet velocity, with range for whistling highlighted in red based on f_2	138
Figure 6.6. Strouhal number as a function of actuation frequency based on f_{St} showing the constant Strouhal number behaviour over a range of actuation frequencies (dashed lines)	139
Figure 6.7. Non-dimensional jet flow parameters (a) jet Reynolds number and (b) stroke length for all three cases. Dashed lines indicate Re_j and f_a threshold respectively for onset of whistling for all three cases.....	140

Figure 6.8. Instantaneous SJA centreline velocity response for Case 1 at (a) $f_a = 25$ Hz, 30 Hz, 35 Hz, 40 Hz and (b) $f_a = 60$ Hz, 75 Hz, 80 Hz, 85 Hz.....	142
Figure 6.9. Instantaneous SJA centreline velocity response on and just before the onset of audible actuator self-noise for (a) Case 2 and (b) Case 3.....	142
Figure 6.10 Schlieren flow visualisation of circular orifice SJA for Case 2 at (a) $f_a = 20$ Hz, (b) $f_a = 25$ Hz and (c) $f_a = 60$ Hz.....	145
Figure 6.11. Jet velocity power spectral density (PSD) for Case 2 (4 V, $f_a = 60$ Hz) as a function of five streamwise positions (exit, 5d, 10d, 15d & 20d) taken at four spanwise positions $x/d =$ (a) 0, (b) 0.5, (c) 1 and (d) 2.....	147
Figure 6.12. Comparison of PSD (top image) to Δ SPL (bottom image) for Case 2	148
Figure 6.13. Effect of varying SJA cavity height, H, on (a) electromagnetically driven SJA acoustic response, where (i) H = 1.2 mm, (ii) H = 5 mm and (iii) H = 8 mm, and (b) piezoelectrically driven SJA centreline exit velocity response, where (i) H = 1.2 mm, (ii) H = 5 mm and (iii) H = 8 mm.....	151
Figure 6.14. SJA velocity response for H = 1.2 mm, h = 2.5 mm and 4.2 mm.....	152
Figure 6.15. Acoustic response for (a) h = 4.2 mm and (b) h = 2.5 mm, where f_1 and f_2 mark the two dominant constant frequency lines in the spectra for h = 4.2 mm that are also present for h = 2.5 mm	154
Figure 6.16. Electromagnetically actuated SJA frequency response as a function of orifice shape (a) Case 1, (b) Case 2 and (c) Case 3, where C = Circular, L6 = Low amplitude 6-lobed, H6 = High amplitude 6-lobed and 4L = 4-lobed orifice.....	155
Figure 6.17. Acoustic spectra of SJA using (a) circular, (b) low amplitude 6-lobed, (c) high amplitude 6-lobed and (d) 4-lobed orifice at the onset of self-noise.....	156
Figure 6.18. Acoustic spectra showing Δ SPL (dB) vs. Frequency (Hz) of SJA using (a) circular, (b) low amplitude 6-lobed, (c) high amplitude 6-lobed and (d) 4-lobed orifice at $f_a = 60$ Hz, where D is the diaphragm SPL	158
Figure 6.19. Noise change showing Δ SPL (dB) vs. Frequency (Hz) for the different orifice shapes at $f_a = 60$ Hz, (a) circular minus low amplitude 6-lobed (C-L6), (b) circular minus high amplitude 6-lobed (C-H6), (c) circular minus 4-lobed orifice (C-4L).....	159
Figure 6.20. Percentage SPL reduction at the dominant frequencies. (a) Case 1, (b) Case 2 and (c) Case 3	159

Figure 6.21. Jet Reynolds number frequency response as a function of orifice shape for (a) Case 1, (b) Case 2 and (c) Case 3	160
Figure 6.22. Dimensionless stroke length frequency response as a function of orifice shape for (a) Case 1, (b) Case 2 and (c) Case 3	161
Figure 6.23. Comparison between dimensionless stroke length and circular orifice acoustic spectra for (a) Case 1, (b) Case 2, (c) Case 3	162
Figure 6.24. Schlieren visualisation at $f_a = 25$ Hz – (a) circular, (b) low amplitude 6-lobed, (c) high amplitude 6-lobed and (d) 4-lobed orifice at peak jet velocity for Case 2	164
Figure 6.25. Schlieren visualisation at $f_a = 25$ Hz – (a) low amplitude 6-lobed, (b) high amplitude 6-lobed and (c) 4-lobed orifice at peak jet velocity for Case 2 with close ups	166

Nomenclature

A	=	Orifice area, m^2
a	=	Speed of sound, m/s
D	=	Cavity diameter, mm
d	=	Orifice diameter, mm
r_D	=	Orifice radius, m
ρ	=	density, kg/m^3
Δ_{p-p}	=	diaphragm peak to peak displacement, mm
H	=	Cavity height, mm
h	=	Orifice height, mm
f	=	Frequency, Hz
f_a	=	Actuation frequency, Hz
f_h	=	Helmholtz resonance frequency, Hz
f_d	=	Diaphragm resonance frequency, Hz
L	=	Dimensionless stroke length
t_d	=	Diaphragm thickness, mm
ξ	=	Empirically obtained damping coefficient
k^2	=	dimensionless frequency parameter
ν	=	Diaphragm Poisson's ration
ϑ	=	Kinematic viscosity of air, m^2/s
\bar{U}_o	=	Time averaged blowing velocity, m/s
U	=	Jet centerline velocity, m/s
U_{peak}	=	Jet peak velocity, m/s
λ	=	Wavelength (spatial period of a complete cycle), m
Q	=	Temporal volume change, m^3/s
Q_f	=	Quality factor

Abbreviations

AFC	Active Flow Control
DIC	Digital Image Correlation
PSD	Power Spectral Density
SJA	Synthetic Jet Actuator
SPL	Sound Pressure Level, dB
C	Circular
L6	Low Amplitude 6-Lobed
H6	High Amplitude 6-Lobed
4L	4-Lobed

1 Introduction

1.1 Rationale for Research

1.1.1 Current state of the civil aviation industry

The introduction of jet propulsion more than 55 years ago has truly transformed global economy and quality of life through empowering trade and tourism. Passenger demand is expected to double over the next 15 – 20 years (Growing Horizons, 2017) (IATA, 2016) with an annual growth rate of around 5 - 6%, as it has since 1950 (Schäfer & Waitz, 2014). In 2001 the Advisory Council for Aviation Research and Innovation in Europe (ACARE) published a ‘vision’ for the year 2020 (Comission, 2001) that targets a 50% cut in fuel consumption and perceived noise, and 80% reduction in landing/take-off NO_x emissions. With 2020 approaching it is clear that despite continued advances in research and technology, aircraft manufacturers will not be able to achieve these goals (Graham et al. 2014). ‘FlightPath 2050’ offers an updated set of ambitious targets for the industry, which calls for a 75% reduction in CO₂ emissions per passenger kilometre, 90% reduction in NO_x emissions and 65% reduction in perceived noise emission by 2050 (Commission, 2011).

Airbus estimates a global demand for 34,900 new aircraft and significant growth of 41% in passenger demand in the Asia Pacific region alone by 2036 (Growing Horizons, 2017). Boeing on the other hand forecasts 41,030 aircraft deliveries with a \$6.1 trillion market value through to 2036 (Current Market Outlook: 2017-2036, 2017), where both agree that the single aisle segment will see the most growth. Airlines across the globe are placing orders on new aircraft to retire an older fleet, increase capacity or both with the key drivers for this growing demand attributed to declining air fares and a rise in economic activity (UK Aviation Forecast, 2013). However, with decreasing opportunities to reduce operating costs and increasing costs associated with CO₂ emissions, it becomes difficult to maintain declining air fares.

Moreover, noise emission of aircraft is increasingly becoming problematic in densely populated environments with local airports, where as a consequence detrimental health effects such as stress, hypertension, sleep disturbance, annoyance and other effects are observed (UK Aviation Forecast, 2013; Greiser, 2006). To minimise these effects, airport night flight restrictions or curfews are imposed on aircraft operators, depending on aircraft noise performance, which prohibits take-off and landing during specified hours (ICAO, 2013). To become more competitive airlines have stretched their daytime operations at the boundaries of the night. This has caused an increase in traffic of 10% in the last four hours of the day (Leleu & Marsh, 2008).

With the above stated challenges and forecasts, the aerospace industry requires significant developments and improvements in the operational efficiency of civil transport aircraft. Recent advancements in material and propulsion technology has helped tackle many of the issues faced. For example, Boeing claims a 20-30% reduction in CO₂ emissions and 60% smaller noise footprint than the aircraft models it replaces (Boeing, 2015). Noise contribution from engines were reduced thanks to improvements in high by-pass ratio turbofan engines and passive noise control measures such as chevron engine nozzles, as shown in Figure 1.1. Engine efficiency is improved through technologies such as Geared Turbofan technology by Pratt & Whitney, where a gear system separates the engine fan from the low-pressure compressor and turbine. This allows the different engine modules to operate at their optimum speeds (PurePower PW1000G Engine, 2018). Flow generated noise on parts of aircraft, including wings or undercarriage, remain an issue (Vathylakis, 2015). However, current and near future generation of civil transport aircraft are based on designs and configurations established in the 1950s. Aerodynamic performance improvements through continuous refinement of the aircraft external geometry is reaching maturity and becoming increasingly non-cost-effective (Bieler et al. 2006).



Figure 1.1. Boeing 787 (top) and F-35B (bottom) engine/nozzle with chevrons for noise reduction

Alternative and promising approaches are being explored, such as active flow control systems, that can offer less intrusive methods to enhance aircraft aerodynamic performance.

1.1.2 Potential of active flow control

Limitations of aircraft geometric optimisation for aerodynamic performance gains has caused the re-emergence of active flow control (AFC) in recent years since it was first deemed cost ineffective in the 1960s. Advancement in sensor and actuator technology has resulted in more efficient systems with potential for industry-wide applications. Different from traditional boundary layer control, today's AFC seeks to modify the flow field behaviour using local active perturbations to produce flow field changes that results in improvement of performance, reliability and efficiency. These perturbations can be small relative to the characteristic velocity of the ambient flow and therefore make use of the unstable nature of the flow, or it can be of the order of the flow velocity, thus forcing the flow (Greenblatt & Wygnanski, 2008).

Full-scale flight tests have recently been performed to evaluate the effectiveness of different AFC methods on aircraft performance. McVeigh et al. (2011) used zero-mass-flux periodic excitation to reduce the download on the wings of a full-scale, hovering XV-15 tiltrotor aircraft. To minimise the download effect and maximise the vertical thrust, design practice dictates the flaperons (flaps/ailerons) are deflected by 65°, decreasing the area exposed to the rotor downwash. However, this leads to the flow separating in the vicinity of the flap shoulders, significantly increasing download. The actuators were fitted in the wing flap, periodically injecting and removing air through slots in the boundary layer on the upper surface of the flap. The results demonstrate the effectiveness of AFC in full-scale flight conditions, with up to 14% reduction in download during hover.

NASA's Environmentally Responsible Aviation (ERA) Project aims to develop and demonstrate integrated systems technologies to a technology readiness level (TRL) of 4-6 by 2020, that will help reduce fuel burn, emissions and noise for future aircraft models (Suder, 2012). As part of this project NASA has been looking to demonstrate the potential benefits of reducing the vertical tail size by using AFC on the ecoDemonstrator- a specially outfitted Boeing 757 that serves as a test platform for various "green aviation technology". 31 Sweeping jet actuators were installed on a full-scale Boeing 757 vertical tail for this purpose (Figure 1.2), with wind tunnel tests showing an increase in side force by 20 – 30%. Similar results were expected in full flight conditions, where an increase in side force by just 20% could potentially allow designers to scale down the vertical tail by 17% and reduce fuel consumption by as much as 0.5% (Barnstorff, 2015).

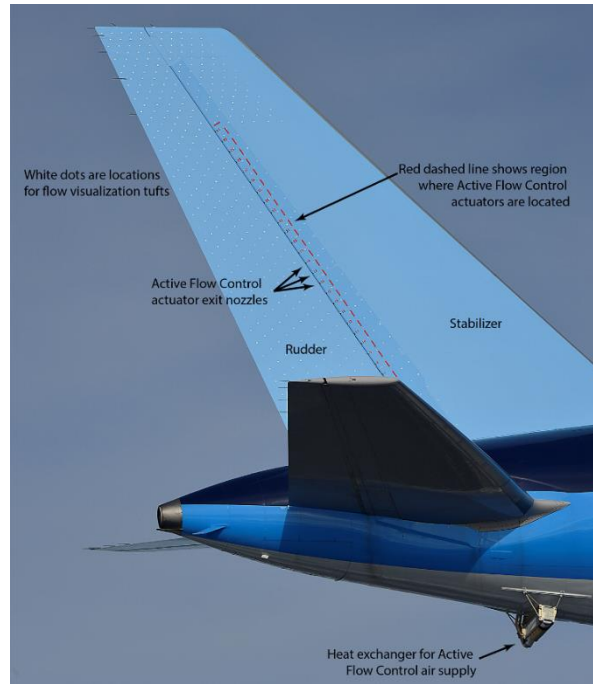


Figure 1.2. Boeing 757 ecoDemonstrator tail section with sweeping jet actuators installed

In April 2015, Boeing and NASA conducted full-scale flight tests using sweeping jet actuators on the aforementioned ecoDemonstrator. Due to flight safety concerns and control characteristics of the aircraft the full operating range was not explored. However, using standard flight test data extrapolation techniques using the previous full-scale lab test results an approximate 14% increase in side force at a rudder deflection of 30° and critical side slip angles was reported (Wahlen, et al., 2016).

1.1.3 Self-noise of synthetic jet actuators

Synthetic jet actuators (SJA) are devices that generate periodic jets, without the need for external air supply, for which they are also referred to as zero-net-mass-flux (ZNMF) actuators. The resulting jet, however, has a non-zero-net momentum flux. A typical SJA consists of a cavity enclosed on one side by an oscillating diaphragm and an orifice plate on the other side (Figure 1.3). As the oscillating diaphragm moves towards the orifice, the cavity volume decreases causing the air trapped inside the cavity to leave through the orifice. The air moving through the orifice forms a shear layer at the orifice walls that, under the right conditions, rolls up into a vortex ring. When the diaphragm moves back, away from the orifice, the cavity volume increases, and air is sucked back into

the cavity and the cycle begins again. The oscillating diaphragm can be of many types, e.g. a diaphragm in the form of metal shim or a rubber membrane, or a piston. Actuation can also be achieved through different transduction methods, which include piezoelectric and electromagnetic types.

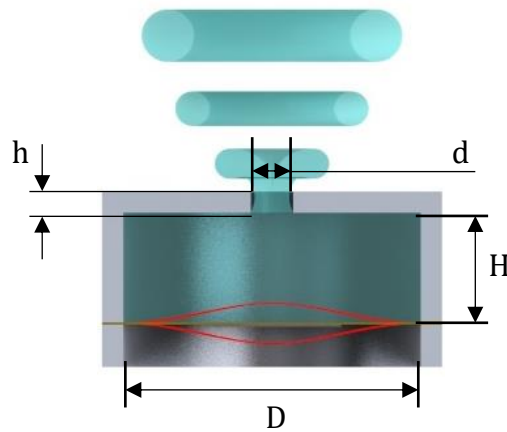


Figure 1.3. Typical Synthetic Jet Actuator geometry

Successive vortex rings formed at the orifice exit can enhance mixing and help redistribute higher momentum fluid from the outer part of the boundary layer to the near wall region (Jabbal & Zhong, 2010), where there is a momentum deficiency. Furthermore, the ZNMF property of SJAs mean they are self-contained systems and work has been conducted towards miniaturising them using micromachining processes (Coe et al. 2006). This has led to an increase in interest and research with many potential applications, such as flow control and heat transfer.

However, a key issue holding this technology back is the self-noise generate during operation, which have been recorded to reach 73 dB (Arik, 2007). In the previous section, the successful employment of sweeping jet actuators on the ecoDemonstrator aircraft for increased rudder authority was discussed. The noise issue of both sweeping and synthetic jet actuators was so great that both were only considered for use in emergency situations, where the increased noise generation would be acceptable. However, the noise generated by the oscillating diaphragm of an SJA can exceed the noise generated by sweeping jet actuators. Furthermore, due the high noise levels the actuators were not permitted to operate simultaneously at full power during testing.

Outside of the aerospace industry, e.g. heat transfer in electronic devices, SJA self-noise prohibits these devices from successful commercialisation despite promising heat transfer capabilities (Mangate & Chaudhari, 2015). As shown in these examples, there is a desperate need to better understand the self-noise generation process in SJAs and develop actuators that have a lower noise footprint while maintaining or enhancing their fluidic performance.

1.2 Aim and Objectives

The aim of the research presented is to define the aeroacoustic characteristics of synthetic jet actuators in quiescent conditions and reduce the self-noise generated using active and passive noise control measures, while minimising adverse effects this might have on the fluidic performance of the device, namely peak exit jet velocity.

To achieve the above aim, the objectives of this work are as follows:

- To design a double chamber synthetic jet actuator that is driven by a single diaphragm and study the effect that the resulting, out-of-phase operation of each chamber has on the sound field produced (active noise control).
- To design a single chamber SJA with variable cavity height and orifice shapes (both circular and lobed orifices). The effect these geometric changes have on the SJA fluidic performance are to be studied. The focus is on the effect of orifice shape on synthetic jet flow structures formed, streamwise jet development and fluidic performance.
- To characterise the aeroacoustics of a velocity optimised single chamber synthetic jet actuator with circular orifice.

- To study the effect lobed orifices have on the self-noise generated by a single chamber synthetic jet actuator by comparing the acoustic and jet flow characteristics to that of a circular orifice to better understand the mechanism behind the noise generation/suppression.

1.3 Methodology Overview

The experimental work conducted throughout this research consists of two primary parts: synthetic jet actuator fluidic and acoustic performance analysis in quiescent conditions. These are realised using a combination of hotwire anemometry and acoustic measurements. Flow visualisation is used to supplement these two quantitative sets of data. The focus of this research is the reduction of SJA self-noise using active and passive noise control techniques. This comes in the form of antiphase operation of a double chamber SJA (active) and a single chamber SJA using lobed, high entrainment/mixing, (passive) orifices instead of the more conventional circular ones. It is believed that the high mixing caused by lobed orifices will help modify and disrupt noise generating flow structures formed by the SJA.

Key here is the design of the two actuators. A SJA intended for full-flight conditions should have orifice diameters constrained to a maximum of 5-20% of the local boundary layer thickness (Tang et al. 2007). This condition, however, makes it a challenge to manufacture the fine details of lobed orifices using readily available and cost-effective manufacturing processes. Another constraining component is the piezoelectric diaphragm, used for a large part of the work, which are off-the-shelf items that are only available in a select range of sizes. Therefore, the SJAs designed are of a scale larger than that stated above and use a combination of machining and stainless-steel additive manufacturing to ensure appropriate quality of the components used. The finished prototype is then piezoelectrical-driven by a PZT diaphragm or electromagnetic-driven by a vibration generator, depending on the test. A sinusoidal input signal is provided by a function generator that is amplified before being supplied to the SJA.

Hotwire anemometry is a measurement technique widely used in the study of fluid mechanics and in several SJA studies (Smith & Glezer, 2005; Bhapkar et al. 2014). Although inherently an intrusive method, at the scale of the SJA it offers better resolution than other non-intrusive measurement techniques such as conventional PIV (Ramasamy et al. 2010). Information such as the synthetic jet velocity profiles, streamwise jet development and power spectral density are obtained for various orifice geometries and cavity dimensions.

Different from most of the existing work in the study of SJA self-noise, acoustic measurements were conducted in an anechoic chamber facility. This facility provides a low noise environment, crucial for the accurate study of SJA self-noise generation and reduction. The PZT diaphragm used in the first part of the research presented generates excessive noise of up to 70 dB, making it difficult to differentiate from non-diaphragm related noise sources. This is especially impractical for the study of lobed orifices and for this reason electromagnetic actuation is later used to characterise the aeroacoustics of the single chamber SJA. The electromagnetic transduction system consists of a vibration generator that sets a latex diaphragm in motion, where the diaphragm noise is much lower, making it easier to define the acoustic characteristics of the SJA and measure the effects of lobed orifices and varying actuator geometry.

An additional experimental component is the use of two flow visualisation methods. Dye flow visualisation captures the jet formation and flow development from various angles and views in the fluid domain without the need for expensive equipment, while giving valuable information on the interaction of the modified flow structures issuing from circular and lobed orifices. For this, a scaled up SJA is tested in a purpose-built water tank under quiescent conditions, where the operating conditions are also appropriately scaled to match those used in air. The second technique used is Schlieren visualisation. Schlieren visualisation is an optical flow visualisation method that relies on inhomogeneity in the fluid medium due to changes in refractive index caused by density changes in the flow. Such density changes can be caused by changes in temperature of the

flow medium or a mixture of different fluid media, each with a different refractive index. This method has been used in a wide range of SJA studies, proving to be as valuable in this work. Density changes are achieved by introducing a fluid of different density to air, in this case carbon dioxide (CO₂), near the orifice that is then entrained by the jet making the jet flow visible.

With these flow visualisation methods, valuable insight into the formation and changes in flow structures is gained that explain the noise generation mechanism, but also how they are attenuated using lobed orifices. Furthermore, they also identify changes in the jet power spectra to be a consequence of flow instabilities and breakup of large-scale structures that form into small-scale turbulent structures.

1.4 Publications and Conferences

Journals Papers

- Jeyalingam, J., Jabbal, M. (2018). Aeroacoustic characteristics of a circular orifice synthetic jet actuator in quiescent conditions, *Sensors and Actuators A: Physical*. Reviewer comments received; manuscript currently being revised.
- Jabbal, M., Jeyalingam, J. (2017). Towards the noise reduction of piezoelectrical-driven synthetic jet actuators, *Sensors and Actuators A: Physical*, 266, 273-284. [Impact factor: 2.499]

Conference Proceedings and presentations

- Jeyalingam, J., Jabbal, M. (2017). Noise reduction of synthetic jet actuators for active flow control, Airbus DiPaRT Symposium, Bristol, 20-22 November 2017.
- Jeyalingam, J., Jabbal, M. (2017). Flow structures of synthetic jet actuators using lobed orifices, 15th ERCOFTAC Osborne Reynolds Day, Manchester, 14 July 2017.

- Jeyalingam, J., Jabbal, M. (2017). Flow structures of synthetic jet actuators using lobed orifices, ERCOFTAC European Drag Reduction and Flow Control Meeting, Rome, 3-6 April 2017.
- Jeyalingam, J., Jabbal, M. (2016). Optimization of synthetic jet actuator design for noise reduction and velocity enhancement, AIAA 2016-4236, 8th AIAA Flow Control Conference, Washington D.C, 13-17 June 2016.

1.5 Organisation of the Thesis

This thesis aims to investigate the self-noise generation of synthetic jet actuators and reduce this noise using passive and active noise control measures, while minimising the effect this may have on the fluidic performance. The work conducted to meet the research objectives are documented in different chapters that are briefly presented in this section.

- **Chapter 2** presents a detailed literature review focusing on flow separation and different flow control technologies and their advantages and disadvantages. Synthetic jet actuator design and operation are discussed with an overview on SJA self-noise generation. Finally, the different noise generation methods are briefly introduced.
- **Chapter 3** discusses preliminary experiments carried out using an existing 3D printed double chamber SJA that uses lobed orifices and antiphase operation of two jets for noise reduction. These experiments help to establish an improved design rationale for the actuators.
- **Chapter 4** provides details about the experimental facilities and different methods used throughout to assess the qualitative and quantitative nature of synthetic jets.

Results and their discussion are separated into two sections, each dealing with a different actuation method.

- **Chapter 5** presents results of both the single and double chamber SJA driven by a piezoelectric diaphragm. The results shown are regarding the fluidic and acoustic performance of the actuators using the active (anti-phase operation) and passive (lobed orifice) noise control measures. Dye flow visualisation is also used to study the flow structures formed by lobed orifices and the effect they have on the jet development.
- **Chapter 6** investigates the self-noise generation of SJAs driven electromagnetically, where the noise contribution from the diaphragm is greatly

reduced compared to piezoelectric actuation. This allows the characterisation of SJA aeroacoustic characteristics and to study the effectiveness of lobed orifice on noise reduction. Furthermore, the effect that SJA geometric parameters have on SJA self-noise are investigated.

- **Chapter 7** presents concluding remarks on the work carried out and suggestions for future work.

2 Literature Review

2.1 A Brief History of Flow Control

The need for flow control on aircraft comes from adverse conditions, such as flow separation or skin friction drag on critical aerodynamic surfaces and structures vital for safe and efficient operation of the aircraft. These implications can range from loss of lift to unwanted noise generation or reduced efficiency and performance of the aircraft. In this section the basic principles of flow separation and passive and active flow control measures are briefly presented and compared with their advantages and disadvantages discussed. The study presented here is of course on synthetic jet actuators with a focus on the performance and acoustic optimisation for practical application. Various types of possible noise sources of a synthetic jet actuator are also presented, and possible noise control measures are explored.

2.1.1 Flow separation on wings and its implications

Consider air flow over an aerofoil, which due its viscosity, μ , adheres to the surface and comes to a halt, i.e. its velocity is zero. This condition where the velocity at the wall is zero is known as the ‘no slip’ condition and with increasing distance normal to the surface, the velocity gradually increasing to that of the free stream. The region between the surface and free stream is called the boundary layer and it grows in thickness (δ) with increasing downstream distance along the aerofoil surface. The presence of friction is a result of the local shear stress, τ , acting tangential to the surface, which according to Newton’s law of shear stress is proportional to the velocity gradient du/dy , as given in Eq. (1):

$$\tau = \mu \frac{du}{dy} \quad (1)$$

Where u is the streamwise velocity, tangential to the wing, and y is the wing-normal coordinate. However, air flowing over a wing is subjected to an adverse pressure gradient, especially at higher angles of attack. The combined effect of the adverse pressure gradient and shear forces lead to the stagnation of the boundary layer that in

turn causes the flow to separate from the surface. At this point the pressure distribution over the aerofoil drastically changes and creates an increase in pressure drag. Given even longer exposure to such conditions, flow reversal (Figure 2.1) will eventually result that further adds to the drag force.

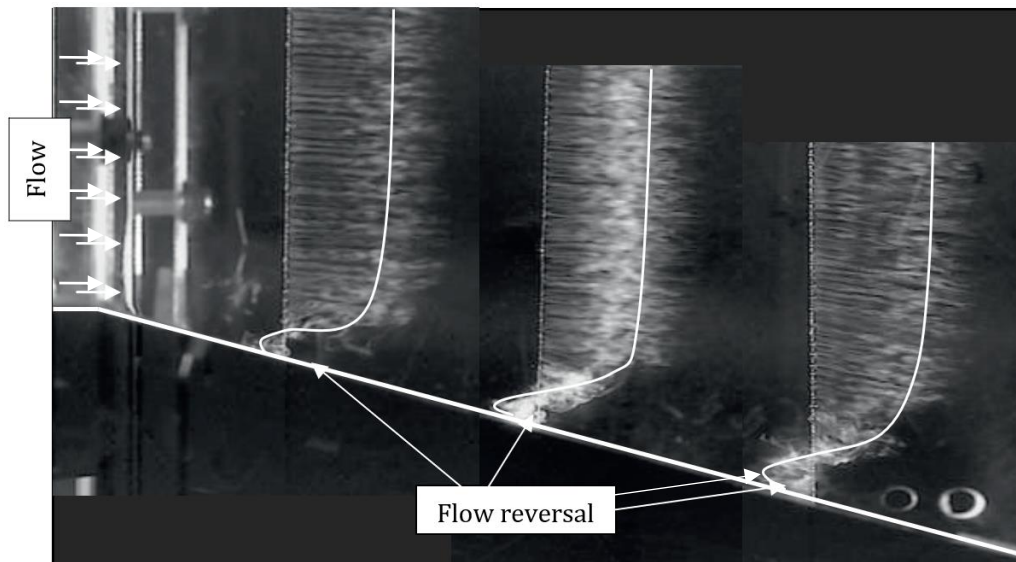


Figure 2.1. Flow separation and reversal of flow on a slope (Mukut et al. 2014)

The concept of boundary layer and the eventual flow separation from a surface was first introduced by Ludwig Prandtl in 1904 (Prandtl, 1904) revolutionising the subject of fluid dynamics. This phenomenon on an aircraft wing can have serious implications since lift generation is interrupted, causing stall. Another less dangerous yet important concern with current and future environmental goals is the generation of separation noise, an effect prevalent in various locations on an aircraft, such as the wings, wing struts and undercarriage.

2.1.2 Traditional flow control

The earliest application of boundary layer control is attributed to Prandtl, who demonstrated the use of suction to suppress separation on one side of a cylinder. In the 1920s research in boundary layer control for lift enhancement became popular with Baumann patenting a lift enhancing device in 1921, that consists of air jets emanating from slots on a wing (Williams & MacMynowski, 2008; Betz, 1961). The effect of boundary layer control on the lift and drag of a 2D aerofoil with a backward opening slot was investigated (Knight & Bamber, 1929), in which a 96% increase in maximum

lift and 27% decrease in minimum drag were achieved, resulting in an increase of 151% in the ratio between the two (L/D).

Although research on boundary layer control on aerofoils using distributed suction already began in the 1920s (Ackeret et al. 1925; Schrenk, 1928; Schrenk, 1931), it wasn't until 1940 that this concept was tested in full flight conditions, yielding promising results. Boundary layer suction proved effective with a 25% increase in lift coefficient on a NACA 64₁A212 aerofoil reported (Nuber & Needham, 1948). Later, in the 1950s, distributed suction was used for turbulent boundary layer control on a TG-3A glider resulting in a lift coefficient increase of 65% from an original value of 1.38 (Cornish, 1953). Distributed suction was soon after applied in powered flight on a L-21, obtaining a maximum flaps-down lift coefficient of 3.98 (Raspet et al. 1956).

With advances in jet engine technology and push towards supersonic flight, wing design dramatically changed, making them thinner and shorter which as a result increased their wing loading. Separation on thin wings often occurs at the leading edge, potentially causing stall. In the 1960s blowing of steady jets of air over flap surfaces was used to delay the onset of separation and stall. Some popular examples of aircraft that used such methods are the F-104 Starfighter or Grumman F9F-4, which helped reduce the landing speed and take-off distance. However, with increasing demands and expectations these traditional flow control systems could not keep up and aircraft designers began seeking alternatives. This came down to two primary reasons: excessive technical complexity (plumbing systems required and additional weight) and the low efficiency for meaningful performance enhancement (Greenblatt & Wygnanski, 2000).

With the interest for active flow control (AFC) increasing again new and improved systems using blowing and suction emerged. The use of microblowing through a perforated (permeable) wall on a flat plate was studied (Figure 2.2a) achieving a total plate drag reduction of 4.5-5% (Kornilov & Boiko, 2012). In that study the authors found flow regions on the plate with reduced friction, which in a following study they excluded from microblowing (Figure 2.2b) with a focus on distributed boundary layer characteristics and increasing the system efficiency by reducing the energy cost

(Kornilov & Boiko, 2014). The result of their optimised setup using the same airflow rate as in their previous study was a total drag reduction of 15-25%.

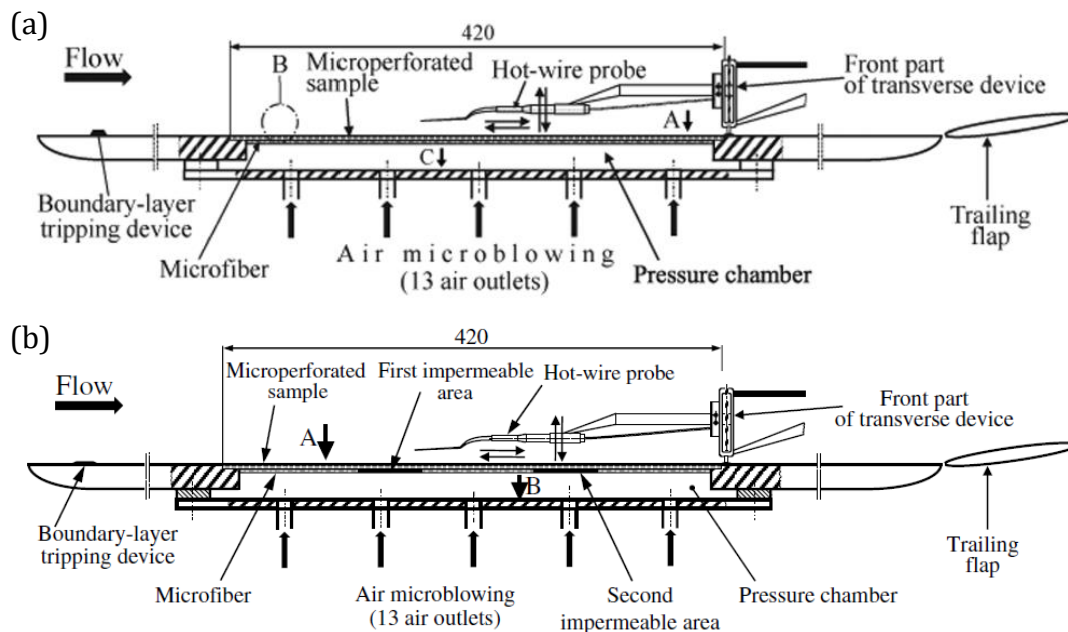


Figure 2.2. Flat plate using microblowing through (a) permeable wall (Kornilov & Boiko, 2012) and (b) permeable sections interlaced with impermeable ones (Kornilov & Boiko, 2014)

However, the issues of system complexity, weight and reliability for the delivery of mass flow from a source, remain unresolved and as such passive control measures continue to be implemented on modern aircraft.

2.1.3 Passive flow control

Today's civil transport aircraft evolved over time from basic designs established in the 1950s and it is becoming less cost-effective to optimize the aircraft geometry to enhance aerodynamic performance (Bieler et al. 2006). Due to their simplicity, passive flow control measures continue to be widely used on aircraft. Examples of passive devices include vortex generators on wings to delay the onset of stall riblets on the wing surfaces for the reduction of friction drag (Kwing, 2000; Bechert & Bartenwerfer, 1989; Mele et al. 2016) and as seen on recent aircraft used in air races helping them increase efficiency by 4% and speed up to 1.56 % (Riblets and Motor Sports, 2018). Another method is to use strakes applied on the nose or between wing and fuselage of aircraft to improve an aircraft's lifting and longitudinal stability characteristics, as seen on F-16, F/A-18 or Mig-29 (Nikolic, 2005; Fischer et al. 1998).

One of the most extensively used passive flow control devices are vortex generators (VG) first introduced in 1947 (Taylor, 1947). These wing-like tabs are embedded in the surface of wings or other bodies, directly placing them in the boundary layer, and generate tip vortices that entrain higher momentum fluid from outside the boundary layer into the near wall region. This process energizes turbulence in the boundary layer (Williams & MacMynowski, 2008) and can prevent or reduce flow separation. Vortex generators, used in flight tests in 1952 (McFadden et al. 1952), were able to successfully improve stability and manoeuvrability of a F-86A aircraft at high transonic speeds. The effect of vortex generators on the total drag of a 1:72 scale model of a C-130 were investigated, with appreciable drag reduction observed depending on the configuration (Calarese et al. 1985). It was shown from a numerical investigation that a maximum 5% drag reduction was possible when using an array of VGs on the back-ramp of a heavy-class helicopter fuselage (Gibertini, et al., 2015). To reduce the parasitic drag generated by VGs and increase their efficiency, low-profile VGs have been developed over time that have a height of between 10-50% of the boundary layer thickness, δ (Lin, 2002). These include different variations of VGs such as submerged VGs (Lin et al. 1990), micro VGs, sub boundary layer VGs and microvanes. In recent times micro VG's have become popular in high speed flow control applications to overcome the adverse effects of separated flow due to shock boundary layer interactions (Lu et al. 2012; Martis & Misra, 2017; Estruch-Samper et al. 2015) .

2.1.4 Active flow control actuator

The first application of Active Flow Control (AFC) using actuators was presented by Schubauer and Skramstad (1948), who were studying the effect of oscillations in a laminar boundary layer along a flat plate undergoing transition to turbulence. They developed an electrodynamic ribbon oscillator placed centrally on a flat plate, where the required tension to maintain the ribbon stability to avoid unwanted vibration was applied using rubber bands. The ribbon was excited by the interaction of a changing electromagnetic force, achieved by applying an alternating current to the ribbon, and a permanent magnet on the other side of the plate. The authors used two hot wires to measure the change in disturbances caused by the oscillating ribbon. They also used

this setup to experiment with feedback control, where the amplified hot wire output is connected to the ribbon.

This is the first demonstration of modern AFC for the control of small-scale flow instabilities using an actuator. Today many new and novel ideas exist for a wide range and different types of applications requiring flow control that utilise actuators and sensors to achieve this.

A wide range and types of actuators for AFC have been developed over time for various applications. These devices make use of different transduction schemes, such as piezoelectric, electromagnetic or plasma, depending on suitability for the task.

An actuator is intrusive by definition, as it outputs flow perturbations for an electrical input. The ideal actuator does this without producing any additional unwanted outputs, such as electromagnetic interference, sound or heat, while providing adequate bandwidth, robust operation, low cost and energy efficiency (Cattafesta & Sheplak, 2008). Table 1 provides a summary of common flow control actuators and their advantages and disadvantages.

Table 1. Summary of active flow control actuators (Cattafesta & Sheplak, 2008)

TYPE	ADVANTAGES	DISADVANTAGES
FLAPS	<ul style="list-style-type: none"> • Simple design amenable to different frequency ranges of interest • Can produce spanwise or streamwise vorticity 	<ul style="list-style-type: none"> • Product of max deflection and bandwidth is constant • Susceptible to fluid loading
SYNTHETIC JET ACTUATOR	<ul style="list-style-type: none"> • Requires no external flow source • Amenable to various types of drivers and sizes 	<ul style="list-style-type: none"> • Peak velocities typically limited to low to moderate subsonic speeds
PULSED JETS	<ul style="list-style-type: none"> • Capable of high velocities with either fast time response OR high-frequency response but generally not both 	<ul style="list-style-type: none"> • May not be amenable to feedback control due to either frequency-or time-response limitations • Requires an external flow source
VORTEX GENERATOR JET	<ul style="list-style-type: none"> • Good control authority similar to mechanical vortex generators • Amenable to pulsing implementations 	<ul style="list-style-type: none"> • Many adjustable parameters (e.g. momentum ratio, pitch and yaw angles) make it non-trivial to optimize • Requires an external flow source
PLASMA	<ul style="list-style-type: none"> • Easily installed on models (arrays) • Can produce spanwise or streamwise vorticity • No moving parts • Able to modify flow over surfaces near atmospheric conditions 	<ul style="list-style-type: none"> • Limited velocity output • Requires high voltage (kilovolts)
COMBUSTION	<ul style="list-style-type: none"> • Capable of producing large perturbations in high speed flows 	<ul style="list-style-type: none"> • Currently limited to relatively low frequencies – a few hundred hertz • Requires combustion
SPARK JET	<ul style="list-style-type: none"> • All solid-state device capable of producing large perturbations in high-speed flows 	<ul style="list-style-type: none"> • Potential issues associated with EMI, acoustic level and high temperature

1. *Electromechanical-fluidic actuators*

- **Synthetic jet actuator (SJA)** – A typical SJA consists of a cavity enclosed on one side by an oscillating diaphragm or piston and the other side an orifice plate. The oscillations of the diaphragm displace volume of air in the cavity causing pressure fluctuations that result in air being ejected and ingested again periodically through the orifice. The resulting jet is thus formed from the ambient fluid with a zero-net mass addition but a non-zero momentum flux. This feature makes SJAs particularly attractive for flow control applications as the system is compact and doesn't require an external air supply, that would inevitably add weight and take up space.

- **Piezoelectric flap** – These devices serve a wide range of flow control applications, such as the control of flow separation, free shear flow and flow-induced cavity oscillations (Mathew, Sankar, Sheplak, & Cattafesta, 2006). Depending on the design of the actuator, spanwise or streamwise vortical perturbations are introduced into the flow. This is achieved through the periodic oscillation of a cantilever shim in the flow that is excited by a piezoceramic material with an alternating voltage applied to it.
- **Pulsed jets** – Pulsed jets exist in either “on” or “off” state with the jet flow having the characteristics of a positive square wave. Further control over the jet flow can be had by varying the duty cycle, which is a percentage of the time the jet is on during an actuation cycle. Unlike SJAs, there is no suction flow and pulsed jets require an external fluid source, such as engine bleed air, which makes them less desirable as complexity increases. More recently micro pulsed jets have been studied, that require significantly less mass flow allowing for closer spacing and increased efficiency (Cattafesta & Sheplak, 2008). Other applications of (micro) pulsed jets include separation control on complex engine inlet ducts (Garnier, 2015) or diffusers (Kumar & Alvi, 2006). However, recent developments have reported pulsed jets on compressor blade cascades that require no external energy injection. This is achieved by generating a jet through the pressure difference between the pressure and suction side of the blade and modulating using a micro device (Chen et al. 2017).
- **Vortex generator jets (VGJ)** – These devices have been of interest for applications in turbomachinery, e.g. axial compressor (Li et al. 2017) and turbine blades (Benton et al. 2013; Benton et al. 2014). By skewing and pitching the jet axis relative to the free stream flow direction, co-rotating vortices are generated. Like conventional vortex generators, VGJs promote momentum exchange between the free stream flow and boundary layer.

2. *Electro-fluidic actuators*

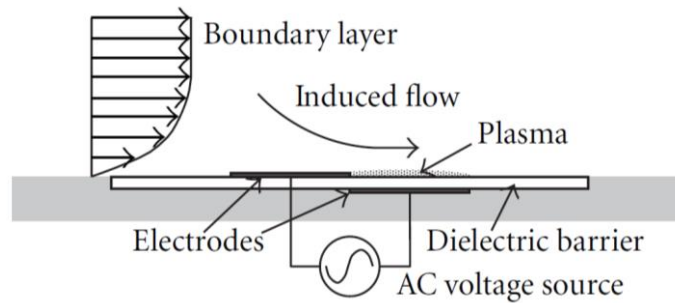


Figure 2.3. Schematic of plasma actuator (Matsunuma & Segawa, 2012)

One of the more popular devices is the Single Dielectric Barrier Discharge (SDBD) actuator, which consists of a dielectric layer sandwiched between a top and bottom electrode (De Griorgi et al. 2017). When high AC voltages (5-20 kV) at high frequencies (1 kHz – 50 kHz) are applied between the two electrodes, a layer of non-thermal, glow discharge plasma across the dielectric surface is formed with a tangential velocity component (Shyy et al. 2002; Matsunuma & Segawa, 2012; De Griorgi et al. 2017). More recent studies have shown a reduction in separation area and lift increase on a NACA 0015 aerofoil at an angle of attack of 15°(Clifford et al. 2016).

3. *Electrochemical-fluidic actuators*

This is a high velocity output combustion-based actuator that exploits the chemical energy of a gaseous fuel and oxidiser mixture to generate a high momentum jet. The actuator is basically an amplifier, where during the actuation cycle a premixed low momentum fuel/oxidiser mixture fills a chamber that is ignited by a spark generating a high pressure burst inside the chamber. As a result of this rapid pressure increase inside the chamber, a high-speed pulsed jet is ejected through one or multiple orifices (Crittenden & Raghu, 2009). The combustion process only takes a few milliseconds with the chamber pressure dropping back to a baseline pressure for refill with the reactants after which the cycle repeats again (Crittenden et al. 2001)

The high jet velocity makes these actuators particularly attractive for high speed applications. However, a limiting factor is the finite cycle duration that doesn't permit higher actuation frequencies ($f_a > 1$ kHz) (Cattafesta & Sheplak, 2008). Another issue is the requirement for an externally supplied fuel mixture that complicates the system architecture.

4. Electrothermal-fluidic actuators

Plasma synthetic jet actuators, sometimes referred to as SparkJet actuators, generate high speed jets through an electric discharge in a small cavity. The discharge causes rapid pressurisation inside the cavity through electrothermal heating. Pressurised air within the cavity is then ejected through an orifice in the form of a high speed, pulsed plasma jet. After discharge the cavity cools down allowing ambient air to enter the cavity again through the orifice. Investigations of such an actuator has reported jet velocities of 250 m/s for discharge energies of 30 mJ per jet and frequencies of up to 5 kHz (Narayansawamy et al. 2010). Furthermore, the actuator was tested in Mach 3 crossflow with the jet ejected normal to the free stream flow and it was shown that the jet penetrates 1.5 boundary layer thicknesses into the crossflow.

However, potential issues arising from electromagnetic interference, efficiency and high temperatures requires further research and development of this concept.

2.2 Synthetic Jet Actuators

2.2.1 Comparison between continuous jets and synthetic jets in quiescent conditions

Flow control by blowing continuous jets tangentially to the free stream flow over surfaces has been used for a long time. It is the addition of linear momentum to the boundary layer, especially near the wall, that helps avoid or delay the onset of flow separation. Lee and Reynolds (1985) and Reynolds et al. (2003) in their experiments showed that appropriate nozzle excitation both axially and circumferentially causes a single continuous jet to undergo a splitting process called "bifurcation" and explode into

a shower of vortex rings called “blooming”. These effects have shown to exhibit much greater mixing ability than continuous jets. In a similar fashion, pulsed jets generate flow structures that can lead to spatial evolution that is significantly different to that of a continuous jet with the same orifice geometry and time-averaged streamwise momentum flux (Glezer & Amitay, 2002). A unique feature of synthetic jets is that they are formed from the working fluid of the flow system they are deployed in making them more versatile. It has been shown that the spreading rate, S_b , for synthetic jets is larger than that of continuous jets (Cater & Soria, 2002) (≈ 0.13 and ≈ 0.10 respectively, Figure 2.4). The benefits of such systems are not just limited to their simplicity, but also the unsteady oscillating nature of the jets generated that have shown to enhance mixing.

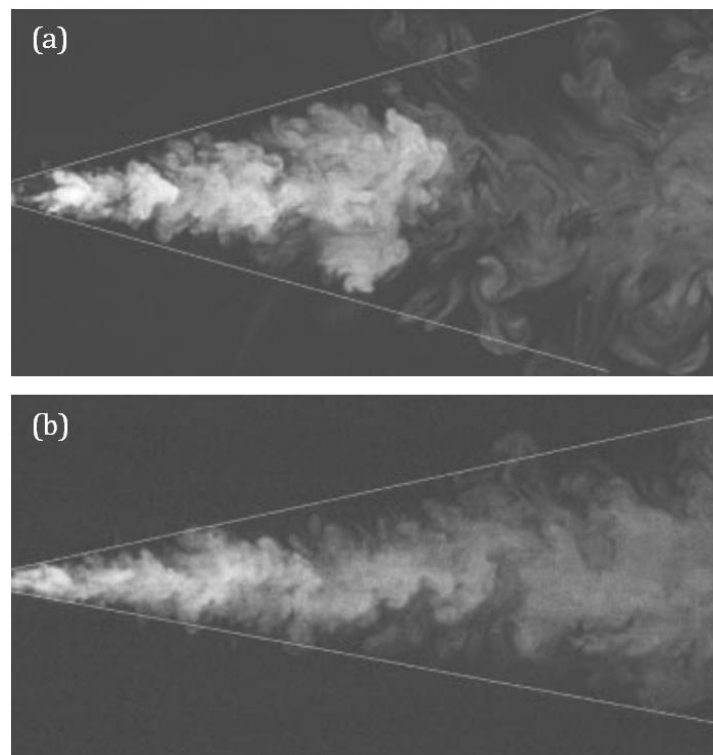


Figure 2.4. Fluorescent dye visualisation of (a) a synthetic jet and (b) an equivalent continuous jet with lines marking the apparent mean boundary of the dye flow (Cater & Soria, 2002)

2.2.2 Comparison between continuous jets and synthetic jets in crossflow

Poisson-Quinton (1948) showed that instead of mass addition it was the addition of momentum that determined the effectiveness of boundary layer separation control. This has led to the introduction of the momentum-coefficient, c_{μ} , which to date remains the standard measure of relative momentum addition. To avoid any detrimental effects

caused by steady blowing, c_{μ} is maintained above 2% (Seifert et al., 1996). Then, in the 70's it was shown that acoustic excitation could also be used to enhance momentum near the surface (Collins & Zelenevitz, 1975). This is achieved through the transfer of momentum from the free-stream to the wall region, without requiring steady blowing. Excitation frequencies used have been shown to be effective over a large range. However, a study by Zaman et al. (1992) showed that the optimum Strouhal number can be orders of magnitude lower than that related to the linear inviscid stability of the separated shear flow, if the excitation amplitude is increased. It is widely accepted that large coherent, vortical, spanwise structures play a crucial role in the mixing layer of shear flow and are responsible for momentum transfer across its extent. It was shown that small amplitude excitation at the origin of a shear layer can significantly change its rate of spreading and entrainment of surrounding fluid (Oster et al., 1978). Momentum addition can therefore be achieved using devices that interact with the flow hydrodynamically to add momentum in an oscillatory, instead of steady, fashion. Periodic perturbations can be introduced through slots or orifices driven by e.g. acoustic drivers, piston, valve systems or piezoelectrically driven diaphragms (Greenblatt & Wygnanski, 2000).

A previous study carried out by Milanovic and Zaman (2005) showed that for synthetic and continuous jets in crossflow the mean velocity distribution, streamwise vorticity and turbulence intensity are the same. In work carried out by Seifert et al. (1993), oscillatory blowing over a flapped NACA 0015 aerofoil was tested and it was suggested that the modulated blowing greatly improved the aerofoil performance much more efficiently than using steady blowing. In a more recent study (De Giorgi et al. 2015), synthetic and continuous jets were compared on a NACA 0015 and a compressor cascade. It was shown that the synthetic jet actuator generated larger vortex structures in the shear layer that remained attached to the aerofoil for longer than those generated by the continuous jet. Moreover, according to Seifert et al. (1996) using periodic addition of momentum for separation control, at frequencies just higher than the natural vortex shedding frequency, can result in 90-99% reduction in the momentum required when using steady blowing for the same gains in performance.

Controlling the trajectory of a synthetic jet and flow structure is always a challenge since too high a jet velocity will result in the jet and flow structures exiting the boundary layer within a short downstream distance. In order to direct the jet trajectory better, McCormick (2000) used directed synthetic jets with a curved neck in the downstream tangential direction and was able to completely suppress boundary layer separation. When using synthetic jets, low momentum fluid is drawn into the actuator during the suction phase, forcing the higher momentum free stream fluid to move towards the wall. During the blowing phase, high momentum fluid is ejected from the SJA orifice into the boundary layer, compensating for some of the momentum deficit and reducing the momentum thickness in this region (Ramasamy et al. 2010).

In work conducted on the optimisation of passive flow control devices it was noted that an “optimal” flow structure would transfer momentum towards the wall, increasing the skin friction (Godard & Stanislas, 2006). In SJAs, counter rotating vortex pairs are formed at the orifice exit that enhance mixing near the wall region. Depending on the operating conditions of the SJA one can generate different types of vortex structures and control their trajectory as to remain within the boundary layer. An experiment using PIV measurements to study various operating conditions and flow structures (hairpin, stretched and tilted vortex rings) and their effect on a zero-pressure gradient boundary layer was conducted to assess their potential in separation control quantified by the increase in shear stress near the wall (Jabbal & Zhong, 2010). This experiment showed that stretched vortex rings offered the best combination of near wall fluid mixing, persistency, and low rms fluctuations for potential separation control applications.

Interest and research in the use of oscillatory jets such as those formed by SJAs for implementation in flight conditions continues. Guoqing et al. (2016) integrated two SJAs, with varying jet angle, at 15% and 40% chord length of a NACA 0021 aerofoil, from which it was found that actuation near the leading edge of the aerofoil dramatically increased maximum lift coefficient and stall angle. Further to this, hot wire and force balance measurements using two arrays of SJAs integrated in a low speed wing model were conducted (Tang et al. 2014; Salunkhe et al. 2016). The results showed a 27.4% increase in lift coefficient, a 19.6% reduction in drag coefficient (Figure 2.5) and

maximum SJA effectiveness at a nominal actuation phase angle of 180° , coinciding with the point of maximum blowing.

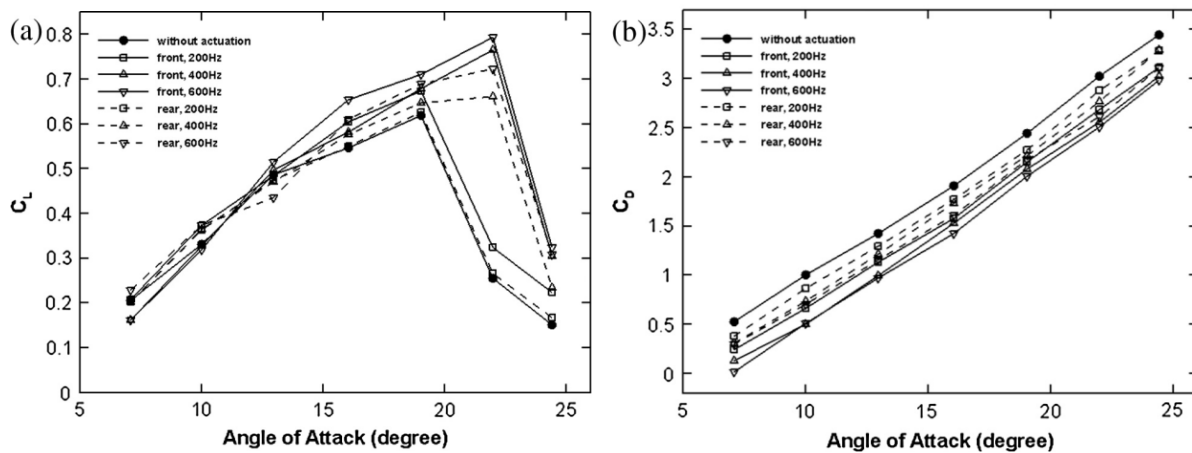


Figure 2.5. Variation of (a) lift coefficient, C_L , and (b) drag coefficient, C_D against angle of attack with and without SJAs (Tang, Salunkhe, Zheng, Du, & Wu, 2014)

2.2.3 Development of synthetic jet actuators

The idea of constructing a synthetic turbulent boundary layer using coherent flow structures was already proposed by Savas and Coles (1985), which they achieved by generating periodic turbulent spots at the leading edge of a flat plate. However, their system for generating these flow disturbances varies greatly from using a SJA, as they periodically protrude a pin from a flat plate into the flow resulting in the formation of hairpin vortices. Ingard and Labate (1950) observed jet formation consisting of trains of vortex rings on either side of an orifice plate attached to a circular tube, where an oscillating velocity field is generated using acoustic excitation. A typical SJA, on the other hand, consists of a cavity enclosed on one side by an oscillating driver (e.g. piston or diaphragm) and an orifice on the other side through which air is periodically expelled and drawn in again. This leads to the formation of a train of discrete vortical structures, which form a jet-like flow with complex spatial and temporal characteristics (Glezer & Amitay, 2002). Using a low frequency mechanical piston actuation, zero net mass flux jets with mean velocities of up to 17 m/s were generated (Mednikov & Novitskii, 1975).

Arrays of actuators can be integrated towards the trailing edge of a wing or flaps (Jabbal et al. 2013) as shown in Figure 2.6.

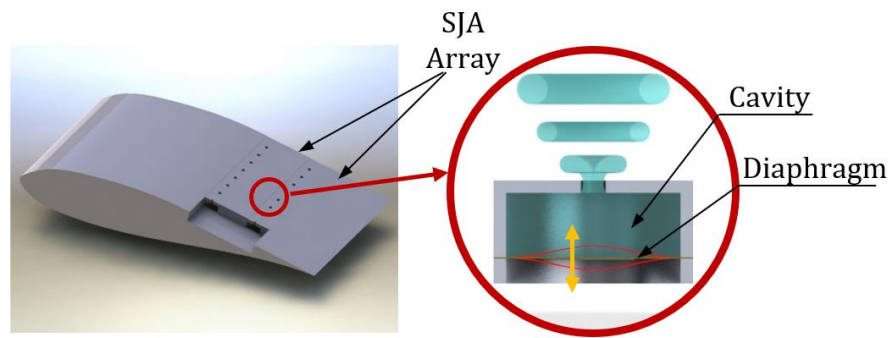


Figure 2.6. Application of SJA on aircraft (left) and typical configuration of a SJA (right)

As mentioned earlier a variety of actuation methods exist to drive a SJA, where the most commonly used methods include piezoelectric, plasma and electromagnetic actuation. The work presented here mostly uses either an electromagnetic transducer, as seen in Gil & Strzelczyk (2016), for its low acoustic output, or a piezoelectric transducer, due to its small size and efficiency. Piezoelectric transducers make the design of small and compact SJAs possible using cheap and readily available, off-the-shelf piezoelectric diaphragms. Piezoelectrically driven SJAs can output a jet over a large range of actuation frequencies. Peak jet velocities of <100 m/s are generally reported, however further studies reached peak velocities of 130 m/s with a velocity optimised SJA (Crowther & Gomes, 2008) and even a peak velocity of 211 m/s was reported (Van Buren et al. 2016).

2.2.4 Operation of synthetic jet actuators

2.2.4.1 Formation of synthetic jets

An oscillating diaphragm inside a cavity causes oscillatory output volumetric flow rate through an orifice. As the air exits the orifice, a vortex sheet is formed that, due to its self-induced velocity, may cause the leading edge of this sheet to curve and roll up to form counter-rotating vortex pairs (Auerbach, 1987; Crook, 2002), as shown in Figure 2.7. As these structures travel downstream they develop instabilities and eventually transition to turbulence, which causes them to lose their coherence through breakup, becoming indistinguishable from the mean jet flow.

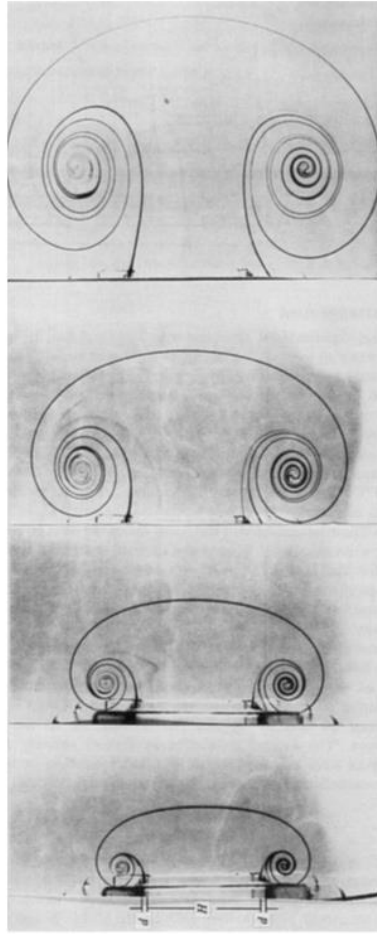


Figure 2.7. Vortex roll-up dyed in the mid-plane at the outlet edge (Auerbach, 1987)

Pullin (1979) considered a moving piston in a tube to impulsively eject fluid to form vortex rings and used the similarity theory of edge vortex growth (Saffman, 1978) in conjunction with this to model the vortex ring formation. Glezer (1988) looked to define conditions under which laminar and turbulent axisymmetric vortex rings, such as those previously studied (Didden, 1979; Blondeaux & De Bernardinis, 1983), are generated using a momentary discharge of pressurised water into a tank using a fast annular-outlet solenoid valve. It was shown that axisymmetric vortex rings can be characterised by two primary dimensionless parameters: Stroke length, L , and jet Reynolds number, $Re_j = \bar{U}_0 d / \nu$.

In his work momentary discharge of a volume of fluid through an orifice of diameter d is modelled as a uniform cylindrical slug moving at a constant velocity U_0 for a time T_0 . The slug length is the previously mentioned Stroke length, L_0 , and is given by Eq. (2):

$$L_0 = U_0 T_0 \quad (2)$$

In cases where the exit velocity is not constant, such as synthetic jets where the velocity variation is sinusoidal, it is more appropriate to use the time averaged jet velocity defined by

$$\bar{U}_0 = \frac{1}{T_0} \int_0^{T_0} \tilde{u}_0(t) dt. \quad (3)$$

Where $\tilde{u}_0(t)$ is the instantaneous space averaged jet velocity at the orifice exit (Zhong, et al., 2007). Using this definition for jet velocity for synthetic jet actuators gives

$$L_0 = \int_0^{T_0} \tilde{u}_0(t) dt = \bar{U}_0 T_0. \quad (4)$$

Normalising the stroke length using the orifice diameter, d , gives the dimensionless stroke length

$$L = \frac{L_0}{d}. \quad (5)$$

The second dimensionless parameter used to characterise synthetic jets is the Reynolds number, which commonly for synthetic jets is based on \bar{U}_0 and stroke length L_0 (Zhong, et al., 2007), (Jabbal, Wu, & Zhong, 2006) according to

$$Re_L = \frac{\bar{U}_0 L_0}{\nu}. \quad (6)$$

A synthetic jet consists of successive vortex pairs traveling downstream, where the spacing between consecutive pairs can be expressed as the inverse of Strouhal number, which in turn is equal to the dimensionless stroke length

$$St = \frac{fd}{\bar{U}_0} = \frac{1}{L}. \quad (7)$$

The dependence of synthetic jet formation and vortex roll-up on these parameters has been shown in several other studies. A threshold dimensionless stroke length of $L > 0.4$ exists for individual vortex ring formation (Didden, 1979). Similarly for round synthetic jets, formation stroke lengths of $L \approx 0.25$ (Milanovic & Zaman, 2005) and $L \approx 1$ (Smith et al. 1999) can be found, where the variation could be due to a difference in the orifice lip radius (Fugal et al. 2005). For a synthetic jet to form, the vortex structures formed at the orifice exit need to overcome the suction velocity during the ingestion part of the actuation cycle.

In a numerical study by Zhou et al. (2009), with the aim of providing a more in-depth understanding behind synthetic jet formation in quiescent conditions, it was found that the dimensionless vorticity of vortex roll-up depends on the dimensionless stroke length, Stokes number and thickness of the Stokes layer. In fact, the Stokes number determines the strength of vortex roll-up in a synthetic jet, therefore playing a crucial role in the jet formation process and is defined in Eq. (8) as:

$$S = \sqrt{\frac{2\pi f d^2}{\nu}} \quad (8)$$

The Stokes number affects the shape and thickness of the Stokes layer and the velocity profile of the jet (Figure 2.8). The same study found that for a synthetic jet with appreciable vortex roll-up to form, a minimum Stokes number of around 8.5 and a dimensionless stroke length $L > 4$ is required, which is similar to other studies that found the Stokes number required to be greater than 10 (Zhong, et al., 2007). Another study found that vortex roll-up only occurs for $S > 5$ and $Re_L > 100$ (Xia & Zhong, 2012). Furthermore, this study notes that based on flow visualisation tests four different flow regimes exist for synthetic jet operation:

- a) No jet formation
- b) Jet formed without vortex roll-up
- c) Vortex roll-up

d) Jet instability

For $S < 2$ or $Re_j < 2$ there is no jet formation regardless of L . Breakup of the flow structures due to flow instabilities is observed for $Re_j > 100$ or $Re_L > 500$, where Re_L is described by Eq. (6) and is based on the stroke length instead of d . Similar conditions for the different synthetic jet flow regimes were observed in a more recent study (Travnicek et al. 2015). It becomes clear based on this and other work that a relationship between vortex roll-up, S and Re_L exists (Figure 2.9). Here the total amount of circulation generated during the ejection of fluid from the orifice is determined by Re_L . The importance of these two quantities in the formation process of synthetic jets has been noted by many studies. Holman et al. (2005) have shown that the formation of synthetic jet is widely governed by the Strouhal number, St , which can also be expressed in term of S and Re_j in the form of $1/St = Re_j/S^2 > K$. This suggests that the inverse of St needs to be greater than a threshold value K , where $K \approx 1$ for two-dimensional jets and $K \approx 0.16$ for axisymmetric jets.

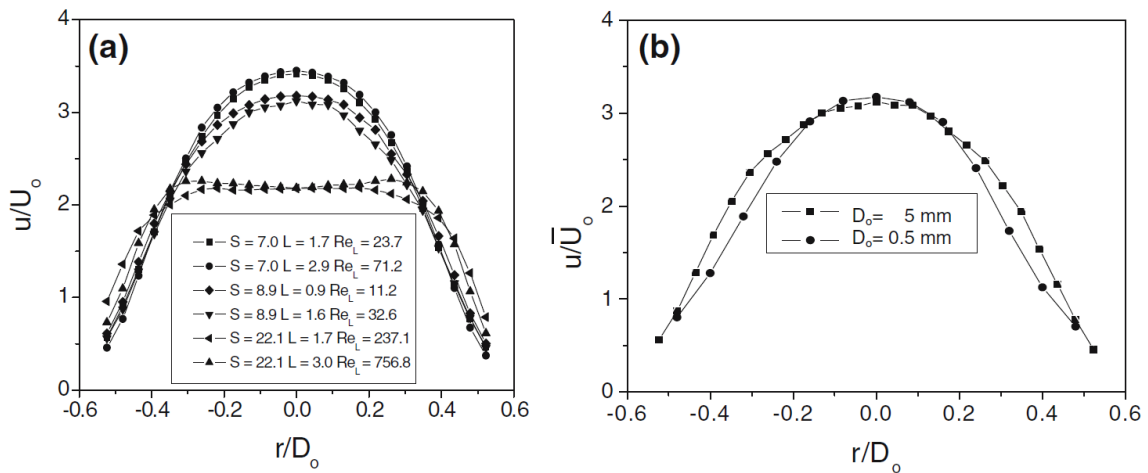


Figure 2.8. Exit velocity profiles of synthetic jets at phase of maximum blowing for (a) $d = 5$ mm and different Stokes numbers; and (b) $d = 5$ and 0.5 mm with $S = 8.9$ and $L = 1.6$ (Zhong, et al., 2007)

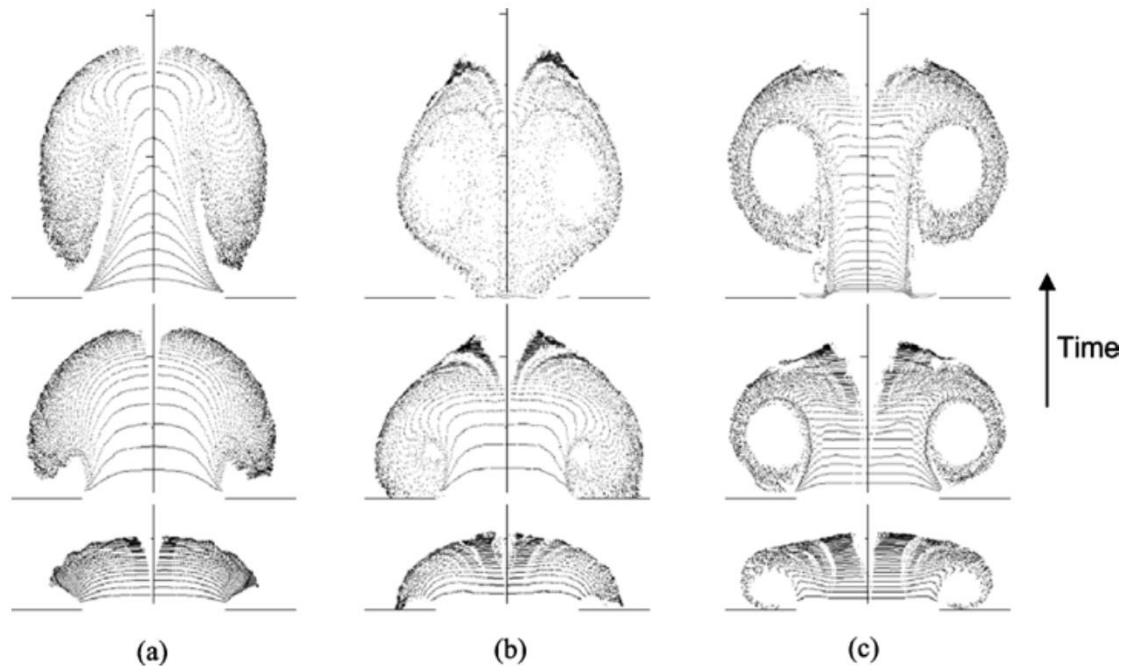


Figure 2.9. Vortex roll-up of synthetic jets issuing from orifice with $d = 5$ mm using particle tracing. Data was taken using PIV, where phases shown are arbitrary, (a) $S = 7$, $L = 2.9$, $Re_L = 71$; (b) $S = 12$, $L = 1.4$, $Re_L = 52$; (c) $S = 22$, $L = 3$, $Re_L = 756$ (Zhong, et al., 2007)

Using this knowledge various types of vortex structures can be formed using synthetic jet actuators in both quiescent and cross-flow conditions.

2.2.4.2 Importance of actuation frequency

Work on developing a Lumped Element Model (LEM) for predicting piezoelectric-driven SJA performance found that the system can be modelled as a coupled oscillator (Gallas et al. 2003; De Luca et al. 2014). This coupled oscillator system consists of an acoustic (Helmholtz) resonator and a diaphragm (mechanical), with the respective resonant frequencies f_H and f_D (Gallas, et al., 2003). The Helmholtz resonance is a result of a mass of air in the orifice neck oscillating at a certain frequency excited by the ‘springiness’ of the air in the cavity (Tang & Zhong, 2007). The SJA output is significantly increased when operating at either one of these resonant modes, Helmholtz or mechanical.

Dauphinee (1957) designed an air circulating pump based on the principle of acoustic wind, where an oscillating speaker diaphragm attached to a cavity-pipe system, like a SJA, generates pulses of air that are expelled through a pipe. In this early work, it was noted that to optimise the device pumping rate the system should be designed to

operate at the combined system resonant frequency, which includes the speaker diaphragm, cavity and pipe. Similarly, in SJA's, coupling has two primary effects: it modifies the nominal Helmholtz and mechanical resonance frequency and it introduces cross-linear reaction terms driving mutually the oscillator (De Luca et al. 2014). This effect is illustrated in Figure 2.10 and was reported in several other studies to date (Crowther & Gomes, 2008; Gomes et al. 2006; Lin et al. 2014). While the mechanical resonant frequency depends on the mechanical properties of the materials that make up the diaphragm, the Helmholtz resonant frequency is determined by the actuator geometry and is given by Eq. (9):

$$f_H = \frac{a}{2\pi} \sqrt{\left(\frac{D_o}{D_c}\right)^2 \frac{1}{Hh}} \quad (9)$$

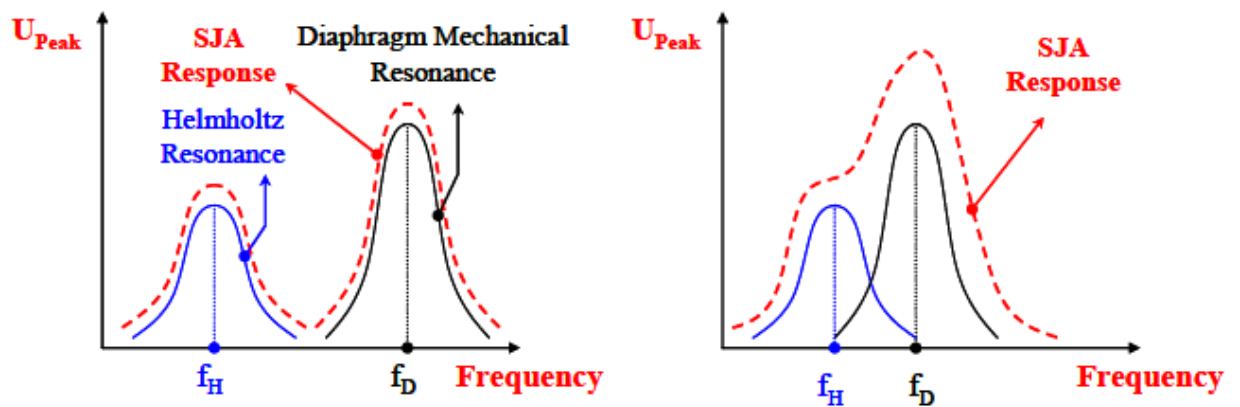


Figure 2.10. SJA frequency response with the Helmholtz and diaphragm resonance shown for (a) uncoupled and (b) coupled system (Gomes et al. 2006)

From Eq. (9) the dependence of the Helmholtz resonance frequency on the orifice and cavity geometry becomes evident.

2.2.5 Design of synthetic jet actuators

2.2.5.1 Cavity

The cavity height, diameter and shape have been shown to play a vital role in the overall performance of an SJA. The cavity usually takes up the largest percentage volume of the overall actuator size and easily becomes the design constraint that challenges actuator

design and integration for some applications where closely spaced actuator arrays are required. In such cases the cavity alignment needs to change so that the neighbouring cavities overlap (Jabbal et al. 2013) as shown in Figure 2.11, or the layout of the SJA geometry may need changing with the orifice adjacent to the diaphragm.

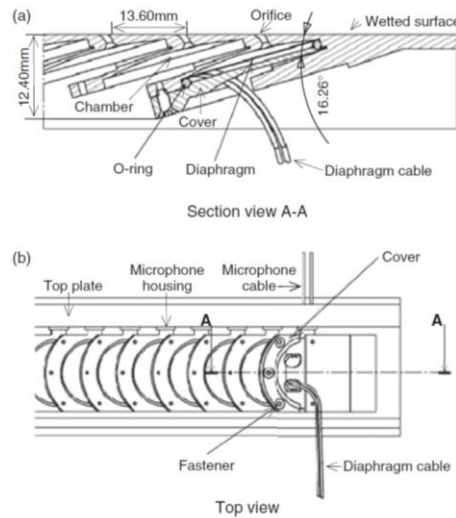


Figure 2.11. Arrangement of inclined opposite SJA array (Jabbal et al. 2012)

When considering steady incompressible flow and a cavity height larger than the cavity diameter, for a fixed diaphragm displacement the jet exit velocity is independent of the cavity height. This, however, is not the case in reality and it was found that decreasing the cavity height results in an increased jet exit velocity. In fact, for piezoelectric driven SJAs it was found that the jet velocity can be maximised by reducing the ratio of volume swept by the diaphragm to the volume of the cavity, which is achieved by reducing the cavity height (Gomes et al. 2006; Xiong et al. 2014). This can be expressed by Eq. (10) as

$$U_{peak} \propto \frac{\Delta V}{V} \propto \frac{1}{H} \quad (10)$$

Where ΔV is the volume of air swept by the diaphragm. With an increasing cavity height it was observed that the diaphragm displacement at the mechanical resonance frequency decreases (De Luca et al. 2014). However, the increase of H also lowers f_H , bringing it nearer to f_D (Chaudhari et al. 2008), which results in higher peak jet velocities. On the other hand, when using electromagnetic actuation, such as loudspeakers (Gil & Strzelczyk, 2016), the exit jet velocity shows little dependence on the cavity volume except at the acoustic resonance mode. Similar results were also

presented, where the root mean square jet velocity shows little change at the mechanical resonance frequency but of course changes for the Helmholtz resonance (Chaudhari et al. 2008). A numerical investigation (Jain et al. 2011) showed that the phase difference between the diaphragm movement and the flow reversal at the orifice exit increases linearly with increasing cavity height (Figure 2.12a). It was also noted that the velocity build-up at the orifice exit is longer for smaller cavity heights (Figure 2.12b), which is caused by the decreasing phase difference between the diaphragm motion and velocity cycle.

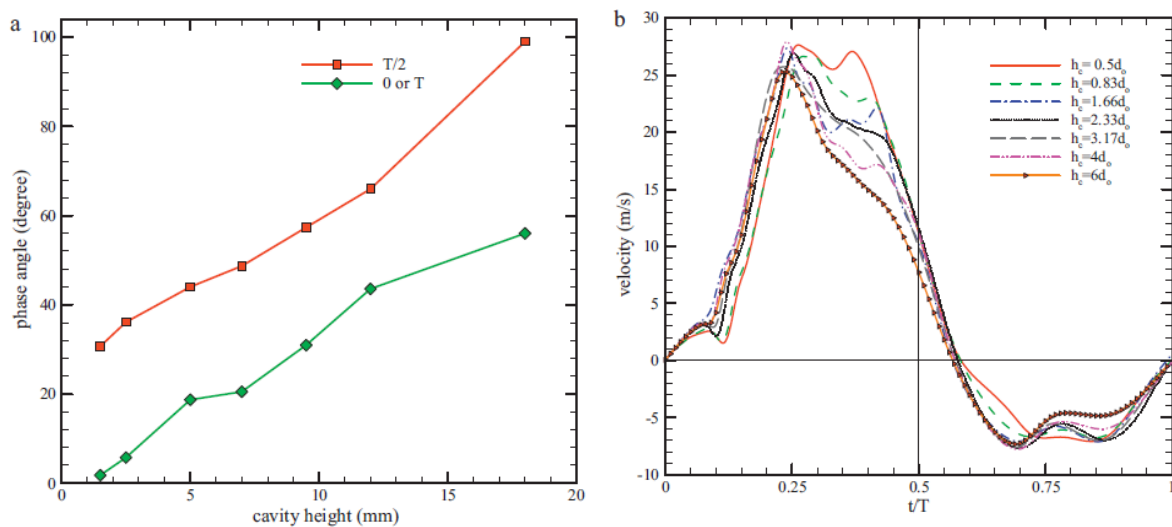


Figure 2.12. Effect of cavity height: (a) phase angle and (b) jet velocity (Jain et al. 2011)

2.2.5.2 Orifice

In a SJA, air enters and exits a cavity through an orifice, which in most cases comes in circular or rectangular (slot) form. A synthetic jet actuator intended for separation control on exterior panels of an aircraft would be embedded underneath the exterior surface with the orifice exposed to the environment on the wetted area. In order to minimise disturbances to the flow when the actuators are inactive, the orifice diameter should be constrained to a maximum of 5-20% of the local boundary layer thickness (Tang et al. 2007). This can be a favourable design constraint in cases where longer jet duration is required. It was shown that to increase the jet duration time for a plasma synthetic jet actuator while maintaining a constant capacitor energy, the orifice diameter should be reduced (Zong, et al., 2015). The same would be applicable for diaphragm actuated SJAs where, for a fixed cavity volume displacement, a smaller

orifice diameter would result in longer jet duration or larger non-dimensional stroke length, L . However, it is reminded that SJAs exist in both macro and micro scale, which refers to orifice diameters in the range of a few millimetres or tens to hundreds micrometers respectively and depending on their application the orifice diameter will be chosen accordingly. For flow control applications this usually is scaled on boundary layer thickness.

Flow passing through an orifice is characterised by both linear (major) and nonlinear (minor) losses (Gallas, 2005). Major losses are associated with a nominally fully developed region in the central region of the orifice and minor losses are related to entrance and exit effect (Gallas, et al., 2004), which for a sharp-edged orifice are governed by the Stokes number, jet Reynolds number and stroke length. The term minor losses can be misleading, as these losses can in many cases outweigh the losses incurred by major losses. Ward-Smith (1979) studied the effect that axial length has on the critical discharge coefficient of cylindrical orifices with sharp edges. According to this study, for orifice height to diameter ratios $h/d < 0.75$ the flow separates at the upstream edge of the orifice to form a discrete jet that contracts to a minimum cross-section (Figure 2.13a). After this point the flow diverges again beyond the downstream edge of the orifice without reattaching, leaving an area of separated flow between the jet and orifice wall. When $h/d \approx 0.75$ (Figure 2.13b) conditions are met for marginal reattachment at the orifice exit with the vena contracta now located further upstream with an increasing cross-sectional area until $h/d \approx 0.75$. As seen from Figure 13, a further increase in h/d has no effect on the vena contracta location (Figure 2.13). The flow as usual separates from the orifice entrance and reattaches again inside the orifice, trapping a separation bubble between the jet and orifice walls.

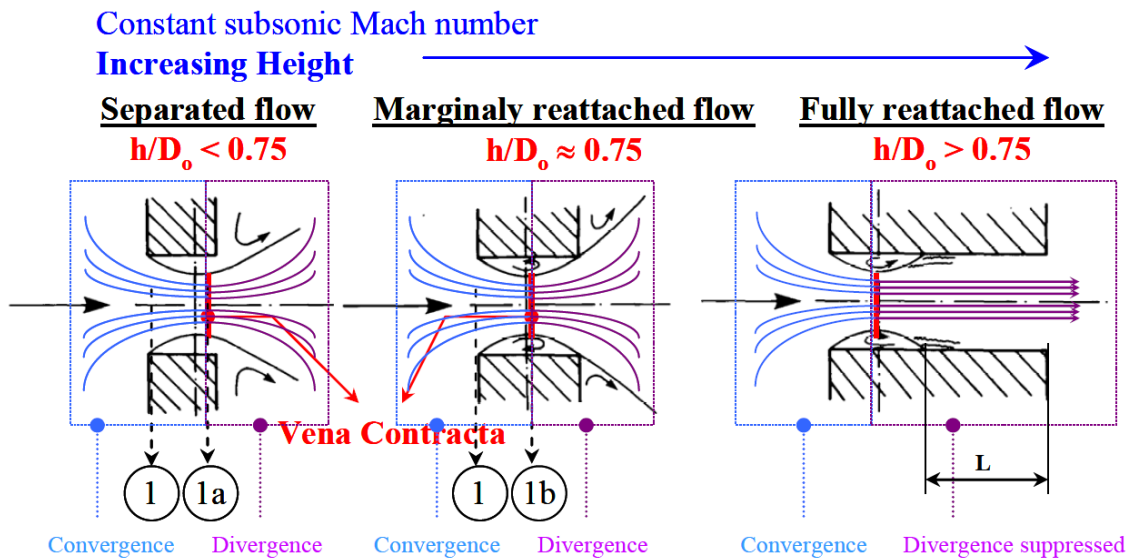


Figure 2.13. flow through a cylindrical orifice with constant diameter and increasing height: (a) separated flow, (b) marginally reattached flow and (c) fully reattached flow (Gomes et al. 2006)

The height of the orifice plays an important role in the final jet velocity at the orifice exit and is dominated by two effects: 1) The damping effect on the flow curvature increases with increasing orifice height, h , which has an acceleration effect on the flow; 2) due to the effects of shear between the slow-moving fluid near the wall and the faster core flow, the boundary layer displacement thickness increases with increasing h . As a consequence, the core flow slows down, resulting in a reduced peak velocity. To find a compromise between these two effects, (Gomes et al. 2006) suggests an orifice height of $1.25d$, which is the length required to achieve marginally attached flow ($h \approx 0.75d$) plus the extension required to achieve uniform flow ($0.5d$).

In order to reduce entrance losses, the sharp edges of the orifice have been rounded which has shown that the losses in an oscillatory flow are smaller than for a steady flow in a similar geometry (Smith & Swift, 2003). In numerical and experimental work (Lee & Goldstein, 2002) a 20% increase in peak velocity and 40% increase in vorticity was seen when using rounded slot edges. This is explained by the rounded edges inhibiting entrance separation and forming a vena contracta through the slot. Also, this feature allows more fluid to be entrained from the side during the suction phase, which in turn causes an increase in the spanwise velocity.

2.2.5.3 Actuation method

A sufficient volume of air inside the SJA cavity must be displaced in order to maximise the synthetic jet velocity, as expressed earlier by Eq. (10). This volume displacement can be achieved by different means, where all have their advantages and disadvantages depending on the suitability and final application of the actuator. The two most commonly used methods are piezoelectric and electromagnetic actuation.

Piezoelectric transducers typically consist of a piezoelectric patch bonded to a metal substructure, that when subjected to a sinusoidal input voltage oscillates. Some of the advantages of this type of actuation is the compact size, with the diaphragm thickness often being < 0.5 mm, broadband output and low electrical power consumption due to its capacitive nature (Cattafesta & Sheplak, 2008). Disadvantages include the need for operation at the mechanical resonance frequency to obtain high enough cavity volume displacements, which naturally reduces the lifespan of the diaphragm due to the high stresses it experiences. Another problem faced by this type of transducer is the high acoustic output.

Electromagnetic actuation offers an alternative option that can consist of a speaker, vibration generators or magnetic shakers (Raman et al. 1991). A primary advantage of this method is the low range of actuation frequencies and large diaphragm displacements compared to piezoelectric diaphragms with meaningful output. The exact displacement depends on the transducer manufacturer specifications, input voltage and actuation frequency. On the other hand, the large size and mass of the transducer, due to the coil and magnet assembly, together with high heat output from the resistive coil (McCormick, 2000) makes them less attractive for aerospace applications.

The shape of the diaphragm can also vary from a piston with a flat surface area or a diaphragm with the outer edge stationary, due to clamping, and maximum displacement typically in the centre. The exact deflection pattern of the diaphragm, however, depends on the resonance mode, where the maximum diaphragm displacement is not always confined to the centre depending on the mode shape. With SJAs being coupled oscillators, it requires optimisation both geometrically and mechanically (diaphragm). However, with geometric optimisation reaching maturity there is ongoing research in

the development of novel, reliable and cheap piezoelectric diaphragm technology for compact high-performance MEMS SJAs (Wang et al. 2015) (Figure 2.14). Some examples include the use of monocrystalline PZT diaphragms promising higher efficiency than the cheaper, off-the-shelf polycrystalline PZT version.

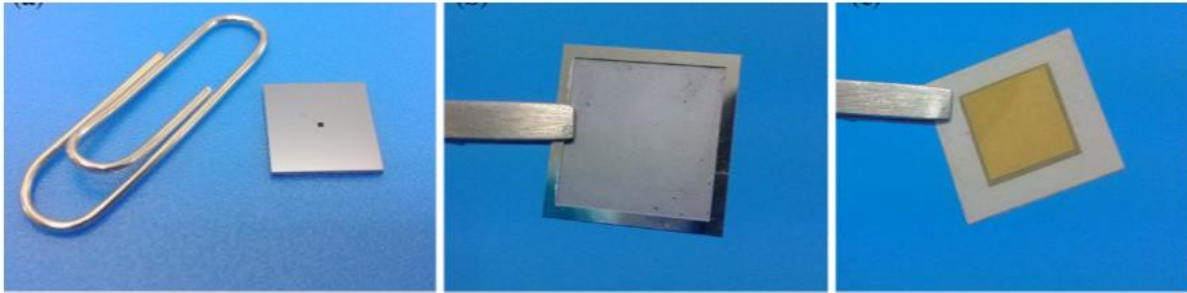


Figure 2.14. A micro SJA with square orifice dimensions of 0.6 x 0.6 x 0.2 mm using PZT ceramic wafer bonded to monocrystalline silicon wafer using epoxy resin at low temperature (Wang et al. 2015) (Wang, Ma, Deng, Qu, & Luo, 2015).

2.3 Synthetic Jet Actuator Noise

2.3.1 Noise of active flow control devices

It is clear that SJAs have a great range of potential applications in flow control, but also in the area of heat transfer enhancement (cooling) in electronic devices. Efficiency of SJAs in converting electric to fluidic power has also increased over time, but a key issue limiting the commercialisation of these devices is the actuator self-noise generated during operation. This is a common problem with several active flow control devices and thus far in cases where the reduction of flow generated noise is required, passive flow control measures, such as serrations or poro-serrations, have been at the forefront of research (Chong & Dubois, 2016). In some recent work active flow control devices were employed for flow generated noise reduction. One such example demonstrated in a numerical study that SJAs could considerably suppress acoustic radiation of a low-speed transitioning aerofoil in a uniform stream (Mankbadi et al. 2015). However, in that study the actuator cavity was not modelled and instead a fluctuating-velocity boundary condition at the bottom of the orifice was used, therefore not taking into account other sources of actuator self-noise. It was successfully demonstrated (Kim et al. 2014) that DBD actuators could reduce the vortex shedding tonal noise. However, the actuator self-noise was larger than the tonal vortex shedding noise thus negating any noise reduction benefit.

For heat transfer applications, a micro-SJA peak jet noise of 73dB for jet velocities of 90 m/s was reported (Arik, 2007). Mangate & Chaudhari (2015)–recorded noise levels as high as 68 dB at $f_a = 0.4$ kHz and an orifice diameter, $d = 8$ mm. In an experimental study by Jabbal & Kykkotis (2014), a similar peak noise level of 70 dB for a single chamber SJA configuration with $d = 1$ mm was reported. A number of other studies reported noise levels unacceptable for the intended use of the SJA in quiescent conditions (Lasance et al. 2008; Lasance et al. 2009; Bhapkar et al. 2013; Bhapkar et al. 2014).

2.3.2 SJA noise sources

A SJA has several noise sources: structure-borne noise from the diaphragm, unsteady jet noise and cavity noise. The focus of this thesis is on aerodynamic sound by the SJA only, which in context with the work presented consists of jet and cavity related noise. However, it must be noted that today it is widely recognised that any type of sound generating method can be presented as aerodynamic sound (Howe, 2003), including complex structure-borne noise originating from the diaphragm.

Because of the function and design of a SJA it can naturally be treated as an acoustic source. With the actuator, regardless of actuation method used, there is mass displacement during its operation and therefore it can be treated as a monopole acoustic source (Devenport & Glegg, 2008). A monopole source represents a pulsating sphere, also known as a simple source, which means the acoustic radiation is independent of the angle (Moeser, 2009). Such a source is characterised by a temporal volume change, Q , outflow of fluid mass, for example from a pipe at velocity v and is given by Eq. (11):

$$Q = \int_S v dS \quad (11)$$

Where S is the pipe cross-sectional area. The sound pressure is then defined by Eq. (12):

$$p = j\omega\rho Q \frac{e^{-jkr}}{4\pi r} \quad (12)$$

Where k is the wave number, $j\omega$ represents time differentiation, e^{-jkr} is a delay of $e^{-j\omega\tau}$, where $\tau = r/c_0$ and allows Eq. (12) to be expressed in the time domain as shown in Eq. (13):

$$p = \frac{\rho}{4\pi r} \frac{dQ(t - r/c_0)}{dt} \quad (13)$$

Eq. (13) suggests that the noise emission can be lowered by reducing the rate of change of the volume velocity. In a pulsed jet for example this could be achieved by releasing air gradually during each cycle instead of using the typical on/off signal that suddenly releases and cuts off air supply.

It has already been established that for maximum jet velocity, operation at a resonance frequency is preferred, which further increases the sound generated, due to increased mass displacement. Lumped element modelling was briefly introduced in Section 2.2.4.2, where the coupling between different energy domains in a SJA system is simplified and represented as elements in an equivalent circuit. Because the cavity encloses a compressible gas, in the LEM it is modelled as an acoustic compliance (Gallas, et al., 2003). As well as incurring losses associated with discharge of the flow from the orifice, a portion of the kinetic energy contained in the oscillating fluid mass is dissipated through viscous effects. This causes an effective acoustic mass and resistance related to the orifice neck.

The periodic orifice mass displacement results in an unsteady jet formation and vortex shedding. According to vortex sound theory, sound is produced through moving boundaries, vorticity within the jet or elsewhere, and the interaction of vortices with boundaries (Howe, 1998; Howe, 2003; Howe, 2008). When considering any synthetic jet an obvious noise source is the jet itself. The source of noise in conventional jets is universally agreed to be generated by fine-scale and large-scale turbulence in the jet flow (Figure 2.15) (Tam et al. 2008).

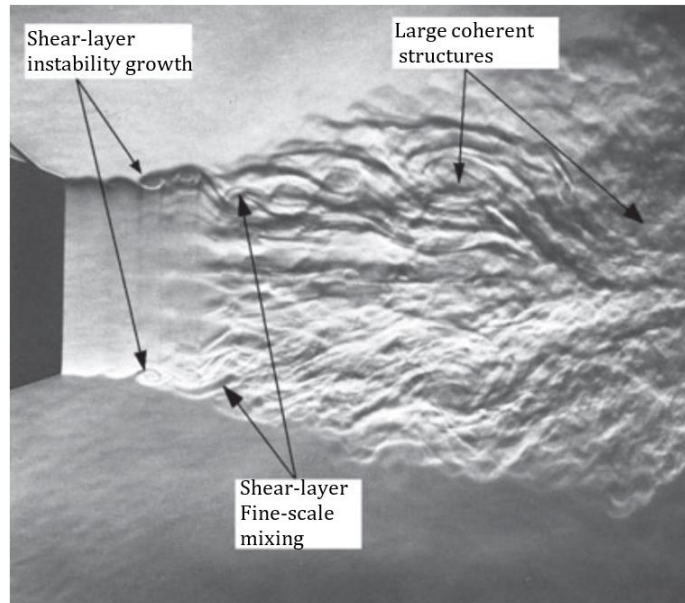


Figure 2.15. Transitional conventional jet (Van Dyke, 1982)

This may result in the formation of broadband quadrupole jet noise in quiescent conditions. Although it must be noted that these assumptions are drawn from the noise generation of continuous jets and may vary significantly for synthetic jets due to the very different entrainment and growth characteristics.

2.3.3 Jet noise and Lighthill's analogy of aerodynamic sound

To better understand jet noise generated by a SJA an understanding of aerodynamic sound is necessary. Sound generated by turbulence in an unbound flow is generally referred to as aerodynamic sound (Howe, 2003). Turbulence typically occurs in motion of fluid over a surface or due to flow instabilities, where a very small fraction of the rotational kinetic energy of the flow results in acoustic radiation. James Lighthill's 1952 paper, 'On sound generated aerodynamically' (Lighthill, 1952), discusses the mechanism behind aerodynamic sound that is produced as a by-product of airflow. Whether it is the intentional sound of wind instruments, caused by regular fluctuations in air flow at low Reynolds numbers or the broadband noise as a results of highly turbulent jet flow from aircraft propulsion systems, the mechanism behind aerodynamic sound generation is the same.

By rearranging the equations of Navier-Stokes and mass conservation, he derived an exact, inhomogeneous wave equation, Eq. (14), where the source terms are only

important within the turbulent region of the flow. According to Lighthill (Lighthill, 1952) a fluid flow, which is inherently unstable and therefore is turbulent or fluctuates, has a sound field that is modelled as a static distribution of acoustic quadrupoles. In quadrupoles the surrounding fluid experiences no net force and instead the sound waves are generated through fluctuating stresses in the fluid.

$$\frac{\partial^2 \rho'}{\partial t^2} - a_0^2 \frac{\partial^2 \rho'}{\partial x_i^2} = \frac{\partial^2 T_{ij}}{\partial x_i \partial x_j} \quad (14)$$

The instantaneous strength of these quadrupoles is given by Lighthill's stress tensor, which according to Lighthill describes the entire sound generation physics by flow, given by Eq. (15):

$$T_{ij} = \rho v_i v_j + p_{ij} - a_0^2 \rho' \delta_{ij} \quad (15)$$

Where ρ is the density, v_i and v_j are velocity components in the i and j directions respectively and a_0 the speed of sound. The term $\rho v_i v_j$ represents the Reynolds stresses in the turbulent flow, p_{ij} the real stresses, which are made up of hydrostatic pressure and viscous stresses, and a_0^2 is the constant of proportionality. ρ' represents the density perturbation and is expressed as: $\rho' = \rho - \rho_0$, where ρ is the fluid density and ρ_0 is the density of the stationary surrounding fluid. This density perturbation can then, through the equation of state, be related to the pressure perturbation to give: $p = \rho' a_0^2$. In this form the left-hand side of the wave equation (Eq. (14)) represents the acoustic pressure wave propagation outside the turbulent flow region and the right-hand side contains all the residual terms in the Navier-Stokes equations. Applying the assumptions of linear acoustics, this term will equal zero outside of the source region. The exact solution for Lighthill's wave equation, without scattering surfaces, with the sound generation at point y in the flow and an observation point x within a volume V is given by Eq. (16):

$$\rho'(x, t) a_0^2 = \frac{\partial^2}{\partial x_i \partial x_j} \int_V [T_{ij}(y, \tau)]_{\tau=t-r/a_0} \frac{dV}{4\pi r} \quad r = |x - y| \quad (16)$$

Assuming sound propagates radially from the source at a fixed speed, accurate spatial derivatives can be deduced in terms of time derivatives at a fixed point. Using dimensional analysis, the timescale of turbulence with a length scale L and convection velocity U , the rms density perturbation can be expected to scale as $\rho_0 L U^4 / a_0^2 r$. It can be found that the far field acoustic intensity scales with the eighth power of the free stream velocity, known as U^8 law. This is an experimentally verified and well-known scaling law for jets, as would be found in high speed synthetic jets.

However, when solid boundaries are taken into account, for instance in impinging synthetic jets, the sound generated changes significantly as a dipole sound source is added to the equation and it is shown that dipoles generate sound in a much more efficient way. This is since the power generated by a quadrupole varies according to the sixth power of its frequency, but a dipole varies according to the fourth power.

2.3.4 Hole tone

Sondhauss (1854) was the first to report on the “hole tone”, however, without describing any mechanism behind the tone generation. Von Gierke (1947) studied the mechanism behind whistling generated by mouth using flow through a pipe with an orifice attached to one end as a model. It was noted that the frequency of a whistling tone through a circular opening only occurred at specific velocities and was proportional to the jet velocity through the hole and inversely proportional to the jet diameter. Furthermore, in the same study, flow visualisation revealed the shedding of circular vortex rings from the orifice during the noise generation (Figure 2.16). It was stated that pressure fluctuations during the vortex formation can excite the cavity. If the vortex formation frequency is close to or coincident with the cavity eigenfrequency, there is coupling between the two and the vortex shedding is driven at the cavity resonance frequency, which leads to the formation of a pure tone. An example of hole tones is the whistling tones (Pfeiftoene) generated through the human mouth.

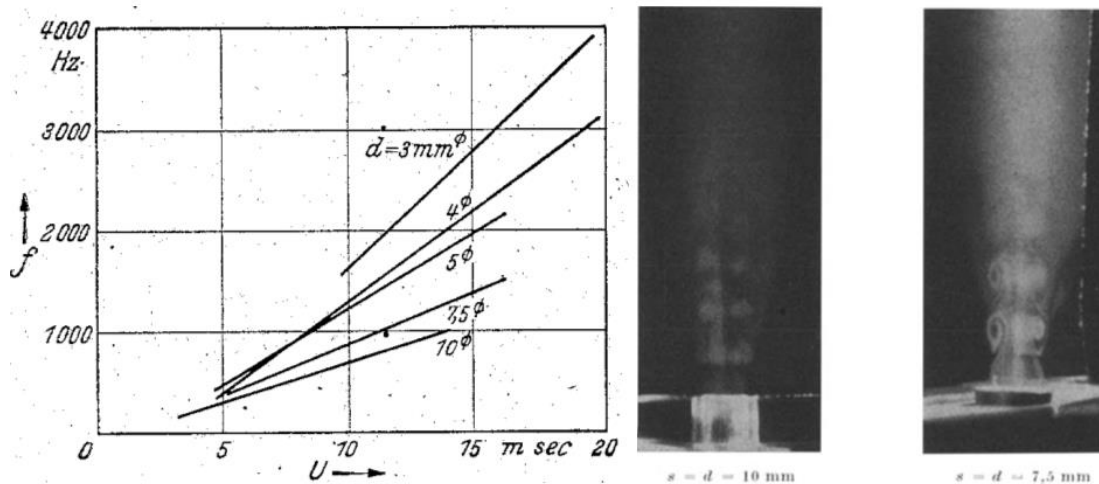


Figure 2.16. (a) linear variation of hole tone frequency with jet velocity and (b) flow visualisation showing the vortex shedding from continuous jet during the tone generation (von Gierke, 1947)

In fact, this type of noise generation is observed in several other applications including edge tones (Powell, 1961), cavity noise (Rockwell & Naudascher, 1978), screech (Panda, 1999) or pipe tones (Anderson, 1955) such as Pfeiftoene mentioned earlier. Feedback from a downstream disturbance plays an essential part in the creation of self-sustained periodic oscillations that result in these tones. Air entering an orifice separates at the entrance generating vortex shedding, as is the case for a SJA. These vortices can then interact with the edge at the orifice exit where fluctuations in the flow can propagate back upstream and interact with the vortex shedding at the orifice entrance. Similarly, if the flow reattaches inside the orifice the jet can still interact with downstream flow structure in the jet and generate acoustic disturbances that interact with the flow upstream in the orifice. If the upstream vortex shedding and the downstream disturbances are in phase, then the vortex shedding is amplified generating a feedback mechanism. The feedback mechanism provides direct communication between processes near the downstream impingement region and the separation region in the orifice, which ensures the shear layer oscillation is a globally organised phenomenon (Rockwell & Naudascher, 1979).

2.3.5 Effect of orifice shape on noise

2.3.5.1 Asymmetric orifices

An interest in asymmetric and more complex nozzle geometries exists due to the self-induction of asymmetric coherent flow structures (Zaman & Hussain, 1980; Zaman,

1996; Lin et al. 1998) . These have found use in applications such as flow mixing, reducing combustion instabilities, noise suppression, heat transfer or thrust vector control (Gutmark & Grinstein, 1999). The type of jet and structures formed have shown to increase mass, momentum and heat transport which has also found use in the attenuation of jet noise.

The cross-sectional area of a jet emanating from an asymmetric nozzle, for example rectangular or elliptic, undergoes complex deformations and sometimes even undergoes a phenomenon referred to as axis switching (Figure 2.17). During this phenomenon the minor and major axis of the jet are interchanged after traveling a downstream distance of only a few equivalent diameters from the nozzle exit (Zaman, 1994).. This gives the appearance that the jet has turned around the streamwise axis by 90° , but instead it is the result of the jet expanding along the minor axis and contracting along the major axis, which means that now the roles of minor and major axis are switched. Similar effects are also observed in other orifice shapes such as square orifices that showcase a 90° as well as a 45° axis switch (Chen & Yu, 2014).

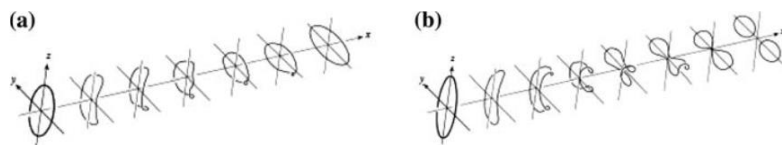


Figure 2.17. Schematic showing (a) deformation and axis-switching of low aspect ratio elliptic vortex ring and (b) deformation, axis switching and splitting of high aspect ratio vortex ring (Husain & Hussain, 1999)

The deformation of elliptical vortex rings is explained by Biot-Savart self-induction caused by nonuniform azimuthal curvature and the interaction between streamwise and azimuthal vortices (Gutmark & Grinstein, 1999). In rectangular jets the variable aspect-ratio feature seen in elliptic jets is combined with the corner vortices generated by square jets (Chen & Yu, 2014). In a recent paper axis-switching as well as bifurcation (splitting), under certain conditions, in SJAs using low aspect-ratio rectangular orifices was demonstrated (Weng et al. 2018).

2.3.5.2 Lobed orifices

In order to increase the entrainment and mixing ability of asymmetric jets passive generators, such as tabs, were introduced in the nozzle geometry (Zaman, 1994; Presz et al. 1994; Zaman, 1996). The idea of passive generators further evolved into lobed and chevron nozzles (Zaman et al. 2003; Presz et al. 2002; Nastase & Meslem, 2007). The enhanced mixing and entrainment chevron and lobed nozzles offer, compared to round or other simple asymmetric nozzles, is far superior as shown by Nastase & Meslem (2010), who reported a maximum entrainment value of 1.1 using a daisy lobed nozzle compared to 0.34 using a circular nozzle. Counter-rotating streamwise vortex structures form between lobes (Figure 2.18) and are responsible for significantly higher volumetric flow rate compared to a reference circular jet (Meslem et al. 2014; Hu et al. 2000). In a study using lobed jets, Hu et al. (2001) found that large-scale streamwise vortices, that form at the trailing edge of the lobed nozzle used, break up into smaller but not weaker streamwise vortices with increasing downstream distance. Eckerle et al. (1992) and Werle et al. (1987) also found that the breakdown of large scale structures downstream of a lobed nozzle cause turbulence that dominates mixing, which is indicated by elevated turbulence levels in this region. The mixing caused by lobed nozzles is controlled by three primary elements according to Belovich & Samimy (1997). These are the streamwise vortices that form due to the lobes of the nozzle, a larger interfacial area between the jet and ambient flow and the Brown-Roshko type flow structures that form in any shear layer due to Kelvin-Helmholtz instabilities.

Noise generated by jets is caused by the presence of large and small-scale structures in the flow, where large-scale structures dominate to a region of about two potential core lengths from the nozzle, referred to as the noise producing region (Alkisar et al. 2007). It was shown that acoustic forcing of a high Reynolds number turbulent continuous jet contains large eddies that increase the far field noise to about 5 dB (Moore, 1977). This is known as broadband noise amplification by tonal excitation and measurements of near-field pressure and velocity identifies the relationship between large-scale eddies and the associated sound field (Coiffet, 2006). If the growth of large-scale structures can be disrupted, then a reduction in jet noise should be observable. This led to intensive research and the development of chevron nozzles (Bridges et al. 2003; Alkisar et al.

2007) that lead to reductions in jet overall sound pressure level (OASPL) and a decrease in shear layer turbulence.

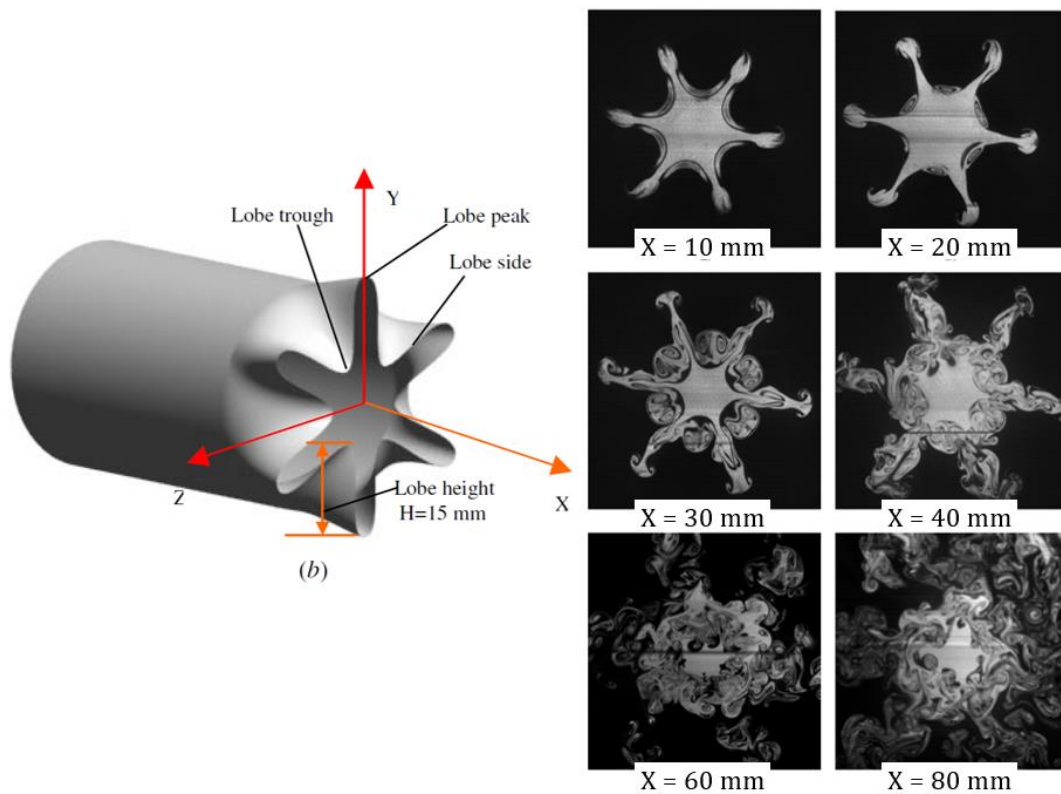


Figure 2.18. LIF flow visualisation results using a lobed nozzle at varying downstream distances (Hu, Saga, Kobayashi, & Taniguchi, 2000)

However, breaking up large scale structures into small-scale ones earlier in the jet flow tends to come with a slightly high-frequency noise penalty (Kopiev et al. 2013), which could increase the OASPL of the jet. Engineers are therefore faced with the challenge of maximising low frequency noise reduction while preventing an increase in the high-frequency end of the acoustic spectrum. The key geometric variable in the design of lobed orifice are the lobe count and lobe penetration, while for chevrons there is a third parameter: chevron length. The mixing effect of a lobed orifice is mostly dictated by the lobe penetration as long as the flow does not separate (Presz et al. 1986). A higher penetration was found to increase high frequency noise but reduce low frequency noise, which was especially true for lower chevron counts (Bridges & Brown, 2004). An extensive study of chevron nozzles with varying geometric parameters by Tide & Srinivasan (2010) showed that a higher chevron count with lower jet penetration attains the highest noise reduction for low and medium pressure ratios. The maximum noise reduction of 4 dB was achieved using eight chevrons, while 2 dB and 1 dB were

achieved using six and four chevrons, respectively. Furthermore, using eight chevrons at 0° taper allowed for the highest noise reduction. However, using four chevrons at 5° and 10° taper results in a noise increase, compared to the baseline circular nozzle.

Due to the potential this method has found use in jet noise reduction and mixing applications in both laboratory and commercial applications. One of the most popular applications must be the new generation Boeing aircraft fleet, which use chevron nozzles as part of a noise reduction strategy that allows for a 60% smaller noise footprint compared to aircraft models it replaces (Boeing, 2015). Recently chevron nozzles have been used in electromagnetically driven SJA's to enhance heat transfer by exploiting the increased mixing abilities of such nozzles (Crispo et al. 2015). The study found that using chevron nozzles azimuthal flow structure would not be disrupted, but instead deforms the vortex ring.

2.3.6 Effect of active noise control on SJA noise

Finally, in section 1.3. the monopole sources-like behaviour of SJAs through the periodic mass displacement driven by the diaphragm was introduced. Therefore, having two actuators next to each other driven in antiphase would superimpose two opposing sound fields on one another. This should lead to a net mass displacement of zero which would in theory leads to a zero source strength (Devenport & Glegg, 2008). The resulting sound field of two sources is given by Eq. (17):

$$p = \frac{j\omega\rho}{4\pi} \left\{ Q_1 \frac{e^{-jkR}}{R} + Q_2 \frac{e^{-jkr}}{r} \right\} \quad (17)$$

Where R and r are the distances from Q₁ and Q₂ to a field point P, respectively. From Eq. (17) it can be seen that the sound field of two sources is just the sum of those components. So, for two equal sources the sound pressure is doubled and there will a fourfold increase in sound power. For two equal but opposite sources at low frequency, or smaller separation ($h/\lambda \ll 1$), where λ is the wavelength, the sound pressure is smaller than that of a monopole source. This is because at smaller separation distances it appears as if both source are in the same place, which leads to a global field sum of nearly zero. With increasing distance, the interference patterns change where for $h =$

$\lambda/2$ there will be constructive interference at the source axis, which results in the total sound field taking a value twice of each individual source. Figure 2.19 shows different sound fields for two equal and opposite sources with varying separation distance. This observation is important when active noise control is considered for double or multi chamber SJAs.

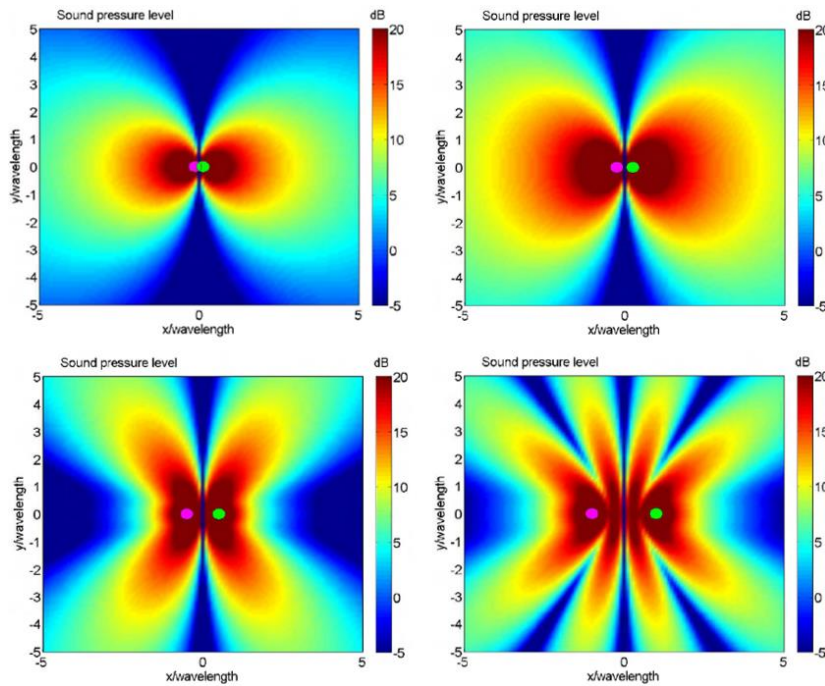


Figure 2.19. Sound field for two opposite but equally large sources with varying separation distance between sources (a) $h = \lambda/4$, (b) $h = \lambda/2$, (c) $h = \lambda$ and (d) $h = 2\lambda$ (Moeser, 2009)

2.3.7 Current SJA self-noise reduction techniques

Although not much work on a fundamental understanding of SJA self-noise exist to date there is an increasing interest and research aimed towards understanding and reducing the adverse acoustic effects of SJAs. Different methods have been employed with the majority taking a passive noise reduction approach or varying operating conditions of the actuator. Table 2 shows a summary of some noise reduction methods for SJAs studied to date.

Table 2. Noise reduction methods employed for SJAs

Study	Orifice	d (mm)	f (kHz)	U_{peak} (m/s)	SPL (dB)	Noise abatement	SPL (dB)
Arik (2007)	Round hole	1	3.6	90	73	Passive muffler	30
Lasance et al. (2008)	Round hole	3	0.11	6.5	43.1 (l=30 mm)	Pipe length	41.5 (l=90 mm)
		4	0.11	6.5	49 (l=120 mm)		36.9 (l=120 mm) 46.4 (l=30 mm) 48.1 (l=90 mm)
Lasance et al. (2009)	Round hole	4	0.03	...	37 (P=1 W)	SJA power	32 (P=0.4 W)
		8	0.08	...	52 (P=0.3W)		46 (P=0.1 W)
Bhapkar et al. (2013)	Round hole	14	0.1	21	58	Orifice diameter	48 (d=8 mm)
							53 (d=10 mm)
							55 (d=12 mm)
Bhapkar et al. (2014)	Elliptical hole	12	0.1	21	58 (h=5 mm)	Orifice height	54 (h=2 mm)
Mangate & Choudhari (2015)	Round hole	8	0.4	...	68	Orifice shape	57 (oval) 64 (diamond)

2.3.7.1 Enclosures

Arik (2007) explored three noise reduction methods: redesign of actuator for noise reduction and preserving the heat transfer capabilities, passive noise reduction by using a muffler and active noise cancellation. Redesigning the actuator to make it noiseless was not possible and active noise cancellation at high frequencies was nearly impossible to achieve and therefore the passive noise control measure was chosen. Their solution was to place the actuator inside an enclosure with a 10 mm hole on one face and attach a muffler on that face (Figure 2.20). Three primary configurations were tested in this study: 1. The actuator on its own without noise control, 2. Placed inside the enclosure and 3. With varying sizes of mufflers attached to the enclosure. With this setup a significant SPL reduction of 30 dB was achieved (Figure 2.21). However, the proposed method would be very impractical for aerospace and many other applications due to its size.

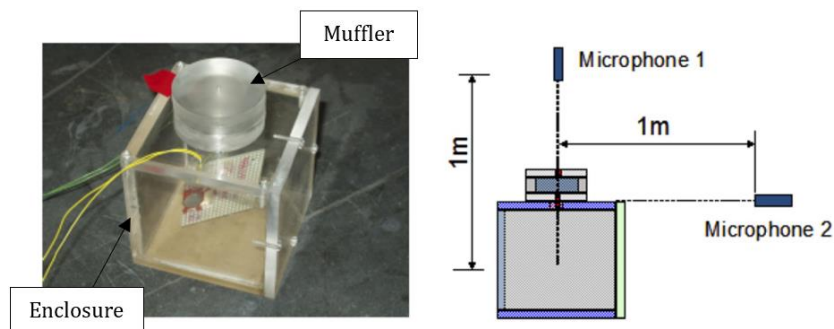


Figure 2.20. SJA noise reduction scheme using an enclosure with muffler attached (Arik, 2007)

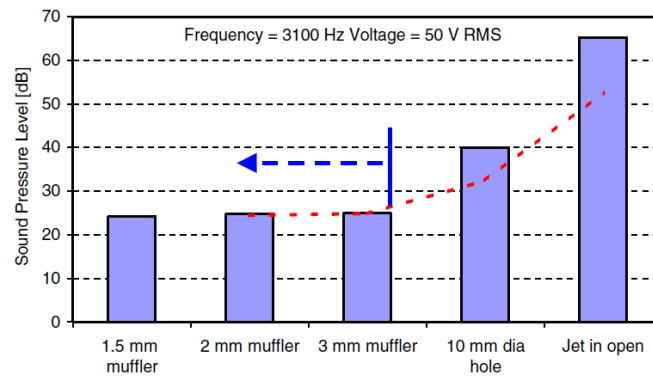


Figure 2.21. Summary of acoustic results in a 3 in x 3 in x 3 in enclosure (Arik, 2007)

2.3.7.2 Operating conditions

Other more recent studies focused their attention towards the operating parameters, such as voltage and actuation frequency, and orifice geometry. For maximum output the SJA is generally operated at a resonance frequency, which inevitably leads to increased noise levels. Also, regardless of the actuation method used the actuator output scales with the energy supplied to the transducer. An increase in supply voltage to an electromagnetic transducer for example would result in a larger diaphragm displacement and jet velocity. However, the noise generated also increases due to the increased displacement of mass by the diaphragm. Therefore, controlling the noise levels using certain operating parameters can be contradictory with fluidic performance requirements (Bhaskar, 2013).

2.3.7.3 Orifice geometry

This leaves noise reduction by geometric amendments the preferred option. Bhaskar et al. (2013) showed that reducing the orifice diameter can result in lower noise levels. This is expected since with increasing orifice diameter the mass associated with the orifice increases which, as mentioned earlier, leads to higher noise levels. All actuators presented in Table 2 are designed for heat transfer applications, in which case a larger orifice diameter is preferred (Chaudhari et al. 2010). For aerospace applications, on the other hand, such orifice dimensions are not suitable. Bhaskar et al. (2014) showed that a smaller orifice height can reduce the sound pressure level by the SJA they tested by up to 10%. But this result is not supported by Lasance et al. (2008), where an orifice length of 120 mm instead of 30 mm ($d = 3$ mm) results in a 6.2 dB noise reduction and in a case

with a larger orifice diameter ($d = 4$ mm) the lowest SPL is recorded for $h = 30$ mm instead of $h = 120$ mm. This suggests that the maximum noise reduction possible has an optimum orifice height value.

Furthermore, similar to previous studies on continuous jets, non-axisymmetric orifice shapes were used to reduce SJA self-noise. Bhapkar et al. (2014) used a number of different orifice shapes (circular, square, rectangular and elliptic) to investigate their effect on heat transfer and acoustic characteristics of a SJA. It was found that a low aspect ratio elliptic orifice offers the best performance for the SJA studied in terms of noise reduction and heat transfer, which is an indication of high entrainment and mixing ability.

2.4 Chapter Summary

In this chapter a review of both passive and active flow control methods and their evolution to date was presented and compared. Benefits of various active flow control devices over passive ones were discussed. Synthetic jet actuators in particular are promising devices due to their compact design and zero-net-mass flux characteristic that, however, still require optimisation from an operational and self-noise point of view.

Flow separation on wings has serious implications in terms of aircraft performance and safety. Secondary, less serious, yet an important factor to meet future industry targets, is flow separation associated noise. The use of synthetic jet actuators (SJA) has shown to help reattach flow by injecting momentum into a boundary without requiring any external mass addition to the device itself. Large-scale flow structures formed at the orifice exit during the jet formation can help increase mixing near the wall region, which further aids in decreasing the momentum deficiencies in this region. As a result, a decrease in drag and increase in lift is observed even beyond the unactuated stall angle of attack.

However, an area of SJAs, and many other AFC devices, that requires attention is the self-noise generated during operation, which can reach unacceptable levels that would make them unsuitable for commercial applications. Noise sources in a SJA have been

presented, which include structure borne noise from the diaphragm, jet noise and cavity/orifice resonance related noise. The focus of this thesis is on the aerodynamically generated noise and several current noise measures have been presented. These measures comprise of enclosures, muffles and changes in orifice shape, which show great potential. None of the work presented has conducted detailed acoustic studies to characterise the nature of actuator self-noise and define contributions from individual sources. Therefore, a review of the complex mechanics behind some passive noise control measures, such as asymmetric orifice shapes, was discussed. An improvement of the more basic asymmetric orifice shapes used in SJA literature are lobed orifices, which have far better entrainment and mixing abilities than circular orifices. As a result, they are able to significantly reduce continuous jet noise by disrupting noise generating flow structures in the jet flow early on, which may make them a suitable addition for SJAs.

3 Synthetic Jet Actuator Design

This chapter gives an insight into the design and development of the synthetic jet actuators (SJAs) used throughout this work. Tests were carried out on an existing double chamber SJA designed for noise reduction using lobed orifice and antiphase operation. The diaphragm clamping conditions were found to play a crucial part in the SJA overall performance. These tests helped better understand some new aspects of SJA design not available from the literature review and define a design specification for two new and improved SJA prototypes used as part of the main research. Individual components used in the actuator assembly are described and presented.

3.1 Original Synthetic Jet Actuator

3.1.1 Design and preliminary tests

Work on the noise reduction of double chamber synthetic jet actuators using lobed orifice has previously been studied by Kykkotis (Kykkotis, 2014) and Kykkotis and Jabbal (Kykkotis & Jabbal, 2014). This study used a double chamber SJA ($d = 1$ mm) with three interchangeable orifice plates, one circular and two 6-lobed orifices which vary in lobe amplitude with an equivalent orifice diameter, $d_e = 1$ mm and orifice height, $h = 1.5$ mm. A PZT diaphragm Figure 3.1 of 27 mm diameter and 0.45 mm thickness, where the clamped part of the diaphragm has a thickness of 0.22 mm, was used. This results in a cavity diameter, $D = 25$ mm. The orifices have a separation distance of $5d_e$ that, combined with the diaphragm thickness, results in a cavity height, $H = 4.78$ mm. An embodiment of the SJA is shown in Figure 3.2. To produce the complex lobed orifice geometries, stainless steel 3D printing was used to manufacture the orifice plates and actuator casing. Using this manufacturing method also meant the cost and processes involved could be kept to a minimum.

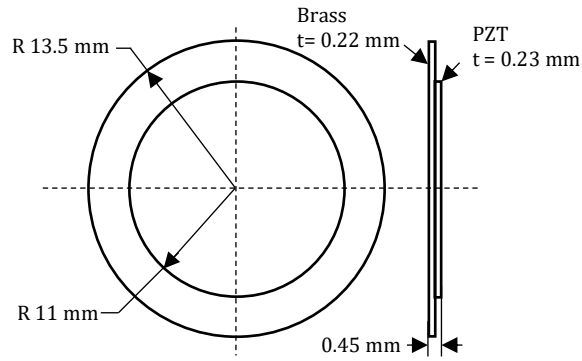
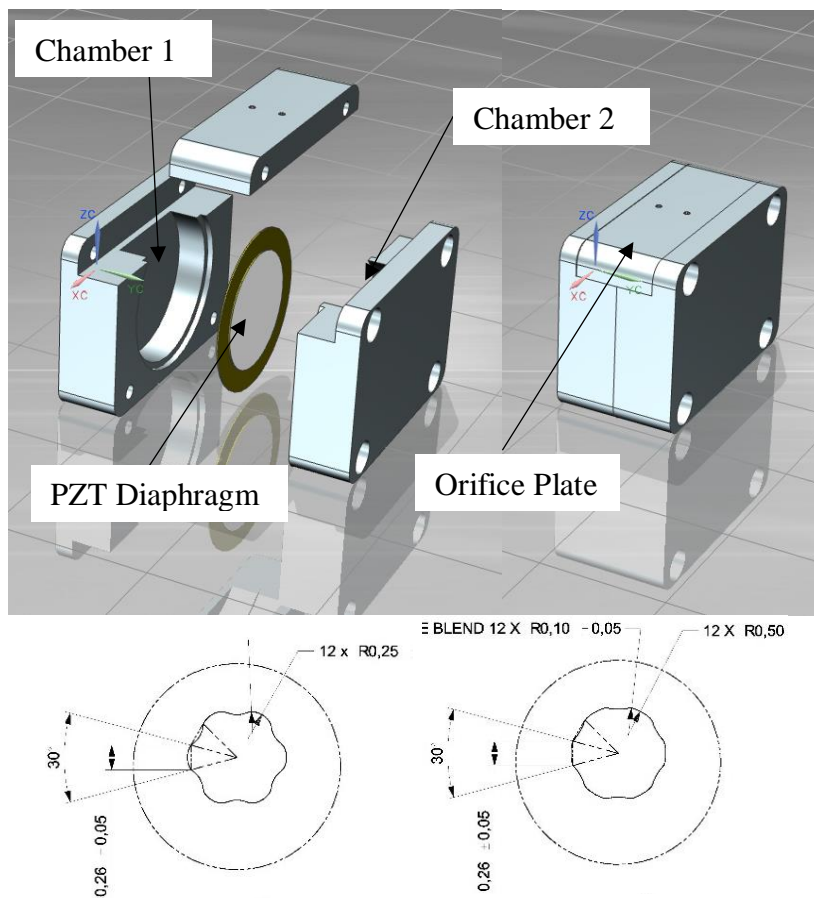


Figure 3.1. PZT diaphragm dimensions (27 mm)



**Figure 3.2. Double chamber SJA assembly (top) and lobed orifice geometry (bottom)
(Kykkotis, 2014)**

It was shown that noise reduction of 3-11 dBA is possible using the out of phase effect and circular orifice. Furthermore, a 24-26% noise reduction was observed using the lobed orifices at the resonant frequencies. This noise reduction was achieved without a negative impact on the actuator exit jet velocity and an electrical-to-fluidic power efficiency of approximately 16%.

3.1.2 Geometric discrepancies

In theory, additive manufacturing would seem the best option for manufacturing the actuator components, several problems were faced in practice. The resolution to which components could be manufactured was ± 0.2 mm, which on the small scale of the actuator used leads to geometric errors that hinder proper alignment of components. On larger components, such as the actuator casings, these can be corrected in post processing, although with some difficulty. However, discrepancies in the lobed orifices are not easily corrected and would contribute to some errors in results. Figure 3.3 shows close ups (x20) of the different orifice shapes taken using an optical measurement machine. The difference in circular and low amplitude lobed orifice are not clear, although hints of lobes are visible in some places. The high amplitude lobed orifice, on the other hand, has a distinctly different shape to that of the circular orifice, however, the lobe penetration is not well defined in some places.

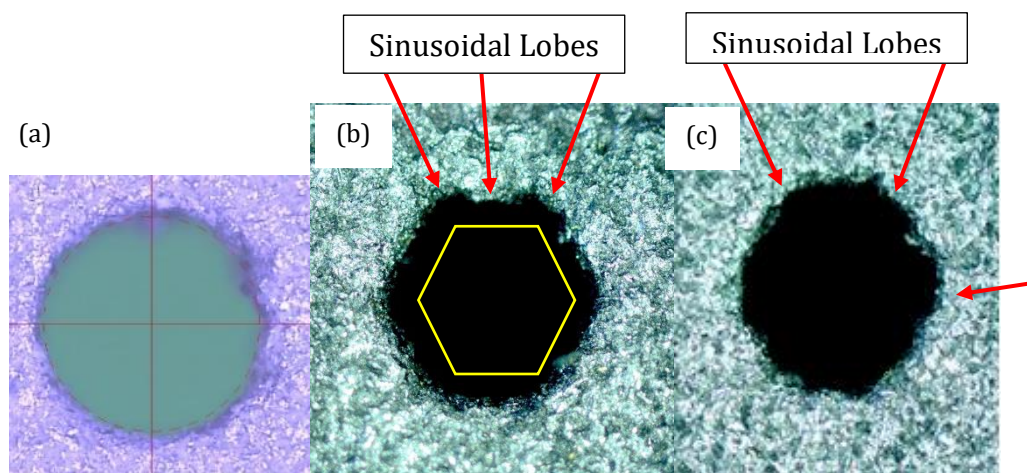


Figure 3.3. Close-up (x 20) of 3D printed orifices (a) circular, (b) high amplitude 6-lobed and (c) low amplitude 6-lobed orifice (Kykkotis, 2014)

Another part of the design that suffered from geometric errors is the slot in each orifice plate designated to fit the overlapping section of the diaphragm ensuring a snug fit around it. Due to the small thickness of the clamped part of the diaphragm (0.22 mm), a printing resolution of the same order resulted in slots too thin to fit the diaphragm. During post processing the slots were opened up, but to a larger width than required due to the lack of readily available tools for such precise work. This led to insufficient clamping around part of the diaphragm, as shown in Figure 3.4 further reducing the actuator performance.

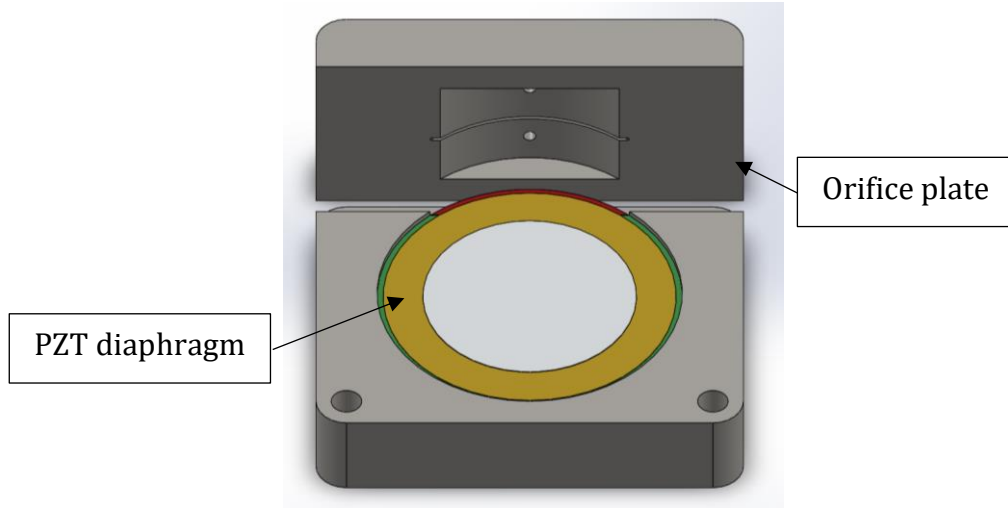


Figure 3.4. Schematic of clamped (green) and unclamped (red) edge of diaphragm

3.1.3 Diaphragm clamping

As discussed in the previous section, the lack of proper clamping or clamping conditions in general have implications on the overall performance of an SJA. The diaphragm resonance frequency for example is primarily a function of its geometry and mechanical properties, but is also affected by its clamping conditions. The resonance frequency of a diaphragm is given in Eq. (18) (Blevins, 1979):

$$f_D = \frac{k^2}{2\pi r_D^2} \left(\sqrt{\frac{EI}{\rho t_D (1 - \nu^2)}} \right) \quad (18)$$

Where r_D and t_D represent diaphragm radius and thickness, respectively; E is Young's modulus, ρ and ν the diaphragm material density and Poisson's ratio, respectively and I is the second moment of area of inertia. The k term is a non-dimensional frequency parameter that depends on the clamping conditions of the diaphragm and is primarily a function of the diaphragm boundary conditions. For example, for tight clamping $k^2 = 10.22$, for medium clamping $k^2 = 7.08$ and for a simply supported plate $k^2 = 4.98$ (Blevins, 1979). Gomes (2010) added the additional damping term, $\sqrt{(1 - 2\xi)}$, to the above equation, where ξ is an empirically obtained damping coefficient. In the work presented by Jabbal et al. (2013), in order to increase reliability, an O-ring was used between the diaphragm and clamping edge of the actuator casing to reduce the

diaphragm bending stresses. In this this case, $\xi = 0.06$ and the resonance frequency was calculated using Eq. (18).

In the following results, the effect of torque applied to the bolts that hold together the actuator is presented. These bolts directly control the force that the 1 mm lip of the actuator casing exerts on the outer edge of the diaphragm. The higher the applied torque, the higher the force exerted on the diaphragm will be. The torque applied is controlled using a Wera torque drive with a torque range of 0.2 – 1.2 Nm. Three torque settings were used: 0.35 Nm, 0.55 Nm and 0.75 Nm, where excessive torque applied will damage or cause excessive wear of the bolt thread.

Figure 3.5 shows the velocity response around the mechanical resonance frequency of the diaphragm, marked with a dashed line for each case. It can be seen that as the diaphragm clamping increases, the resonance frequency increases pushing the peak velocity rightwards). This observation is in agreement with Eq. 18, where with increased clamping, k^2 , and hence f_D will increase. The highest output velocity is also measured when using 0.55 Nm of torque. For Orifice 1, the peak velocities at 0.35 Nm and 0.75 Nm reach 91% and 94% of the peak velocity measured for 0.55 Nm, respectively. Similarly, for Orifice 2, 98% and 95% of the maximum velocity is measured for 0.35 Nm and 0.75 Nm respectively. This shows that diaphragm clamping conditions is non-trivial and should not be arbitrarily chosen, as the peak jet velocity can be optimised by varying clamping conditions.

Furthermore, the ‘sharpness’ of the frequency response is also affected by the clamping conditions set. With tighter clamping, the actuation frequency range across which peak jet velocity is observed becomes smaller, which is typical of an underdamped system and would affect the damping coefficient, ξ , used in Eq. (18). To quantify how underdamped the SJA system is, the non-dimensional quality factor, Q_f , is used, given by Eq. (19):

$$Q_f = \frac{\omega_n}{\omega_u - \omega_l} \quad (19)$$

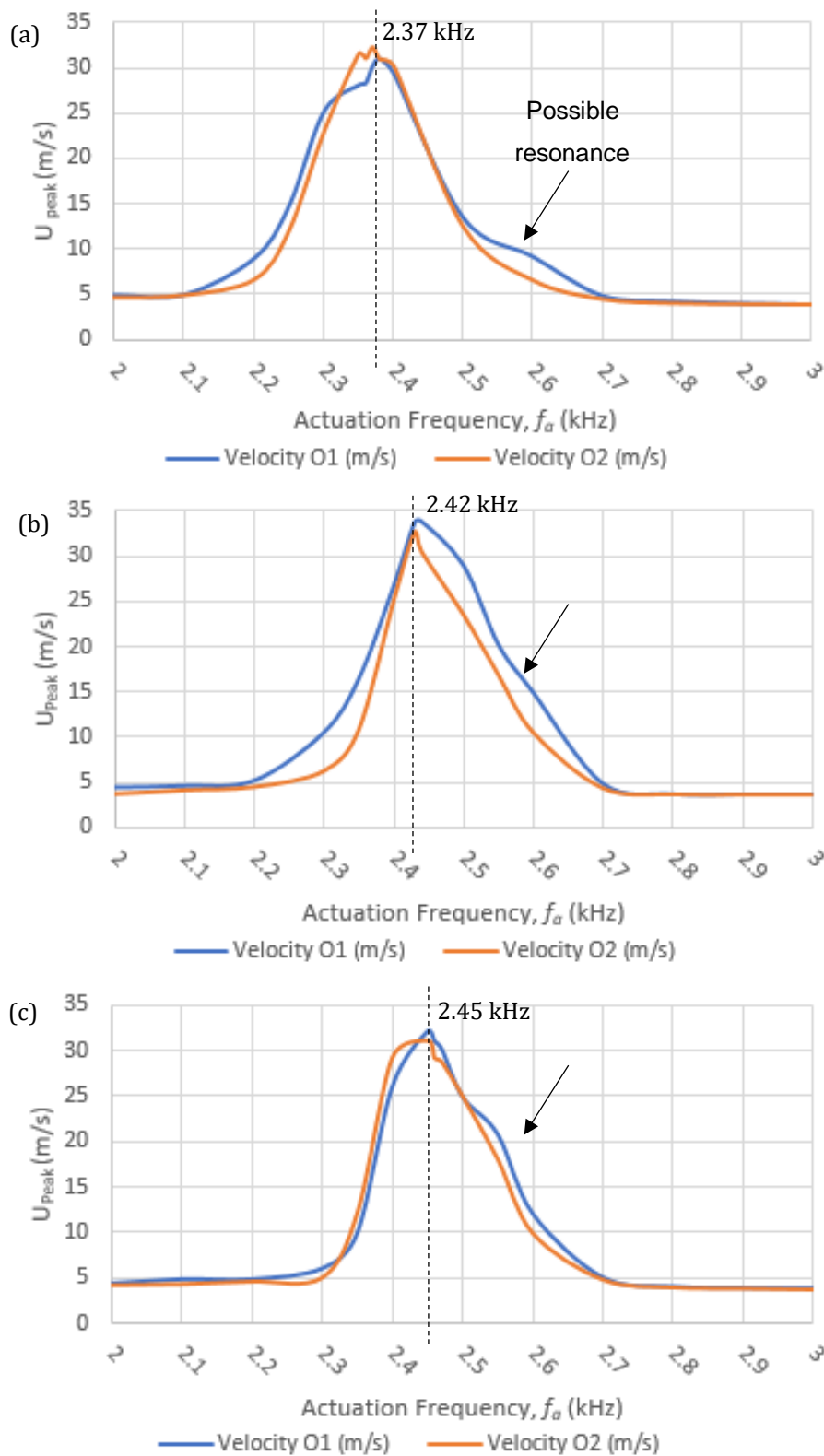


Figure 3.5. Circular orifice velocity response of the double chamber SJA with varying torque applied to the bolts (a) 0.35 Nm, (b) 0.55 Nm and (c) 0.75 Nm (dashed line marks the diaphragm resonance)

Where ω_n is the system resonance frequency, ω_u and ω_l are the frequencies for which the average power has dropped to one half of its resonance value (Kinsler et al. 1982). The airflow power of a SJA is by Eq. (20):

$$\dot{F} = \frac{1}{2} \rho A U^3 \quad (20)$$

Table 3 below summarises the quality factors for both orifices.

Table 3. Quality factor for circular orifices in the double chamber SJA

Orifice		01	02
Torque (Nm)	0.35	18.2	21.3
	0.55	21.7	32.4
	0.75	25.0	20.8

The quality factor for Orifice 1 shows a clear increasing trend with clamping. Orifice 2 on the other hand suggests that the system is most underdamped when 0.55 Nm of torque is used. Although the clamping seems to affect the quality factor there is not a uniform trend identifiable for both orifices. The actuation frequency ranges at which the velocity peaks occur decrease with increasing clamping, resulting in a sharper velocity response. This may not be a preferred property of the SJA during operation for a number of applications as fine tuning is required for each actuator to achieve any meaningful output. Furthermore, it would be expected that the trend for Orifice 2 would closely follow that of Orifice 1. However, this is not the case and is likely caused by the orifice discrepancies and uneven clamping that effects both cavities differently.

3.2 New Synthetic Jet Actuator

It is clear that the overall design and quality of individual components used in the SJA assembly is crucial to ensure reliable and consistent measurements. Therefore, the new SJA concepts developed took the following factors into consideration:

- Quality of components (dimensional tolerances and finish)
- Design for manufacture
- Design for ease of operation

- Control over individual physical characteristics of the SJA without changing others, for example orifice shape/height, cavity height and diaphragm clamping

In addition to the double chamber configuration a conventional single chamber SJA, with the orifice opposite the diaphragm (opposite configuration), is designed as it allows for much smaller cavity heights that make higher jet velocities possible (Eq. 10). Before designing the new actuator, a reference actuator was chosen with a high velocity output. In this case the design by Crowther & Gomes (2008) was chosen as a reference for the single chamber SJA due to reported jet velocities of up to 130 m/s. It was also decided to scale up the actuator geometry to achieve higher fidelity resolution of the lobed orifices. In the next sections a detailed description of the actuator design and manufacturing choices are presented and discussed. Design decisions are informed by the literature, preliminary results and simulation.

3.2.1 Diaphragm selection

For the new SJAs, the orifice diameter is doubled to $d_e = 2$ mm to improve the quality of the lobed orifice geometry through higher manufacturing resolution. Accordingly, the remaining actuator geometry needs to be scaled up too. This is achieved through the use of non-dimensional geometric scaling parameters for the velocity-optimised SJA design: $D/d \approx 20$, $H/d = 0.56$ and $h/d = 2.1$ (Crowther & Gomes, 2008). The ideal geometry based on these parameters is given in Table 4. However, the cavity diameter is dictated by the diaphragm, which in this case are off-the-shelf, PZT disc benders. The closest diaphragm available was a 50 mm diameter disc bender, that when clamped by a 1 mm lip around its perimeter results in a cavity diameter of 48 mm. The diaphragm is unimorph type with a 25 mm diameter PZT patch bonded to a 50 mm brass shim, and has a total thickness of 0.23 mm +/- 0.1 mm. (Figure 3.6)

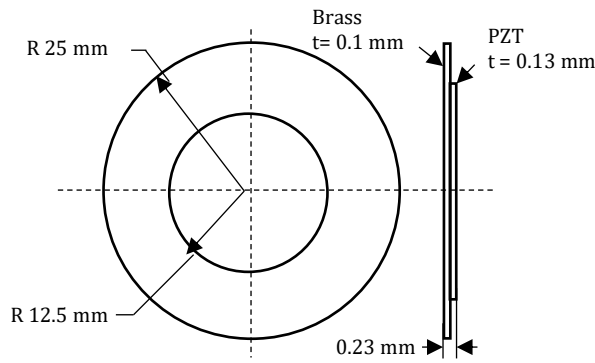


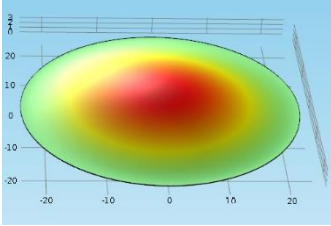
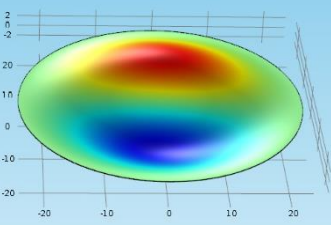
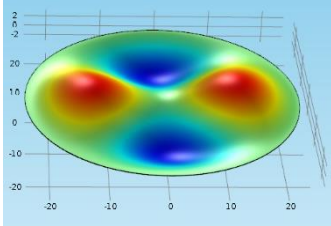
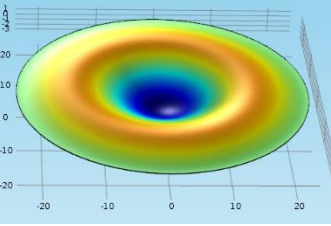
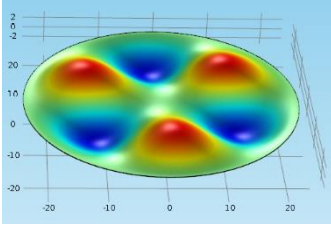
Figure 3.6. PZT diaphragm dimensions (50 mm)

Table 4. SJA dimensions scaled on peak velocity optimised design (Crowther & Gomes, 2008)

	Ideal	Actual
D	40 mm	48 mm
d	2 mm	2 mm
H	1.1 mm	1.2mm
h	4.2 mm	4.2 mm

A FEA-based eigenfrequency analysis of the brass shim, conducted in COMSOL Multiphysics, revealed eigenmodes together with mode shapes of the diaphragm. Table 5 shows a summary of the key resonance related information. Diaphragm related resonance usually only generates any meaningful output at the first resonance mode - at successive modes, positive diaphragm deflections are accompanied by an opposite deflection resulting in a zero or near zero net diaphragm and cavity volume displacement. However, it is worth noting that manufacturing imperfections and solder on the diaphragm, to apply an input signal, will affect the actual diaphragm deflection and eigenfrequencies.

Table 5. Key eigenfrequencies and mode shapes of PZT diaphragm obtained from eigenfrequency analysis (results shown are qualitative, red/blue indicate displacement in the +/- y direction, respectively)

Eigenfrequency (Hz)	Mode shape
312	
699	
1068	
1218	
1729	

3.2.2 Single chamber synthetic jet actuator

The most commonly used and simplest actuator layout consists of a cavity enclosed by an orifice plate on one end and a diaphragm on the other. In this layout the orifice is located opposite to the diaphragm and therefore the cavity height is not limited by the

orifice diameter. For instance, in a SJA using the adjacent layout with an orifice diameter of 2 mm, the cavity height cannot be made smaller than the orifice height, whereas the opposite configuration allows any cavity height as long as it is greater than the diaphragm displacement. As presented in Chapter 2, the peak jet velocity can be greatly enhanced with a significantly reduced cavity height due to the reduced phase difference between the diaphragm motion and jet formation. The dimensions of this actuator were summarised in Table 4 and the design is shown in Figure 3.7.

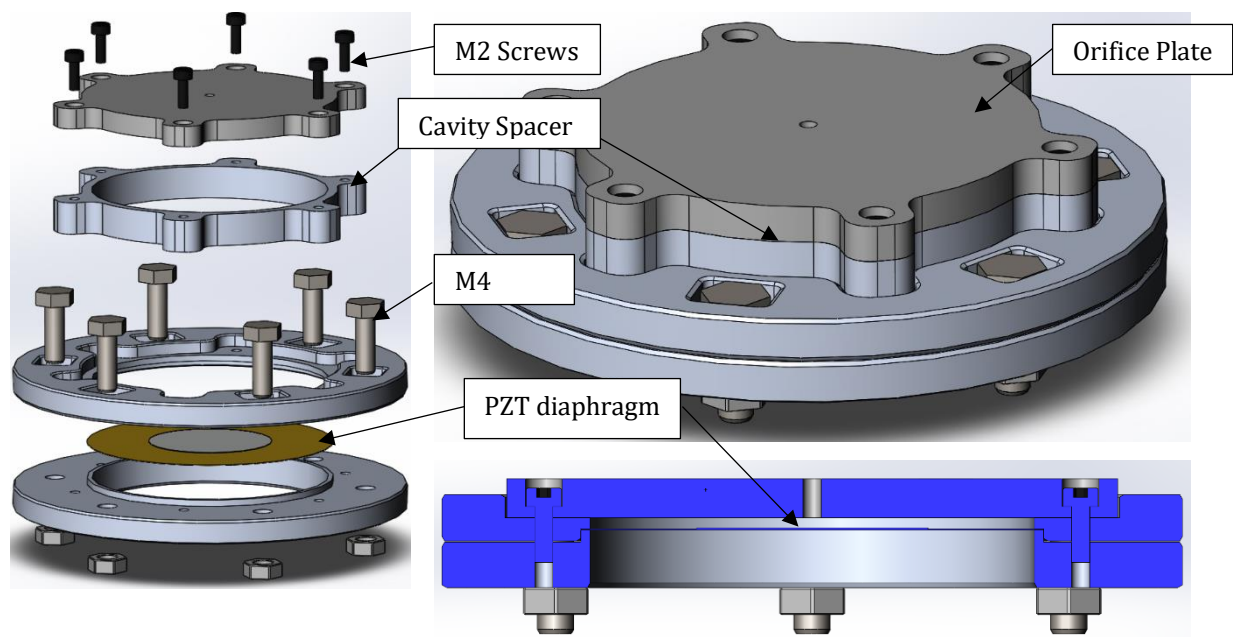


Figure 3.7. Single chamber SJA layout

Although the cavity height of 1.2 mm, scaled from a velocity optimised orifice, would achieve the highest jet velocity, the effect of cavity height will be investigated in the acoustic studies. The proposed SJA has a modular design with several cavity spacers to vary the cavity height ($H = 1.2 \text{ mm}, 3 \text{ mm}, 4 \text{ mm}, 5 \text{ mm}, 6 \text{ mm}$ and 8 mm). There are also four orifice plates, each with a different orifice shape, as discussed further in Section 3.2.4. An important feature of this design is the diaphragm clamping, which will be fixed throughout all experiments - an important requirement as seen from the preliminary tests in Section 3.1. This is achieved by separately clamping the diaphragm between two rings, where orifice plates and cavity spacers are independently screwed to these rings using a different set of screws. This ensures clamping conditions remain consistent between tests.

3.2.3 Double chamber synthetic jet actuator

The double chamber configuration (Figure 3.8) has some significant benefits over the single chamber SJA. These include an increase in efficiency due to the use of a single diaphragm to drive two cavities and ease to put together an array of actuators without the limitations imposed by the cavity or diaphragm diameter on orifice spacing.

However, the aim here is the self-noise reduction of SJAs and using this configuration can help achieve this goal. The periodic mass displacement by the SJA diaphragm, similar to a loudspeaker, allows it to be treated as a monopole source. When two coherent and out of phase sources, as shown in the double chamber SJA, interact there will be destructive interference between both sound fields along a line between the two sources. Using this on a SJA should produce a sound field similar to that shown in Figure 2.19.

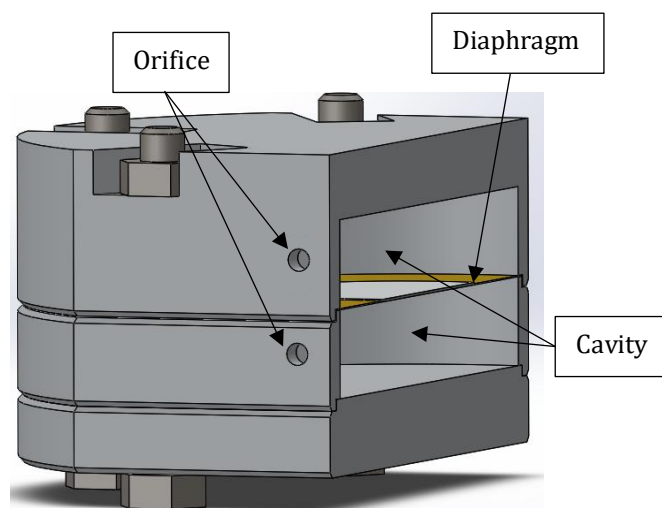


Figure 3.8. Double chamber SJA layout

The “adjacent configuration” places the orifice adjacent to the diaphragm unlike the opposite configuration, as seen on the single chamber SJA. This allows the orifices of adjacent cavities to be placed much closer to each other as required by SJA arrays for effective flow and also noise control in a practical setting. Furthermore, a significant benefit of this configuration is that a single diaphragm can be used to drive both cavities, which should in theory double the diaphragm efficiency. The cavity height in

the double chamber SJA is driven by the diameter of the orifices and the spacing between them. From an operational point of view, too closely spaced orifices may interfere with each other due to the phase difference, where one orifice may ingest the ejected jet from the other orifice. An orifice spacing of $5d$ was shown to prevent this mutual interference (Greco et al. 2013). Furthermore, smaller cavity volumes are associated with higher jet velocities. However, as discussed in Chapter 2, a smaller spacing between the two orifices is preferable to maximise the effect of noise cancellation, where the spacing should be much smaller than the acoustic wavelength associated with the actuation frequency, $\lambda = c_0 f_a$. Given that the first few diaphragm resonance modes are all below 2 kHz, the maximum actuation frequency for the tests is limited to 2 kHz. This means that the associated wavelength, $\lambda = 0.17$ m, which is significantly larger than $5d$. However, $5d$ leads to a cavity height $H = 10$ mm and smaller cavity heights are associated with higher jet velocities. For this reason, a compromise is made and the orifice spacing is reduced to $4d$ giving a cavity height of 8 mm. Furthermore, the orifice height is 2.5 mm, based on the optimal orifice height $h = 1.25d$ (Gomes et al. 2006) (Gomes, Crowther, & Wood, Towards a practical piezoceramic diaphragm based synthetic jet actuator for high subsonic applications – effect of chamber and orifice depth on actuator peak velocity, 2006).

3.2.4 Orifice design

The circular orifice has a diameter of 2 mm, while the lobed orifices all have an effective diameter $d_e = 2$ mm, that is they all have the same cross-sectional area as the circular orifice. When designing lobed orifices, two main parameters need to be considered: lobe count and lobe penetration. Lobed orifices form streamwise counter-rotating vortex pairs between lobes that enhance the mixing process. A high lobe count is preferred for noise reduction, while lobe penetration causes more aggressive mixing. At the same time, because of the finite volume of air ejected per actuation cycle, the increased mixing of the jet and ambient causes the jet to spread and lose momentum at a faster rate. Therefore, a balance between both parameters is needed, i.e. noise reduction while maintaining as much of the initial jet momentum as possible.

Three lobed orifices were designed for evaluation, that consist of varying number of lobes and penetration (Figure 3.9). The maximum number of lobes that was deemed

reasonably possible in terms of quality and resolution of the final part with the proposed 3D printing technology was six and a minimum of four. Lobe penetration is another key design parameter for these orifices and is also limited by manufacturing capabilities. Different levels of lobe penetration were needed to investigate the effect they have on the flow structures, which were discussed in more detail in Chapter 2. Two 6-lobed orifices with high and low amplitude lobes, H6 and L6 respectively, (high and low penetration) and a 4-lobed (4L) orifice was designed. The low amplitude 6-lobed orifice has very subtle features and is the least intrusive design, while the high amplitude 6-lobed and 4-lobed orifice are designed to have similar penetration ratio (ratio between minor and major axis), but different number of lobes. The high amplitude 6-lobed orifice penetration was limited by the lobe width that would become narrower and increasingly difficult to achieve using additive manufacturing with increasing lobe penetration. The 4-lobed orifice penetration ratio was then closely matched. This serves to validate the hypothesis of better noise reduction with a higher number of lobes with similar penetration.

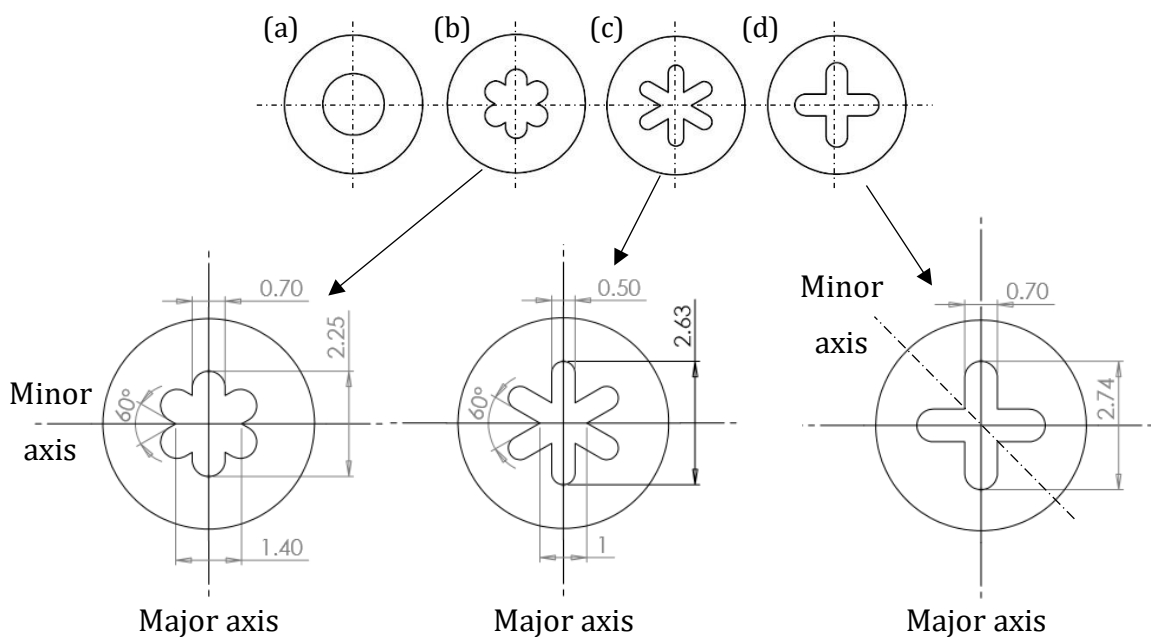


Figure 3.9. Orifice designs: (a) circular, (b) low amplitude 6-lobed, (c) high amplitude 6-lobed and (d) 4-lobed orifice with dimensions shown below

3.2.5 Manufacture

Due to the manufacturing discrepancies in the 3D printed lobed orifice plates and the actuator body in the preliminary work, a different approach had to be taken for the new SJA. The limiting factor in the manufacturing process is the resolution of the finished orifices that affect the lobe details. The main body of the actuator and orifice plates are CNC machined in aluminium. Although machining provides a quality finish and high tolerances, it is not a suitable manufacturing process for the high detail lobes. Holes of 4.5 mm are cut in the orifice plates for the fitting of orifice inserts made using a more suitable method. Two manufacturing methods were considered for this – wire erosion and 3D printing. The manufacturing cost of each orifice insert using 3D printing was achieved at 4-6% of the cost of wire erosion, where both offer similar quality final products.

A newer additive manufacturing technique was used for the orifice inserts that offers a better resolution of up to 0.1 mm instead of 0.2 mm, as seen in the original SJA manufacture. Each layer of the orifice is formed by printing layers of ultra-fine grains of stainless steel using precision inkjet-like printer and depositing a binding agent. An overhead heater dries each layer after which a new layer is printed until the orifice in its “green state” is formed. To complete the orifice, this version of the part is then sintered in an oven at 1300 °C after which it is ready for post processing. The finished parts had minor imperfections, such as dust or metal debris stuck inside the lobes, which were easily remove using an ultrasonic cleaner. Finally, the orifice inserts were press fitted into the orifice plates (Figure 3.10a-c). The same processes were employed in the manufacture of the double chamber SJA.

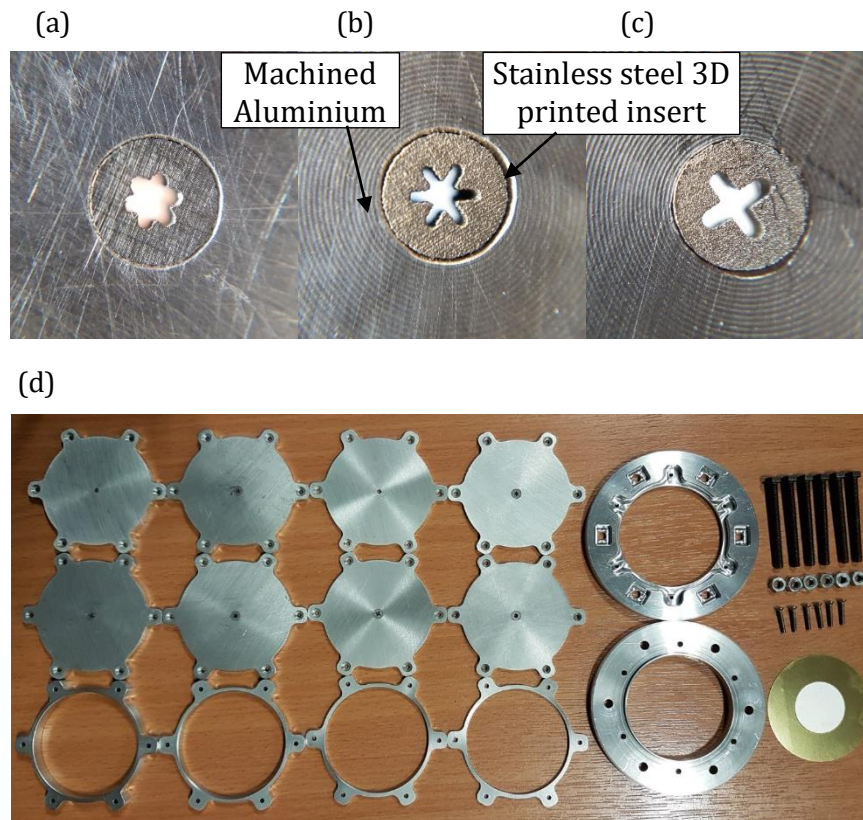


Figure 3.10. Close-up of (a) low amplitude 6-lobed, (b) high amplitude 6-lobed, (c) 4-lobed orifice and (d) all SJA components

3.3 Chapter Summary

In this chapter the design of the SJAs used throughout the experimental work presented in later chapters was discussed. Preliminary test results using an earlier double chamber SJA, designed for noise reduction using lobed orifices and antiphase operation, was shown. The aim of this study was to help create design specifications for SJAs to be used in extensive acoustic and fluidic performance measurements with design improvements based on the preliminary tests.

The acoustic performance improvements possible with lobed orifices was recently shown (Jabbal & Jeyalingam, 2017). However, fluidic performance tests show that the quality and design of individual components are crucial in order to obtain reliable and accurate results during experiments. Furthermore, a new parameter – diaphragm clamping conditions - has been considered for later experiments. It was shown that increased clamping force on the diaphragm edge, i.e. torque on the clamping bolts, results in a sharper velocity response that occurs over a smaller range of frequencies.

This was quantified using the quality factor, an indicator of how underdamped the coupled oscillator system is. Also, it was observed that clamping affects the jet peak velocity, where an optimum clamping condition exists. Clamping conditions in this work are quantified by the amount of torque applied to the six bolts used in the assembly of the SJA. For the preliminary tests (25 mm diaphragm diameter) this was found to be 0.55 Nm.

Using the results and data collected from the preliminary tests it was possible to generate a design specification for an improved SJA design. Designs for a modular single and double chamber SJA were presented, where the single chamber SJA is based on a velocity optimised design by Crowther & Gomes (2008) and the double chamber SJA is designed with noise reduction through antiphase operation in mind, taking into account the orifice separation distance and cavity geometry from a sound and flow field interference point of view. To realise the goal of manufacturing high quality and cost-effective SJA components, a combination of CNC machining and high-detail stainless steel additive manufacturing methods were used. The ideal torque applied to clamp the larger 50 mm PZT diaphragm was found to be 0.70 Nm in this case.

4 Methodology

In this chapter a detailed outline of the experimental setups used for various experimental procedures are given. The experiments consist of four parts: jet velocity measurements, diaphragm deflection measurements, SJA acoustic measurements and flow visualisation.

4.1 Jet Velocity Measurements

4.1.1 Hotwire setup

For velocity measurements of the SJA across a range of actuation frequencies and input voltages, hot wire anemometry was conducted using a Dantec MiniCTA (Constant Temperature Anemometer) system with a single-sensor miniature 55P11 probe. The sampling frequency was set between 10 - 20 kHz, (depending on measurements taken) and number of samples was 60,000, with the appropriate anti-aliasing filters applied for specific measurements through the Dantec Streamline software. For PSD (Power Spectral Density) measurements higher sampling frequencies were used to target the frequency range of interest in the spectra. The test rig is shown in Figure 4.1, while the setup is shown in Figure 4.2.

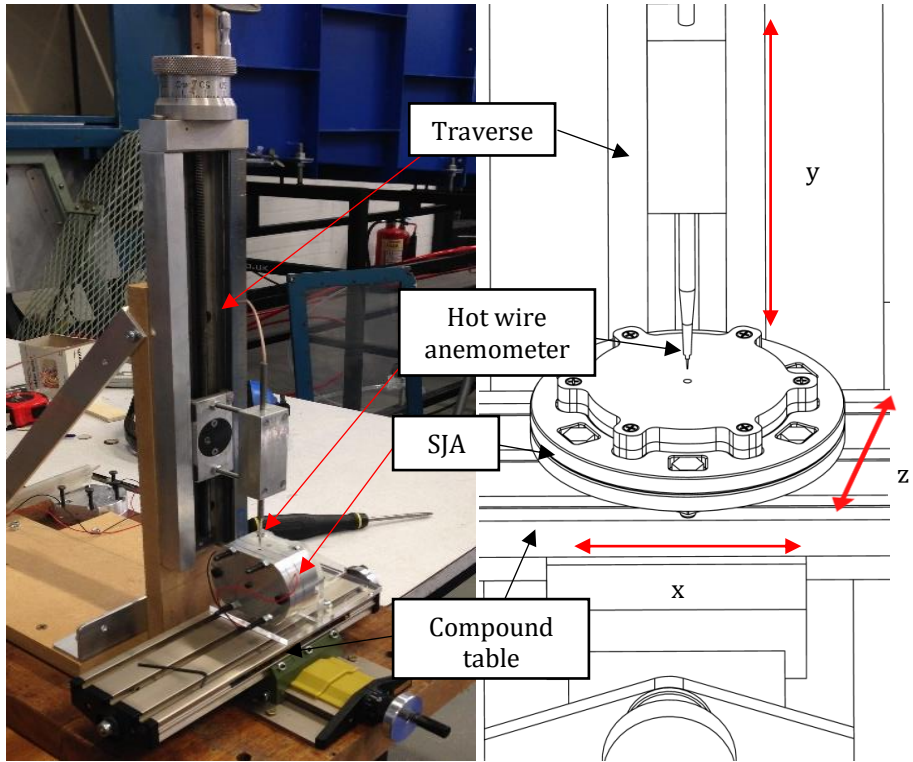


Figure 4.1. SJA hotwire test rig setup with schematic of traverse system (right)

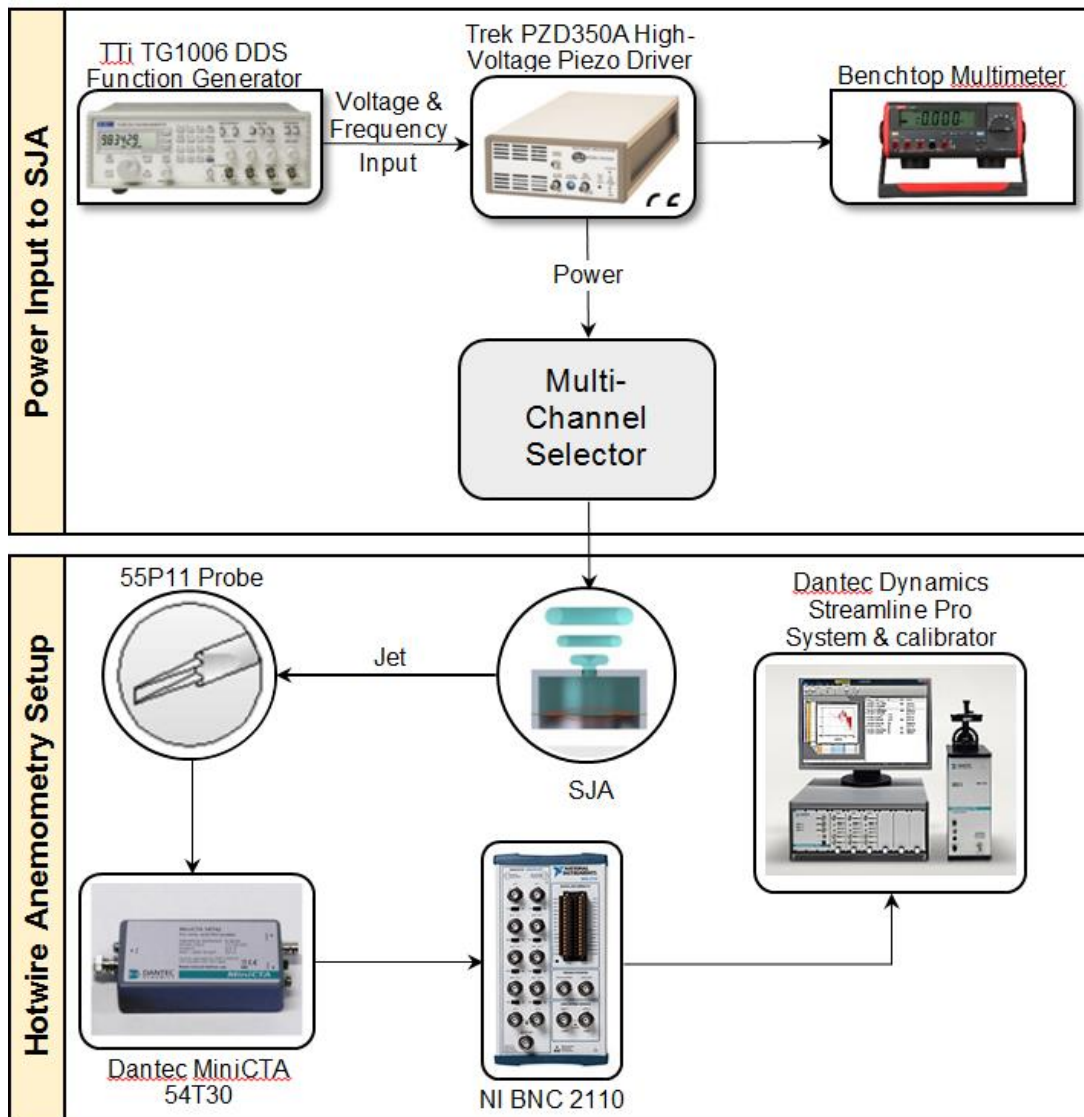


Figure 4.2. Hot wire anemometry test setup

A benchtop test rig was designed for testing the different actuator designs and conducting various measurements. The SJA is securely mounted to a micro compound table allowing movement in the x- and z-direction with an accuracy of 0.05 mm, while the hotwire probe is fitted to a micrometer head with a useable range of 150 mm in the y-direction. This provides a rigid platform for SJA tests with high dimensional resolution in all directions, which was useful for detailed measurements of velocity profiles across the orifice span and at several streamwise positions. Once the SJA is mounted to the compound table, it can be traversed in the x-direction at 0.1 mm increments to measure the velocity profile, while adjustments in the y-direction are used to measure the streamwise jet velocity. The closest point at which hotwire measurements were taken is

about 1 mm from the orifice exit referred to as “exit” in discussions presented later. Data collected from this system is also used later for the analysis of jet power spectral density (PSD), as detailed further in Chapter 5.

4.1.2 Hotwire calibration

A hotwire probe consists of a thin wire connected across a Wheatstone bridge that is heated by an electric current. In order to maintain a constant wire resistance and temperature as air flows over the wire, enhancing heat transfer, the bridge current is kept balanced by a servo amplifier. The voltage across the bridge, E , is then recorded which represents the heat transfer from the wire and is thus a function of the velocity. This relationship between the bridge voltage, E , and velocity, U , can be expressed as a 4th order polynomial equation (Eq. 21):

$$U = C_0 + C_1E + C_2E^2 + C_3E^3 + C_4E^4 \quad (21)$$

To apply this curve fitting method, the wire calibration needs to be conducted in a known reference flow. This is provided by the Dantec Hotwire Calibrator (Figure 4.2), used to generate a low turbulence reference jet of velocities ranging from 0 – 45 ms⁻¹. The hotwire calibration process was carried out before experiments in the same laboratory as the measurements were conducted to ensure ambient conditions remain constant. Before and during calibration, ambient pressure and temperature (T_{meas}) data were recorded. Depending on the velocity range required for testing, 10 – 20 calibration points were used with the hotwire probe placed centrally at the jet nozzle exit. The maximum error for a velocity range of 0-5 m/s is +/- 20.1%, +/- 6.4% for 5-20 m/s and +/- 3% for 20-45 m/s.

Between measurements, temperature changes can cause additional errors of around 2% for a change of 1 K. Temperature corrections were applied to obtain the corrected bridge voltage, E_{corr} , using the ratio between the over-temperatures during calibration ($T_w - T_0$) and measurements ($T_w - T_{meas}$) and is given by Eq. (22):

$$E_{corr} = E \left(\frac{T_w - T_0}{T_w - T_{meas}} \right)^{0.5} \quad (22)$$

4.2 Diaphragm Deflection Measurements

4.2.1 Displacement

The Microtrak 3 system is used to collect displacement information of the latex diaphragm used in the electromagnetically actuated SJA. Meaningful diaphragm displacement is achieved for an actuation frequency range of $5 \text{ Hz} < f_a < 100 \text{ Hz}$, therefore making the 300 Hz sampling frequency of the Microtrak 3 system suitable. This is because the sampling frequency $f_s = 300 \text{ Hz}$, which is above Nyquist frequency. The system uses laser triangulation to compute the standoff to the laser target fixed to the vibration generator shaft connected to the diaphragm (Figure 4.3), with measurements errors of $\pm 4 \mu\text{m}$. The diaphragm was also tested without an orifice plate attached to the SJA, to measure the effect an enclosed cavity has on it. In this case the laser of the displacement sensor was directly aimed at the diaphragm centre instead of a target.

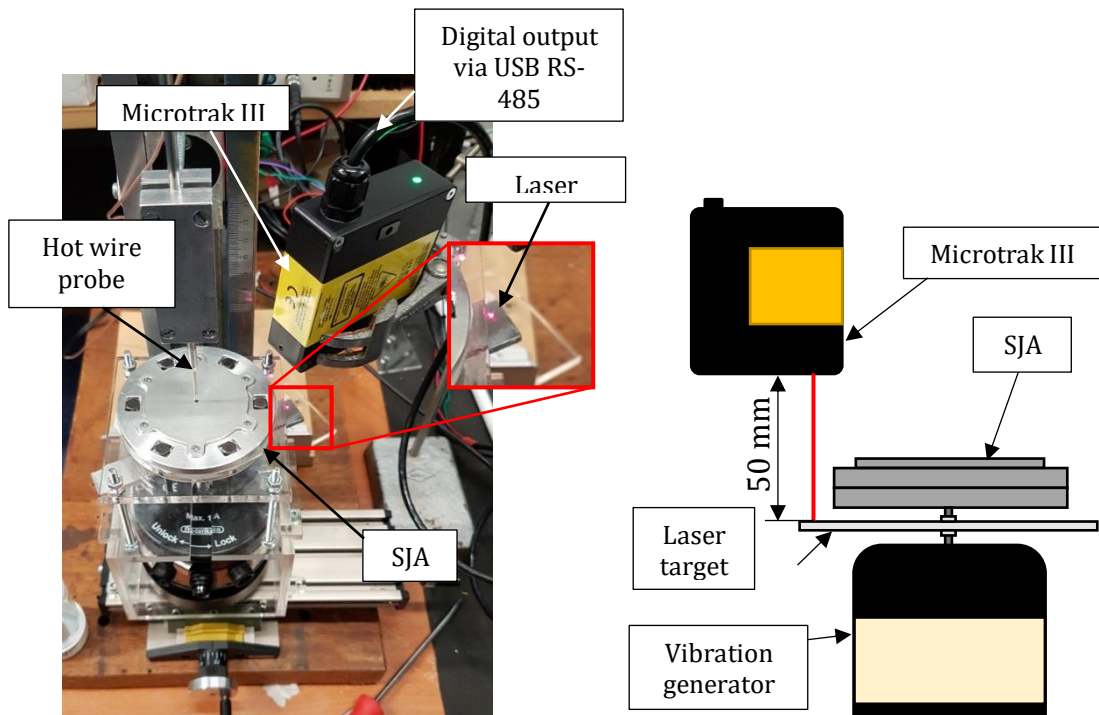


Figure 4.3. Microtrak 3 system setup on benchtop test rig

4.2.2 Mode shape

Peak actuator performance is observed at the system resonance frequencies. Mechanical resonance frequencies can be identified by distinct mode shapes, which vary greatly depending on the resonance mode. For instance, the diaphragm's first mode has a single deflection peak in the centre, while the second has two peaks. With an actuation frequency range of 0-2 kHz, the motion of the piezoelectric diaphragm cannot be captured using the Microtrak laser displacement sensor, that takes measurements at single points. Also, the different mode shapes mean that the maximum displacement is not always confined to the centre of the diaphragm. To carry out an Experimental Modal Analysis (EMA), a Digital Image Correlation (DIC) system test was conducted at the University of Nottingham, as shown in Figure 4.4.

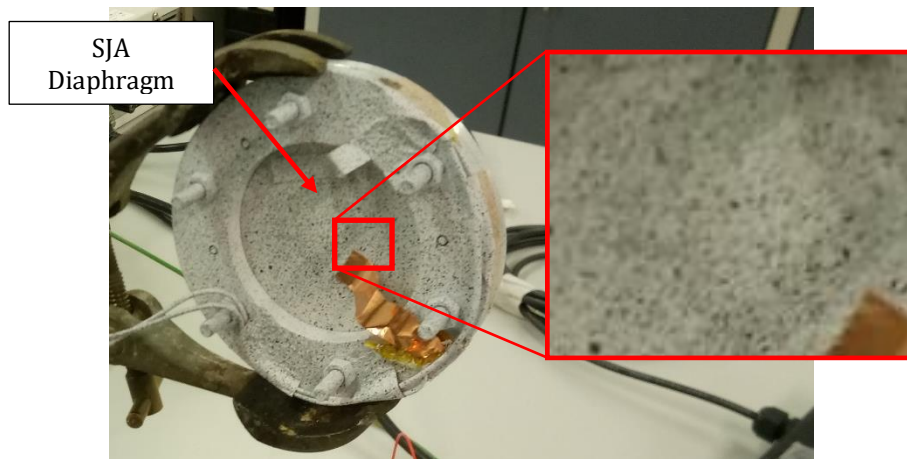
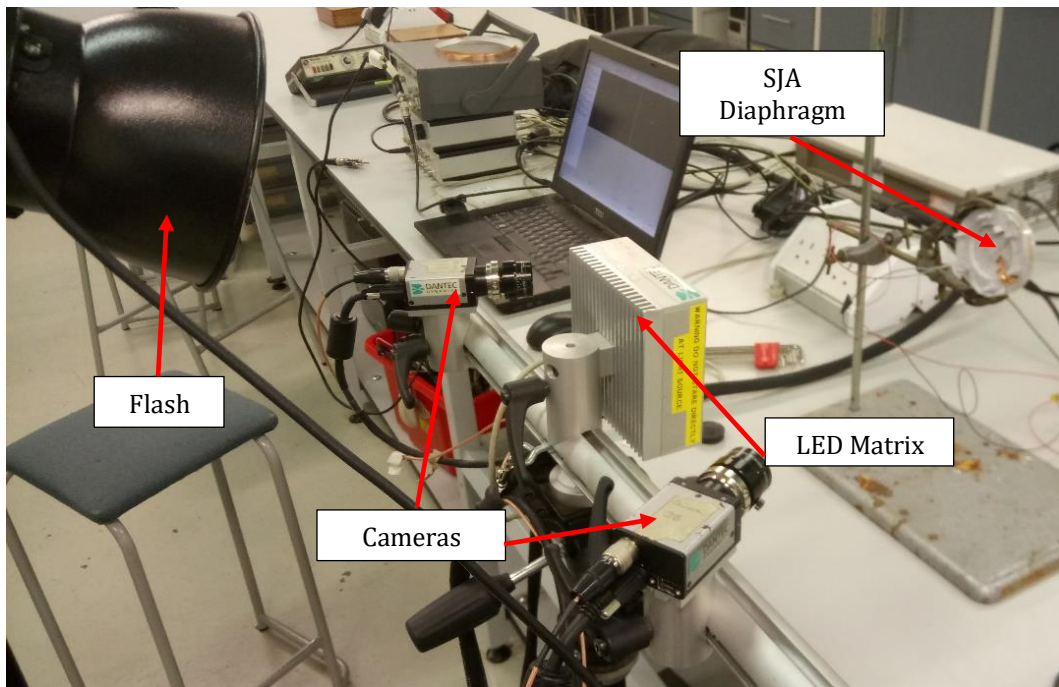


Figure 4.4. Dantec Q-400 DIC system setup (top) and close-up of stochastic speckle pattern on the diaphragm (bottom)

The objective of this test is to view the mode shapes of a 50 mm PZT-diaphragm fitted inside a SJA with a circular orifice and a cavity height $H = 1.2$ mm. The system used is a Dantec Q-400 3D digital image correlation system using two 5-megapixel cameras with a frame rate of up to 6 fps. Signal input was monitored using an oscilloscope. A GW-Instek GDS-1022 Bowens model ProLite 60 flash lamp was used as the light source, which is triggered by the Q400's 'sync' output signal. A high intensity LED matrix was used for calibration and focusing of the camera. A stochastic speckle pattern was applied to the diaphragm using aerosol paint spray as shown in Figure 4.4. Calibration of the cameras was done according to the DIC system internal procedures, where the system's LED acted as the light source. The actuation frequencies to be studied were

approximated from the peak values of the velocity response of the single chamber SJA, where $H = 1.2$ mm. For each frequency a set of 60 images were taken at 0.5 Hz, while the processing is done using the Dantec ISTR-4D software.

4.3 Acoustic Measurements

4.3.1 Anechoic chamber

All acoustic measurements were carried out in the aeroacoustic research facility at Brunel University London. This facility is aimed at aerofoil noise studies which are subjected to a free jet in a low noise environment, where this low noise environment is a crucial requirement for accurate measurements of SJA noise characterisation. This ideal measurement environment is achieved through the use of triangular noise absorbing polyurethane wedges mounted to the chamber wall and floor. In most other work focused on SJA noise studies so far this was not the case (Chapter 2), where tests were conducted in open laboratories where background or reflected noise contamination is likely to occur.

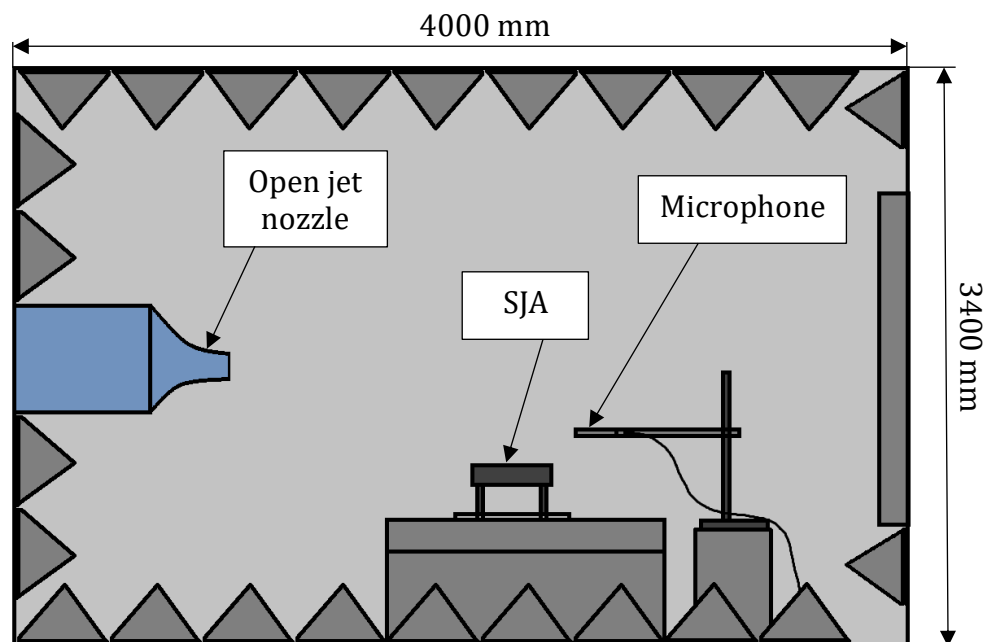


Figure 4.5. Schematic of Brunel University London anechoic chamber facility

4.3.2 Microphone selection

A number of parameters need to be considered when selecting which microphone to use, such as the type of sound field, dynamic range requirements or standards that need to be met.

Three types of sound fields exist that need to be considered (Ahuja, 2003):

- Free field
- Pressure field
- Diffuse field

In a free field it is assumed that the sound waves can propagate freely without any disturbing object through a continuous medium. A field where the sound pressure has the same magnitude and phase at any position is called a pressure field. For example, this would be the case in the actuator cavity, where the cavity is small compared to the wavelength. And in a diffuse field it is assumed that all sound waves of equal probability and level arrive at a fixed location more or less at the same time, or in other words, the sound pressure is the same everywhere in the test environment. An example where this may occur is a room with rigid walls that reflect sound waves. For the current actuator and test environment (anechoic chamber) it is fair to assume a free field without any/minimal reflections, with appropriate measures taken.

Typically, smaller microphones are suitable for higher frequency noise measurements and also disturb the sound field less due to their size. However smaller microphones generally have higher inherent noise and lower sensitivity, which makes them unusable for lower sound levels. This effect is known as the electronic noise and typically increases with increasing frequency (Viswanathan, 2006). The microphone used in the present experiments is a PCB Piezotronics prepolarised 377B02 free-field condenser microphone with sensitivity of 50 mV/Pa (+/-1.5 dB) in conjunction with a PCB 426E01 preamplifier and a model 480C02 signal conditioner.

4.3.3 Microphone setup

Once the microphone has been selected, the position and orientation of the microphone relative to the SJA needs to be considered. The two orientations considered are normal

and grazing. When using normal orientation to the sound source, the microphone is directed at the centre of the orifice exit plane. It is assumed that the source is concentrated at this point and can be treated as a point source. When placing the microphone at grazing incidence to the jet, the microphone is placed such that it is tangential and coincides with a plane drawn through the jet centreline (Figure 4.6). Placing the microphone at normal incidence, however, means that it is placed directly in the path of the jet and may cause interference. Therefore, the microphone is directed towards the sound source at an angle of 30° relative to the orifice plate. This ensures the jet will not impinge on the microphone. Both methods described have been used throughout the experiments, where the inclined microphone setup was used for the measurement of the interference pattern of the double chamber SJA and grazing incidence for all single chamber SJA measurements.

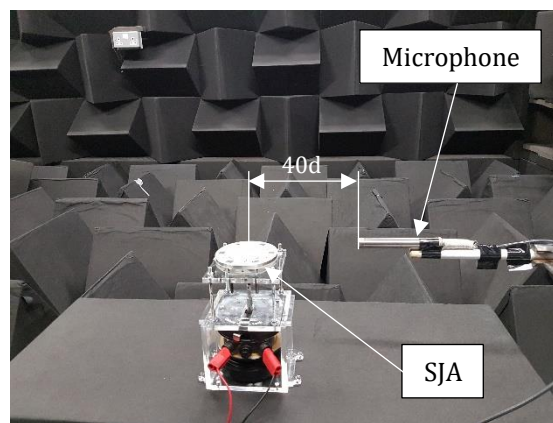


Figure 4.6. SJA acoustic measurement setup: microphone placed at grazing incident to jet

For far field directional measurements, the microphone was placed at a distance of 300 mm ($150d$, where $d = 2$ mm) attached to a microphone holder with the microphone pointing centrally between the two double chamber SJA orifices at angle of 30° . Measurements were taken 360° around the actuator y-axis at 10° increments. This setup is used to determine the change of the sound field due to the interference of the two monopole sound sources (orifices). For the single chamber SJA the acoustic test setup was different, as jet induced noise only is to be measured. The microphone was placed at 80 mm ($40d$, where $d = 2$ mm) from the orifice at grazing incidence relative to the jet. This distance is recommended by Ahuja (2003), who recommends a distance of $40-72d$ for true far field jet noise measurements, and Viswanathan (2006), suggests a minimum distance of $35d$.

4.3.4 Acoustic measurement metrics

Far field noise measurements were carried out using the setup shown in Figure 4.6, with samples taken at 44 kHz using a NI 16-bit analogue – digital (A/D) card. Each measurement lasted 20 seconds; the acquired data was then converted to Sound Pressure Level (SPL), as defined in Eq. (23):

$$SPL(f) = 10 \log \left(\frac{S_{pp}(f)}{p_0^2} \right) \quad (23)$$

Where S_{pp} is defined as the mean square pressure and p_0 is the reference sound pressure level (2×10^{-5} Pa). The microphone was calibrated prior to tests using a GRAS 42AB sound calibrator that provides a 1 kHz +/- 0.2% reference frequency at 114 dB +/- 0.2 dB, corresponding to 10 Pa. The SPL errors are found to be in the range of +/- 1.5 dB.

4.4 Flow Visualisation

4.4.1 Dye flow setup

The purpose of flow visualisation is to gain a better understanding of flow structures and their complex interactions with each other in synthetic jets issuing from circular and lobed orifices under operating conditions typical of current synthetic jet actuators using piezoelectric actuation.

To minimise the effort and equipment needed to visualise flow structures and jet development, the SJA model used is a scaled-up version of the single chamber SJA with an effective diameter $d_e = 5$ mm instead of the 2 mm used for the SJAs operating in air.

The single and double chamber SJA presented in Chapter 3 served as a reference geometry, while the commonly used dimensionless geometric scaling parameters D/d , H/d and h/d were used to ensure a comparable model. In total 4 orifices were designed for testing throughout the work presented here: one circular orifice and three lobed orifices, which are scaled from the same orifices presented in Chapter 3. Figure 4.7 shows the final dimensions of the SJA used.

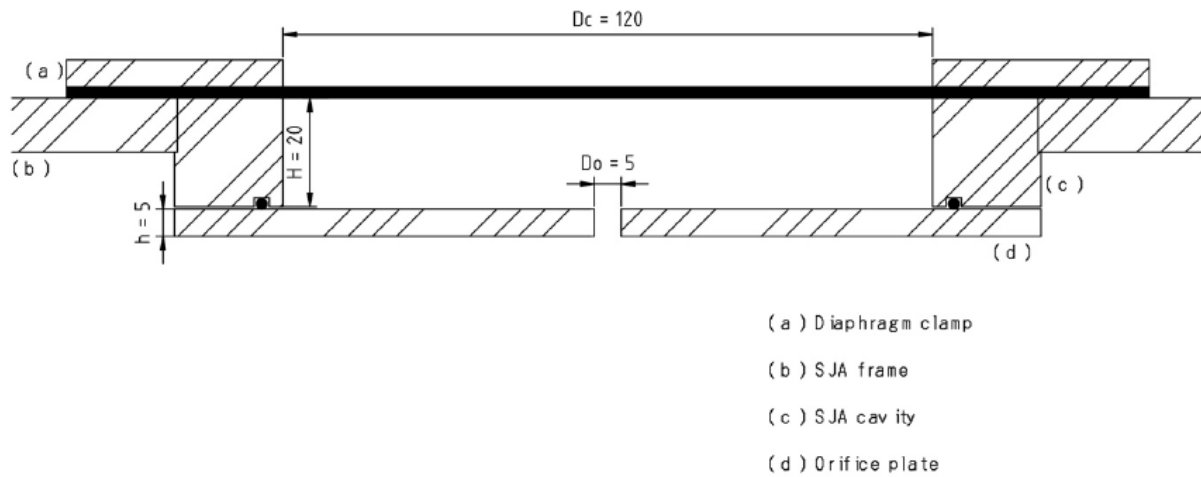


Figure 4.7. SJA geometry for dye flow visualisation (Conibear, 2016)

A schematic of the experimental setup is shown in Figure 4.8. The tank was built for the purpose of this experiment (Conibear, 2016) using clear Perspex that once assembled has a depth of 185 mm (37d) from the orifice exit and a width of 300 mm (60d), giving the jets and flow structure enough room without interfering with the tank boundaries. A rubber diaphragm is forced to periodically oscillate by a Frederiksen 2185.00 vibration generator that is connected centrally to the diaphragm via a shaft. The sinusoidal input for the vibration generator comes from an amplified signal from a function generator. Dye is injected into the cavity through a syringe which colours the water contained within the cavity. During actuation of the rubber diaphragm coloured water exits the cavity making the jet and flow structures, formed at the orifice exit, visible. To avoid misinterpretation of the observed flow field it is important to choose a dye carefully (Smits & Lim, 2000). Two types of dyes were considered: conventional food colouring and Patent Blue V solution. Unlike the Patent Blue V solution, the food colouring, although initially dissolving, was not as buoyant because it is a concentrate and began accumulating at the bottom of the tank after some time. Patent Blue V solution, on the other hand, dissolves easily in the cavity and has better buoyancy in water than food colouring, ultimately making it more suitable for these tests.

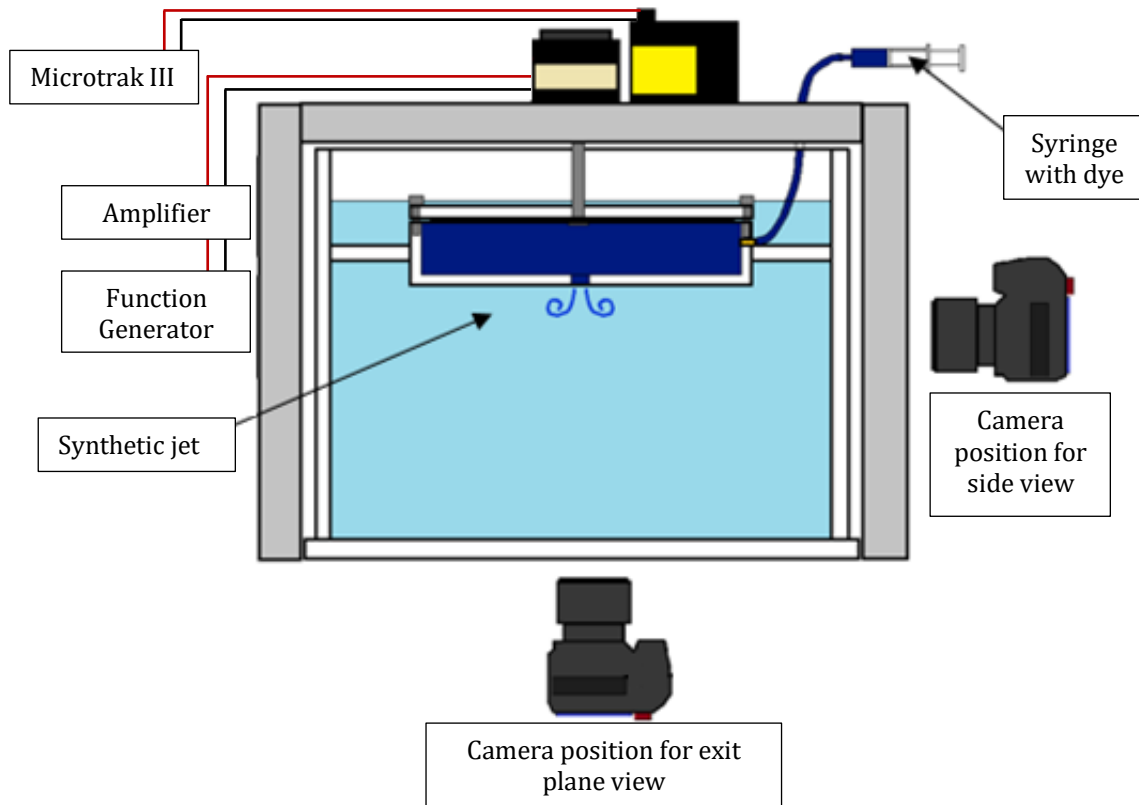


Figure 4.8. Dye flow visualisation setup

For precise measurement of the diaphragm peak-to-peak displacement, Δ_{p-p} , the MTI Microtrak 3 laser displacement sensor was used. It is expected that lobed jets break up and spread faster than circular ones. To view this effect the camera is positioned to the side of the tank (Figure 4.8). The evolution of synthetic jets from the orifice exit plane is also of interest, as complex spanwise developments are expected. For this the camera is placed below the tank in line with the orifice exit (Figure 4.8). A Samsung Galaxy S7 rear facing camera was used for capturing video footage that provides a resolution of 1280 pixels by 720 pixels at 240 fps or 1920 pixels by 1080 pixels at 60 fps. Depending on the desired view the resolution was varied, where for side views 60 fps was sufficient, the spanwise jet development was recorded at 240 fps, due to the fast-changing flow structures in the exit plane.

Considering this test setup was used as a tool to aid with the design of small scale lobed orifices for tests in air, the reference for the test conditions are based on operating parameters presented later in Chapter 5. Based on these values, the dimensionless stroke length, L , and jet Reynolds number, Re_j , can be found using Eq. (4) and Eq. (24)

respectively. These dimensionless operating parameters, according to Glezer (1988) are key in the characterisation of synthetic jets. Since the flow visualisation is conducted in a different medium (water), the challenge is to match L and Re_j to the conditions in air.

$$Re_j = \frac{\bar{U}_o d}{\nu} \quad (24)$$

Since jet velocity is not measured in this experiment, the resulting jet velocity in water needs to be approximated using existing models. Tang and Zhong (2006) showed that for incompressible flows, based on the conservation of mass in the cavity, the peak and time-averaged blowing velocity are given by:

$$\tilde{U}_{peak} = \frac{\pi}{4} \Delta f \left(\frac{D}{d}\right)^2 \quad (25)$$

$$\bar{U}_o = \frac{1}{T} \int_0^{T/2} \bar{u}_0(t) dt = \frac{1}{3} f \Delta \left(\frac{D}{d}\right)^2 \quad (26)$$

As it wasn't possible to match L and Re_j simultaneously, two different cases were considered where each case matches one of L and Re_j . A detailed summary of test conditions is presented in Chapter 5.

4.4.2 Schlieren visualisation

Dye flow visualisation proved to be a helpful tool in the design of new orifice plates and studying flow structures formed by a SJA. However, dye flow visualisation has its limitations with the most obvious being the medium it works in. For the validation and study of small scale actuators in air, Schlieren visualisation is more useful. Schlieren visualisation is an optical flow visualisation method that relies on inhomogeneity in the fluid medium due to changes in refractive index caused by density changes in the flow. Such density changes can be caused by changes in temperature of the flow medium or a mixture of different fluid media, each with a different refractive index. A solution is to introduce a gas of different density near the orifice to be entrained by the jet. Two relatively cheap and easily obtainable gases were considered and tested – isopropanol

and carbon dioxide (CO₂). Isopropanol is commonly used in cleaning or degreasing applications and evaporates rapidly at room temperature. However, during application in its liquid state it may run into the orifice, blocking it and the fast rate of evaporation does not allow for capture of longer video footage. CO₂ on the other hand is commonly used in SJA experiments, where the heavier CO₂ is introduced at a low flow rate near the SJA orifice plate¹. The gas spreads over the orifice plate and is entrained by the ensuing jet, making it visible in contrast to the surrounding air. In the results presented in later chapters both methods were used, as both successfully help visualise the jet flow. Chapter 5 uses isopropanol, while results shown in Chapter 6 use CO₂ as the second medium. Although, it is noted that CO₂ was easier to work with due to the continuous regulated flow of the gas and better visibility achieved on unedited footage. This makes post processing easier and quicker.

The test setup used is shown in Figure 4.9. A light source, in this case a white LED, emits light that is reflected by a parabolic mirror placed behind the SJA. The light then travels through the gas mixture that makes up the jet and is refracted. A knife edge is placed in such way as to focus and partially obstruct the reflected and refracted light to form the shadow. A DSLR camera can be used, but in this case a high-speed camera (FPS 1000) with a telephoto lens attached was used. The image sequence was captured at 1000 fps and a resolution of 1280 x 720 pixels. Images were then post processed and enhanced using Adobe After Effects CC. The point in the actuation cycle of individual images was determined by tracking the motion of the vibration generator shaft.

¹Ari Glezer private communication

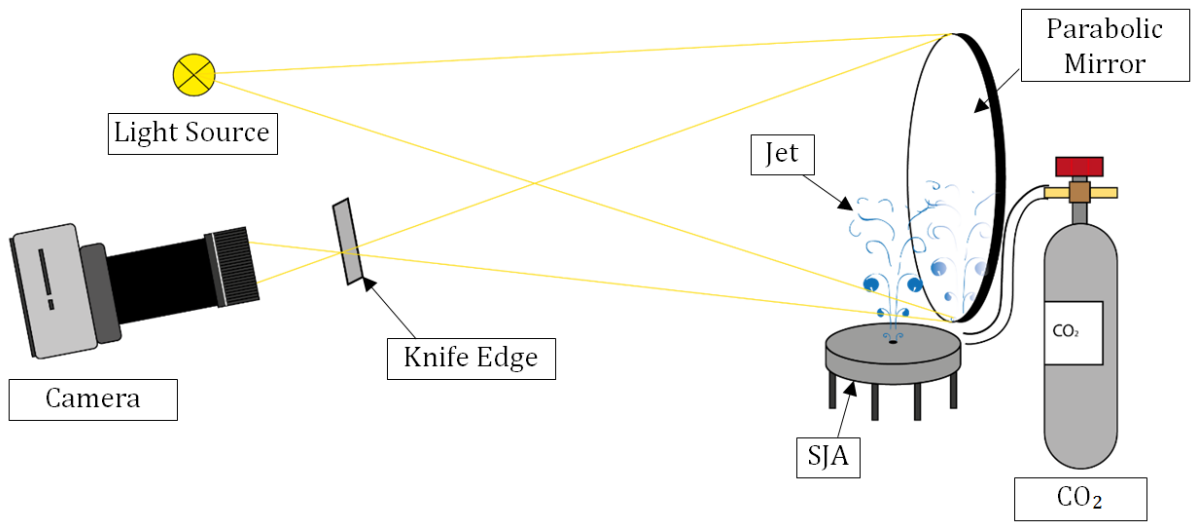


Figure 4.9. Schlieren flow visualisation test setup

5 Jet Flow and Acoustic Characteristics of Piezoelectric-driven SJA in Quiescent Conditions

In this chapter, piezoelectrical-driven SJA performance results are presented for both single and double chamber configuration in quiescent conditions. The actuator cavity and orifice geometries are varied to study their effect on overall actuator fluid performance, while different orifice shapes are employed to study the effects they have on the acoustic response. The experiments consist of three parts: SJA hotwire measurements in quiescent air, SJA acoustic measurements in quiescent air and SJA flow visualisation in quiescent conditions (dye flow in water and Schlieren visualisation in air).

5.1 Jet Flow Parameters

5.1.1 Circular Orifice SJA

5.1.1.1 Test conditions

Both actuators presented in these tests have a modular design, where for example the conventional single chamber SJA allows the change of orifice shape, orifice height and cavity height. The double chamber SJA on the other hand has a fixed cavity geometry, and its purpose is to test active noise reduction through antiphase operation of two monopole-like behaving orifices. Detailed information on the designs for both devices have been presented previously in Chapter 3. To summarise, Table 6 presents the geometrical parameters of both actuators.

Table 6. SJA geometric parameters

	Single Chamber	Double Chamber
Orifice diameter, d_e (mm)	2	2
Orifice height, h (mm)	2.5, 4.2	2.5
Cavity diameter, D (mm)	48	48
Cavity height, H (mm)	1.2, 3, 4, 5, 6, 8	8
Orifice shapes	Circular; Low amplitude 6-lobed; High Amplitude 6-lobed; 4-lobed	Circular; High amplitude 6-lobed

Tests were conducted with a sinusoidal, peak-to-peak input voltage of 30 V applied to the PZT disc and oscillation frequencies of 100 – 2000 Hz at 25 Hz increments.

5.1.1.2 Effect of actuator configuration on frequency response

The two actuator configurations tested, single and double chamber, were introduced in Chapter 3, where the orifice location relative to the diaphragm varies. In the conventional configuration the orifice is located opposite to the diaphragm, on the other hand the double chamber configuration has the orifice adjacent to the diaphragm. Although all geometric parameters are kept constant.

Figure 5.1 shows the frequency response for both actuators with fixed cavity height, $H = 8$ mm for an actuation frequency range of $0 < f_a < 1$ kHz. The justification for the chosen cavity dimensions can be found in Chapter 3. It can be seen that the output for both actuator types are very similar in magnitude. The single chamber SJA has a peak velocity that reaches 91% of the peak jet velocity achieved by Orifice 2 of the double chamber SJA and exceeds the peak velocity of Orifice 1 by 1%.

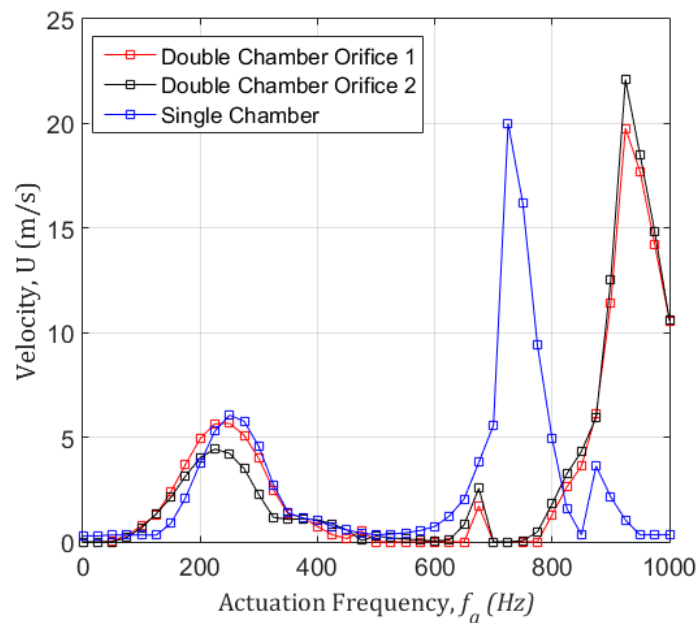


Figure 5.1. Comparison of single and double chamber actuator frequency response

There are several peaks in the velocity response located around the same actuation frequency for both configurations. These peaks appear at $f_a = 250$ Hz, 725 Hz and 875

Hz for the single chamber SJA and at $f_a = 250$ Hz, 675 Hz and 925 Hz for the double chamber SJA. The amplitudes for the second and third peaks look as if they are switched around, but their locations are within 50 Hz to each other. This is not surprising as the orifice height used in the double chamber SJA is shorter ($h = 2.5$ mm) which according to the Helmholtz resonance equation leads to a higher resonance frequency. The amplitude of the second and third peaks, therefore, are an example of coupling that results in higher jet velocities. It should be noted that although great care was taken in the design and manufacturing process to ensure the clamping methods and conditions could be kept constant across the different actuators, the diaphragms used in each experiment were different. Each diaphragm is unique and the slightest deviation in overall dimensions can change their mechanical properties and the resulting response. Furthermore, the mass of solder and wire that influence the diaphragm displacement will have some effect on the overall performance. These may cause certain discrepancies if diaphragms are changed during tests.

5.1.1.3 Effect of cavity height on frequency response

The following tests were conducted using the single chamber SJA, which has a modular design allowing it to vary its cavity height. Spacers are used to vary the cavity height of the actuator while keeping the orifice geometry the same.

Figure 5.2 shows the SJA frequency response with varying cavity height of between 1.2 mm – 8 mm measured centrally at the orifice exit. It can be seen that although there is a similar trend in all cases there is, also a shift in the response to the right, towards higher frequencies, with decreasing cavity height. Several velocity peaks are visible, which can be attributed to the different mechanical and acoustic resonance modes, as will be shown later in the chapter. The first peak occurs between $f_a = 200 - 400$ Hz and shows that the jet velocity increases with decreasing cavity height, with the smallest jet velocity observed with $H = 8$ mm and the highest at $H = 1.2$ mm. The second noticeable peak consists of two velocity peaks closely placed next to each other for all cases. However, there is no coupling visible between the two peaks, which may suggest that the peaks are both related to different mechanical modes close to each other. Simulations presented in Section 3.2.1 identified such resonance modes. And finally, at $f_a \approx 1600$ Hz and 1750 Hz there are velocity peaks visible again, regardless of cavity

height, indicating a mechanical resonance effect. This agrees once again with the simulation and the PZT disc manufacturer’s own specifications, with a stated resonance frequency of 1.7 ± 0.50 kHz (Piezo, 2014).

A peak jet velocity of 23.02 m/s is achieved using a cavity height of 1.2 mm at $f_a = 1225$ Hz and the lowest peak jet velocity recorded was 18.09 m/s at $f_a = 825$ Hz with a cavity height of 5 mm. Jain et al. (2011) noticed that reducing the cavity height resulted in a slight increase in peak jet velocity. This is expected as shown by equation 10 in Chapter 1, where the jet velocity is proportional to the ratio between the volume of air swept by the diaphragm and the cavity volume. Of course, other effects such as the different resonance modes and the coupling between the two can enhance the velocity output.

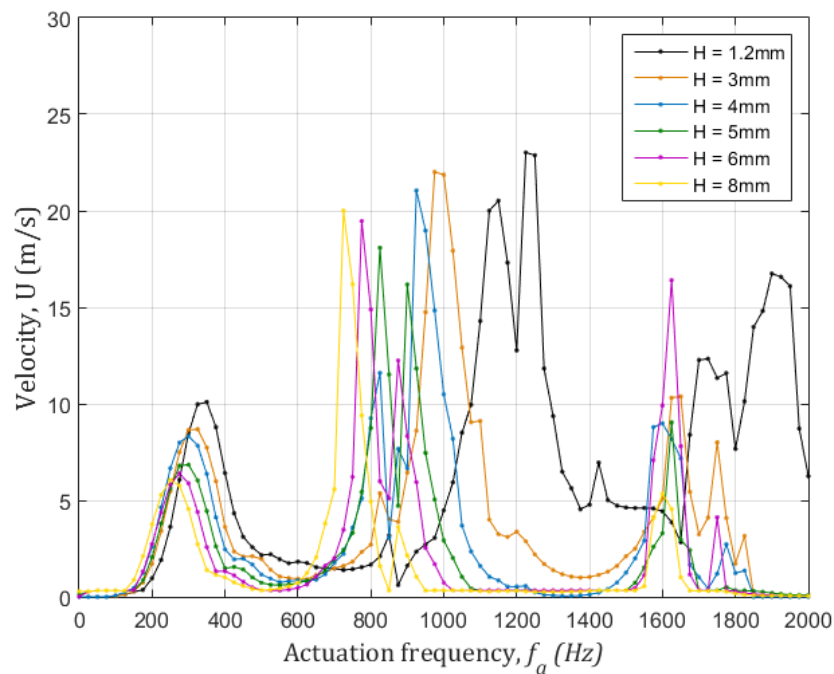


Figure 5.2. Single chamber, circular orifice SJA frequency response as a function of cavity height

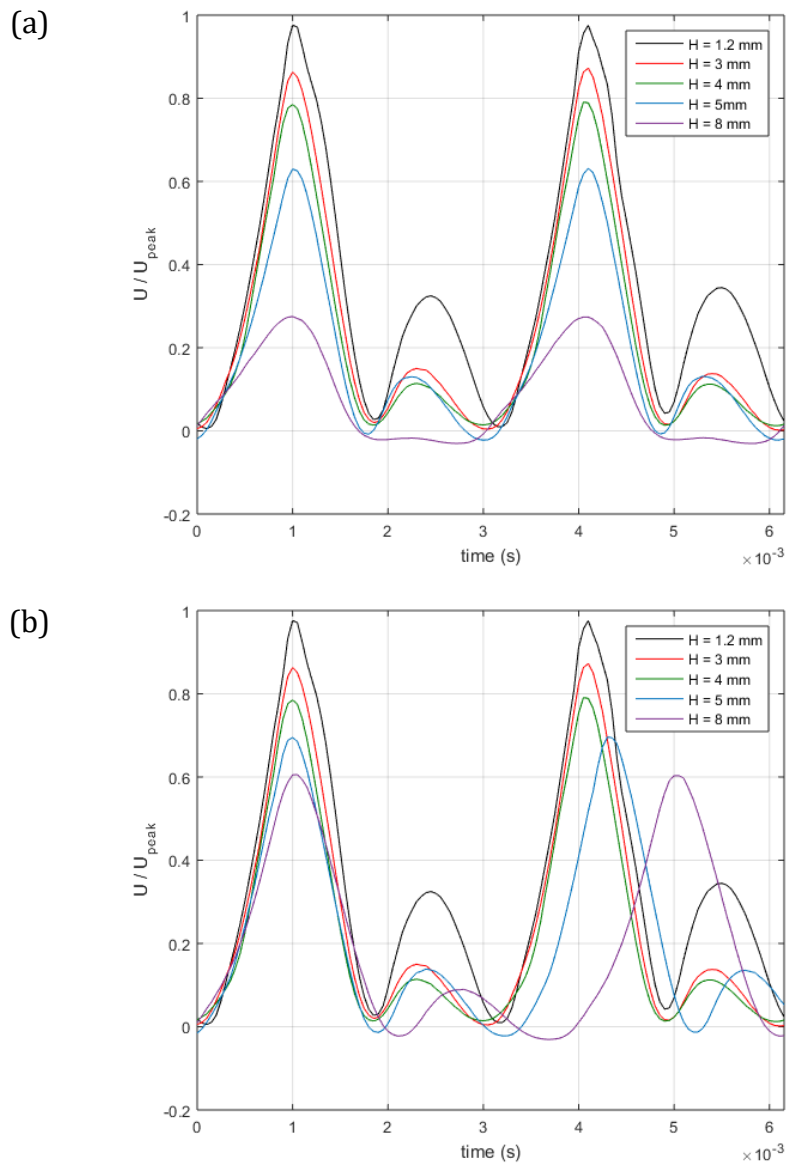


Figure 5.3. Instantaneous exit centreline velocity response at the first mechanical resonance mode, where (a) shows the SJA output cycle at the actuation frequency where the peak velocity, U_{peak} , is obtained (325 Hz) and (b) shows the peak output at the corresponding actuation frequency for each cavity (275 - 325 Hz)

With increasing cavity height, the jet velocity is also reduced. In Figure 5.3 the actuator output at the orifice exit over two cycles is shown for the first velocity peak in the frequency response presented in Figure 5.2 as a function of cavity height. From Figure 5.3b a trend is seen for the jet blowing part of the cycle where there is a steady decrease in the jet velocity with increasing cavity height. The suction cycle for cavity heights above 1.2 mm achieve similar peak velocities. However, for a cavity height $H = 1.2$ mm the suction velocity is 2.2 times larger than for a $H = 3$ mm. Also, the blowing peak for $H = 1.2$ mm is wider compared to other cavity heights. This can be explained by the

reduced phase difference between diaphragm motion and jet formation at the orifice exit (Jain et al. 2011).

5.1.2 Lobed Orifice SJA

5.1.2.1 Frequency response

The orifice shape plays a key role in the jet development and consequently the type of flow structures formed at the orifice exit. In this study a total of four different orifice shapes were investigated (circular, low-amplitude 6-lobed, high-amplitude 6-lobed and 4-lobed orifice shown in Figure 5.4) with the primary aim of modifying flow structures emanating from the orifice. The transition to turbulence and dissipation of periodic coherent structures in the flow that contribute to the self-noise, is a result of using such orifices.

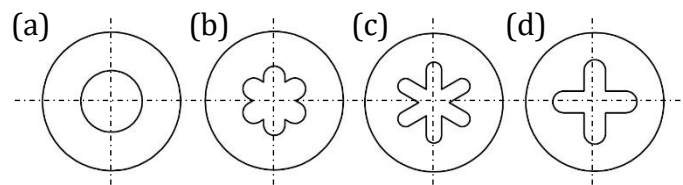


Figure 5.4. Orifice designs with the same effective diameter and area: (a) circular, (b) low amplitude 6-lobed, (c) high amplitude 6-lobed and (d) 4-lobed orifice

Each orifice has the same effective diameter, d_e , of 2 mm and a height of $h = 4.2$ mm. This orifice height was chosen as the frequency response gives more comparable jet peak velocities for all orifice shapes. With $h = 2.5$ mm the differences in jet peak velocities vary greatly and it would therefore be difficult to isolate the effect of orifice shape for acoustic measurements. As mentioned before (2.2.5.2), this is due to the extra orifice length which allows the separated flow upstream of the orifice to reattach to the orifice walls and straighten before being ejected.

Figure 5.5 shows the SJA frequency response as a function of cavity height and orifice shape for a fixed orifice height. Regardless of orifice shape, the trend of the frequency response is nearly identical for a given cavity height. This means that as the orifice shape varies, while the effective diameter (or cross-sectional area) is kept constant, both the mechanical and acoustic resonance frequencies do not change for a fixed cavity

height. In some cases, the peaks are slightly broader when using a lobed orifice, which is especially true between $f_a = 200 - 400$ Hz. Marked on Figure 5 are the different resonant frequencies and it can be seen that with increasing cavity height one of the resonant frequencies decreases gradually, while the other resonant frequencies in the response remain nearly constant. For example, when H is increased from 1.2 mm to 3 mm (Figure 5.5a and 5.5b) the velocity peak at $f_a = 1150$ Hz decreases to 975 Hz, while the other peaks remain unchanged. Based on this observation it can be deduced that the changing peaks are related to acoustic resonance, which is a function of the cavity geometry and is expected to change accordingly. The mechanical resonance modes have a deviation of ± 50 Hz with changing cavity height, e.g. at $f_a = 300$ Hz, 825 Hz or 1625 Hz, and agree well with the eigenfrequency and DIC study of the diaphragm (Figure 5.6). Maximum volume change of the cavity is expected only at the first resonance mode of the diaphragm due to the mode shape, which has a single peak. Higher modes tend to be less effective as their mode shapes consist of multiple peaks, where a positive peak is offset by a negative one resulting in zero or negligible volume change. This is, however, only true in the ideal case, where in reality this offset may not result in zero volume displacement but instead a small detectable output velocity. Such a velocity peak can be found in Figure 5.5a-c for actuation frequencies of ~ 1200 Hz. It seems varying levels of coupling between the mechanical and acoustic resonances are able to reveal such peaks. As the acoustic resonance decreases further with increasing cavity height (Figure 5.5d-f) the peak at 1200 Hz disappears. This does not however mean that the mechanical resonance is suppressed but rather that, as mentioned before, the resulting volume change for the higher resonance modes is so small that with the mechanical resonance alone at this point no significant output can be achieved.

This is depicted in Figure 5.6, where the different diaphragm mode shapes are shown. There is good agreement in resonance frequencies of up to 99.5% ($f_a = 1218$ Hz) between the numerical and empirical results and discrepancies of up to 9.3 % ($f_a = 1563$ Hz). The blank space on the bottom right of the experimental images is caused by conductive tape used to supply electrical power to the diaphragm. Mode shapes, on the other hand, vary in some instances, which could have been caused by the addition of said tape and the influence of coupling between the mechanical and acoustic resonance. Such discrepancies are also to be expected if the DIC measurement was not conducted

at the exact resonance frequency. It is reminded that the frequency sweeps for the velocity response were conducted at 25 Hz increments, within which the mode shape may vary slightly. Furthermore, as mentioned in Chapter 4, the accuracy of the DIC measurements deteriorates with increasing oscillating frequency. Based on the simulation, the first resonance mode has a single peak that results in the largest volume swept out of all the other resonance modes. At higher modes it can be seen that for a positive deflection there is an opposite deflection of similar size that reduces the overall volume swept by the diaphragm.

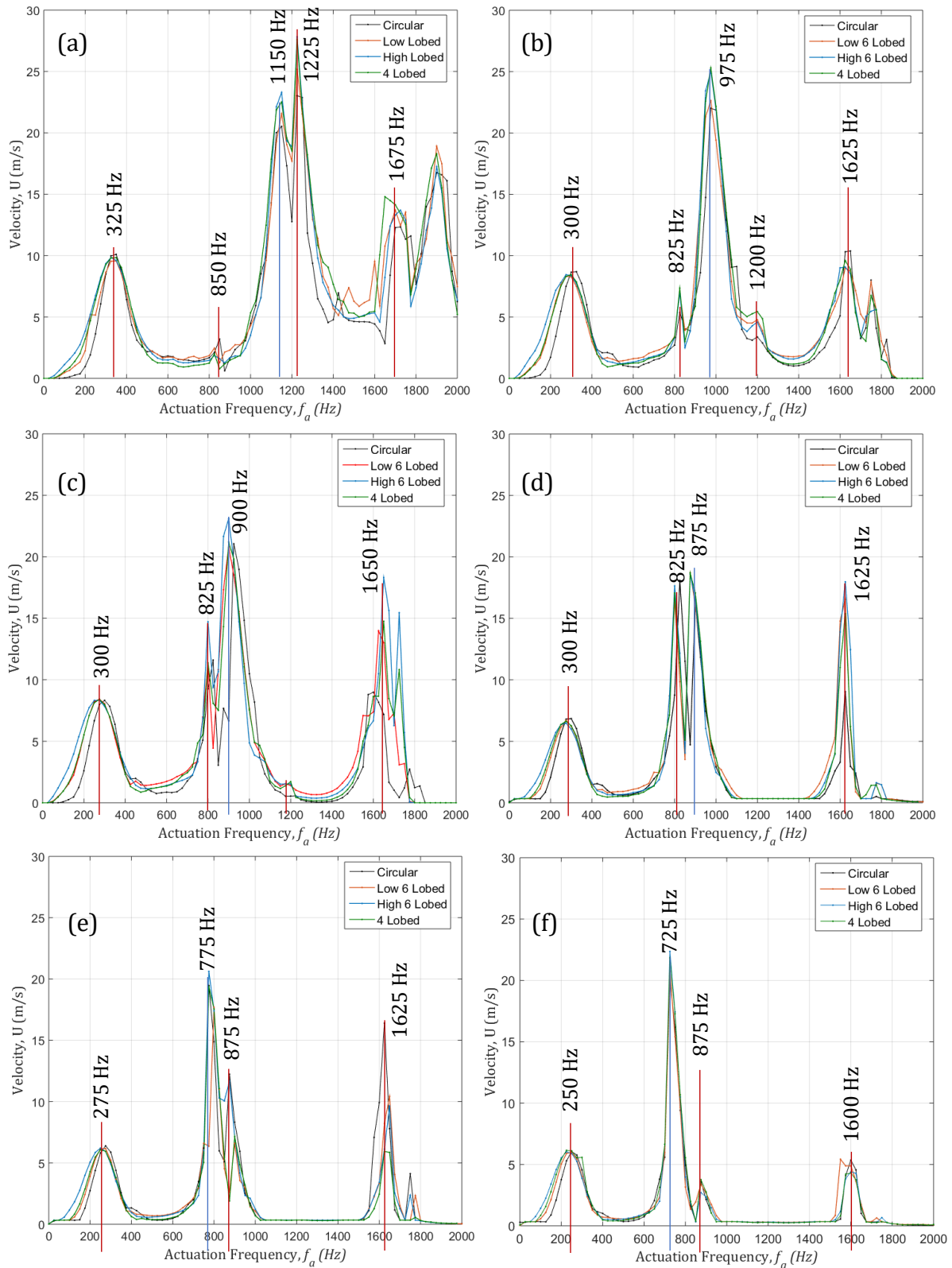


Figure 5.5. Frequency response of SJA as a function of orifice shape (a) $H = 1.2$ mm, (b) $H = 3$ mm, (c) $H = 4$ mm, (d) $H = 5$ mm, (e) $H = 6$ mm, (f) $H = 8$ mm, where the red lines mark the constant resonant frequencies in the response and blue lines mark the changing resonant frequency

The highest jet velocity attained is 27.6 m/s when using a cavity height of 1.2 mm with the 4-lobed orifice at $f_a = 1225$ Hz, which is almost 20% higher than what is achieved using the circular orifice at the same actuation frequency. In fact, for all cases the highest velocity is achieved using a lobed orifice.

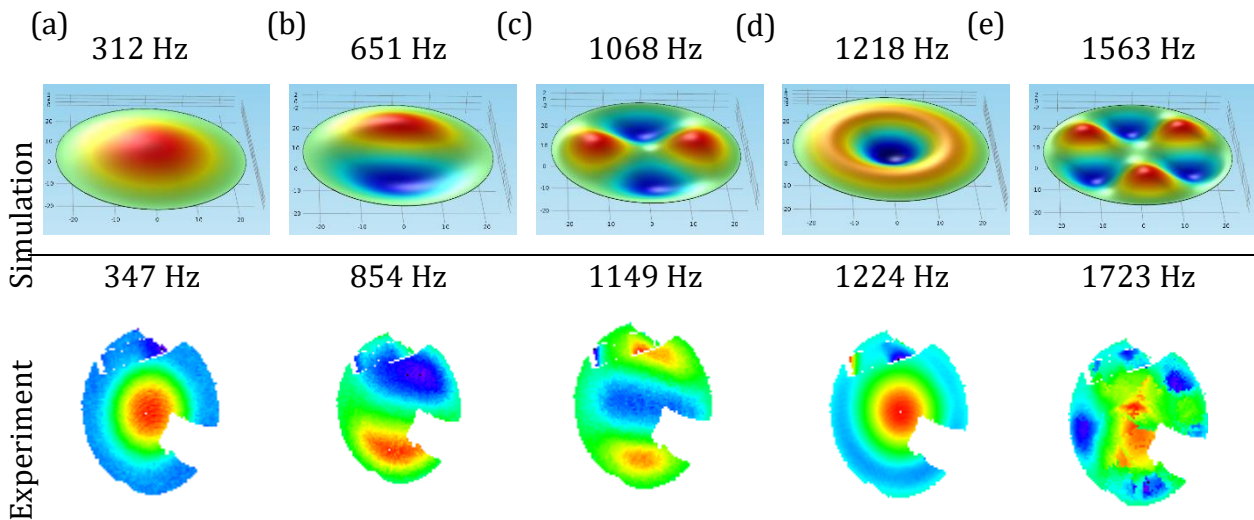


Figure 5.6. Diaphragm resonance frequencies and mode shapes from simulation (COMSOL; top) and experiment (DIC; bottom)

5.1.2.2 Velocity profiles

With varying orifice shape, the SJA flow characteristics and jet development are expected to change. As shown in Chapter 2, for both continuous and periodic jets, an increase in momentum and mass transfer was noticed when using asymmetric orifice shapes instead of conventional circular ones.

Velocity profiles across the major axis for the different orifice shapes for the SJA for $H = 1.2$ mm are investigated. Figure 5.7 shows the velocity profiles at $f_a = 1150$ Hz, across half the orifice span, where one of the resonance peaks occurs. The difference in exit velocity at this actuation frequency relative to the peak velocity at this frequency is smaller than higher resonance frequencies. It should be noted that for the results presented in this section, a new diaphragm was used hence the slight variation in resonance frequencies and velocity amplitudes. At $f_a = 1150$ Hz the exit velocities vary slightly from each other for the different orifice shapes, however, an even bigger change in exit velocity in this frequency sweep can be seen at $f_a = 1225$ Hz, where the velocity difference between the circular and 4-lobed orifice is nearly 20%.

Just a quick glance at the results reveals that the circular jet velocity (Figure 5.7a) dissipates the least with increasing distance from the orifice exit. With increasing lobe count and penetration, the jet velocity decay is accelerated. The circular jet exit velocity profile indicates it is not fully developed at the point of ejection until it reaches a downstream distance of $0.5d$ from the first measurement point. At a downstream distance of $6d$, due to the much lower mixing, the peak velocity of the circular jet only fell by 19%. The effect of lobe penetration against lobe count is demonstrated when comparing Figure 5.7b-c. Although both the low and high-amplitude 6-lobed orifice have the same lobe count their velocity profiles and dissipation are very different. The low amplitude 6-lobed orifice (Figure 6b) has a similar exit profile as the circular jet, where the highest velocity occurs near the lobe walls. There is also a slight increase in velocity towards the centre, where the minor and major axis come together. At a downstream distance of $6d$ from the exit the initial centreline velocity has reduced to 67% of its original value. The high amplitude 6-lobed orifice (Figure 5.7c) on the other hand produces two distinct peaks with the highest velocity towards the centre ($x/d = 0.5$) where the centre velocity, like in the circular and low-amplitude 6-lobed jet, is slightly lower. The velocity profile for the high amplitude 6-lobed jet becomes more uniform by $y = 2d$ and the jet velocity dissipates at a much faster rate than the previous two cases (circular and low amplitude 6-lobed jet), only reaching 45% of the initial peak centreline velocity by $6d$. Finally, Figure 5.7d shows the 4-lobed jet profiles, which similar to the high amplitude 6-lobed orifice has 2 distinct peaks that are, however, almost identical in magnitude. The spanwise velocity decreases the most for this jet with increasing distance from the orifice exit with a final centreline velocity at $y = 6d$ reduced to only 36% of its original velocity.

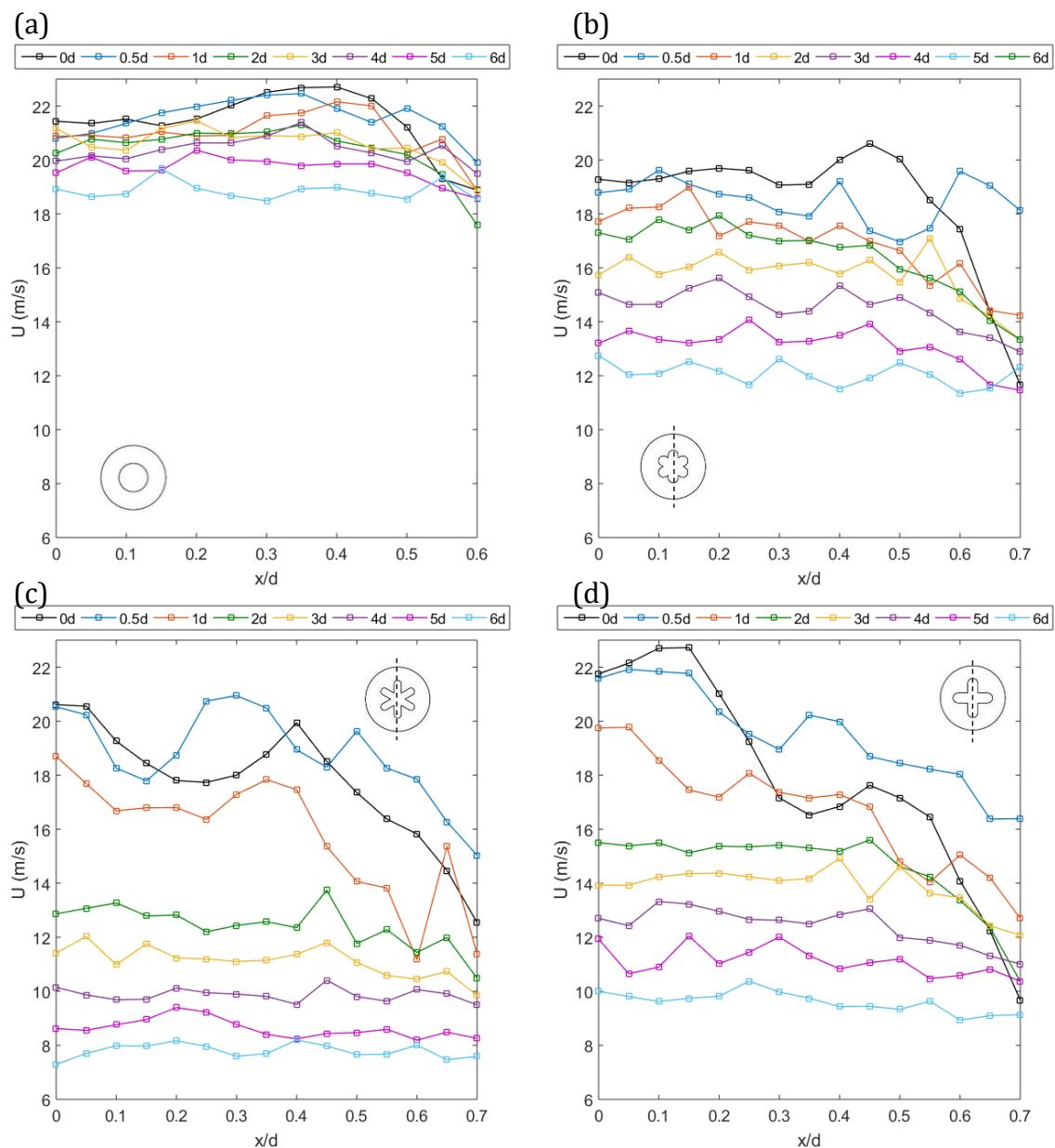


Figure 5.7. Velocity profiles with $H = 1.2$ mm, $S = 43$ & $Re_j = 938$ of (a) circular, (b) low amplitude 6-lobed, (c) high amplitude 6-lobed and (d) 4-lobed orifices measured along the major axis, where $x/d = 0$ represents the centre of the orifice.

The velocity profiles for $f_a = 325$ Hz (Figure 5.8) are quite different to that for $f_a = 1150$ Hz (Figure 5.7). This is due to the different Stokes number, as a consequence of using a lower actuation frequency that determines the shape of the velocity profiles and strength of vortex roll-up. The velocity decay is obvious in the lobed orifice cases again, where the 4-lobed orifice is responsible for the greatest streamwise velocity decay and the low amplitude 6-lobed orifice for the least effect.

The circular jet velocity profile is that of a fully developed jet (Figure 5.8a). As the measurements are taken further downstream a uniform profile is slowly achieved and

the jet velocity decays at a much slower rate compared to the other orifices. At a distance of $7d$ from the orifice, the centerline velocity still amounts to 72% of the exit centerline velocity. The 6-lobed orifices (7b & c) show again that penetration, and not lobe count, has the greater impact on the streamwise jet velocity. Here the decrease in centerline jet velocity at $7d$ compared to the orifice exit for the low amplitude 6-lobed and high amplitude 6-lobed orifices are 39% and 59% respectively. The highest centerline jet velocity reduction is recorded for the 4-lobed orifice (Figure 5.8d) with a reduction of 67%. Comparing these values to the previous cases in Figure 6 shows that the velocity reductions are very similar for the different operating conditions.

A big difference between the circular and lobed orifices is the existence of a second distinct velocity peak originating from the lobes (around $x/d = 0.25$, 4-lobed orifice). These peaks have a lower velocity, but this is caused by the lobed curvature and different shear layer thicknesses in the lobe peaks and troughs. Due to the varying velocity across the span of the lobed orifice the large vortex structures formed at the exit are inherently unstable as the vortex ring stretches before breaking up. The boundary layer around the lobed orifices is not uniform due to boundary layer stretching (Alkislar et al. 2007), which is one of the causes for the formation of streamwise vortex pairs that enhance mixing and breakup of large scale coherent structures as described in Chapter 2.

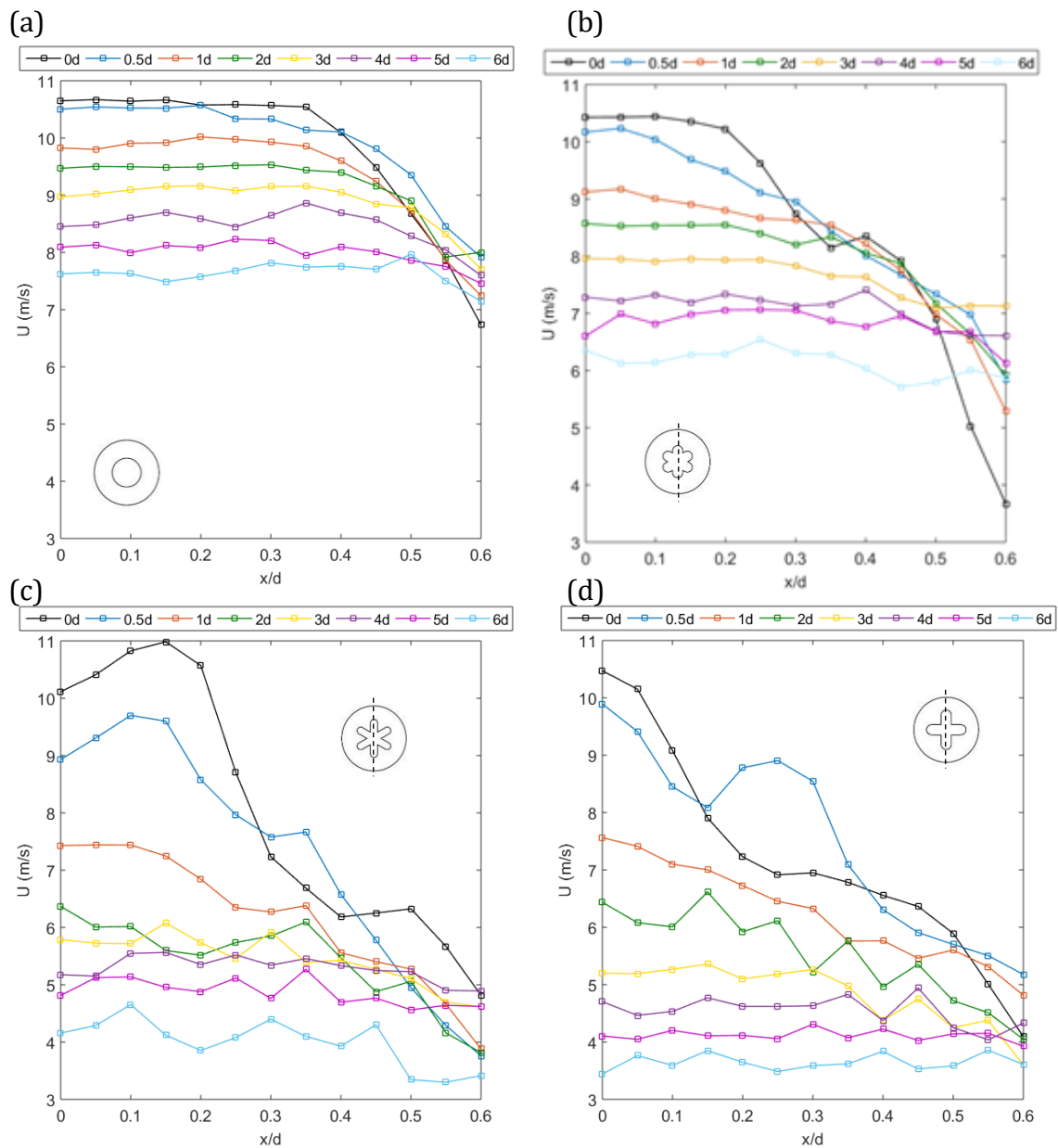


Figure 5.8. Velocity profiles with $H = 1.2$ mm, $S = 23$ & $Re_j = 449$ of (a) circular, (b) low amplitude 6-lobed, (c) high amplitude 6-lobed and (d) 4-lobed orifices measured along the major axis

5.1.2.3 Streamwise development

In Chapter 2 the complex three-dimensional mechanics behind the modified flow structures from lobed orifices along with the benefits they have on mass and momentum transport. However, a drawback is the rapid diffusion and loss of velocity with increasing downstream distance from the orifice. In this section the development of lobed jets is investigated in more detail. For this all results, as before, are based on the same SJA configuration with $H = 1.2$ mm and $f_a = 325$ Hz.

Figure 5.9 shows the reduction of centreline velocity as a function of orifice shape. As expected, the jet velocity rapidly decreases for lobed orifices. This is due to the higher entrainment of ambient fluid and mixing with the jet core, resulting in increased jet spreading and reduction in velocity. As already seen in the velocity profiles in Figure 5.7 & 7 the circular jet is not fully developed at the exit, which is again seen from the axial centreline velocity profile in Figure 5.9. The potential core in all cases does not last any further than $y/d = 2$, with the high amplitude 6-lobed and 4-lobed jet dissipating slightly faster. It is also after $y/d = 2$ that there is a sudden decrease in centreline velocity. The high amplitude 6-lobed and 4-lobed orifice centreline velocities decay the fastest with the highest dissipation taking place in the 4-lobed jet.

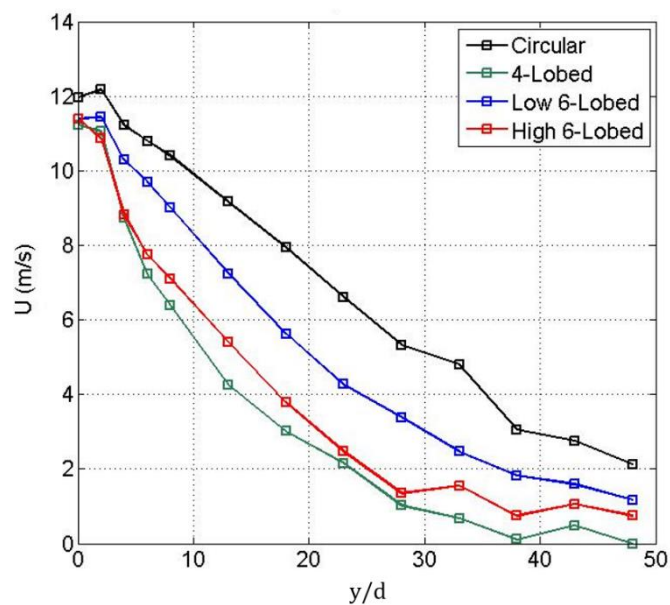


Figure 5.9. Reduction of jet centreline velocity with streamwise distance from the orifice

From the exit profiles (Figure 5.7 & Figure 5.8) a better understanding of the different velocity distributions due to the non-uniform shear layer within the lobed orifices is established. For instance, the high amplitude 6-lobed orifice has three peaks across the major axis (at $x/d = 0.05$ and 0.35 , Figure 5.7c), which, due to the differences in shear layers formed at the lobe peaks and troughs, contribute to different strengths of vortex rollup. This non-uniform development of asymmetric jets across two different axis causes flow structures formed at the exit to deform and mix more rapidly with the

surrounding making the jet inherently unstable. This will be further investigated and explained in more detail later with the aid of qualitative (flow visualisation) results.

The lobed orifices used have different geometric characteristics, with the lobe count and lobe penetration being the most important in jet decay. It can be seen from the low amplitude 6-lobed and high amplitude 6-lobed orifice (Figure 5.9) that the lobe penetration plays a more important role in the velocity decay than the lobe count. In this case both have the same number of lobes, however the jet dissipation occurs at a faster rate for the high amplitude 6-lobed orifice. An appropriate non-dimensional parameter to compare the effect of lobe penetration is the penetration ratio, P , shown in Table 7. It is the ration between the length of the minor and major axes, where a value of 1 represents a circular orifice. The lower P is, the higher the lobe penetration will be for the orifice. Comparing these values for P to Figure 5.9 a clear relationship can be observed between lobe penetration and velocity decay. The lower P is the higher the axial velocity decay will be. Also, the small difference in the centreline velocities for the high amplitude 6-lobed and 4-lobed orifice is represented in the value of the penetration ratios where the difference between the two is just 0.02.

Table 7. Value of lobe penetration, P , for the different orifice shapes

Orifice shape	P
Circular	1
Low amplitude 6-lobed	0.62
High amplitude 6-lobed	0.38
4-lobed	0.36

5.1.2.4 Jet spreading

In this section the spanwise effect of lobed orifices will be investigated. A key characteristic of periodically excited and asymmetric jets, including lobed orifices, is the increased jet spreading, which is caused by enhanced ambient fluid entrainment and premature breakup of large coherent structures. In the previous section the velocity decay in the streamwise direction was presented, which was explained to be due to the jet spreading and mixing. Here a closer look at the spanwise development of the jet and

flow structures is presented by comparing Schlieren images and the spanwise velocity Power Spectral Density (PSD) for the different orifice shapes.

In Figure 5.10 Schlieren images are presented showing the jet emanating from the major axis, where $S = 23$ and $Re_j = 449$. It can be seen that the laminar jet, comprised of large-scale coherent structures, breaks up to form a turbulent jet earlier as lobe penetration increases. For the circular orifice under these operating parameters the vortex rollup is slightly delayed, but once established forms a tall column of periodic vortex rings (Figure 5.10a). These large-scale structures persist until $y = 12d$, whereas for the 4-lobed orifice (Figure 5.10d), they only persist until $y = 6d$, after which they break up. According to Hu et al. (2001) the large coherent structures break up into smaller, but not weaker structures, which means that due to the much earlier breakup of the large-scale structures turbulent mixing is greater in this region when using lobed orifices. As the 4-lobed jet breaks up small-scale structures are visible that facilitate the rapid spreading in the spanwise direction. Also, in both high amplitude 6-lobed and 4-lobed orifices (Figure 5.10c & d) smaller scale structures are visible for longer. This is because as mentioned earlier, the large-scale structures break up into smaller scale structures with the same strength, which creates a region of increased turbulent mixing that leads to the faster dissipation of the jet. As seen earlier the velocity profiles for the circular and low amplitude 6-lobed orifice were similar, although with higher velocity decay than in a circular jet. However, here the vortex rings produced at the exit are much narrower forming a train of vortex rings before breaking up at around $y = 9d$ (Figure 5.10b).

Power Spectral Density (PSD), derived from the hot wire data can reveal valuable details regarding the flow and flow structures involved. One can identify frequencies present in a function f and determine dominant frequencies in the flow by examining the Fourier transform of this function. This means for the mentioned function $f(t)$ the Fourier transform can be written as Eq. (27):

$$g(\omega) = FT[f(t)] = \frac{1}{2\pi} \int f(t) e^{-i\omega t} dt \quad (27)$$

In Figure 5.11 the PSD from the hotwire data, across six spanwise locations, is shown for the downstream locations marked on Figure 5.10. At the exit, the actuation frequency and its higher harmonics dominate the spectrum in all four orifice cases (Figure 5.11a). With increasing downstream distance, however, there is an increase in the PSD first around the actuation frequency and then also in the lower frequency band, while there is a decrease in the higher frequency range. This, according to Tesar and Kordík (2011), is indicative of the decay of the large-scale structures formed at the orifice and the gradual development of the turbulent jet. The attenuation of the actuation frequency peak with its harmonics and the formation of a continuous spectrum is due to energy transfer from large scale down to smaller scale structures, which leads to the formation of the characteristic continuous spectrum of turbulent jets. A continuous spectrum is achieved much sooner with higher lobe penetration due to increased mixing and breakup of large scale structures. This is evidenced by looking, for example, at Figure 5.11b.

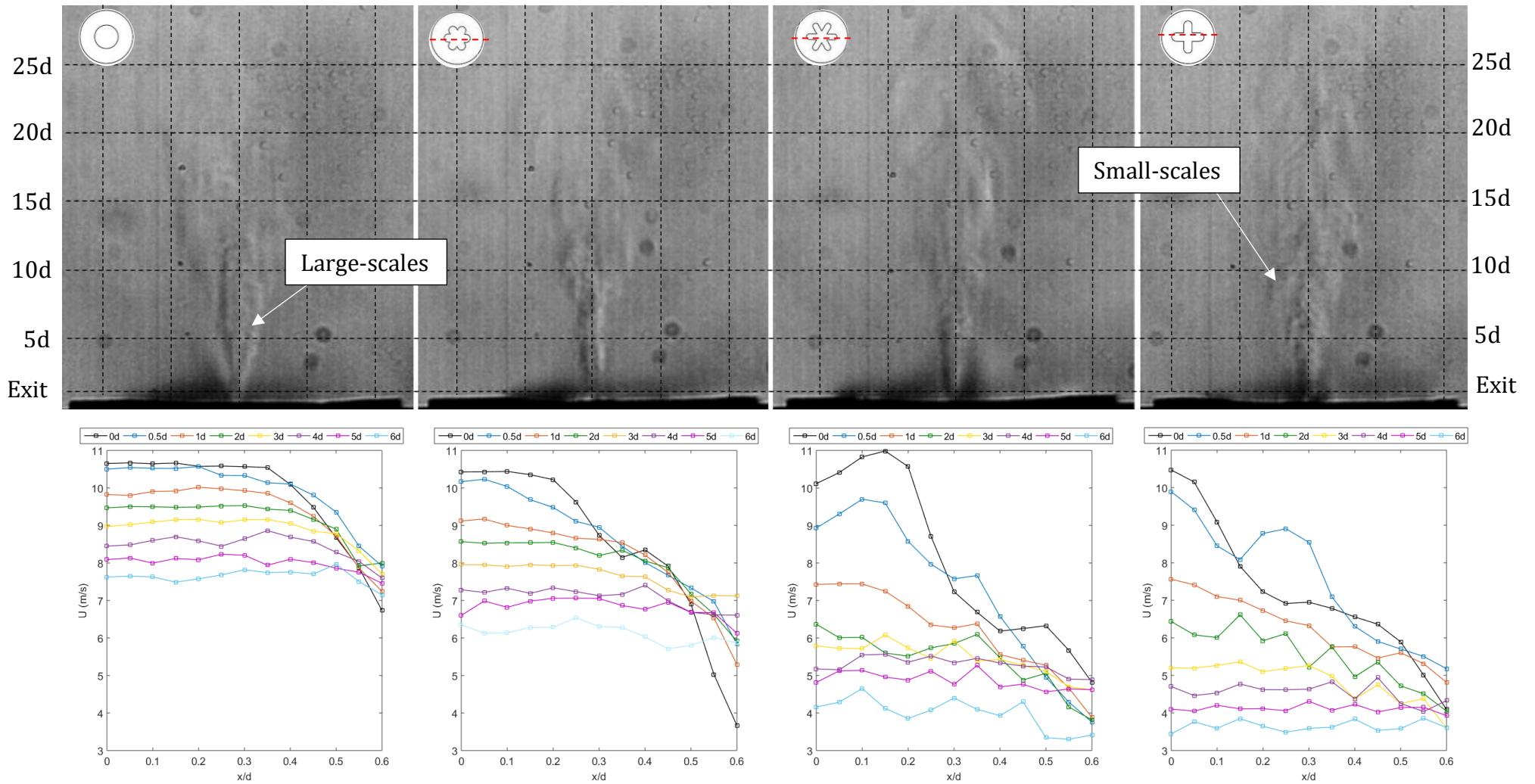


Figure 5.10. Schlieren visualisation of the mean flow with corresponding velocity profiles, $S = 23$ & $Re_j = 449$, for (a) circular, (b) low amplitude 6-lobed, (c) high amplitude 6-lobed and (d) 4-lobed orifices, taken along the major axis (red dash lines)

Spanwise PSD measurements indicate increased rate of jet spreading and mixing using lobed orifices, best seen in the high amplitude 6-lobed and 4-lobed orifices. At $y/d = 5$ for the 4-lobed orifice (Figure 5.11(iv)) there is an increase in PSD at all spanwise locations and the spectrum is almost fully continuous, which indicates transition to the turbulent jet and spreading due to increased turbulent mixing. At $y/d = 5$ and $x/d = 1$ for the 4-lobed orifice, the spectrum indicates a highly turbulent jet where the energy is higher than for the other jets at the same location. When compared to the Schlieren images it can be seen that this location roughly corresponds to a region where large-scale structures have broken up to form high turbulent mixing. Similarly, the same effects can be seen for the high amplitude 6-lobed orifice at $y/d = 10$ (Figure 5.11c (iii)), especially at $x/d = 2$. The PSD results are in agreement with the Schlieren images presented in Figure 5.10. It shows that although the large-scale structures diminish there is a broadband energy increase in eddies of various sizes, which enhances mixing in these regions, potentially making them useful in flow control applications. Although the breakup of large-scale structures can lead to the attenuation of low frequency noise, the small-scale structures are not weaker and may cause an increase in high frequency noise.

It is apparent that the 4-lobed orifice causes the jet to spread and dissipate in the spanwise direction the fastest as seen at $y/d = 15$. This is evident from the spectra at the different spanwise measurement locations, which are closer together indicating a nearly uniform distribution of flow structures of similar scale.

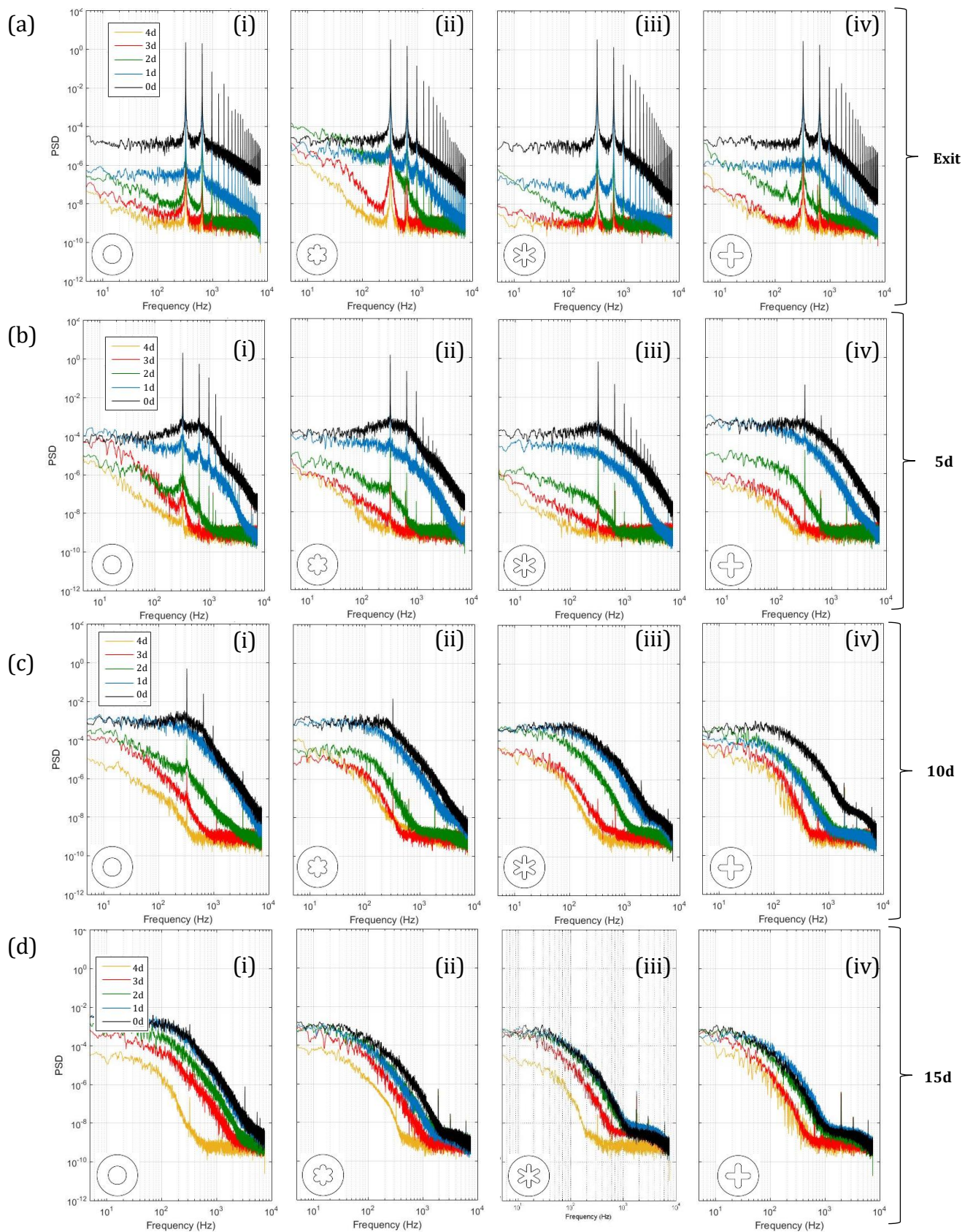


Figure 5.11. Power Spectral Density (PSD) as a function of spanwise location across the orifice at $f_a = 325$ Hz for (a) exit, (b) $y=5d$, (c) $y=10d$ and (d) $y=15d$ streamwise locations

5.2 Acoustic Characteristics

5.2.1 SJA noise reduction using double chamber antiphase operation

The double chamber SJA was designed with increased efficiency and noise reduction in mind. Efficiency was shown to increase significantly in other work when using this configuration (Kykkotis & Jabbal, 2014), due to the use of a single diaphragm for driving two cavities simultaneously. An additional benefit of such an actuator is that the diaphragm is fully enclosed by the actuator housing, which helps attenuate some of the mechanical noise from the diaphragm. However, the main purpose of using this configuration in this study is to investigate the far field noise characteristics of the double chamber SJA, where two jets are generated out of phase. Figure 5.12a shows the velocity response for both orifices and Figure 5.12b shows a directivity plot of the actuator noise measurements with the SJA in the middle. The actuation frequency for this test is $f_a = 925$ Hz, which is where the peak jet velocity is reached, and as intended there is a clear noise attenuation observable, with noise minima between the two orifices. This is possible because the orifices can be treated as a dipole source consisting of two coherent point sources operated out of phase with each generating a sound field. The radiated sound waves from the orifices interfere with each other destructively along a line between the orifices on the y-z plane to achieve a maximum noise reduction of 14 dB.

However, the noise map is not completely symmetrical as it appears that the noise generated on one side of the actuator (Figure 5.12b, Orifice 2) is louder than the other. This could be explained by the inherent asymmetry of the actuator design. In the tests conducted long bolts extend from one side of the actuator as they are used to secure a diaphragm and cavity wall to the actuator. During the operation of the SJA at high actuation frequencies (resonance modes) the vibrations are transmitted via these extended screws to the surroundings as surface borne noise. Another surface borne noise source are the cavity walls themselves, which due to the modular design of the actuator are also not equal in thickness causing differences in structural and therefore acoustic properties.

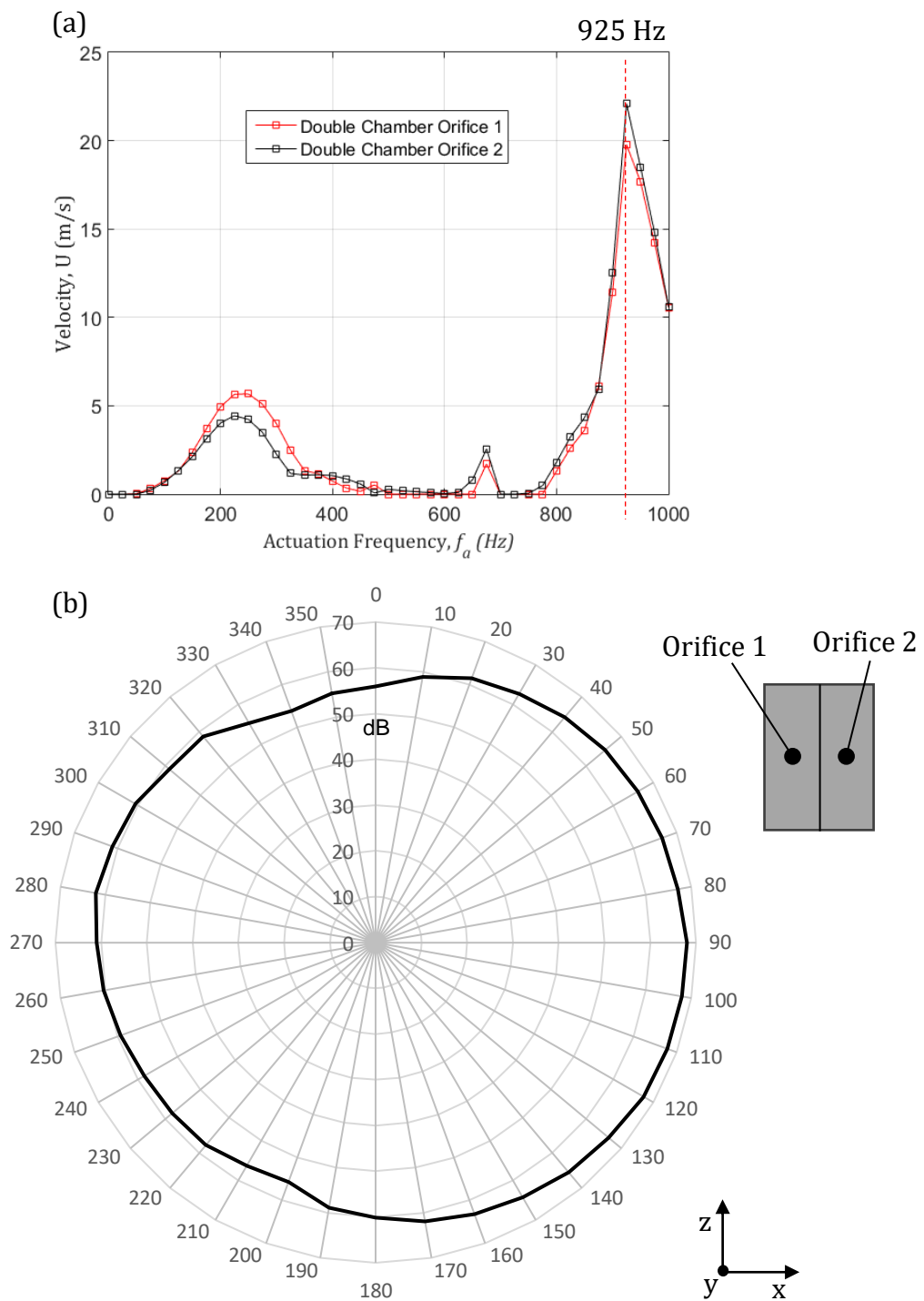


Figure 5.12. (a) Double chamber SJA velocity response, (b) directive noise plot of far field noise measurements for $f_a = 925$ Hz

Although the noise map shows a reduction of actuator self-noise when operating two orifices out of phase within close proximity, there are several noise sources in a SJA contributing to the overall sound pressure level. Figure 5.13 shows the acoustic spectra at three different directive positions around the SJA, with a noise output minimum at 0°

and maximum at 90°. From these spectra it can be observed that the noise reduction occurs at and below the actuation frequency, $f_a = 925$ Hz, while from the first harmonic (1850 Hz) onwards the noise remains the same. This suggests that the reduced noise source is related to the diaphragm forcing. As already discussed in Chapter 2, the diaphragm periodically displaces mass in the orifice, which causes acoustic radiation from this point. The results reinforce the assumption of monopole-like behaviour of the orifice, that when coupled with a second source in anti-phase nearby the classic dipole sound field forms. Jet noise, on the other hand, has a broadband noise characteristic, where change on the low frequency end of the spectrum causes a change in the high frequency spectrum. This is the case for high speed jets where chevron nozzles are used to reduce jet noise. Chevrons form streamwise structures and deform large-scale structures (low frequency) in the jet flow, which break up into high energy smaller scale structures (high frequency) earlier compared to round jets. Since the small-scale structures have higher energy, the resulting turbulent mixing causes a slight noise increase in the high frequency end of the spectrum. There is, however, no such broadband change in the spectrum and therefore the noise reduction is not jet related. More on this will be discussed in the next chapter.

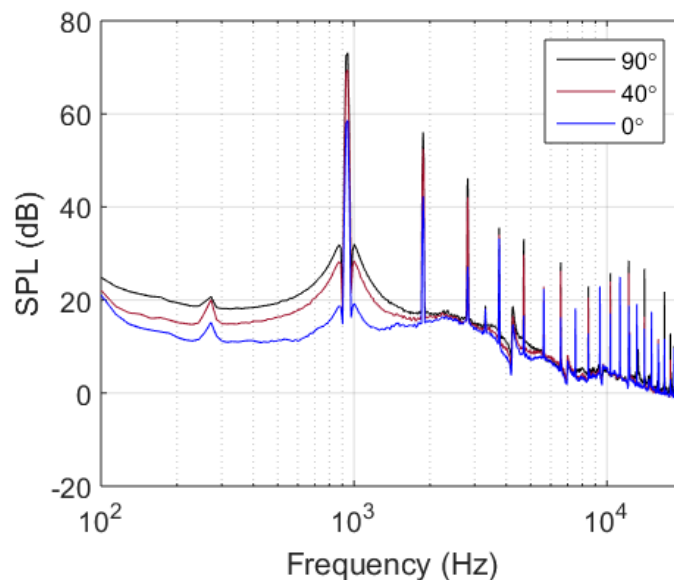


Figure 5.13. Acoustic spectra at different directive positions around the actuator

5.2.2 SJA noise reduction using lobed orifices

For a piezoelectrical-driven SJA there are two main noise contributors, which are jet and diaphragm related. The dominant noise source is the piezoelectric diaphragm, especially when operated at resonant modes. Figure 5.14 shows the typical acoustic response of the PZT diaphragm used in these experiments at the first actuator resonance frequency, $f_a = 325$ Hz, and the resonance frequency at which the highest jet velocity is reached, $f_a = 1225$ Hz. To obtain these results the diaphragm was fully clamped inside the single chamber SJA housing without an orifice plate attached, preventing any damping or jet related effects influencing the results. The acoustic spectrum consists of several distinct peaks, with maxima reaching up to 81 dB. In both cases shown, higher levels of noise output are recorded at the actuation frequencies and its harmonics or subharmonics.

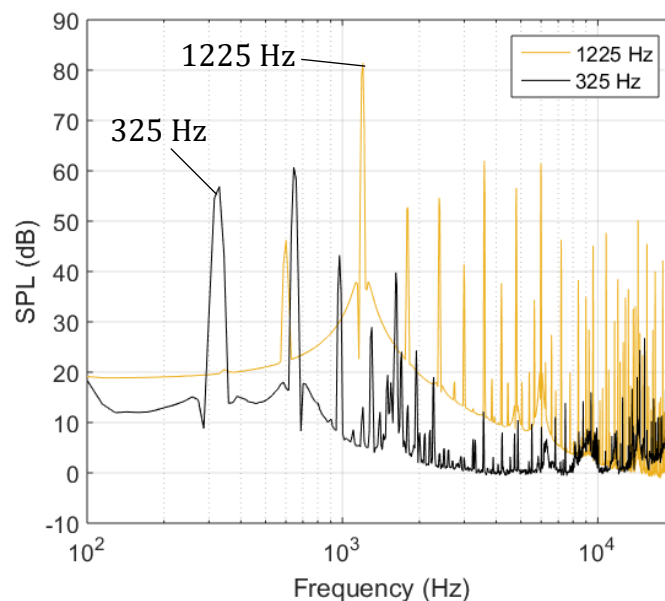


Figure 5.14. Acoustic response of the PZT diaphragm at the two system resonant frequencies

SJAs, when driven piezoelectrically, generate audible noise over a very large range of actuation frequencies regardless if a jet is generated or not. The noise generated typically increases with increasing input voltage and when operating at resonance modes of the SJA system. Based on these results lobed orifices are used here to study the effect on SJA self-noise reduction.

Similar to the results shown in Figure 5.14, the results shown in Figure 5.15 correspond with measurements taken at the first resonance mode ($f_a = 325$ Hz) and the fourth

resonance mode with the highest exit velocity ($f_a = 1225$ Hz). The acoustic spectra for all orifice shapes at these actuation frequencies are presented in Figure 13. It is evident that excessive noise is present in the data. However, with careful inspection changes in the spectra are noticeable with a clear noise reduction benefit using the high amplitude 6-lobed and 4-lobed orifice between $1 \text{ kHz} < f < 4 \text{ kHz}$ at $f_a = 325$ Hz. For $f_a = 1225$ Hz, changes in the spectra are visible, but the diaphragm noise is too significant to identify any clear changes.

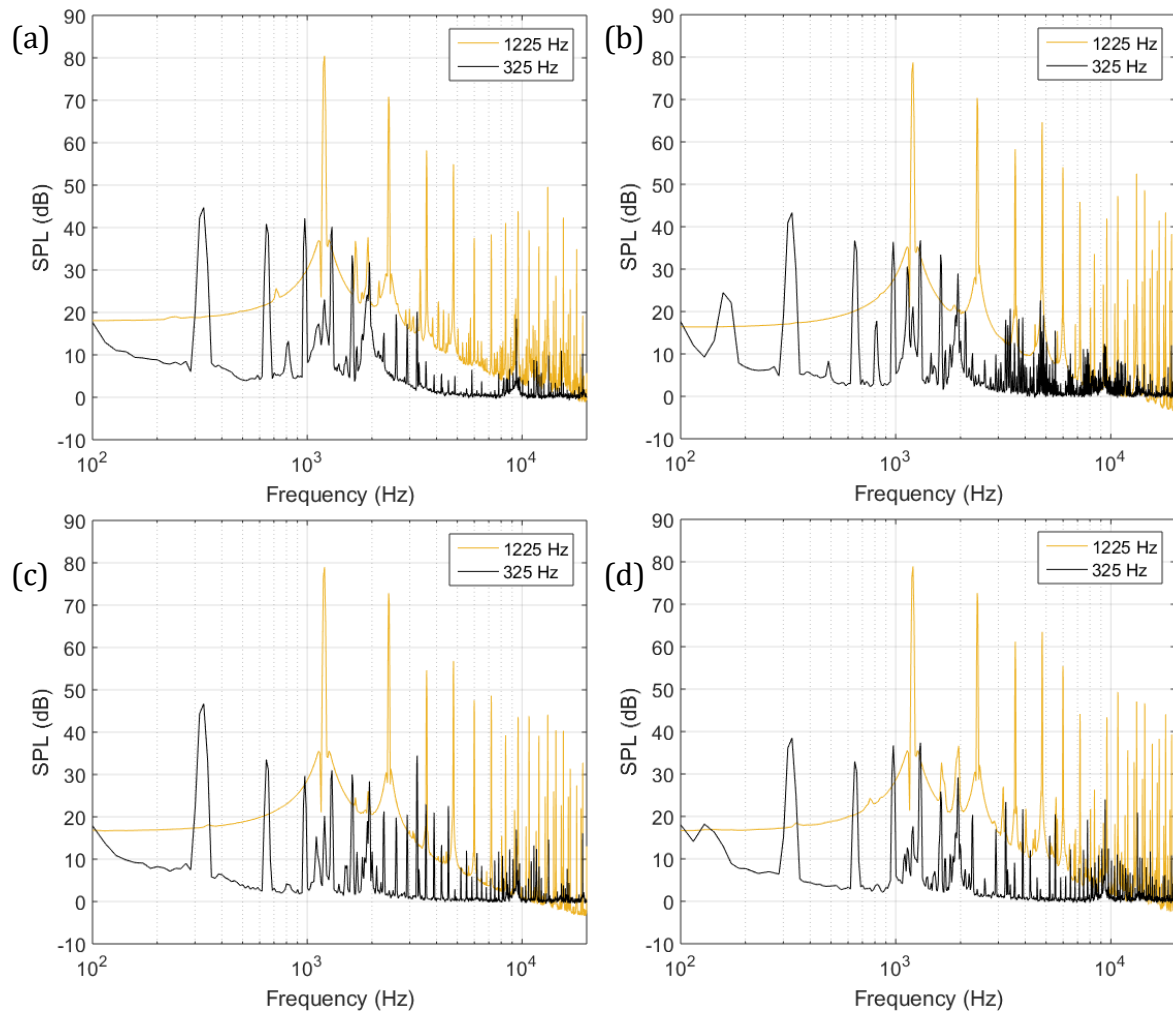


Figure 5.15. Single Chamber SJA acoustic spectra at $f_a = 325$ Hz and $f_a = 1225$ Hz as a function of orifice shape: (a) circular, (b) low amplitude 6-lobed, (c) high amplitude 6-lobed and (d) 4-lobed orifice

To make the level of noise reduction clearer, the change in SPL is shown according to Eq. (28):

$$\Delta\text{SPL (dB)} = \text{SPL}_{\text{circular}} \text{ (dB)} - \text{SPL}_{\text{lobed}} \text{ (dB)} \quad (27)$$

In the ideal case the diaphragm noise could be subtracted from the noise data using various orifice plates to isolate non-mechanical noise sources from the spectra. However, the PZT diaphragm performance and resonance frequencies can change considerably when enclosed inside a cavity, even if the clamping conditions are kept constant, leading to an inaccurate comparison.

The results shown in Figure 5.16 make it easier to appreciate the change in noise generation by the actuator using various orifice shapes. At the first resonance mode, $f_a = 325$ Hz and $U_{\text{peak}} = 12$ m/s, there is initially some noise reduction noticeable at the $\frac{1}{2}$ harmonic of the actuation frequency for the low amplitude 6-lobed (Figure 5.16a & c-check) and 4-lobed orifices. Most of the noise reduction is seen between $325 \text{ Hz} < f_a < 4000$ Hz, with the highest reduction seen using both high penetration lobed orifices (Figure 5.16b & c-check) and a peak reduction of 12 dB using the high amplitude 6-lobed orifice.

On the other hand, at the higher actuation frequency, $f_a = 1225$ Hz, the sound pressure level data recorded is much noisier. Changes in the spectra can only be noticed after 1650 Hz continuing into the higher frequency band of the spectrum. Unlike in the previous case, at lower actuation frequency there is no noise reduction at the actuation frequency or its higher harmonics. The small changes that occur in other places are likely related to the actuator geometry, i.e. cavity and orifice.

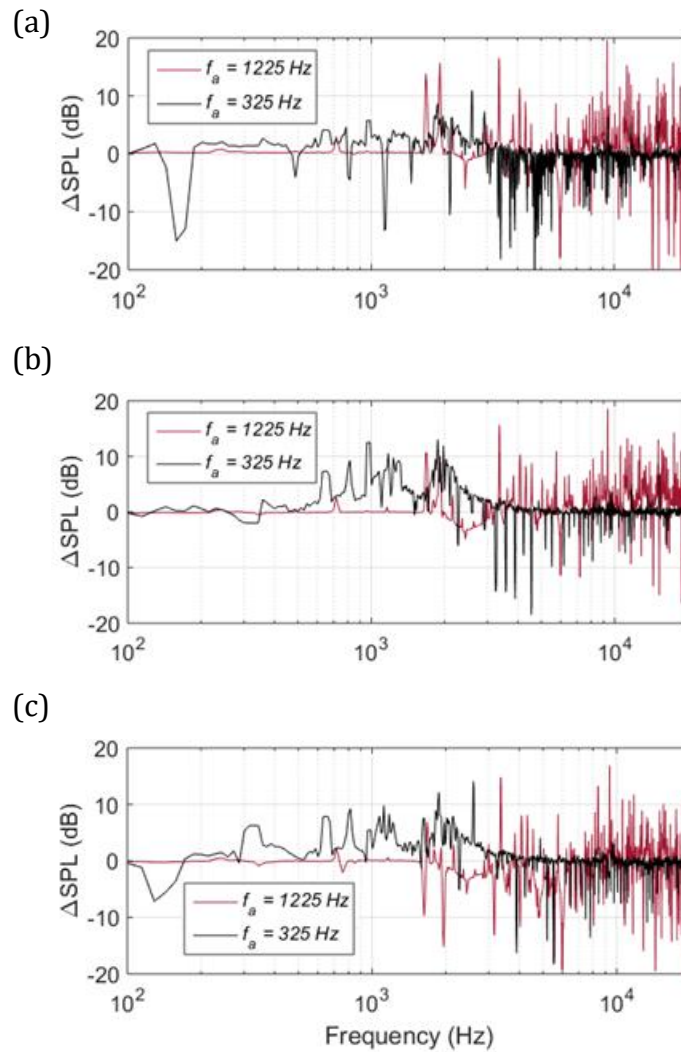


Figure 5.16. Acoustic spectra of Δ SPL as a function of frequency (a) C-L6, (b) C-H6 and (c) C-4L

These measurements show once again that noise reduction can be achieved using different shaped orifices, in particular lobed orifices. There is strong correlation between lobe geometry and noise reduction as evidenced from the results for $f_a = 325$ Hz, where the high amplitude 6-lobed orifice is able to reduce noise over a broader band of frequencies with a maximum reduction of 12 dB. However, measurements taken at higher resonance modes of the diaphragm make it increasingly difficult to identify patterns and noise sources. A different approach to overcome this issue is presented in Chapter 6.

5.3 Jet Flow Visualisation

5.3.1 Test conditions

It was shown in the previous section that using lobed orifices on a SJA instead of a more traditional circular orifice leads to actuator self-noise reduction and reduced jet velocity further downstream from the orifice. This effect is further enhanced with increasing lobe penetration into the jet. To better understand the fluid mechanics behind the rapid velocity dissipation, dye flow visualisation in water is used.

A challenge here is to match the two key, non-dimensional, jet flow parameters of SJAs operating in quiescent conditions: the non-dimensional stroke length, L , and jet Reynolds number, Re_j , both of which according to Glezer (1988) characterise the jet flow of a SJA. In this chapter all test conditions are based on Figure 5.5f ($H = 8$ mm) because of the similarity of the velocity response and the peak jet velocities of all orifice shapes for this case. The peak velocity was measured at $f_a = 725$ Hz, where $L = 5$ and $Re_j = 918$. However, to match both L and Re_j is unrealistic since a low actuation frequency is desired for visualisation of the jet formation, whereas matching L and Re_j at the same time will result in higher actuation frequencies. For this reason, two different cases were considered: matching L and Re_j separately. The corresponding operating parameters are summarised below in Table 8.

Table 8. SJA operating and jet flow parameters

Δ_{p-p} (mm)							
0.13 (matched L case)				0.5 (matched Re_j case)			
f (Hz)	U (m/s)	Re_j	L	f (Hz)	U (m/s)	Re_j	L
1	0.078	125	5	2	0.6	960	19

5.3.2 Flow structure streamwise propagation

Four different orifice shapes were investigated, where all have the same equivalent diameter, $d_e = 5$ mm, which ensures that all orifices have the same cross-sectional area.

Figure 5.17 shows the side view of the jet formation for the matched L case. The faster break-up and reduced jet velocity are obvious from the images, where the 4-lobed orifice shows the most aggressive break-up. All orifices show clear vortex roll up at the

orifice exit and in the case of the circular jet secondary vortex shedding is evident. It was previously shown that for $L > 4$ the total circulation of the primary vortex ring from a circular synthetic jet is saturated and results in secondary vortex shedding (Jabbal et al., 2006), as seen in the results presented here. Since this phenomenon is not observed for the lobed orifices under these operating conditions, it seems that there are different conditions for lobed jet secondary vortex shedding. While a single dye trail is visible behind the circular and 6-lobed jets, four trails are visible behind the 4-lobed jet emanating from each lobe. These are due to the larger lobe peak-to-peak distance and lobe width compared to the 6-lobed orifice making it more difficult to mix with the jet core and surroundings to form a single trail.

The slowing jet core velocity was shown in hotwire measurements and its extent was found to be determined by the jet penetration of the lobes. Here this slowing down is visualised again, giving more insight into the fluid mechanics behind this effect from the side view. The distance between each vortex ring from formation at the exit to the next two rings downstream have been compared. This comparison shows that the 4-lobed orifice (Figure 5.17d) has the largest impact on jet downstream rate of propagation and the circular orifice the least. These results are in agreement with the hotwire measurements presented in the previous section. On the other hand, the low amplitude 6-lobed orifice (Figure 5.17b) shows little difference from the circular orifice on the jet development. As mentioned earlier there is the absence of secondary vortex shedding here, which may have a positive impact on overall SPL as these vortices could be a source for additional noise.

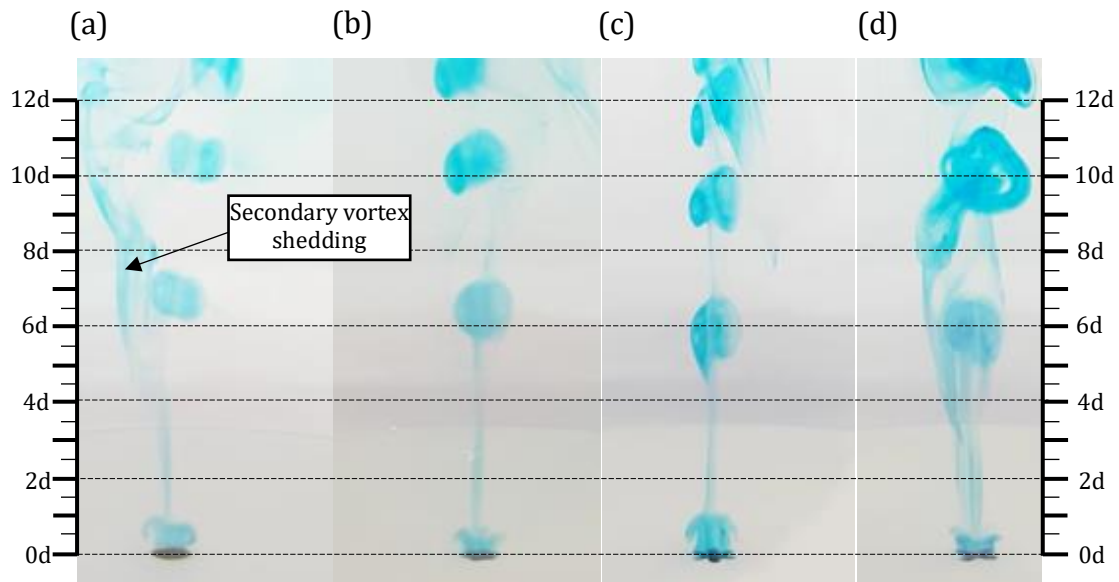


Figure 5.17. Side view of dye flow visualisation for the matched L case ($Re_j = 134$, $L = 5.4$): (a) circular, (b) low amplitude 6-lobed, (c) high amplitude 6-lobed and (d) 4-lobed orifice taken at the same phase in the cycle

In Figure 5.18 the results for the Reynolds number matched case are presented. Secondary vortex shedding is present in all four jets this time. Surprisingly the low amplitude 6-lobed orifice (Figure 5.18b) has almost no effect on jet velocity and the vortex structures remain intact for a much longer time than the other lobed jets. Comparing the circular and high amplitude 6-lobed orifice in Figure 5.18a & 18c, the vortex rings break up at a much earlier stage for the high amplitude 6-lobed jet and creates a region of turbulent mixing where small scale structures dominate. These small-scale structures, given they contain enough energy at high velocities, are a source of high frequency noise. This highly turbulent region also results in a slower jet velocity further downstream compared to a circular jet. For the 4-lobed orifice (Figure 5.18d) it becomes apparent that this would be a poor choice for noise reduction, especially at higher frequencies due to the aggressive breakup of the large-scale structures. Also, the propagation rate of flow structures was the lowest in the presented cases. The low amplitude 6-lobed orifice (Figure 5.18b) on the other hand shows very little change from the baseline circular jet. It can however be seen that the size of the vortex rings is larger in this case.

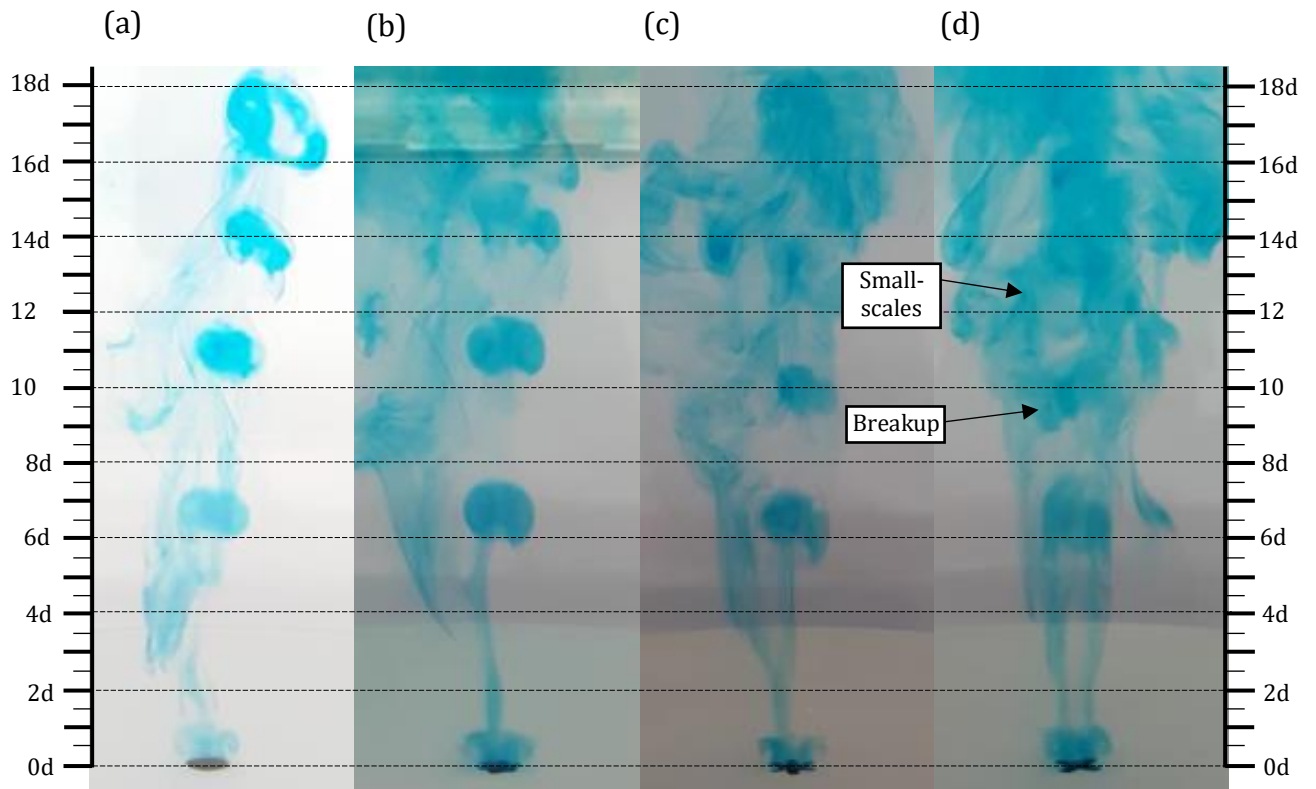


Figure 5.18. Side view of dye flow visualisation for the matched Re_j case ($Re_j = 1152$, $L = 23$): (a) circular, (b) low amplitude 6-lobed, (c) high amplitude 6-lobed and (d) 4-lobed orifice taken at the same phase in the cycle

5.3.3 Jet axis-switching

Figure 5.19a shows the jet formation from the high amplitude 6-lobed orifice in the exit plane view. These image sequences are in good agreement with results from previous studies carried out on continuous jets. According to theory, it is the presence of streamwise vortices that cause enhanced entrainment between the jet core and shear layer. This increased mixing disrupts the growth of large-scale flow structures in the jet flow, which reduces low frequency noise and ultimately causes the jet to breakup earlier.

Nastase and Meslem (2010) investigated the vortex dynamics of straight and inclined 6-lobed nozzles and found that the jet mean streamwise vorticity component, ω_x , from such nozzles was 7-8 times larger than that of a circular jet emanating from a nozzle with the same effective diameter. It was shown that the lobe geometry organizes the vorticity field in six pairs of counter-rotating vortices. Though these vortices are not directly visible in the flow visualisation presented here, their effect on the jet formation is evident in the form of axis switching. The initially 6-lobed jet shows rapid dye entrainment from the jet core in between the lobe troughs (Figure 5.19) and causes the

jet to take on an initial hexagonal shape taking form around $t = 0.20T$. Further downstream, at $t = 0.27T$ the fluid entrainment between the lobe troughs continues and expands further outwards catching up and overtaking the azimuthal vortices' growth. The rapid expansion is a result of the counter-rotating vortex pairs that cause an outflow from the jet core, made visible by the dyed water. This leads to the trough region now expanding further in to a hexagon shape again, however, with new corners giving the perception that the jet has rotated by 90° . This perceived rotation is referred to as axis switching. Finally, at $t = 0.80T$ the jet cross-section displays a very faintly visible axis switch once again towards the left side of the image. This increased fluid entrainment from the core seen here is also the cause for the faster divergence of the jet seen in Figure 5.18b-c.

In the 4-lobed jet case (Figure 5.19b) a similar behaviour can be observed, where dye from the core is entrained and mixes with the surrounding between the lobes. Once again axis switching is the result where the square jet cross sectional shape ($t = 0.14T$) downstream from the orifice exit appears to rotate by 90° ($t = 0.24T$). As in the previous case for the high amplitude 6-lobed orifice the streamwise vortices are the cause for this phenomenon.

The low amplitude 6-lobed orifice (Figure 5.19c), like the large amplitude 6-lobed orifice, displays axis switching, however, it is much weaker in comparison and this is why the adverse impact on the jet velocity is lower in this case.

The noise reduction capabilities of these orifices need to be further analysed, but it is expected that low frequency noise is reduced as seen in the high amplitude 6-lobed orifice due to the disruption of the vortex ring formed at the exit and at the same time the breakup of this ring occurs at a later stage, similar to the circular jet which would result in similar high frequency noise to the circular baseline case.

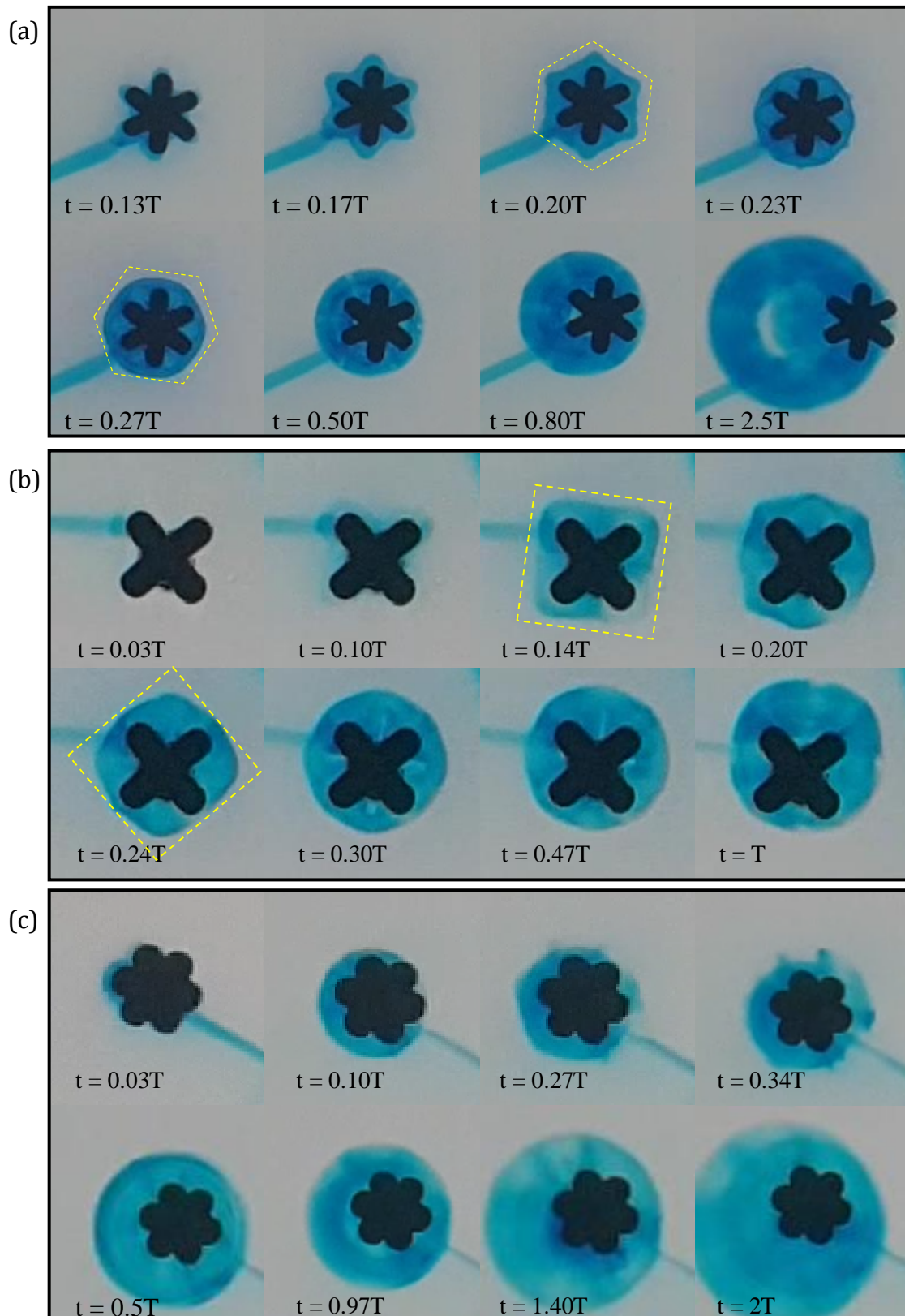


Figure 5.19. Close up view of the orifice exit plane showing jet formation for the (a) high amplitude 6-lobed, (b) 4-lobed and (c) low amplitude 6-lobed orifice. Dash outlines marks axis switching

5.3.4 Lobed vortex ring dynamics

The results presented in Figure 5.17 – 18 show snapshots of synthetic jets at a fixed point in the cycle for different orifice shapes. In Figure 5.19 it was shown how the lobed synthetic jets develop in the orifice exit plane, which shows evidence of increased mixing and entrainment between lobes and significant deformation of the azimuthal vortex ring. This deformation results in axis switching before the vortex structures break up and is most severe in the high amplitude 6-lobed and 4-lobed orifices, where both have similar penetration ratios of 0.38 and 0.36 respectively.

Although both high penetration lobed orifices show great deformation of the large-scale flow structures, the higher lobe count in the high amplitude 6-lobed orifice makes it more difficult to identify details in the flow development. For this reason, the 4-lobed orifice was used for the next analysis. In Figure 5.20 phase locked snapshots of the 4-lobed orifice through an actuation cycle is shown, where $f_a = 2$ Hz resulting in $L = 11.5$, $S = 17.7$ and $Re_j = 576$. As the fluid is ejected from the orifice, vortex roll up can be seen at the lobes ($t = 0.06T - 0.09T$). The jet column formed slowly increases in thickness a small distance away from where the vortex roll up occurs and the vortex ring starts to become elongated axially ($t = 0.14T$). At $t = 0.21T$ secondary flow instabilities (K-H instability) can be seen developing in the jet column, which as they become weaker are shed quickly. As before (Figure 5.20), four distinct dark trails can be seen originating from the lobes. The elongation of the primary vortex ring continuous until around $t = 0.27T$ where the jet core seems to catch up and move ahead. This is a result of the enhanced outer layer of the jet mixing with the surroundings causing to slow down and allowing the jet centre to catch up. Similar results were observed by Amitay & Cannelle (2006), who investigated the streamwise and spanwise evolution of finite span (non-axisymmetric) synthetic jets with PIV. In that study they found that further downstream from the slit a vortex line forms developing a horseshoe-like pattern with the centre moving faster than the sides. In Figure 5.20 eventually this leads to the vortex ring becoming unstable and breaking up earlier than the circular jet at $t = 0.41T$.

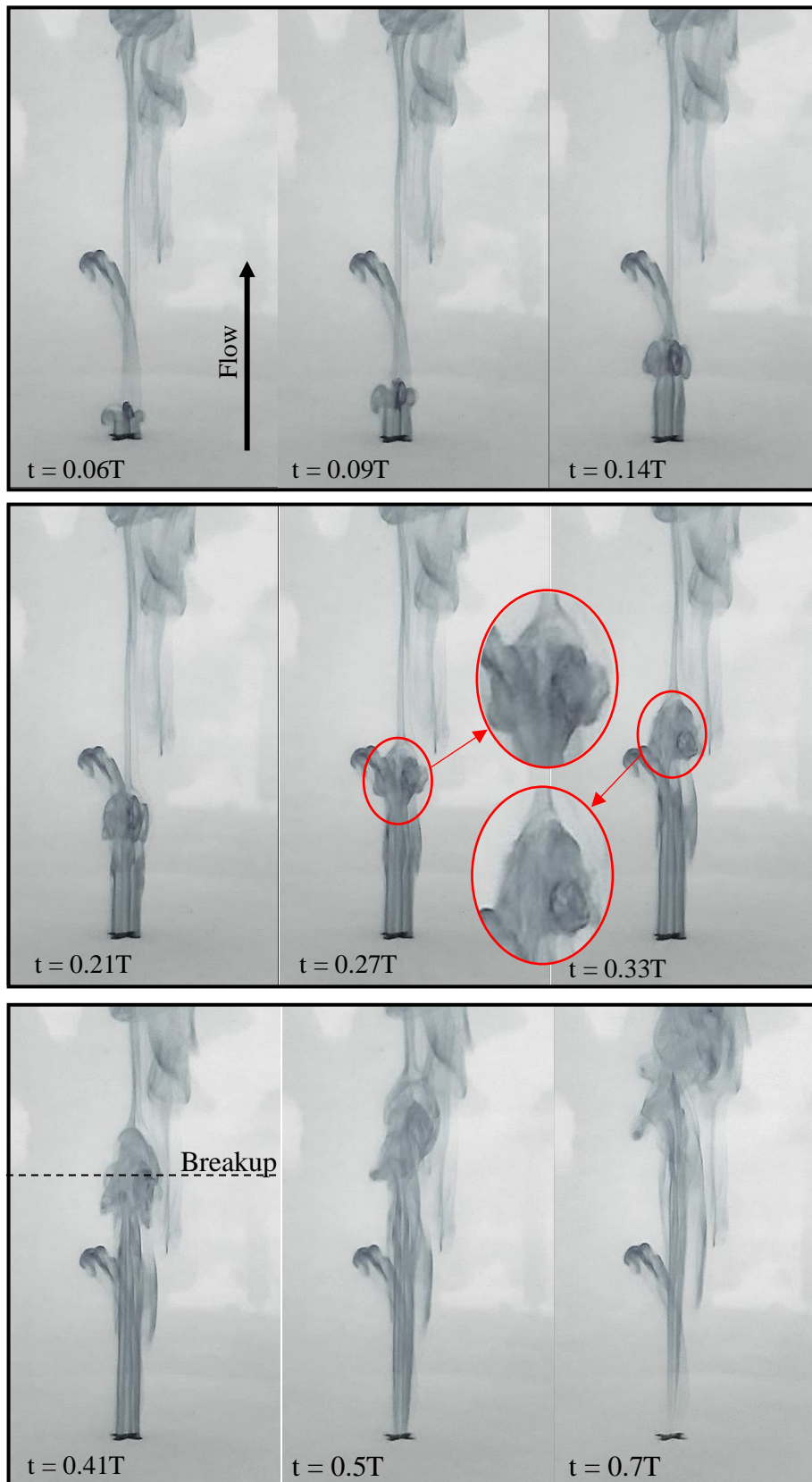


Figure 5.20. 4-Lobed jet development, $L = 11.5$, $S = 17.7$ & $Re_j = 576$

Using the information obtained from the above presented results and theory a better idea of the fluid mechanics now exists. Figure 5.21 shows an illustration of the vortex

dynamics of a 4-lobed synthetic jet. As the fluid leaves the orifice the varying boundary layer at the walls causes different strengths of vortex rollup and variations in the velocity profile of the jet. This uneven development of the jet results in the flow structure being deformed with the minor axis, in the core, catching up and leading the part of the structure originating from the lobes. The deformation stretches the vortex structure axially, so that when looking at the oncoming vortex structure from a plane perpendicular to the jet streamwise axis, the views from Figure 5.19 would be visible.

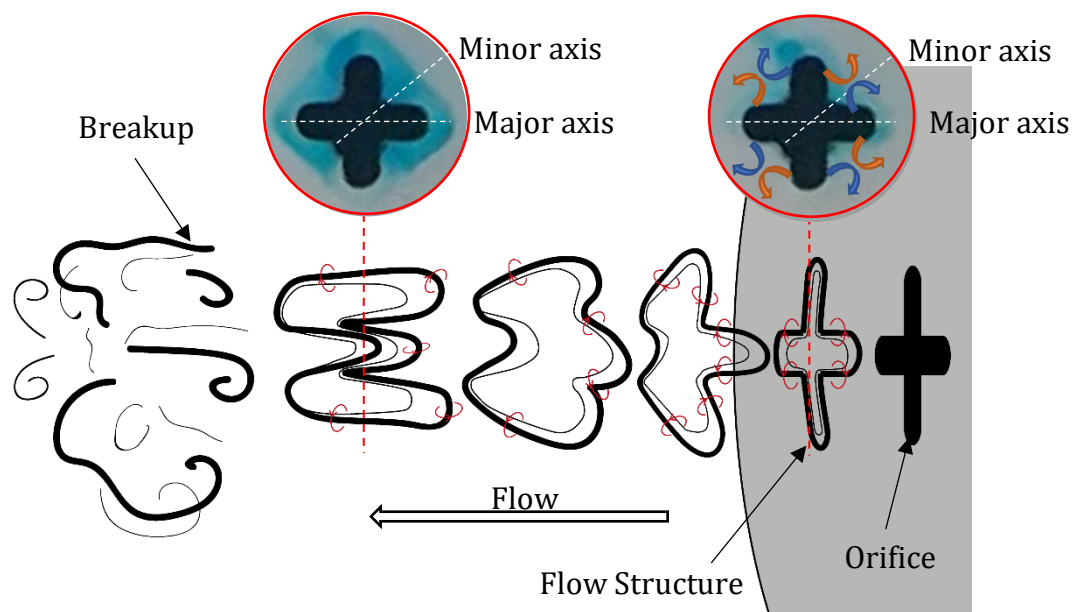


Figure 5.21. Illustration showing 4-lobed jet formation and vortex dynamics

5.4 Summary

The performance characteristics of both, the single and double chamber SJA have been presented in this chapter. In the frequency responses for both actuators several velocity peaks appear, which, with the help of numerical and empirical data, were shown to be related to both mechanical and the Helmholtz resonance frequencies. According to the numerical results, the shapes of higher order diaphragm resonance modes ($m > 1$) show an equal and opposite deflection for each positive deflection, that results in a net volume sweep of zero. However, the DIC results show that in reality this is not exactly the case due to asymmetric deflection that has a net volume change slightly higher than zero. This is reflected in the smaller velocity peaks at higher modes mentioned earlier. With increasing cavity height, the Helmholtz resonance frequency decreases and as it approaches different diaphragm resonance frequencies there is coupling that results in

amplified jet peak velocities. Furthermore, the highest jet velocity was measured using the smallest cavity height as expected.

Far field velocity measurements reveal that the jet centreline velocity diminishes at a faster rate with increasing lobe penetration and decreasing lobe count. The velocity profiles are more complex for lobed jets, with smaller velocity peaks appearing inside the lobes, caused by different shear layer growth rates. With increasing Stokes number, the exit velocity profiles of lobed jet become more uniform losing some of their distinct features visible at lower Stokes numbers. Power spectral density measurements indicate that large-scale structure in the flow lose coherence quicker, breaking up and transferring their energy down to smaller scales faster. This results in the formation of a turbulent jet faster with higher energy small-scale structures than in a circular jet. Schlieren visualisation confirms this early breakup, with the most aggressive breakup seen in the 4-lobed jet.

Each actuator employs different noise reduction methods, where both have the potential to reduce the actuator self-noise. The single chamber SJA uses lobed orifices for noise reduction and relies on enhanced mixing and the disruption and dissipation of large scale vortex structures formed at the orifice. From the test cases presented it was seen that noise reduction was effective only at the lower actuation frequency ($f_a = 325$ Hz) and can effectively help reduce noise over a range of frequencies. This ranges from frequencies near the actuation frequency, its harmonics and additional frequencies that are not diaphragm related ($300 \text{ Hz} < f < 1200 \text{ Hz}$). The noise sources in this frequency range could originate from the jet or the cavity/orifice geometry, but further investigation is needed to determine their origins. At the higher actuation frequency, $f_a = 1200$ Hz, the jet peak velocity for the actuator geometry used is achieved. This peak is a result of coupling between a mechanical and Helmholtz resonance frequency, where the noise from the diaphragm is exceptionally high which may outweigh the noise reductions using the lobed orifices. Such noise contamination makes the acoustic analysis of non-diaphragm related noise sources difficult. A solution to this is presented in the next chapter.

The second experiment investigates the use of a double chamber SJA driven by a single PZT diaphragm. This means that two out of phase alternating jets are generated at the orifices. The resulting sound fields radiating from each orifice interact with each other causing destructive interference between the orifices, which in turn significantly reduces the self-noise in those regions without affecting jet velocity.

In the last part of this chapter, dye flow visualisation results of synthetic jets issuing from circular and lobed orifices was presented. The test cases were based on typical actuator operating conditions, with the test setup serving as a design tool for validation of orifice designs before manufacture. Secondary vortex shedding was visible in the circular jet at $L = 5.4$, as is expected for $L > 4$. This same condition does not appear to apply to lobed orifices, but in the second test case with $L = 23$ secondary vortex shedding is seen in all jets. As predicted the high amplitude 6-lobed orifice and 4-lobed orifice cause the jet to break up quicker than the circular or low amplitude 6-lobed orifices. It was also seen that the high amplitude 6-lobed jet breaks up later than that issuing from a 4-lobed jet. Since both have very similar penetration ratios, it is once again shown that a higher lobe count leads to less aggressive mixing and break up of flow structure, therefore, impacting the jet velocity less than the 4-lobed orifice. Jet axis switching suggests the existence of streamwise vortices that enhance entrainment between lobes that leads to this outward deformation of the jet.

6 Jet Flow and Aeroacoustic Characteristics of Electromagnetic-driven SJA in Quiescent Conditions

This chapter offers a better understanding of the aeroacoustic response of a SJA. Electromagnetic actuation incorporating a vibration generator and latex membrane diaphragm has been used for this purpose, which has the benefit of far quieter diaphragm operation compared to piezoelectric actuation. For additional insight into the behaviour of synthetic jets and their contribution to noise generation, Schlieren flow images are presented. The insight gained from this series of experiments, helps better understand SJA jet flow related acoustic sources and presents some solutions to mitigate these.

6.1 Circular Orifice SJA

Peak velocity performance of a piezoelectrically actuated SJA is achieved by operating the device at one of the system characteristic resonant frequencies, which closely coincides with the mechanical and acoustic resonance frequencies. However, due to the increased noise generated by the diaphragm and “noisy” acoustic spectrum with the presence of several harmonic frequencies of the actuation frequency, f_a , (Figure 6.1) it makes it difficult to distinguish the diaphragm noise from jet noise (Jeyalingam & Jabbal, 2016). For this reason, electromagnetic actuation was chosen to study the effect of jet related noise without the excessive influence of diaphragm noise in the acoustic data (Figure 6.1). A vibration generator that oscillates a latex membrane, clamped at one end of the cavity, at lower frequencies (between 5 - 90 Hz) to generate synthetic jets is used for this purpose. The acoustic spectrum for this is much smoother and makes it easier to isolate flow related noise. Another important benefit over PZT diaphragms is the reliability and repeatability of tests with electromagnetic actuation, crucial for testing the fundamental mechanism behind SJA jet noise.

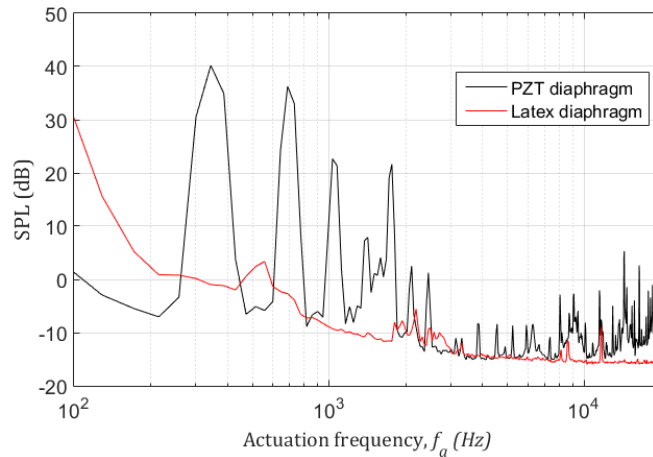


Figure 6.1. Comparison of PZT diaphragm noise ($f_a = 325$ Hz) to stretched Latex membrane (diaphragm) noise ($f_a = 60$ Hz) clamped in SJA

Acoustic spectra obtained from these experiments can then be compared to power spectral densities calculated from the jet velocity data for coherence. To understand what kind of relationship exists between the flow generated noise and operational parameters of a SJA, if any, the two characteristic operational parameters of synthetic jets in quiescent conditions are to be compared. These parameters are the jet Reynolds number, Re_j , and non-dimensional stroke length, L (Glezer A., 1988), defined previously in Chapter 2. Using the hotwire data, these parameters can be derived for later use when comparing for correlation. This will help better understand the actuator self-noise generation mechanism and establish geometric and operating parameters for optimal SJA operation with minimal self-noise generation when using a circular orifice and are further discussed later.

6.1.1 Test conditions

The actuator used has a modular design with variable cavity heights ($H = 1.2$ mm, 3 mm, 4 mm, 5 mm, 6 mm & 8 mm) and tests were carried out to determine the optimum cavity height for maximum jet centreline velocity measured close to the orifice exit. The jet exit velocities for different cavity heights show very little change at all actuation frequencies (Figure 2a). However, it was found that a cavity height of 1.2 mm yields the highest jet centreline velocity. The difference in peak centreline jet velocity is very small, where the lowest peak velocity measured ($H = 8$ mm) reaches 94% of the maximum peak jet velocity ($H = 1.2$ mm). Using the latter cavity height, a total of three test cases are considered, which differ in voltage and range of actuation frequencies, f_a ,

as summarised in Table 1. These are Case 1 (3V), Case 2 (4V) and Case 3 (5V), where $f_a = 5-90$ Hz (Case 1 & 2) and $10-90$ Hz = $10-90$ (Case 3). The difference in the range for f_a is to avoid exceeding the limit supply voltage of the amplifier at low f_a .

Table 9. Test conditions

	V_{p-p} (V)	f_a (Hz)	H (mm)	h (mm)
Case 1	3	5 – 90	1.2	4.2, 2.5
Case 2	4	5 – 90	1.2, 3, 4, 5, 6, 8	4.2, 2.5
Case 3	5	10 – 90	1.2	4.2, 2.5

In Figure 6.2b the diaphragm peak to peak displacement is shown. Comparing this to the velocity response (Figure 6.2a) reveals that the peak velocity is achieved at the maximum diaphragm displacement (this is due to the absence of compressibility effects resulting from low jet velocities), which is expected as at this point the maximum amount of cavity volume is displaced. After the peak displacement is reached there is a sharp drop in peak to peak displacement, but the actuator is able to maintain high jet velocities till around $f_a = 65$ Hz. However, this is only seen for lower cavity heights, such as $H = 1.2$ mm and 3 mm. This is likely an effect associated with the phase difference between diaphragm motion and jet formation.

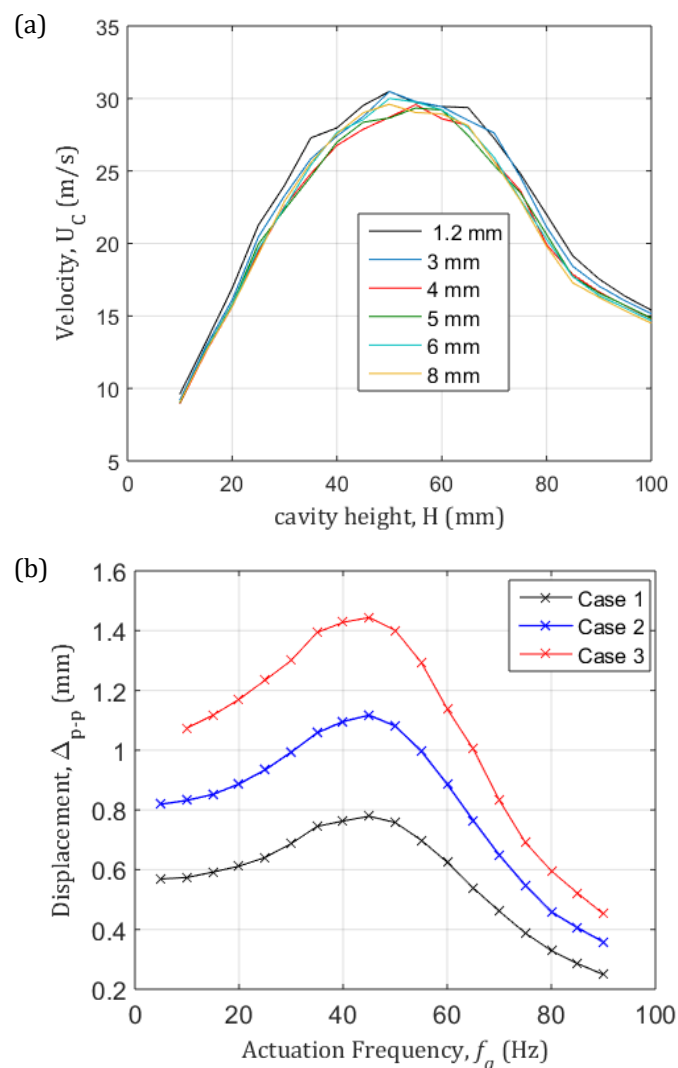


Figure 6.2. (a) SJA frequency response as a function of cavity height, H , for Case 2 and (b) diaphragm peak-to-peak displacement for different test cases

It was shown that the actuation frequency for peak jet velocity coincides with the maximum diaphragm displacement, which is associated with the largest change in cavity volume (Figure 6.2). For the following tests a new diaphragm was used and therefore the frequency response slightly changed. However, the diaphragm displacement behaviour remains the same. Peak jet velocity is recorded at 55 Hz (3 V) and 60 Hz (4 V and 5 V) in the presented case. Furthermore, the diaphragm peak-to-peak displacement (Figure 6.2b) shows linear proportionality to input voltage, whereas the gain in peak jet velocity becomes smaller with increasing voltage input (Figure 6.3).

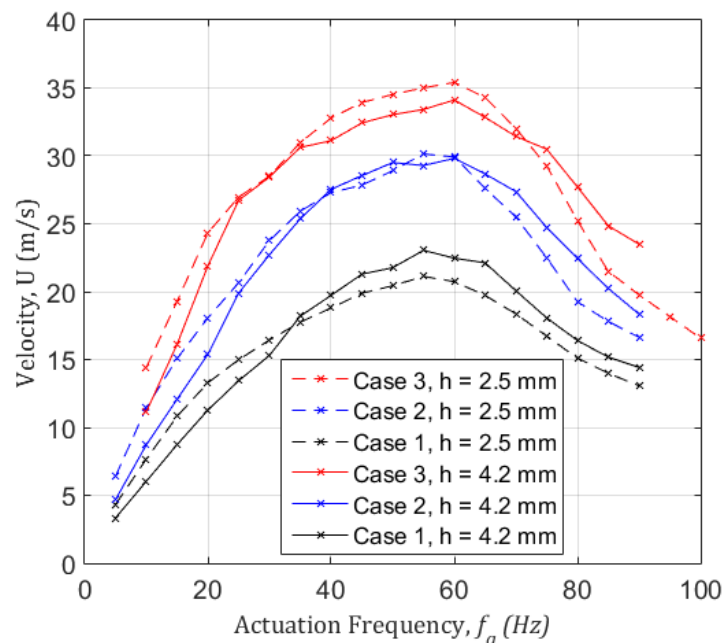


Figure 6.3. Frequency response of SJA (a) jet centreline velocities vs. actuation frequency for $h = 4.2$ mm (solid line) and $h = 2.5$ mm (dashed line)

6.1.2 Acoustic response

The acoustic response of the SJA comprises of the vibration generator, which becomes more dominant after $f_a = 80$ Hz with decreasing jet velocity of the oscillating jet expelled through the orifice. To separate the two noise sources, measurements of the actuator with and without the orifice plate were taken to obtain ΔSPL , i.e.:

$$\Delta\text{SPL} = \text{SPL}_{\text{Overall}} - \text{SPL}_{\text{Diaphragm}} \quad (29)$$

Measurements of just the vibration generator noise (and small noise contributions that may originate from the diaphragm and possible vibrations associated to the system) can

be labelled as a “background noise” source that is subtracted from the overall noise data of the SJA operating with the orifice plate attached, where the remaining noise can be attributed to aeroacoustic noise. Although this does not guarantee full isolation of aeroacoustic noise from the vibration generator and diaphragm, it helps to minimise their noise contribution to the acoustic spectrum.

When operating the SJA a distinct fluctuating whistling sound can be heard. Figure 6.4 shows the acoustic spectra for all three cases through the entire range of actuation frequencies. At low actuation frequencies and jet velocities, the resulting Δ SPL remains around zero until there is a sudden spike between 2 and 5 kHz. For Case 1 (Figure 6.4a) this spike in self-noise is first recorded at 3781 Hz at an actuation frequency of 35 Hz, corresponding to a jet velocity of 18.2 m/s. For cases 2 and 3, the spike occurs at actuation frequencies of 20 Hz (15.4 m/s) and 15 Hz (18.3 m/s) respectively (Figure 6.4b and 4c). Distinct patterns are evident in the spectra, which can help identify possible noise sources. These are constant frequency lines and a bow like pattern seen at higher frequencies of roughly 3800 Hz.

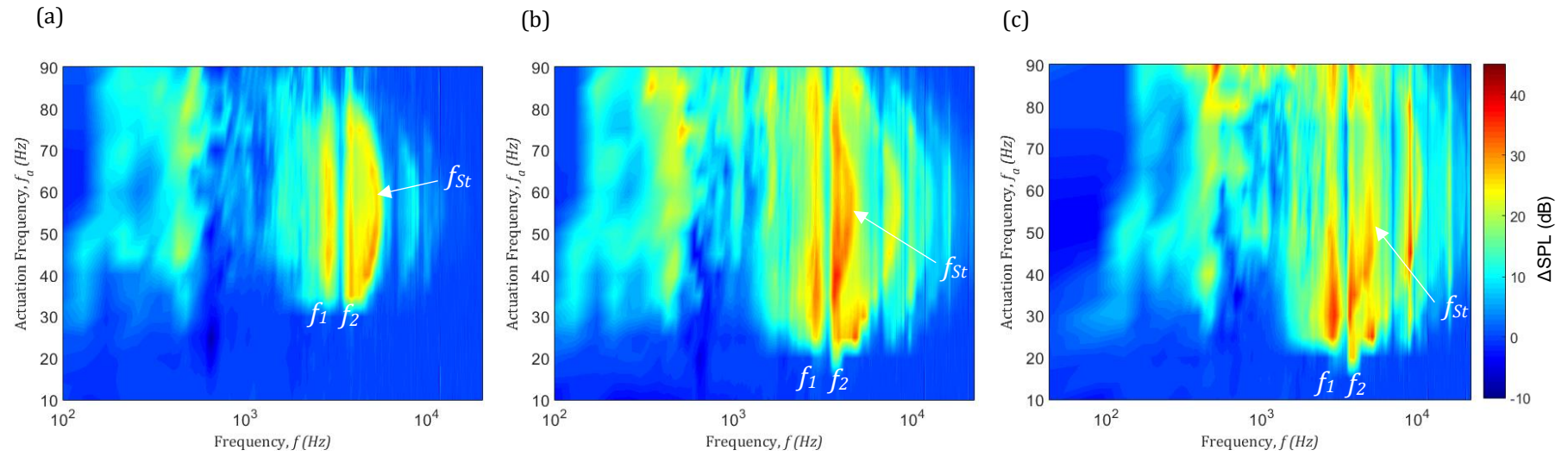


Figure 6.4. Acoustic response for $h = 4.2$ mm and $H = 1.2$ mm (a) Case 1, (b) Case 2 and (c) Case 3, where f_1 and f_2 mark the two dominant constant frequency lines and f_{St} marks a constant Strouhal number behaviour in the spectra

Constant frequency lines in the spectrum, such as the ones originating from 2879 Hz (f_1), and 3781 Hz (f_2) (Figure 6.4a-c), indicate an acoustic mode of the SJA system that is dictated by the actuator geometric parameters as being the source. This is because operating parameters, such as actuation frequency and the resulting jet velocities, change throughout the different test cases and one would expect to see only varying patterns accordingly in the spectra. Instead lines of constant frequency values are seen, suggesting the source is a constant parameter. Further cases investigating changing geometric configurations will be discussed in Sections 6.1.7 and 6.1.8 to support this claim.

During operation of the SJA, different scale structures are formed due to hydrodynamic effects in the flow. When the frequency of such scales match that of an acoustic resonance frequency of the actuator (geometry dependent), self-sustained periodic oscillations are established due to a feedback mechanism (Nair & Sujith, 2016). In addition to these fundamental frequencies, f_1 and f_2 , their subharmonics and higher harmonics become visible with increasing input voltage. The most dominant frequencies in the spectra are marked f_1 and f_2 . Also, the actuation frequency where the onset of these SPL peaks, or noise, first appears varies. For Case 1 the onset is at $f_a \approx 35$ Hz, Case 2 $f_a \approx 20$ -25 Hz and for Case 3 $f_a \approx 15$ Hz. While the constant frequency lines can be attributed to geometric parameters, it does not explain the different actuation frequencies for the onset of noise. These characteristics will be further explored by analysing the flow-related and system characteristic, non-dimensional parameters.

6.1.3 Strouhal number dependence

Oscillating characteristics are an intrinsic part of synthetic jet and noise generating flows. A useful non-dimensional parameter to describe such flow is the Strouhal number, St . In various literature it has been established that the whistling in pipe systems and jets emanating from an orifice are related to flow instabilities that occur within a specific St range based on the fundamental frequency, as shown in Eq. (7) (Arthurs & Ziada, 2009).

$$St = \frac{fd}{U} \quad (28)$$

Arthurs and Ziada (2009) found a Strouhal number range of $0.26 < St < 0.56$ for an annular duct with closed coaxial side-branches to cause resonance. Henrywood and Agarwal (2013) recorded a Strouhal number range of $0.2 < St < 0.6$, which is indicative of vortex shedding due to jet instabilities (Michalke & Fuchs, 1975). Using Eq. (7) the calculated Strouhal number, based on f_2 (the most dominant frequency in the spectrum, Figure 6.4) and the jet exit velocity, is $St = 0.22$ for Case 1 at an actuation frequency of 60 Hz. In fact, the Strouhal numbers for jet velocities associated with the different acoustic modes, f_1 and f_2 , seen in the spectra for all cases fall within the range $0.22 < St < 0.50$, as shown in Figure 5, and are thus in close agreement with the literature.

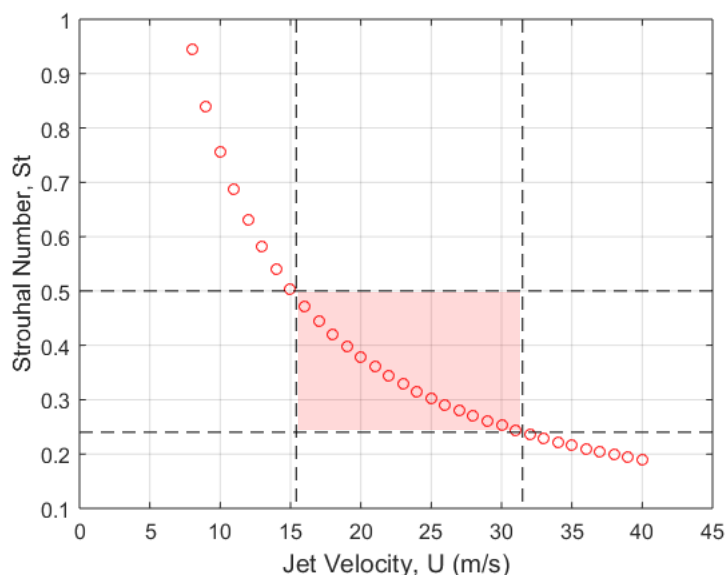


Figure 6.5. Jet Strouhal number as a function of jet velocity, with range for whistling highlighted in red based on f_2

Figure 6.5 shows the change in Strouhal number with jet velocity, with the range for the constant frequency lines on the acoustic spectra marked in red. As mentioned before this is indicative of acoustic modes of the SJA system. On the other hand, the bow-like SPL peak lines in the spectra branching off from f_2 and some higher frequencies cannot be attributed to the SJA geometry and therefore are not caused by acoustic modes of the cavity and/or orifice. Instead, when plotting the Strouhal numbers based on the frequencies and jet velocities along this line, at which the SPL peaks form the bow pattern, against the actuation frequency, f_a , a distinct, constant Strouhal number trend is obtained for an actuation frequency range (Figure 6.6). For Case 1 this is between $f_a \approx 35 - 80$ Hz, Case 2 between $f_a \approx 30 - 75$ Hz and Case 3 between $f_a \approx 25 - 90$ Hz. The

frequencies along this bow line that result in the constant Strouhal number characteristic are labelled f_{St} .

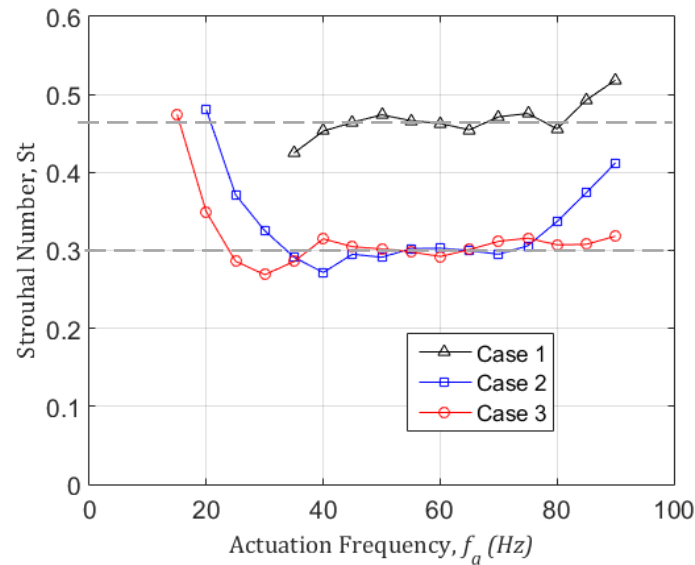


Figure 6.6. Strouhal number as a function of actuation frequency based on f_{St} showing the constant Strouhal number behaviour over a range of actuation frequencies (dashed lines)

6.1.4 Reynolds number dependence

The jet Reynolds number, Re_j , defined in Eq. (24) is shown as a function of actuation frequency for all cases in Figure 6.7a. The variable is \bar{U}_0 , but presented as Re_j allows for universal identification of SJA operating conditions that result in the generation of jet noise. When compared to the acoustic spectra (Figure 6.4) specific self-noise conditions related to Re_j become evident. For all cases, a threshold range for Re_j exists at $624 < Re_j < 742$ (Figure 6.7a), within which whistling noise contributes to the actuator self-noise (as marked by the dash lines). When compared to the acoustic spectra for Case 1 (Figure 6.4a) ΔSPL at $f_a = 90$ Hz has diminished to near zero above 1 kHz. Although acoustic and velocity measurements were not taken beyond $f_a = 90$ Hz, similar trends are observed with the other two cases, where ΔSPL approaches zero at $Re_j \cong 650$.

Furthermore, from an actuation frequency of around 40-45 Hz there is a shift in high frequency noise branching from f_1 towards higher frequencies, which appears as a bow in the spectrum. This is clearly Reynolds number dependent as the shift increases with increasing Re_j until a peak is reached that coincides with peak jet velocity. For example, the maximum shift for Case 1 is reached at $f_a = 55$ Hz, after which the shift decreases again until merging back together with the mode it branched off from. This together

with the constant Strouhal number behaviour seen earlier and frequency shift indicates the presence of a second noise source in addition to the acoustic modes of the actuator. This source is likely due to jet instabilities and more aggressive breakup of flow structures that results in increased turbulent mixing further downstream with increasing jet velocity. Similar observations in the same Strouhal number range were noted by Henrywood and Agarwal (2013).

6.1.5 Stroke length dependence

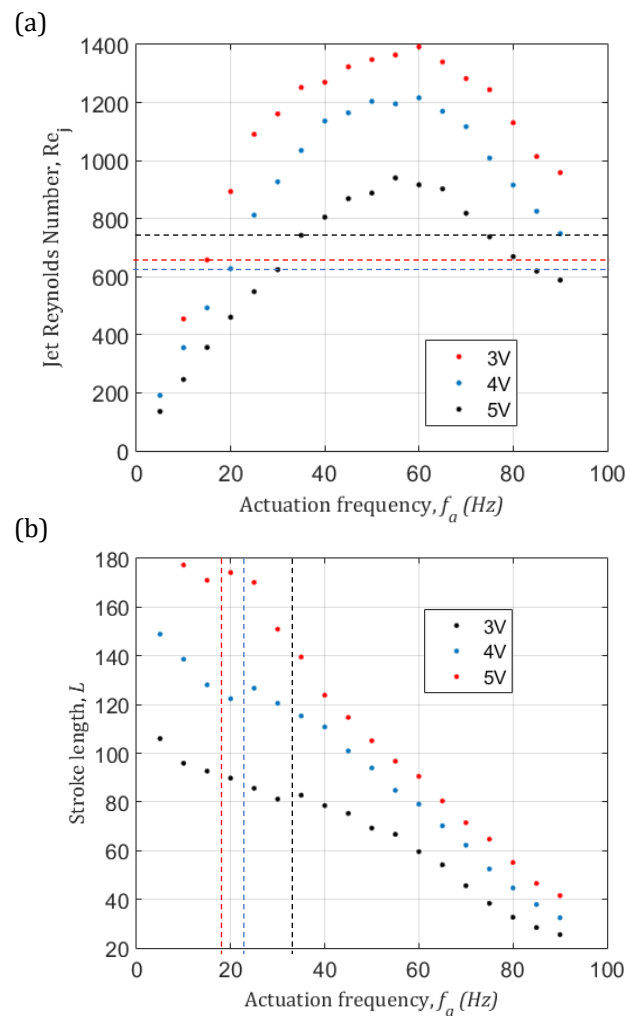


Figure 6.7. Non-dimensional jet flow parameters (a) jet Reynolds number and (b) stroke length for all three cases. Dashed lines indicate Re_j and f_a threshold respectively for onset of whistling for all three cases

The non-dimensional stroke length, L , defined in Eq. (5), is shown as a function of actuation frequency in Figure 6.7b for the cases studied. Again, the only variable that changes for L in this case is \bar{U}_0 . A noticeable trend for all cases is a sudden jump in L ,

marked by the dash lines. It was shown, in Figure 6.4, that these actuation frequencies roughly correspond to the onset of actuator self-noise. For example, for Case 1 this jump takes place at $f_a = 35$ Hz, the same actuation frequency where whistling noise is first measured. This could be explained as the effect of onset of jet instabilities and vortex shedding or jet breakup that results in generating whistling noise once a threshold Reynolds number is reached.

6.1.6 Velocity spectra and Schlieren visualisation

The Strouhal number analysis indicates the self-noise source to be related to self-sustained periodic oscillations caused by growing jet instabilities and vortex shedding, which should be detectable in the hotwire data acquired. For the instantaneous velocity response of the actuator for Case 1 at different actuation frequencies (Figure 6.8), differences in the flow profiles are observed. At actuation frequencies below which the acoustic spectra show a mean $\Delta\text{SPL} \cong 0$, the response is a smooth curve with no noise in the signal. However, at and beyond the onset of whistling noise, there is considerable noise in the instantaneous SJA velocity response. This is visible in Figure 6.8a, where until $f_a = 25$ Hz a generally smooth response is observed whereas from $f_a = 35$ Hz the output velocity gives a noisier response. Similarly, from Figure 6.4a the actuator self-noise starts to decrease suddenly again after around $f_a = 80$ Hz and accordingly the velocity response is smoother again (Figure 6.8b). The noisy response starts near the curve peak, i.e. towards the end of the blowing part of the cycle ($t \approx 0.02$ s), after which the jet becomes unstable and transitions to turbulence near the exit. Furthermore, comparing Figure 6.8 to Figure 6.4a shows that for Case 1, with increased turbulence, the actuator self-noise increases while with decreased noise in the velocity signal the acoustic noise also decreases.

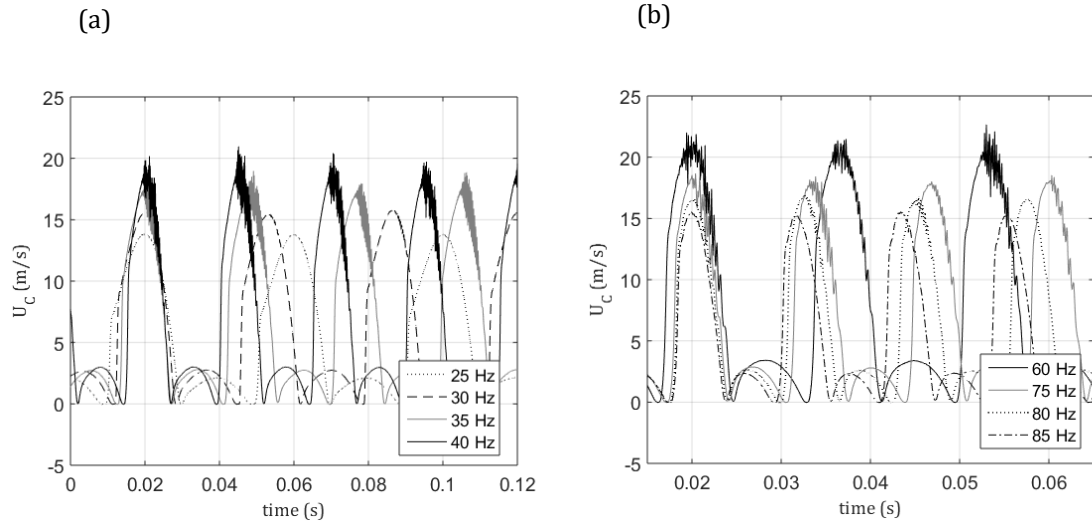


Figure 6.8. Instantaneous SJA centreline velocity response for Case 1 at (a) $f_a = 25$ Hz, 30 Hz, 35 Hz, 40 Hz and (b) $f_a = 60$ Hz, 75 Hz, 80 Hz, 85 Hz

A similar behaviour is observed with Case 2 and Case 3, as shown in Figure 6.9a and b respectively. Before the onset of whistling noise, the velocity response is smooth ($f_a = 20$ Hz, Figure 6.9a). However, once a critical actuation frequency is reached the output shows turbulent characteristics evidenced by a noisy velocity signal ($f_a = 25$ Hz, Figure 6.9a). In Case 3 (Figure 6.4c) there is a range of actuation frequencies where the acoustic response suddenly decreases between $f_a = 60 - 80$ Hz for f_l , f_2 and f_{st} . As expected, noise in the velocity response has also decreased at $f_a = 60$ Hz, where the SPL at the dominant frequencies has decreased (Figure 6.9b).

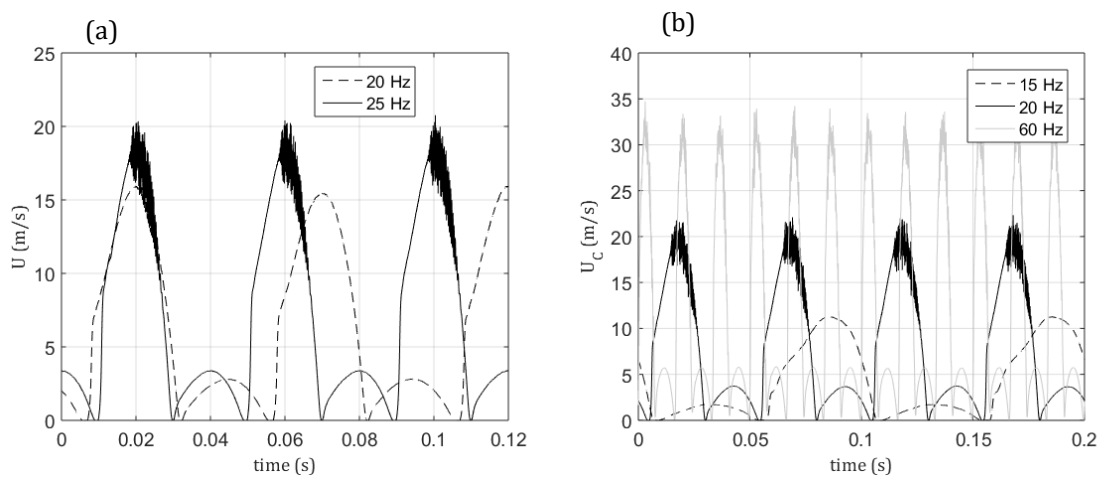


Figure 6.9. Instantaneous SJA centreline velocity response on and just before the onset of audible actuator self-noise for (a) Case 2 and (b) Case 3

According to the literature (2.3.4.), flow instabilities and vortex shedding have been linked to the excitation of the cavity-orifice system at their fundamental modes.

Evidence of this was observed in the acoustic spectra in the form of constant frequency lines that occur within a specific range of Strouhal numbers typical of such noise mechanism. The results presented in Figure 6.8 and 9 show evidence of a turbulent flow during certain phases of the actuation cycle. The flow at the orifice exit becomes turbulent, evidenced by the noisy instantaneous velocity signal near the end of the blowing cycle (peak of the velocity response) and before the velocity reduces as the flow direction is reversed and air enters the cavity again. Such behaviour can be explained by vortex shedding that may be amplified by a feedback mechanism, where the shedding frequency coincides with the system fundamental modes. Self-sustained oscillations in the flow cause turbulence and periodic whistling noise if the jet meets the right Reynolds number and Strouhal number conditions. The jump in the non-dimensional stroke length, L (Figure 6.7b), is related to the highly fluctuating and changing velocity of the transitioned turbulent jet.

A visual representation of these findings is shown in Figure 6.10 in the form of Schlieren visualisation for Case 2. Case 2 is used for comparison as the beginning and end of the constant frequency characteristics are fully visible in the acoustic spectrum, unlike Case 3, and the features are more pronounced than for Case 1. At an actuation frequency of $f_a = 20$ Hz, a laminar jet forms at the exit with some initial vortex rollup (Figure 6.10a). The vortex pair formed is weak and is elongated ($t = 0.08T$) as it quickly moves downstream with the jet flow before breaking up relatively early at $t = 0.22T$ (7d) to form a turbulent jet. The point of transition to turbulence is pushed further downstream and reaches its furthest point at $9d$ from the orifice exit, which is also at the end of the blowing part of the cycle ($t = 0.48T$) with a peak centreline jet velocity of 15.4 m/s. Once the diaphragm starts moving in the opposite direction, for the suction part of the cycle, the jet slows down and dissipates. Increasing the actuation frequency by 5 Hz to $f_a = 25$ Hz marks the onset of the periodic whistling noise for Case 2 (Figure 6.4). Similar to the previous case of $f_a = 20$ Hz, a clearly laminar jet forms at the orifice exit (Figure 6.10b), which breaks up at around $8d$. The transition point is again pushed further downstream ($10d$) as more air exits the orifice ($t = 0.275T$). However, as the diaphragm moves back in the opposite direction, initiating the suction cycle, the transition point begins to move upstream towards the orifice until the entire jet becomes fully turbulent ($t = 0.325T$). At this point on either side of the fully turbulent jet shear layers are visible. At $t = 0.45T$ a

closer look at the shear layer reveals small periodic flow structures starting to take shape within it. These structures are more visible at $t = 0.45T$ (highlighted in Figure 6.10b) and may be a result of periodic vortex shedding caused by excitation by the SJA system at an acoustic mode, which in turn induces and amplifies vortex shedding near the orifice exit.

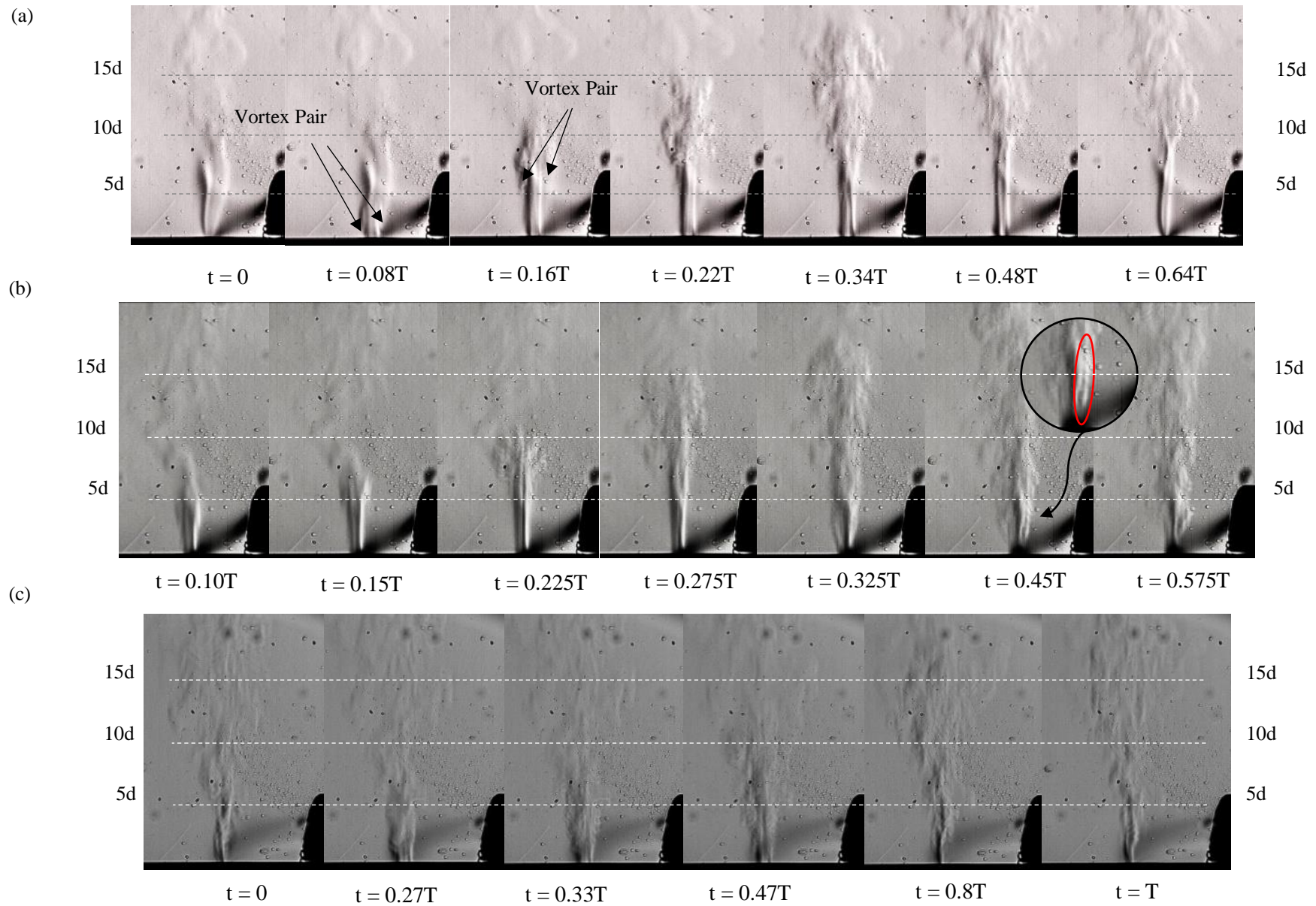


Figure 6.10 Schlieren flow visualisation of circular orifice SJA for Case 2 at (a) $f_a = 20$ Hz, (b) $f_a = 25$ Hz and (c) $f_a = 60$ Hz

Finally, Figure 10c shows the jet development for $f_a = 60$ Hz where the highest jet velocity of 29.81 m/s is measured. Once again, the jet starts off laminar, however between $t = 0.27T$ and $t = 0.33T$ it becomes turbulent within $1d$ from the orifice exit. This is further supported by the instantaneous velocity measurements taken at the same location (Figure 6.8b), where the “noise” in the velocity signal begins near the top of the blowing cycle ($t \approx 0.02$ s). This transition reveals the turbulent shear layer, which shows the jet diverging and mixing with the surroundings. From the acoustic spectra in Figure 4b, the SPL level of f_2 is about the same at $f_a = 60$ Hz and $f_a = 25$ Hz, but a key difference is the high frequency noise that appears as a bow in the spectrum. The Schlieren images and velocity plots presented here show a clear relationship between the actuator self-noise generation and turbulent jet flow. In all cases, at the onset of whistling, the jet becomes fully turbulent at the orifice exit, where small periodically repeating structures can be found forming in the shear layer ($t = 0.45T$ in Figure 6.10b). This transition begins at some downstream distance from the orifice when the jet becomes unstable. Once turbulent the flow instabilities travel progresses upstream to the orifice, causing the entire jet to become turbulent. During this time, small-scale ordered flow structures are shed in the shear layer, again highlighted in Figure 6.10b ($t = 0.45T$). This is typical of a feedback loop, where the SJA is excited at an inherent system resonance frequency by flow instabilities that occur in proximity to the orifice, unless the jet dissipates before the next blowing cycle.

However, at this stage it is not known if the vortex shedding frequencies indeed match the system resonance frequencies. For this, the frequency components that make up the jet velocity signal (PSD) can be analysed to establish if coherence between acoustic and velocity data exists. The procedure for this is the same as described in Chapter 4. The velocity spectra (PSD), at various streamwise and spanwise locations from the orifice centre for Case 2 at $f_a = 60$ Hz (peak velocity output) are shown in Figure 6.11. Along the centre of the orifice (Figure 6.11a) there is an increase in the spectral band in the low to mid-frequency range from the exit until a downstream distance of $y=10d$, which suggests the formation of the jet (Smith & Glezer, The formation and evolution of synthetic jets, 1998). With increasing distance downstream from the orifice, the low frequency peaks are quickly attenuated. This attenuation leaves a continuous spectrum, characteristic of turbulence, which indicates the existence of eddies of various sizes

(Tesar & Kordík, 2011). In the spanwise direction, between $x/d = 0$ and 0.5 (within the orifice) at the exit (Figure 6.11a and 11b respectively), the magnitude of low frequency band increases slightly, suggesting the development of the jet.

Moving along the spanwise direction at $y = 5d$, there is no change in the spectrum until $x=1d$ (Figure 6.11c), where an increase in some high frequency components is seen. This region is located just outside the orifice where it was shown, in Schlieren images ($t = 0.33T$, Figure 6.10c), a turbulent shear layer develops at $f_a = 60$ Hz with periodic small-scale flow structures occurring. Also, as the jet spreads in the spanwise direction the large-scale structures continue to dissipate as they transfer their energy to the smaller scales, evidenced by the dissipation of low frequency components and the gain or slower decrease of high frequency components, slowly becoming a continuous spectrum. In Figure 6.11d ($x/d = 2$) the spectra at the exit and $y = 5d$ positions contain very little energy because these lay outside the main influential region of the jet.

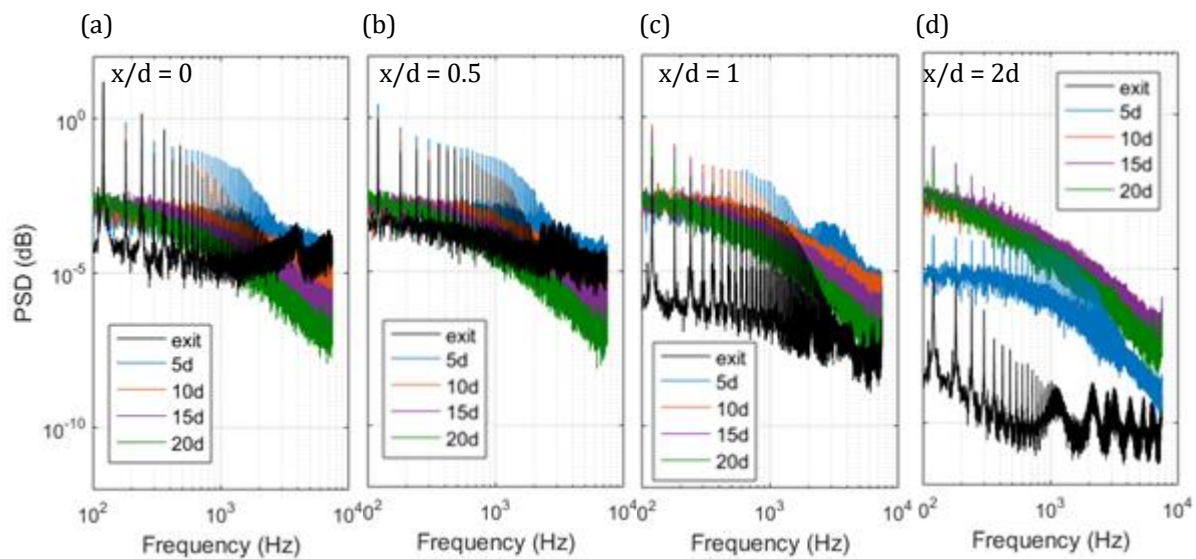


Figure 6.11. Jet velocity power spectral density (PSD) for Case 2 (4 V, $f_a = 60$ Hz) as a function of five streamwise positions (exit, 5d, 10d, 15d & 20d) taken at four spanwise positions $x/d =$ (a) 0, (b) 0.5, (c) 1 and (d) 2

As the noise radiation from the jet is a result of flow structures formed in the separating shear layer from the orifice (which, under the right conditions, can also excite and amplify acoustic modes of the SJA) and energy dissipation from turbulence, it is now possible to compare acoustic and velocity spectra for coherence. Figure 6.15 compares the velocity and acoustic spectra for Case 2. In this comparison the velocity spectrum shown in Figure 6.15 is chosen as the variation in energy across the spectrum,

especially at $y=5d$, shows clear agreement with the acoustic spectrum. Similar agreement is, however, also seen at other points, especially at the exit. The chosen point for this comparison is located within the jet shear layer, where most of the jet noise sources originate from. This coherence confirms that the noise generation is due to a feedback mechanism, which amplifies vortex shedding from the orifice when the SJA is excited at its resonance modes. However, it also must be said that not all noise contributions are explained by the velocity spectrum. Equally not all peaks in the velocity spectrum can be linked to jet related noise. This is mainly due to hot wire rectification (Smith & Glezer, 1998; Yang et al. 2010), a source of error that needs to be considered when using a 1D probe that does not take the flow direction into account.

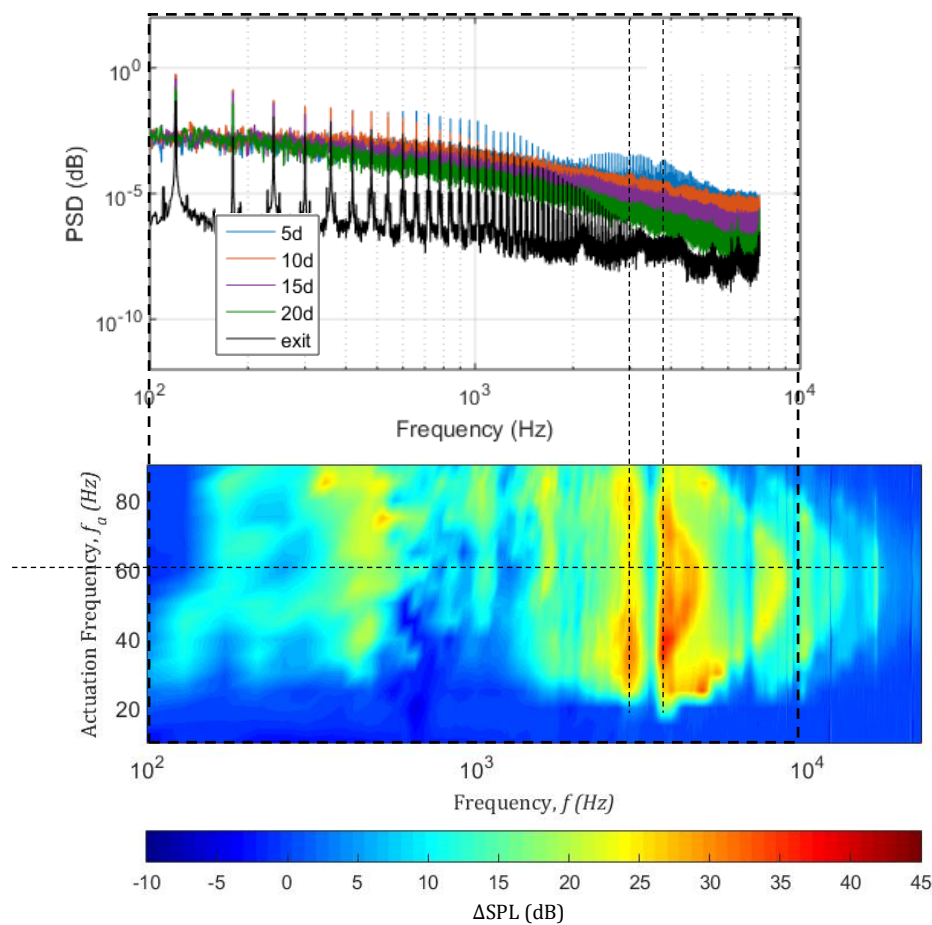


Figure 6.12. Comparison of PSD (top image) to Δ SPL (bottom image) for Case 2

6.1.7 Effect of cavity height on the acoustic and velocity response

In the previous section it was established that the whistling noise generated by the SJA is mostly dependent on the actuator geometry, where fundamental frequencies or resonant modes of the system are excited by flow instabilities when certain operational

conditions are met. A smaller contribution is directly dependant on the jet velocity and has a characteristic constant Strouhal number behaviour as a result. In the next two sections the influence of actuator geometry will be further explored in terms of cavity height, H , and orifice height, h , on the actuator self-noise response.

In Chapter 5 it was shown that the velocity response of a piezoelectrically driven SJA changes significantly when the actuator cavity height, H , is changed. However, according to Figure 6.2a changing the cavity height of the actuator has very little effect on the velocity response when electromagnetic actuation is used. However, this does not mean that the acoustic response will also remain unchanged, because from the Helmholtz resonance equation (Eq. 9) it can be seen that the actuator geometry determines the resonant mode. The Helmholtz resonance is, however, only one of many types of acoustic resonances possible for such cavity orifice-coupled systems. Furthermore, it was shown in the previous section that the jet vortex shedding can cause excitation of the SJA's acoustic modes creating a feedback mechanism that repeats through each actuation cycle. Figure 6.13a shows the acoustic frequency response for the electromagnetic actuated SJA with varying cavity heights of 1.2 mm, 5 mm and 8 mm.

Although for a given diaphragm displacement the jet velocity is mostly unaffected, from Figure 6.13 it can be seen that the cavity height indeed impacts the spectral response of the self-noise generated by the actuator. Between approximately 1 and 2 kHz the acoustic spectrum splits from a more broadband single peak response of around 34 dB ($H = 8$ mm) to two distinct narrowband peaks at 1650 Hz and 2879 Hz of around 23 dB and 26 dB respectively ($H = 1.2$ mm), where it can be recalled that 2879 Hz in the previous section is labelled as f_1 .

Furthermore, the constant Strouhal number peaks, f_{St} , exist in the same actuation frequency range and at similar frequencies (± 300 Hz) in the spectrum for all cases. In this test it was shown that the jet velocity varies little with changing cavity height, which further shows the bow-shaped peak in the spectra is a function of jet velocity. On the other hand, the constant frequency lines originate from the actuator geometry.

If as stated, a large portion of the SJA acoustic response is determined by the cavity-orifice geometry, it should be possible to find a relationship between the acoustic and velocity response of the actuator regardless of the actuation method. If the cavity is excited by the jet flow and its inherent instabilities, actuation of the SJA system at the same frequencies should give a velocity response. A significant enough excitation is, however, not possible using electromagnetic actuation at the distinct frequencies of interest in the acoustic spectrum. Therefore, under each acoustic response the velocity response obtained from the same SJA driven piezoelectrically (Figure 6.13b), as originally presented in Chapter 5, is compared to the corresponding cavity height. It can be observed that for the range of actuation frequencies presented for the piezoelectrically driven SJA there is some agreement between the acoustic and velocity data. The velocity response is a result of a combination of mechanical and acoustic resonances of the SJA system. For example, the velocity peaks at approximately $f_a = 1050$ Hz and $f_a = 1600$ Hz for $h = 1.2$ mm (Figure 6.13b) match quite well the corresponding Δ SPL peaks and similar matches are seen across the entire velocity spectrum where the acoustic and velocity peaks match at the same frequencies. This does not, however, suggest that the mechanical resonance of the diaphragm does not contribute to the velocity response. Instead a coupling between the acoustic and mechanical modes could amplify the velocity response, which could be the case for $H = 1.2$ mm, where the numerically predicted mechanical resonance modes closely match velocity peaks and their actuation frequencies. In fact, the DIC results confirmed diaphragm resonance modes at actuation frequencies of velocity peaks. As discussed in Chapter 5, the first diaphragm resonance mode will generate a meaningful velocity peak without requiring coupling with acoustic resonance. This is due to the single diaphragm deflection peak that displaces a large enough cavity volume. For $h = 1.2$ mm the velocity at the first resonance ($f_a = 350$ Hz, Figure 6.13a) is, however ~ 10 m/s compared with ~ 7 and 6 m/s in Figure 6.13b and 13c respectively. At the same time in the acoustic spectrum (Figure 6.13a) increased SPL can be seen at similar frequencies for electromagnetic actuation. This suggests that the increased jet velocity at the first SJA resonance mode for $H = 1.2$ mm is likely a result of coupling.

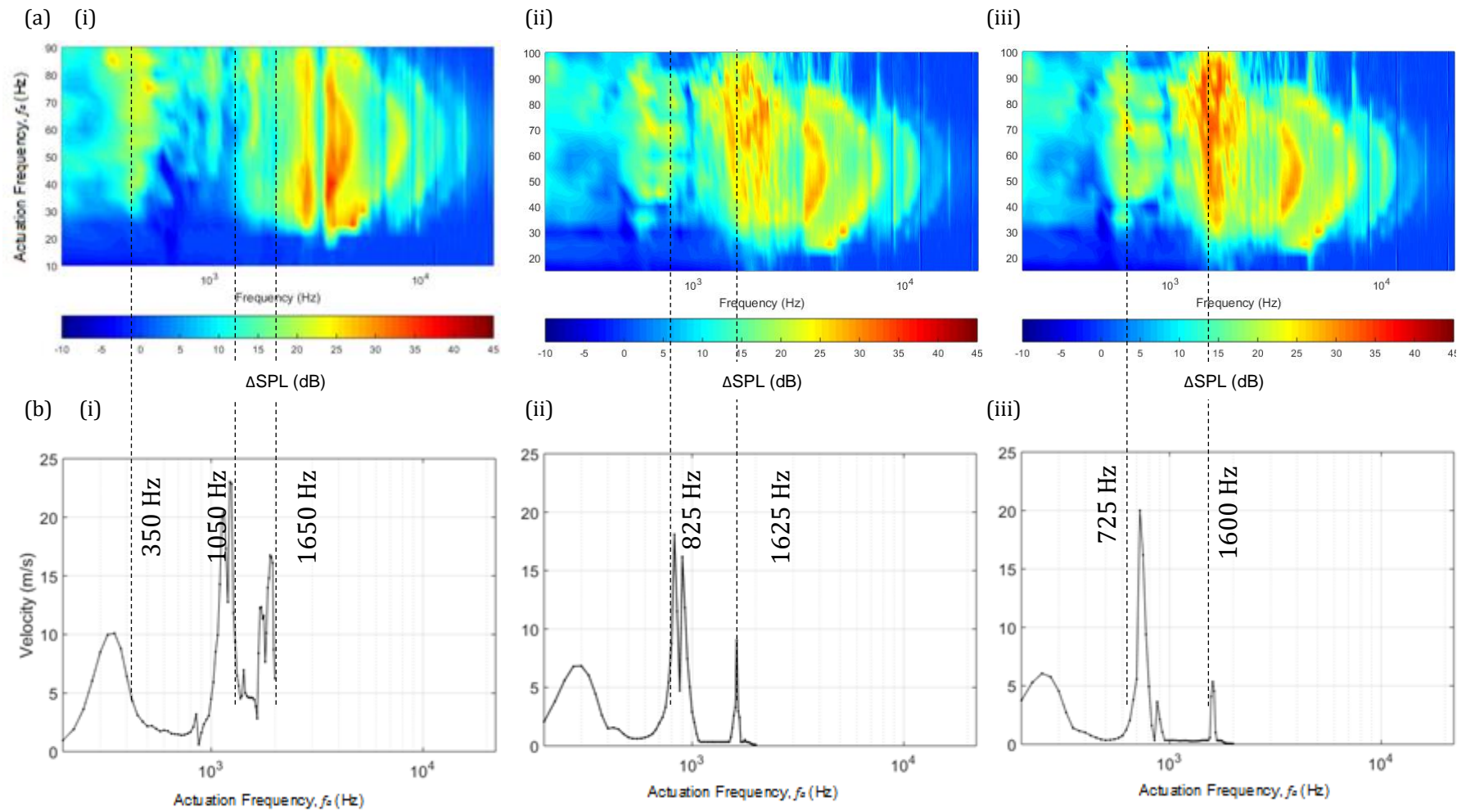


Figure 6.13. Effect of varying SJA cavity height, H , on (a) electromagnetically driven SJA acoustic response, where (i) $H = 1.2$ mm, (ii) $H = 5$ mm and (iii) $H = 8$ mm, and (b) piezoelectrically driven SJA centreline exit velocity response, where (i) $H = 1.2$ mm, (ii) $H = 5$ mm and (iii) $H = 8$ mm

6.1.8 Effect of orifice height on the acoustic and velocity response

While the variation of cavity height shows frequency shifts in the acoustic spectrum, the SJA geometry can also be changed in terms of the orifice height, h . The orifice plates used in the experiments consist of two different heights, $h = 2.5$ mm and $h = 4.2$ mm with the same effective diameter, $d_e = 2$ mm, with the velocity response showing mixed results (Figure 6.14). Apart from Case 1 using $h = 2.5$ mm yields slightly higher jet velocities with a gain of 1.1% for Case 2 and 3.8% for Case 3. Although these changes are small, changing the orifice height greatly affects the noise footprint of the actuator.

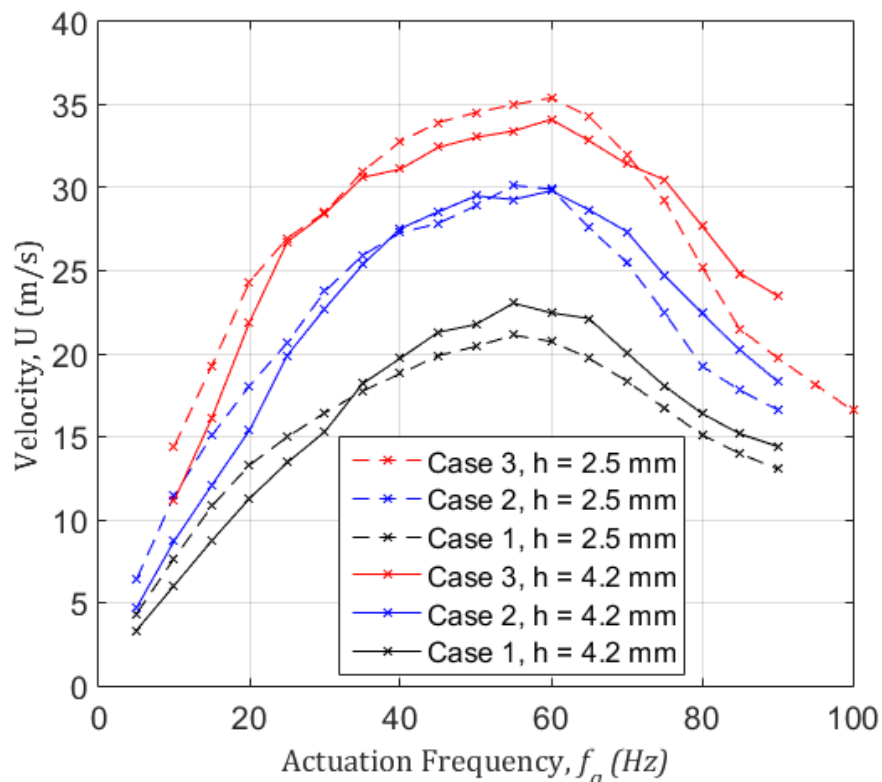


Figure 6.14. SJA velocity response for $H = 1.2$ mm, $h = 2.5$ mm and 4.2 mm

The acoustic responses at first sight (Figure 6.15) look the same with the same frequencies showing up in the spectra, but the SPL amplitudes are different. For $h = 2.5$ mm (Figure 6.15b), low frequency noise ($f < 1250$ Hz) is lower compared to having a larger orifice height. On the other hand, above this frequency the noise generated is significantly higher for $h = 2.5$ mm. The onset of self-noise or whistling again shows a Reynolds number and Strouhal number dependency, with similar patterns in the same locations in the spectra. That the constant frequency and constant Strouhal number patterns reoccur in the same locations, but with increased SPL, suggests that the cavity

geometry dominates the acoustic modes of the SJA system, while the orifice height determines the sound level. The behaviour for this could be explained by the ability of the separated flow inside the orifice to reattach and its resulting trajectory (2.2.6.2). As air is forced into the orifice the flow separates at the sharp orifice edge at the entrance. If h is long enough the flow will reattach to the orifice walls and exit with a straight trajectory. With a shorter orifice height, the flow will not be able to reattach to the wall, thus causing a curved trajectory at the exit making the jet unstable. This jet may break up earlier generating a turbulent jet where the small-scale structures now have higher energy than those in a jet that breaks up later. The increased energy can cause increased amplification of the acoustic modes of the actuator.

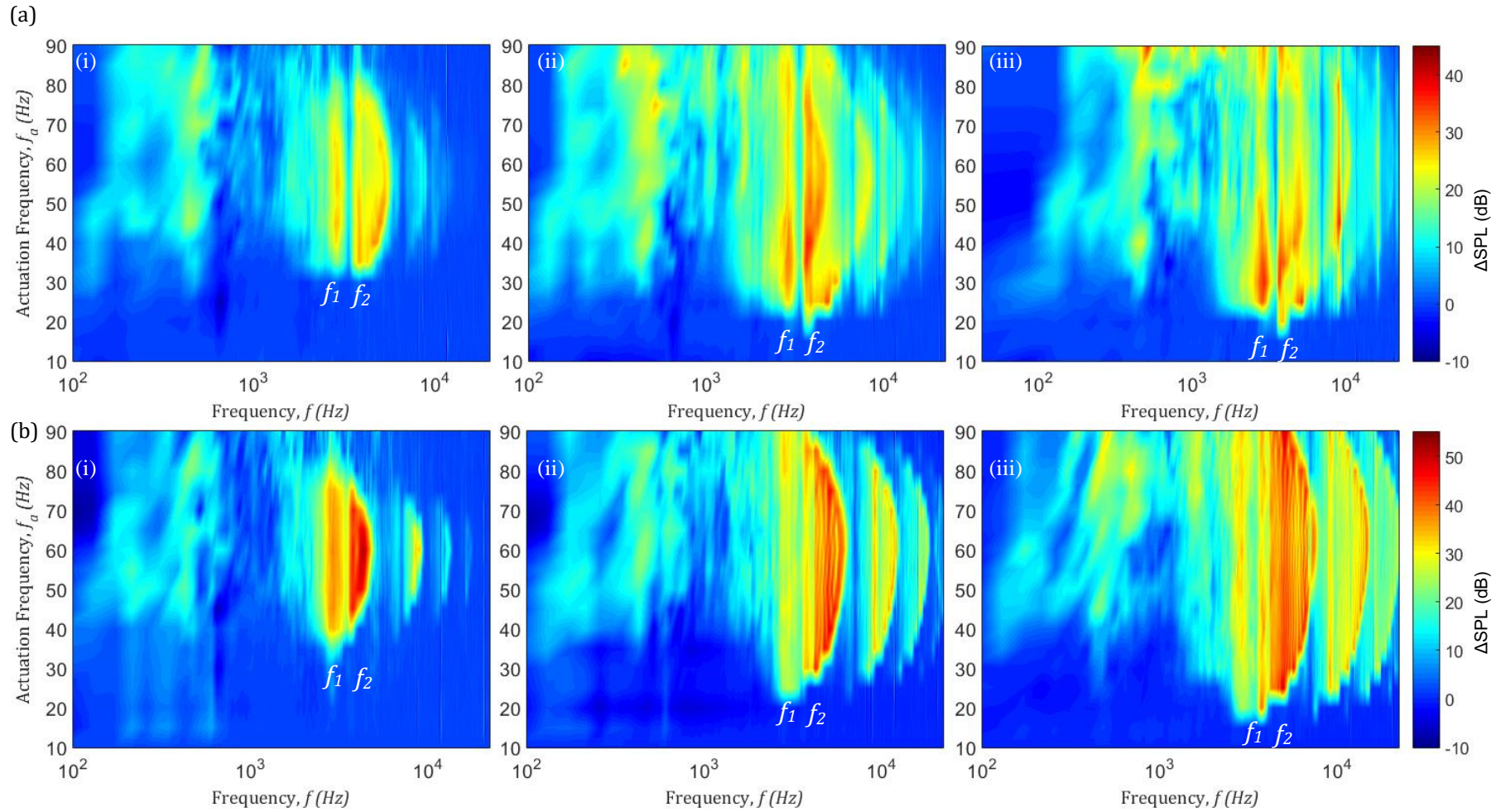


Figure 6.15. Acoustic response for (a) $h = 4.2$ mm and (b) $h = 2.5$ mm, where f_1 and f_2 mark the two dominant constant frequency lines in the spectra for $h = 4.2$ mm that are also present for $h = 2.5$ mm

6.2 SJA Self-Noise Reduction Using Lobed Orifices

6.2.1 Frequency response

The jet centreline velocities, taken at approximately $0.5d$, for lobed orifices (Figure 6.16) follow a very similar trend to that of the circular orifice. On closer inspection some discrepancies are noticeable, where the lobed jet responses are generally smoother than the circular jet. At lower actuation frequencies, the lobed jets have a higher velocity and after a certain actuation frequency the baseline case jet velocity is higher. These actuation frequencies where the circular jet velocity suddenly increases to higher values than for the lobed jets coincides with the same actuation frequencies that have earlier been shown to be the point of whistling onset (35 Hz for Figure 6.15a, 20 Hz for Figure 6.15b and 15 Hz for Figure 6.15c). However, the jet velocities are all within 10 per cent of the circular orifice output, where the peak centreline velocity of the 4-lobed jet reaches 94% of the circular jet for Case 1, 92% for Case 2 and 96% for Case 3.

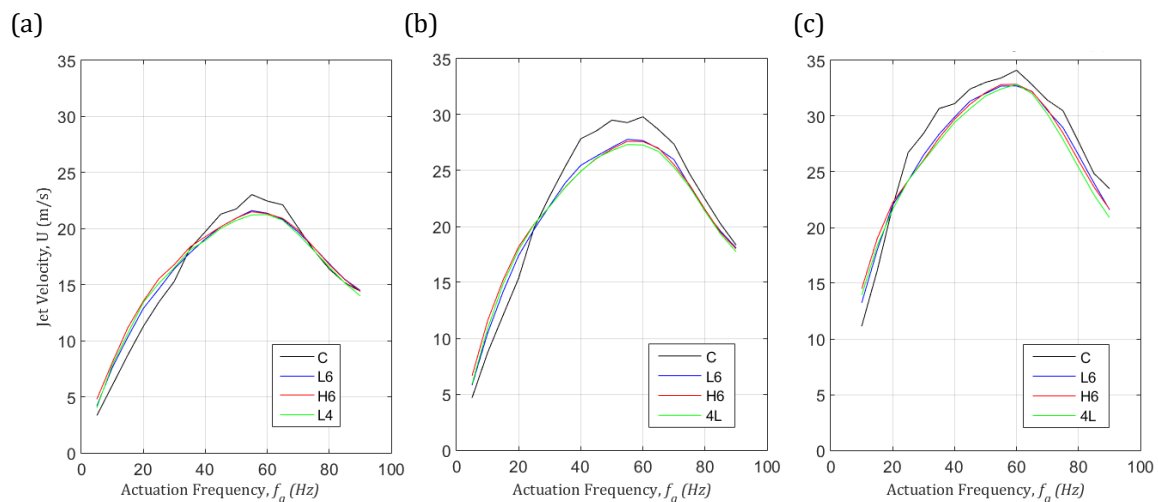


Figure 6.16. Electromagnetically actuated SJA frequency response as a function of orifice shape (a) Case 1, (b) Case 2 and (c) Case 3, where C = Circular, L6 = Low amplitude 6-lobed, H6 = High amplitude 6-lobed and 4L = 4-lobed orifice

6.2.2 Acoustic response

Since it has been established that the velocity response of the actuator using lobed orifices is close to that of a circular orifice near the orifice exit, the acoustic response can be analysed. Figure 6.17 shows the acoustic response using the different orifice cases at the actuation frequency of the onset of whistling for all cases (Case 1, 35 Hz; Case 2, 20 Hz; Case 3, 15 Hz). Here the spectra show Δ SPL, where:

$$\Delta\text{SPL} = \text{SPL Orifice Shape} - \text{SPL Diaphragm} \quad (30)$$

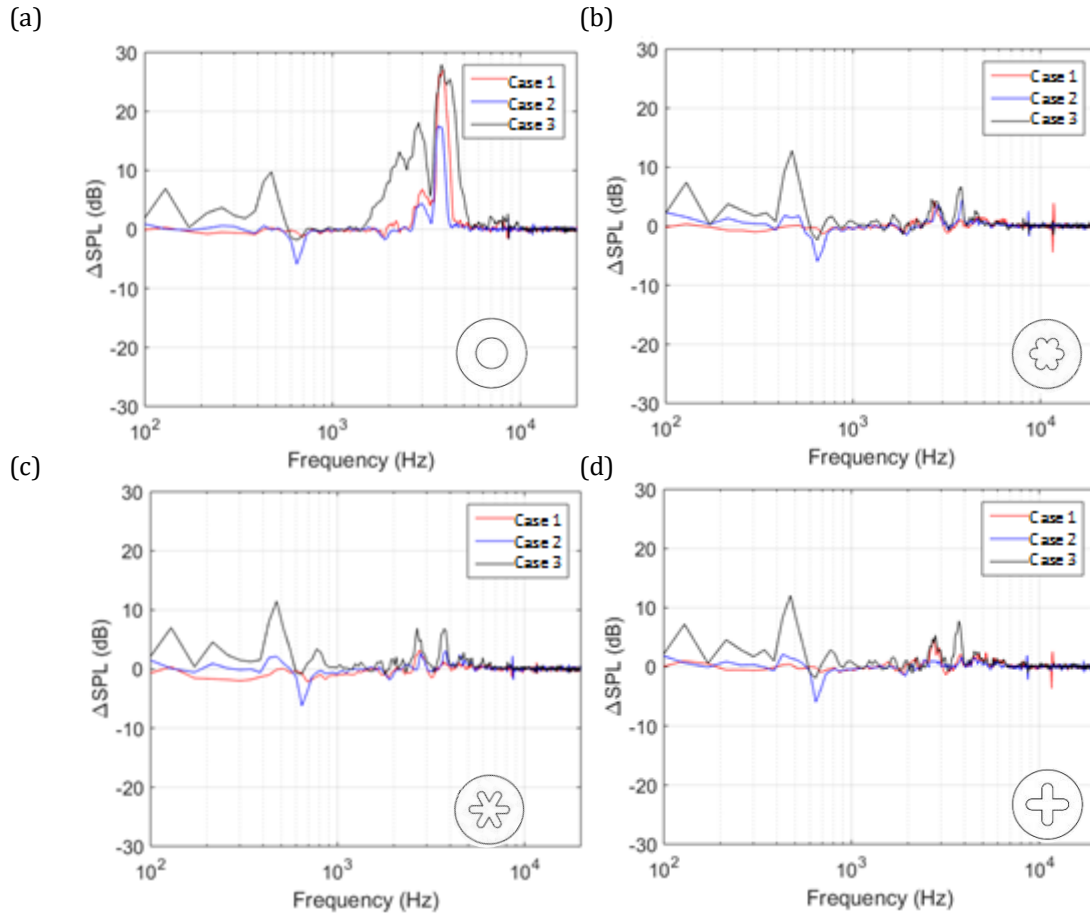


Figure 6.17. Acoustic spectra of SJA using (a) circular, (b) low amplitude 6-lobed, (c) high amplitude 6-lobed and (d) 4-lobed orifice at the onset of self-noise

The results shown in Figure 6.17a show the acoustic spectra at the onset of whistling noise from the circular orifice, which occurs at different actuation frequencies for each case. This, as shown earlier, is because the threshold Reynolds and Strouhal number requirements for self-noise are met at different actuation frequencies for each case. In an otherwise near zero acoustic response, the onset of noise first appears at the two dominant frequencies f_1 and f_2 with magnitudes of up to 18.12 dB and 27.84 dB respectively for Case 1 (Figure 6.17a). Of the two dominant frequencies, f_2 is larger in magnitude at the lower actuation frequencies. When the lobed orifices are used in Case 1 (red line) it can be seen that low frequency noise, below 1 kHz, appears regardless of orifice shape and the response is generally more broadband and higher than expected at the lower input voltage. This is because the actual

onset of noise appears between $f_a = 30 - 35$ Hz and a finer frequency sweep would be required to identify the actual actuation frequency of noise onset. The key difference in the spectra, however, is the noise amplitude, especially at the dominant frequencies, for the lobed orifices. These are significantly lower than for the circular orifice case and proves the effectiveness of lobed orifices at such low actuation frequencies. For example, the highest noise attenuation is seen at f_2 with a value of 26 dB between the circular and low amplitude 6-lobed orifice for Case 3 (Figure 6.17b). This does not, however, lead to the conclusion that the low amplitude 6-lobed orifice is the most effective orifice shape in reducing actuator self-noise as this depends on the overall noise reduction across the entire spectrum.

In most SJA applications the jet velocity is one of the most important performance characteristics, where a higher magnitude is desirable. For this reason, Figure 6.18 shows the acoustic response for $f_a = 60$ Hz, where as evidenced from the velocity response (Figure 6.16) the peak jet centreline velocity is achieved. Under these operating conditions the acoustic response for the circular orifice case is broadband in nature with the highest noise contribution from f_1 , f_2 and f_{st} . As the input voltage is increased, a noise increase is mostly noticeable for $f < 1$ kHz and at higher frequencies $f > 6.5$ kHz. When using lobed orifices there is a broadband noise reduction at all frequencies beyond $f > 1$ kHz. Comparing the noise reduction at the onset of whistling there was no clear indication as to which lobed orifice would be most suitable as they all had very similar noise reduction capabilities under the noise threshold conditions for the circular orifice. However, at higher actuation frequencies and consequently larger jet velocities, the orifices with higher lobe penetration (high amplitude 6-lobed and 4-lobed orifice (Figure 6.18c-d) are more effective at noise attenuation. The amount of Δ SPL reduction or gain for each orifice shape is quantified and compared to the circular orifice in Figure 6.23.

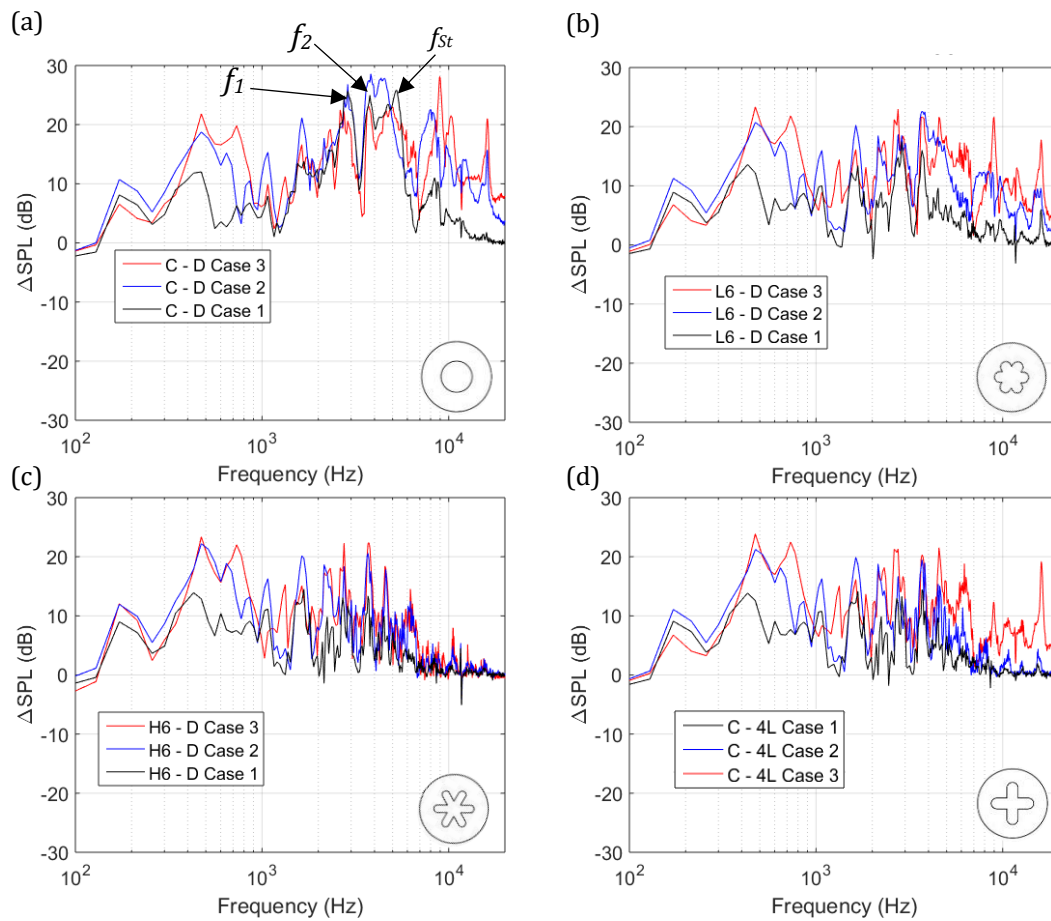


Figure 6.18. Acoustic spectra showing Δ SPL (dB) vs. Frequency (Hz) of SJA using (a) circular, (b) low amplitude 6-lobed, (c) high amplitude 6-lobed and (d) 4-lobed orifice at $f_a = 60$ Hz, where D is the diaphragm SPL

Low frequency noise reduction is achieved at lower input voltages (Case 1 & Case 2) and as V_{p-p} is increased the low frequency noise reduction decreases and instead high frequency noise reduction increases. It is evident from Figure 6.19b that the high amplitude 6-lobed orifice is most effective in SJA high frequency noise reduction ($f > 7$ kHz) at higher input voltage with a peak noise reduction of 28 dB at $f = 8980$ Hz for Case 3. From the above it can be said that lobe count and penetration are key to the noise reduction of SJA jet induced and generated noise, where a higher number of lobes and larger penetration into the jet causes larger noise reductions.

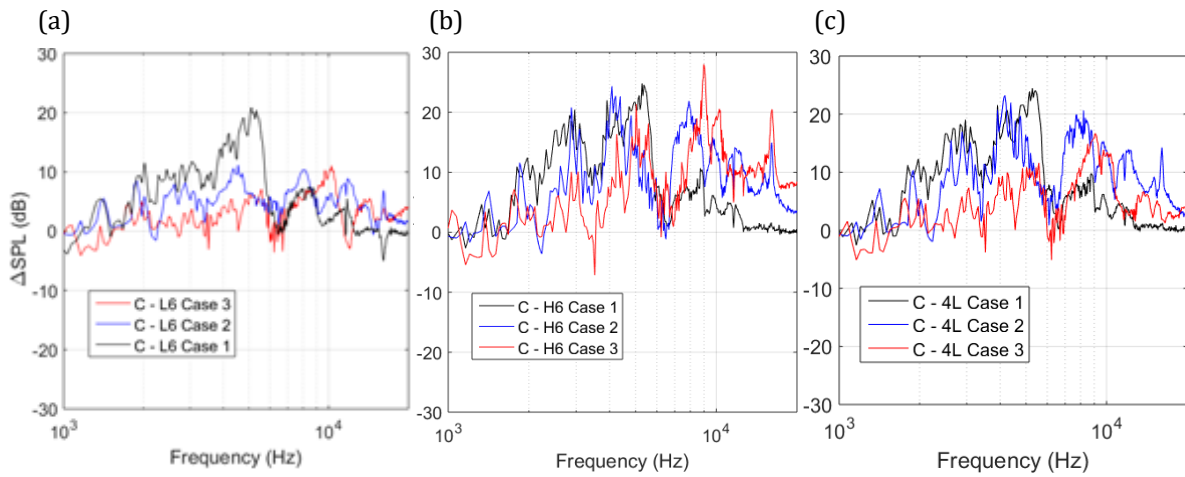


Figure 6.19. Noise change showing Δ SPL (dB) vs. Frequency (Hz) for the different orifice shapes at $f_a = 60$ Hz, (a) circular minus low amplitude 6-lobed (C-L6), (b) circular minus high amplitude 6-lobed (C-H6), (c) circular minus 4-lobed orifice (C-4L)

Figure 6.20 shows the percentage noise reduction for the different orifice shapes at the three dominant frequencies in the spectrum, f_1, f_2 and constant Strouhal number, f_{St} , at $f_a = 60$ Hz. The lobed orifices effectively attenuate broadband noise above 1 kHz with significant reduction at f_1 and f_2 , which are the dominant frequencies of the system. Another frequency with large SPL amplitude where an almost complete suppression of noise can be observed is in the constant Strouhal number region shaped like a bow in the spectrum. In all cases f_{St} is reduced the most, with a maximum reduction of 97% for Case 1 using both 6-lobed orifices.

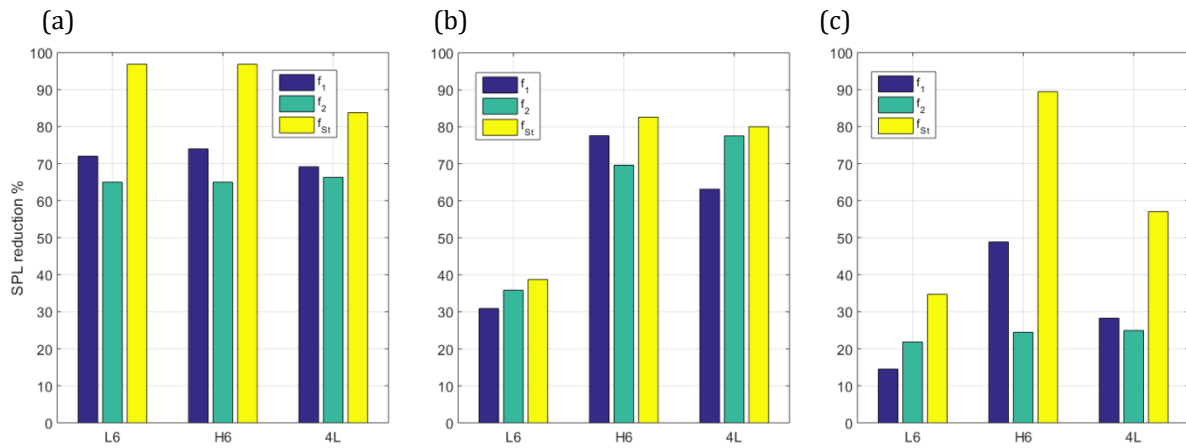


Figure 6.20. Percentage SPL reduction at the dominant frequencies. (a) Case 1, (b) Case 2 and (c) Case 3

6.2.3 Effect of non-dimensional jet flow parameters

For a circular synthetic jet, it was shown that there is a threshold jet Reynolds number, Re_j , above which conditions are established for self-noise generation. At the same time a jump in stroke length, L , is observed at the actuation frequency corresponding to the

onset of whistling. It was also shown from Schlieren visualisation that these characteristics are due to the transition of a laminar jet at the orifice exit to a turbulent one some distance downstream. Comparing Re_j of the lobed orifices to the circular orifice (Figure 6.21), similar trends are seen with the exception that the noise output is significantly reduced. In other words, using lobed orifices does not come with any performance losses in terms of Re_j at the orifice exit.

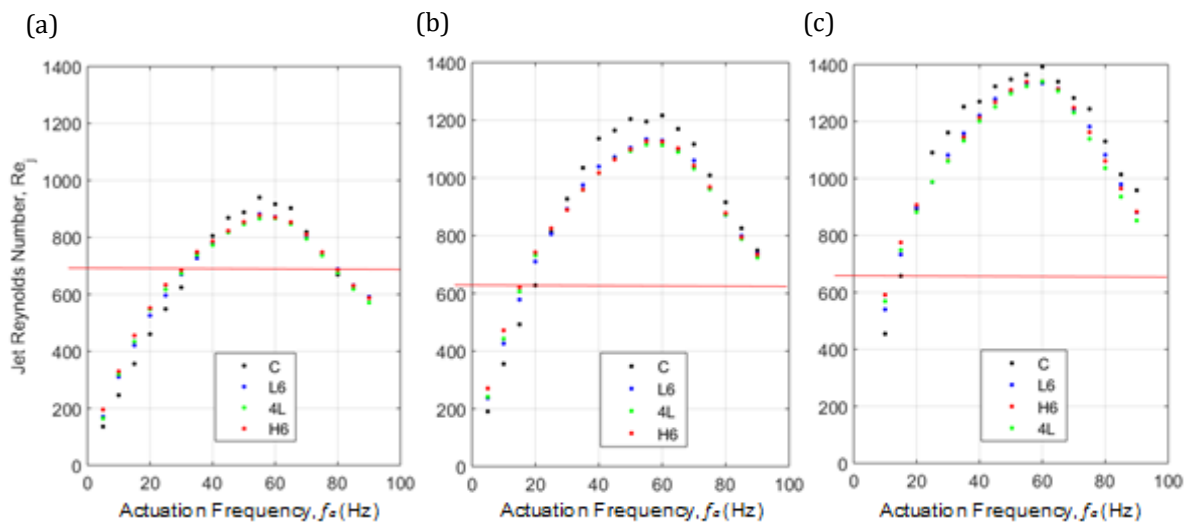


Figure 6.21. Jet Reynolds number frequency response as a function of orifice shape for (a) Case 1, (b) Case 2 and (c) Case 3

The non-dimensional stroke length, L , is shown in Figure 6.22 for the cases studied. A noticeable trend for the circular orifice was a sudden increase in L at the onset of the SJA periodic whistling. For Case 1 in Figure 6.22a this jump takes place at $f_a = 35$ Hz, the same actuation frequency where jet noise is first measured (Figure 6.17a). Also, L starts off higher when using lobed orifices which is due to the higher jet velocities at lower frequencies. Beyond the actuation frequency where self-noise first appears, the trend of the circular orifice closely follows that of the lobed orifices. The lobed orifices have higher centreline jet velocities at lower actuation frequencies, however once the feedback mechanism for the circular orifice begins, introducing self-noise, the exit velocities for the circular orifice increases slightly. The lobed orifice stroke lengths are very similar to each other and remain lower than that seen for the circular orifice before merging again at higher actuation frequencies (Figure 6.22).

The actuation frequency range for which the circular jet velocity is elevated, compared to lobed orifices (Figure 6.22), closely matches f_i (Figure 6.4a-c). Where there is a small

sudden increase in jet velocity, the Δ SPL also has a slight spike. For example, in Case 1 this is seen at $f_a = 45$ Hz, 55 Hz and 65 Hz (Figure 6.16a for velocity and Figure 6.4a for acoustic response). Comparing the change of the dimensionless stroke length with actuation frequency (Figure 6.22) reveals that the trends in stroke length, a function of jet velocity, is very similar for all lobed orifices. However, for the circular orifice the stroke length is higher than that of the lobed orifices for the same range of actuation frequencies at which f_1 exists in the acoustic spectra for all cases (Figure 6.23). An example of this can be seen in Case 3 (Figure 6.23c), where the Δ SPL for f_1 significantly decreases within a small range of actuation frequencies ($f_a = 50 - 70$ Hz, Figure 6.23c (ii)). For this range a corresponding decrease is also seen in the stroke length (Figure 6.23c (i)), nearly merging with the stroke length curves for the lobed orifices, yet still slightly higher (close-up in Figure 6.23c (i)). Once f_1 increases again the stroke length also increases slightly, detaching itself from the lobed orifice stroke length lines. This can be explained by the excitation of the cavity by the feedback mechanism, which amplifies the pressure fluctuations within the cavity resulting in increased jet velocity and acoustic output. This also explains the non-linear increase in jet velocity with linear increase of input voltage and diaphragm displacement seen in 6.1.2. Since there is a drop in cavity excitation for Case 3 for a range of actuation frequencies ($f_a = 50 - 70$ Hz), the resulting jet velocity also decreases.

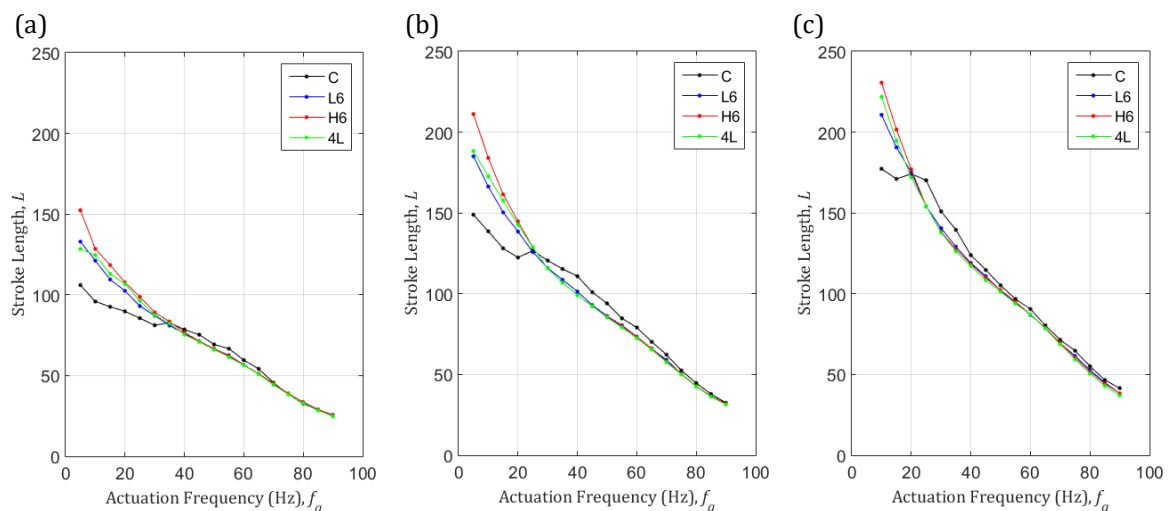


Figure 6.22. Dimensionless stroke length frequency response as a function of orifice shape for (a) Case 1, (b) Case 2 and (c) Case 3

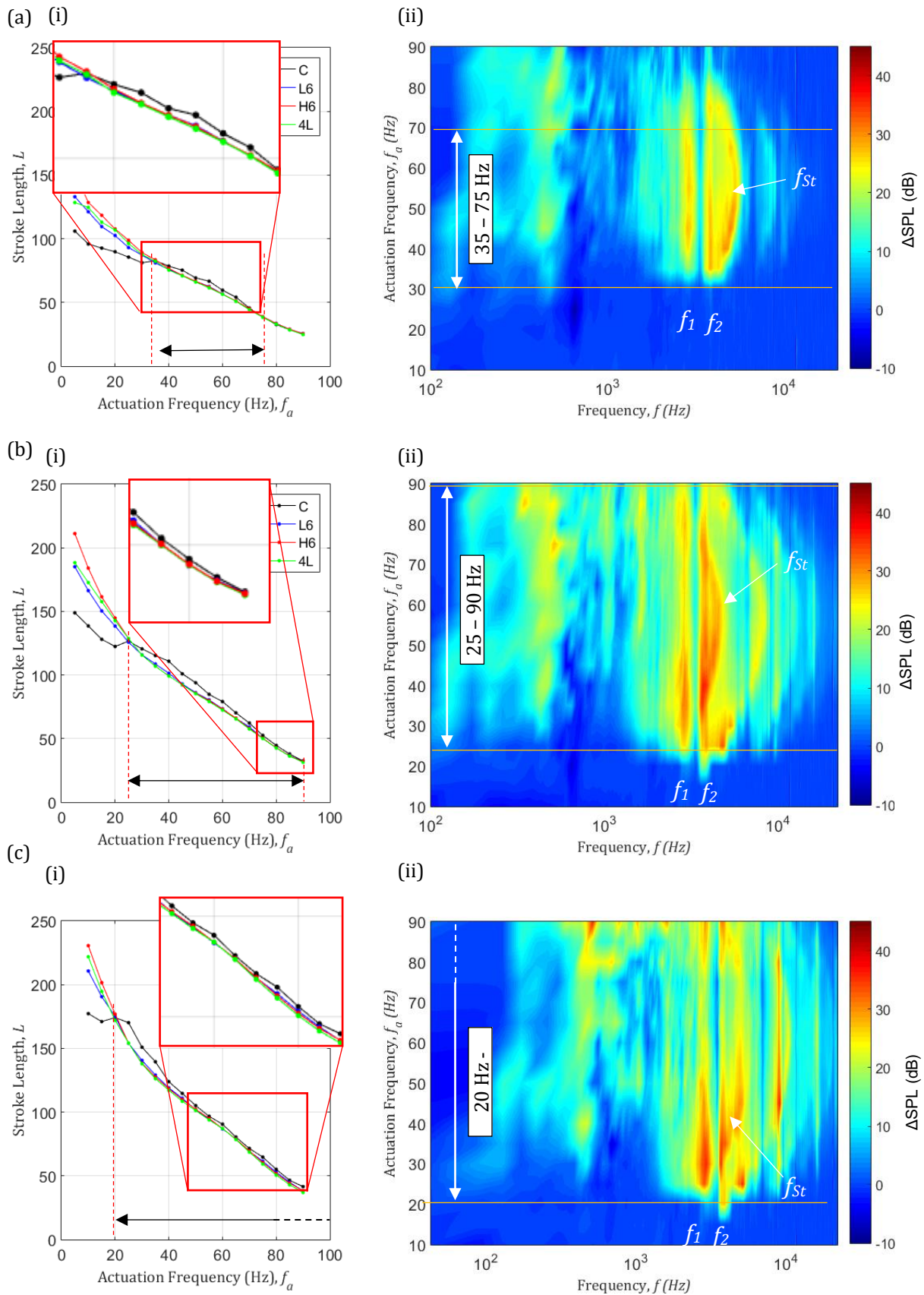


Figure 6.23. Comparison between dimensionless stroke length and circular orifice acoustic spectra for (a) Case 1, (b) Case 2, (c) Case 3

6.2.4 Flow structures of lobed and circular jets

Schlieren visualisation of circular jets in Figure 6.10 revealed valuable information regarding the flow development and provided evidence of the existence of a feedback noise mechanism, where a laminar jet breaks up causing flow instabilities to grow upstream. A fully turbulent jet is the result with self-sustained periodic fluctuations visible in the jet shear layer that are the cause for periodic whistling. Acoustic and flow data shows that the lobed orifices effectively attenuate the SJA self-noise under the same operating conditions near the orifice exit. Therefore, comparing the difference in flow characteristics of the jets emanating from different orifice shapes using Schlieren visualisation will help better understand the mechanism behind the noise reduction and how to optimise orifice geometries for this purpose.

Figure 6.24 and 25 show Schlieren images taken across the SJA actuation cycle using circular and lobed orifices, where the operating conditions are those of Case 2. In Figure 6.24 the visualisation is conducted at the actuation frequency for the onset of noise ($f_a = 25$ Hz) and in

Figure 6.25 the actuation frequency corresponds to the peak jet centreline velocity ($f_a = 60$ Hz). The flow behaviour of the circular jet was discussed earlier using Schlieren images (Figure 6.10) and will be compared here to the lobed jets behaviour through the SJA cycle. The jets emanating from lobed orifices begin laminar and break up some distance downstream. At $f_a = 25$ Hz, the low amplitude 6-lobed jet behaves very similar to the circular jet and breaks up at around $7d$ ($t = 0.17T$, Figure 6.24b). The breakup point does not move further downstream and instead remains at the same distance from the orifice exit. However, a key difference with the low amplitude 6-lobed jet is that it does not transition to turbulence near the exit and instead remains laminar until the breakup point. This means there is no feedback loop established that causes self-noise. The high amplitude 6-lobed jet breaks up much later at approximately $y=12d$ (Figure 6.24c) with the point of breakup pushed as far downstream as $y=19d$ at $t = 0.62T$. Similarly, the 4-lobed jet break up point (Figure 6.24d) is also further downstream (approximately $11d$ at $t = 0.22T$) and remains laminar from the exit throughout the cycle, thereby not allowing a feedback loop to exist.

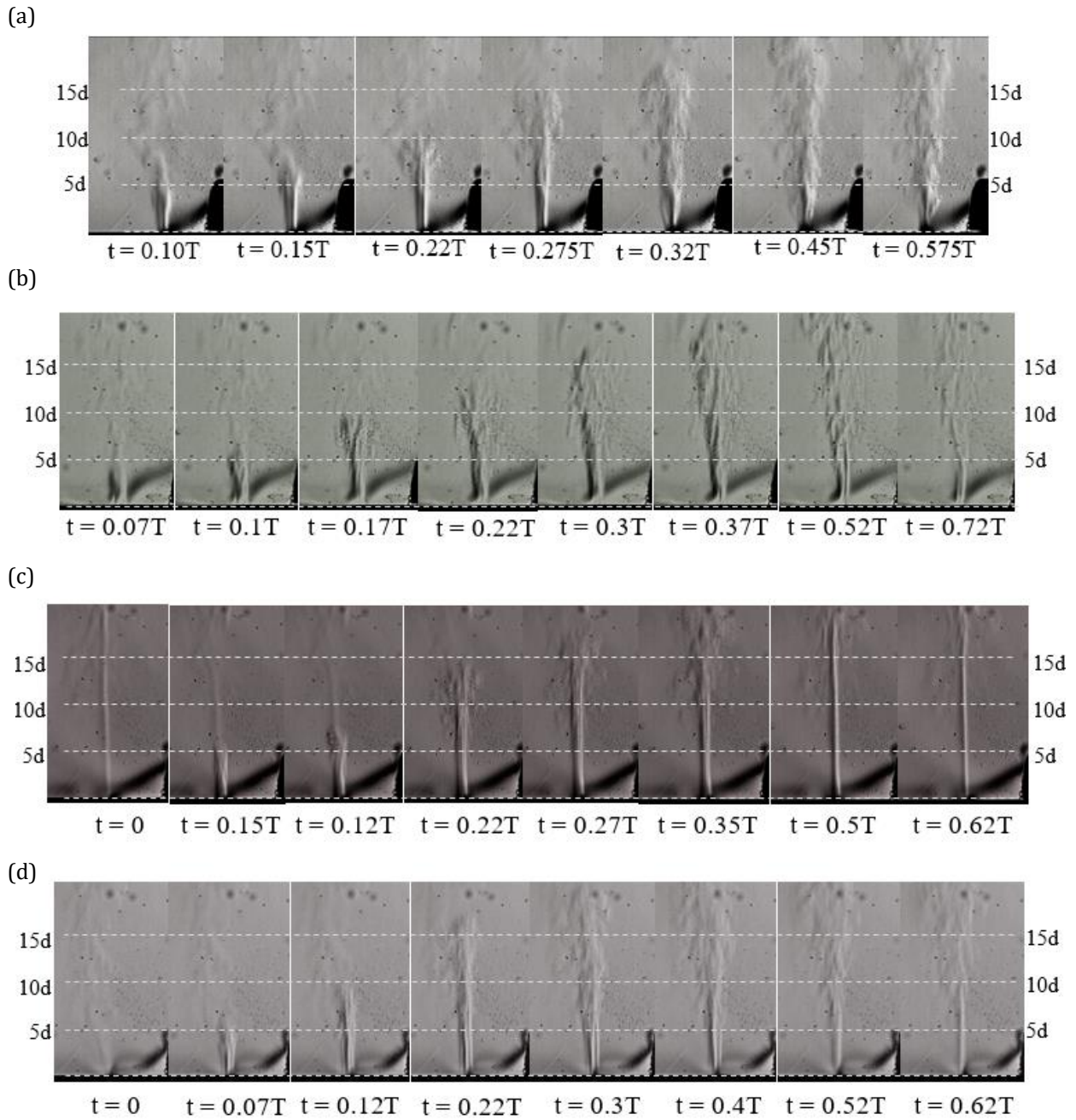


Figure 6.24. Schlieren visualisation at $f_a = 25$ Hz – (a) circular, (b) low amplitude 6-lobed, (c) high amplitude 6-lobed and (d) 4-lobed orifice at peak jet velocity for Case 2

At $f_a = 60$ Hz, it can be seen that for the circular orifice the jet is initially laminar, but undergoes transition to turbulence just shortly after exiting the orifice exit at $y=2d$ (Figure 6.25a). At the end of the blowing part of the cycle ($t = 0.33T$) small periodic structures are visible in the jet shear layer near the orifice exit that remain until the end of the actuation cycle. Similar flow characteristics can be seen with the low amplitude 6-

lobed orifice, where the jet column is thinner with small periodic flow structures in the jet shear layer near the orifice exit (Figure 6.25b). On the other hand, the high amplitude 6-lobed orifice results in a jet that breaks up downstream but remains laminar near the orifice exit throughout the actuation cycle (Figure 6.25c). This results in minimal excitation of the cavity and as a consequence, a lower self-noise output. This is again the case for the 4-lobed orifice (Figure 6.25d). A laminar jet evolves at the orifice exit that starts to develop jet instabilities, as seen on close inspection as small scale ordered structures in the jet shear layer near the orifice exit at $t = 0.27T$. However, the flow recovers quickly and becomes laminar again ($t = 0.4T$) once positive forcing is taken away and eventually breaks up at $5d$. The jet, however, remains laminar for the rest of cycle. It is clear from the results presented that the actuator self-noise and jet flow regime are linked and affect each other.

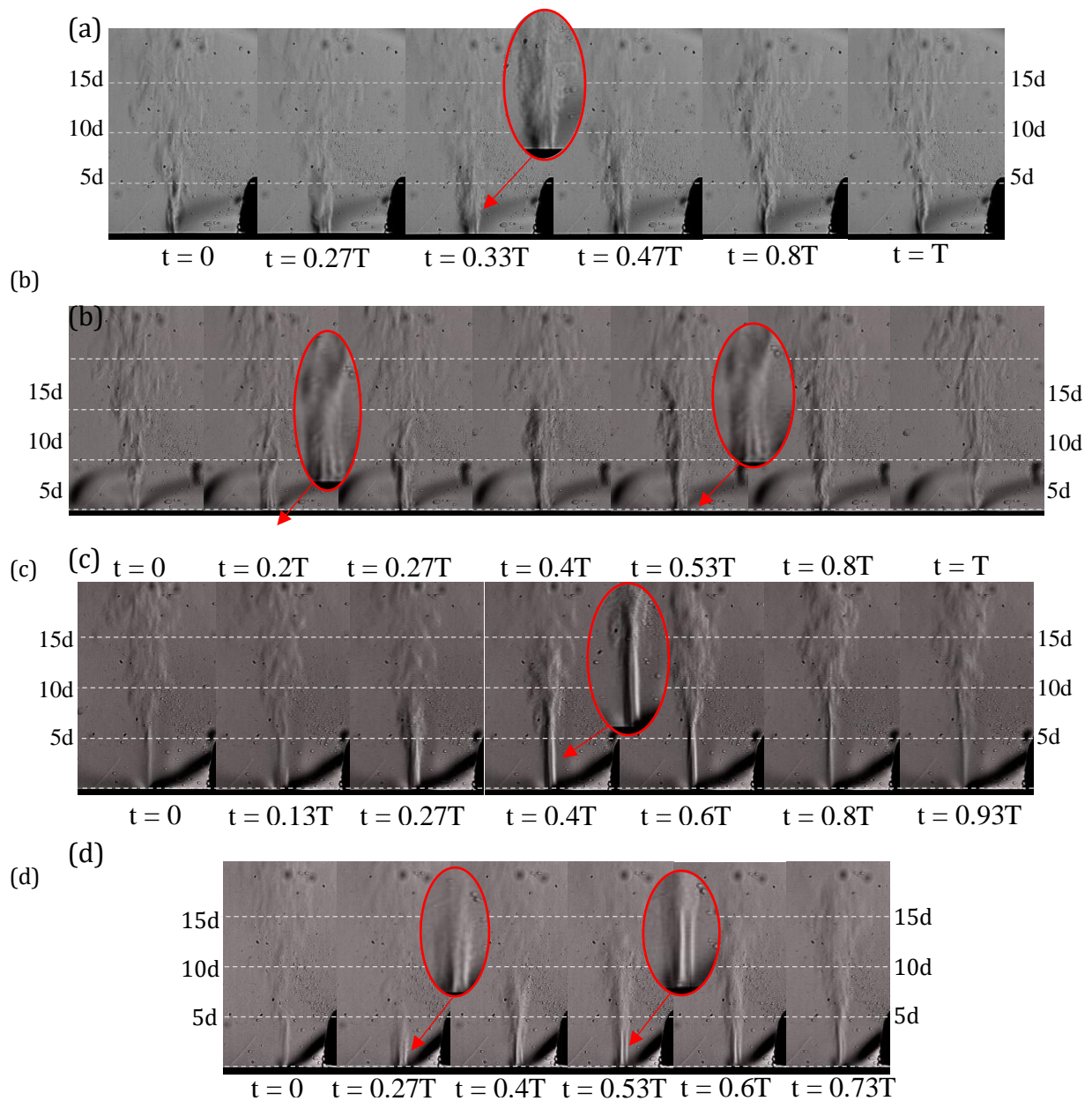


Figure 6.25. Schlieren visualisation at $f_a = 25$ Hz - (a) low amplitude 6-lobed, (b) high amplitude 6-lobed and (c) 4-lobed orifice at peak jet velocity for Case 2 with close ups

Since the high amplitude 6-lobed and 4-lobed orifice both have very similar penetration ratios and function in similar ways by delaying the breakup of the jet further

downstream, the lobe penetration plays a key role in jet induced noise reduction. However, the high amplitude 6-lobed orifice outperforms the 4-lobed orifice in SJA self-noise reduction in all cases indicating that the lobed count also plays a vital role in effective noise reduction. The periodic vortex shedding near the orifice exit is indicative of cavity excitation that in turn amplifies the vortex shedding making it visible in the flow visualisation. In the previous section it was suggested that f_1 is caused by the cavity excitation and when comparing the Schlieren images to the percentage noise reduction (Figure 6.20b) further support for this claim can be deduced. The reduction of f_1 is slightly higher when using the high amplitude 6-lobed orifice, which would be expected due to the very small instability that exists in the 4-lobed jet.

6.3 Summary

The acoustic characteristics of an electromagnetic-driven synthetic jet actuator (SJA) with circular orifice were investigated with the aim of characterising its aeroacoustic response. Acoustic and hot wire measurements were used to test the actuator under quiescent conditions. Electromagnetic actuation proved to be desirable over piezoelectric actuation for this work due to the reduced diaphragm noise contribution to the overall actuator self-noise, thus making it easier to identify jet related noise.

In circular synthetic jets it was shown that there is a relationship between the actuator self-noise and the jet flow regime with two types of noise-generating mechanisms present. This is supported by two distinct patterns present in the acoustic response: a constant frequency pattern and one varying with jet velocity. The constant frequency noise occurs at two dominant frequencies, f_1 and f_2 . Schlieren visualisation and hotwire measurements revealed that the jet was fully turbulent with closely spaced vortices shed near the orifice exit within a specific jet Reynolds number range of $600 < Re_j < 750$. The dominant frequencies mentioned have a constant frequency behaviour existing within a Strouhal number range of $0.22 < St < 0.50$, typical of a feedback mechanism often seen in pipe and orifice systems such as wind instruments, responsible for “Pfeiftone” or whistling. Due to the inherent periodic nature of synthetic jets, the whistling only occurs periodically. Schlieren visualisation shows that a laminar jet is synthesised by the actuator that breaks up some distance downstream. At the onset of noise, where the above-mentioned flow conditions are met, the jet breaks up causing the upstream flow

to become unstable and transition to turbulence. The instabilities in the flow near the orifice are able to excite the actuator cavity and amplify vortex shedding from the orifice, resulting in noise and periodic vortex shedding seen in the jet shear layer. The second mechanism shows a strong dependence on jet velocity or Reynolds number and displays a constant Strouhal number behaviour.

These results show the dependence of actuator self-noise on the actuator geometry. Reducing the orifice height only amplifies the noise without changing the fundamental or dominant frequencies in the acoustic response. Varying the cavity height, on the other hand, significantly alters the constant frequency patterns in the acoustic response. The constant Strouhal number pattern remains in a similar position for all cases as the Reynolds number response with changing actuation frequency does not change.

Lobed orifices were then used to reduce the actuator self-noise by altering the jet flow by dissipating the broken-up jets quicker and thereby reducing the effect of the feedback mechanism or interrupting it completely. This reduction of noise is possible due to the high mixing capabilities of the lobed jets and, as seen in the previous chapter, has the consequence of reduced jet velocity further downstream. Increased jet penetration was shown to be the biggest contributor to noise reduction, however this can be further optimised by increasing the lobed count. In this study the high amplitude 6-lobed orifice was the most effective orifice in broadband self-noise reduction.

7 Conclusions and recommendations

7.1 Conclusions

The work presented in this thesis is an effort towards reducing SJA self-noise in quiescent conditions, a problem that hinders the successful application of such devices where stringent noise requirements need to be met. In Chapter 1 the aim of this thesis was described as follows:

The aim of the research presented is to define the aeroacoustic characteristics of synthetic jet actuators in quiescent conditions and reduce the self-noise generated using active and passive noise control measures, while minimising adverse effects this might have on the fluidic performance of the device, namely peak exit jet velocity.

Both numerical and extensive experimental analysis were used to meet the research objectives originally set in Chapter 1. The experimental work includes hotwire anemometry, acoustic measurements in an anechoic chamber and different flow visualisation techniques conducted at Brunel University London. Mode shape determinations of the piezoelectric diaphragm used for some experiments were carried out at the University of Nottingham. With these tests, it was possible to establish a better understanding of SJA self-noise generation using different actuation methods and propose active and passive noise control measures for the successful noise attenuation of SJAs.

In terms of active noise control, a maximum overall SPL reduction of 14 dB was achieved due to two alternating synthetic jets generated from a double chamber SJA causing destructive interference between the resulting sound fields.

The fluidic performance comparison of a single chamber SJA using both circular and lobed orifices reveal that the velocity response remains largely unchanged regardless of orifice shape, as long as the cross-sectional area is constant. Peak centreline velocities vary, but this is due to the very different and complex jet development of lobed jets

compared to conventional circular ones. For a SJA, several noise sources exist including structure borne noise from the diaphragm and noise as a result of the jet. The experimental work presented here suggests two primary jet related noise sources. The first is directly caused by high turbulence in the jets, which becomes more apparent with increasing jet velocity. The second is induced by jet instabilities that match a cavity resonance frequency. As a consequence, these instabilities excite the cavity and amplify vortex shedding near the orifice that results in noise generation. This establishes a feedback loop that exists for a particular range of jet Reynolds number and Strouhal number, which are similar to those for hole tones. Lobed orifices have been shown to interrupt and reduce the effects noticed by this feedback mechanism with the highest noise reduction obtained with a high amplitude, 6-lobed orifice. The investigation on lobed orifices shows that a higher number of lobes is preferable for noise reduction, while a higher lobe penetration leads to increased jet velocity dissipation.

More details on the conclusions related to the thesis objectives first presented in Chapter 1 are presented below:

- ***To design a double chamber synthetic jet actuator that is driven by a single diaphragm and study the effect that the resulting, out-of-phase operation of each chamber has on the sound field produced (active noise control).***

Preliminary tests using an existing double chamber SJA helped understand and lay out a design specification for a new and improved prototype. These tests highlighted the importance of quality of components that make up the actuator, in terms of finish and accuracy to design specifications, to ensure accurate and repeatable tests. The importance of this was also shown when investigating the effect of diaphragm clamping conditions, which have an optimum value for maximum velocity output and diaphragm damping. At the same time, a low-cost approach was taken to minimise manufacturing costs associated with the SJA using a combination of precision CNC machining and stainless-steel additive manufacturing. A SJA displaces mass during its operation and can be treated as a monopole sound source, much like a loudspeaker. In full-scale flight conditions several actuators are expected to operate in close proximity to each other, where the sound field radiated from each orifice will interact with others. In the double

chamber SJA tested, two out-of-phase jets are generated that form a dipole sound source. Due to the inherent phase difference (180°) between the two jets, their sound fields interfere with each other destructively in certain regions, leading to partial noise suppression of up to 14 dB. The perceived sound level, therefore, depends on where the observer is in the sound field. When SJA arrays are to be implemented on aircraft wings their orientation will play a key role to minimise noise levels in the cabin. However, in the tests conducted complete attenuation was, however, not possible due to some asymmetries in the design of the actuator.

- ***To design a single chamber SJA with variable cavity height and orifice shapes (both circular and lobed orifices). The effect these geometric changes have on the SJA fluidic performance are to be studied. The focus is on the effect of orifice shape on synthetic jet flow structures formed, streamwise jet development and fluidic performance.***

A variable geometry, single chamber SJA was designed that is driven by a PZT diaphragm. It is shown that, as expected from literature, the highest performance is achieved using a configuration inspired by a velocity optimised design that also has the smallest cavity height ($H = 1.2 \text{ mm}$). Analysis of the diaphragm mode shapes using Digital Image Correlation (DIC) allows differentiation between diaphragm and Helmholtz resonance modes. It was shown that the mode shapes of higher order diaphragm resonance modes ($m > 1$) display an equal and opposite deflection for each positive deflection, that results in a net volume displacement of near zero. As a result, the jet velocity at higher diaphragm resonance modes is minimal unless there is coupling with the Helmholtz resonance frequency, at which point the peak jet velocities are observed. Therefore, to maximise the peak jet velocity there must be coupling between the mechanical and Helmholtz resonance frequency, as previously found by several studies.

High entrainment lobed orifices were designed to investigate their effect on SJA self-noise by manipulating the jet developing from the orifice. The lobed orifices

have the same effective diameter, $d_e = 2$ mm, which ensures the same cross-sectional area for all orifice shapes. The lobed orifice designs are defined by the lobe count and lobe penetration. In total three such orifices were investigated: low amplitude 6-lobed, high amplitude 6-lobed and 4-lobed orifice. The velocity profiles are more complex for lobed jets, with smaller velocity peaks appearing inside the lobes, caused by different shear layer growth rates in the minor and major axis. With increasing Stokes number, the exit velocity profiles of lobed jets become more uniform, closer to that of a circular jet, losing some of their distinct features visible at lower Stokes numbers. Furthermore, compared to a circular jet the jet velocity of lobed jets decreases at a faster rate with increasing streamwise distance from the orifice as the lobe penetration increases. Power Spectral Density (PSD) analysis shows that in lobed jets the breakup of large-scale flow structures occurs early on, passing energy down to smaller scales to form a turbulent jet characterised by a continuous spectrum. This observation was also confirmed using Schlieren visualisation, where large-scale structures break up into smaller ones much earlier in the jet development. Dye flow visualisation on a scaled up SJA presented similar behaviour where, with increasing lobe penetration, the vortex structures formed at the orifice break up faster. The most aggressive mixing and breakup was observed when using the 4-lobed orifice. Furthermore, evidence of the existence of streamwise vorticity between the lobes is made visible in the form of jet axis-switching. This phenomenon is also most visible for the higher penetration lobed orifices (high amplitude 6-lobed and 4-lobed orifice).

- ***To characterise the aeroacoustics of a velocity optimised single chamber synthetic jet actuator with circular orifice.***

Initial acoustic measurements of the piezoelectric driven SJA were carried out at two test conditions that vary in actuation frequency, where the first corresponds with the first mechanical resonance mode ($f_a = 325$ Hz) and the second is a coupled resonance mode between mechanical and Helmholtz resonance ($f_a = 1225$ Hz). Promising results were observed when using lobed orifices instead of a circular orifice at the first condition, with broadband noise reductions of up

to 12 dB at particular frequencies. However, mechanical noise from the diaphragm at the higher actuation frequency ($f_a = 1225$ Hz) is significantly higher making it difficult to identify various noise sources.

Electromagnetic actuation in the form of a Latex membrane diaphragm driven by a vibration generator was then used as it reduces the noise interference from the actuation transducer, thereby making it more desirable in terms of the above-mentioned noise contamination issues of PZT diaphragms. Most importantly, these tests helped establish a better understanding of and to identify SJA self-noise generation mechanism when using a circular orifice. This mechanism is characterised by a constant frequency behaviour visible in acoustic spectra for the chosen cavity height ($H = 1.2$ mm) for a specific jet Reynolds number range of $600 < Re_j < 750$ and Strouhal number range of $0.22 < St < 0.50$. Similar Strouhal number ranges were noticed by several other studies that investigate similar noise generation mechanism, such as in wind instruments or other pipe-cavity systems that lead to a whistling or so-called hole tone noise. With the aid of Schlieren visualisation and analysis of the PSD it was possible to identify a feedback mechanism. In this mechanism, instabilities in the flow near the orifice are able to excite the cavity-orifice system to resonate and amplify vortex shedding from the orifice, resulting in noise and periodic vortex shedding seen in the jet shear layer at the previously defined Reynolds and Strouhal number conditions.

Furthermore, a second mechanism identified is characterised by a constant Strouhal number behaviour, that is, however, independent of the actuator geometry. Therefore, this mechanism is not caused by a feedback mechanism but rather by the jet itself. This phenomenon exists for a specific range of actuation frequencies, but further data is required to determine characteristic operating parameters that cause this.

Changes in geometry were also found to impact the SJA acoustic frequency response, where for a reduction in orifice height the frequency response remains the same, but there is an increase of SPL at the fundamental acoustic frequencies.

For changes in cavity height, while maintaining very similar velocity responses, the acoustic response changes greatly with a shift in the fundamental frequencies. The constant Strouhal number behaviour, however, is almost unchanged. Therefore, it is evident that the acoustic characteristics of a SJA, with very similar velocity response, is highly dependent on the cavity geometry.

- ***To study the effect lobed orifices have on the self-noise generated by a single chamber synthetic jet actuator by comparing the acoustic and jet flow characteristics to that of a circular orifice to better understand the mechanism behind the noise generation/suppression.***

Lobed orifices were used to investigate their effectiveness on the SJA self-noise suppression, which work by (altering the jet flow through faster dissipation of flow structures. It was shown that the enhanced mixing and entrainment induced by the lobed jets disrupts or completely interrupts the feedback mechanism that is responsible for the excitation of the SJA cavity and the resulting noise. The most effective orifice for disrupting this feedback mechanism was the high amplitude 6-lobed orifice, giving noise reductions of up to 24 dB at one of the fundamental acoustic frequencies of the SJA ($H = 1.2$ mm).

7.2 Recommendations for Future Work

Both noise reduction methods explored in this research proved effective and can be combined in future designs of SJAs. For the use of sweeping jet actuator arrays as seen on NASA's ecoDemonstator, where the noise generation of actuators was a limiting factor, the out-of-phase operation of closely spaced actuators provides a viable solution. As highlighted in Chapter 3, careful design considerations have to be made in terms of orifice spacing and cavity geometry to maximise the velocity output and noise reduction. Further noise reduction could be achieved by using lobed orifices in the actuators making up an array. However, the work contained within this thesis focuses on SJA operation in quiescent conditions only and hence the next step of this research should be the study of lobed synthetic jets in crossflow conditions. In particular, the behaviour and evolution of jet and flow structures emanating from lobed orifices under such conditions has not been investigated. It has been shown that an increase in

entrainment and mixing is present in such jets in quiescent conditions, but their effectiveness in a boundary layer separation control needs further investigation. It is expected that these qualities of lobed jets can enhance mixing near the wall region and improve flow control effectiveness.

The double chamber SJA is a right step towards improving the efficiency of SJAs, since they rely on a single diaphragm to generate two jets, unlike a single chamber SJA. Further developments towards improvement of transduction efficiency in terms of power consumption is needed to make these devices more attractive for commercial applications.

Piezoelectric actuation allows dramatic reduction of the SJA overall size, but at the same time it was shown that they are the main noise contributor in the tests presented here. More research along with the development of high efficiency transduction systems is required that also take into account the need for noise reduction of such disc benders.

Another consideration to make these devices viable for aerospace applications is to scale them down to suit full flight conditions, which requires smaller orifice diameters. The SJA overall dimensions need miniaturisation to be implemented on aircraft, which presents a manufacturing challenge. Other methods such as micromachining or wire erosion already exist but may not be cost-effective. This can be overcome by further improvements in the already fast growing additive manufacturing field, used in this work.

References

- Ackeret, J., Betz, A., & Schrenk, O. (1925). *Versuche an einem Flugel mit Grenzschichtabsaugung (Experiments with an Airfoil from which the Boundary Layer Is Removed by Suction)*. Goettingen, Germany: Vorlaufige Mitteilungen der Aerodynamischen Versuchsanstalt zu Goettingen.
- Ahuja, K. K. (2003). Designing clean jet-noise facilities and making accurate jet-noise measurements. *International Journal of Aeroacoustics*.
- Alkislar, M. B., Krothapalli, A., & Butler, G. (2007). The effect of streamwise vortices on the aeroacoustics of a Mach 0.9 jet. *578*.
- Alkislar, M. B., Krothapalli, A., & Butler, G. W. (2007). The effect of streamwise vortices on the aeroacoustics of a Mach 0.9 jet. *Journal of Fluid Mechanics*, *578*, 139-169. doi:10.1017/S0022112007005022
- Amitay, M., & Cannelle, F. (2006). Evolution of finite span synthetic jets. *Physics of Fluids*, *18*(5).
- Anderson, A. B. (1955). Structure and velocity of the periodic vortex-ring flow pattern of a primary Pfeifenton (Pipe Tone) Jet. *The Journal of the Acoustical Society of America*, *27*(6), 1048-1053.
- Arik, M. (2007). An investigation into feasibility of impingement heat transfer and acoustic abatement of meso scale synthetic jets. *Applied Thermal Engineering*, *27*, 1483-1494.
- Arthurs, D., & Ziada, S. (2009). Flow-excited acoustic resonances of coaxial side-branches in an annular duct. *Journal of Fluids and Structures*, *25*(1), 42 - 59.
- Auerbach, D. (1987). Experiments on the trajectory and circulation of the starting vortex. *Journal of Fluid Mechanics*, *183*, 185-198.
- Barnstorff, K. (2015, April 2). *NASA Tests Green Aviation Technology on Boeing ecoDemonstrator*. Retrieved from NASA: <https://www.nasa.gov/aero/nasa-tests-green-aviation-technology-on-boeing-ecodemonstrator.html>
- Bechert, D., & Bartenwerfer, M. (1989). Experiments on Drag-Reducing Surfaces and Their Optimization with an Adjustable Geometry. *Journal of Fluid Mechanics*, *206*, 105-129.
- Belovich, V. M., & Samimy, M. (1997). Mixing Processes in a Coaxial Geometry with a Central Lobed Mixer-Nozzle. *AIAA Journal*, *35*(5), 838-841.
- Benton, S. I., Bernardini, C., Bons, J. P., & Sondergaard, R. (2014). Parametric optimization of unsteady end wall blowing on a highly loaded low-pressure turbine. *Journal of Turbomachinery*, *136*(7).
- Benton, S. I., Bons, J. P., & Sondergaard, R. (2013). Secondary Flow Loss Reduction Through Blowing for a High-Lift Front-Loaded Low Pressure Turbine Cascade. *Journal of Turbomachinery*, *135*(2).

- Betz, A. (1961). Boundary Layer and Flow Control. In *History of Boundary Layer Control in German* (pp. 1-20). New York: Pergamon Press.
- Bhapkar, U. S., Srivastava, A., & Agrawal, A. (2013). Acoustic and heat transfer characteristics of an inclined impinging synthetic jet generated by acoustic actuator. *International Journal of Thermal Sciences*, 74, 145-155.
- Bhapkar, U. S., Srivastava, A., & Agrawal, A. (2014). Acoustic and heat transfer characteristics of an impinging elliptical synthetic jet generated by acoustic actuator. *International Journal of Heat and Mass Transfer*, 79, 12-23.
- Bieler, H., Abbas, A., Chiaramonte, J.-Y., & Sawyers, D. (2006). Flow Control for Aircraft Performance Enhancements -Overview of Airbus - University Cooperation -. *3rd AIAA Flow Control Conference, AIAA*. San Francisco.
- Blevins, R. D. (1979). *Formulas for natural frequency and mode shape*. New York: Von Nostrand Reinhold Company.
- Blondeaux, P., & De Bernardinis, B. (1983). On the formation of vortex pairs near orifices. *Journal of Fluid Mechanics*, 135, 111-122.
- Boeing. (2015). *Our cleaner and quieter Family of new airplanes*. Boeing Commercial Airplanes.
- Bridges, J., & Brown, C. (2004). Parametric Testing of Chevrons on Single Flow Hot Jets. *10th AIAA/CEAS Aeroacoustics Conference*. Manchester, UK.
- Bridges, J., Wernet, M. P., & Brown, C. A. (2003). *Control of jet noise through mixing enhancement*. NASA TM 2003-212335.
- Calarese, W., Crisler, W., & Gustafson, G. L. (1985). Afterbody drag reduction by vortex generators. *23rd Aerospace Sciences Meeting, AIAA*. Reno.
- Cater, J. E., & Soria, J. (2002). The evolution of round zero-net-mass-flux jets. *Journal of Fluid Mechanics*, 472, 167-200.
- Cattafesta, L., & Sheplak, M. (2008). Actuators and Sensors. In *Fundamentals and Applications of Modern Flow Control* (pp. 149-176). AIAA.
- Chaudhari, M., Puranik, B., & Agrawal, A. (2010). Heat transfer characteristics of synthetic jet impingement cooling. *International Journal of Heat and Mass Transfer*, 53, 1057-1069.
- Chaudhari, M., Verma, G., Puranik, B., & Agrawal, A. (2008). Frequency response of a synthetic jet cavity. *Experimental Thermal Fluid Science*, 33, 439 - 448 .
- Chen, J., Lu, W., Huang, G., Zhu, J., & Wang, J. (2017). Research on Pulsed Jet Flow Control without External Energy in a Blade Cascade. *Energies*, 10(12).
- Chen, N., & Yu, H. (2014). Mechanism of axis switching in low aspect-ratio rectangular jets. *Computers and Mathematics with Applications*, 67, 437-444.
- Chong, T. P., & Dubois, E. (2016). Optimization of the poro-serrated trailing edges for airfoil broadband noise reduction. *The Journal of the Acoustical Society of America*, 140(2).

- Clifford, C., Singhal, A., & Samimy, M. (2016). Flow Control over an Airfoil in Fully Reversed Condition Using Plasma Actuators. *AIAA Journal*, 54(1).
- Coe, D. J., Allen, M. G., Rinehart, C. S., & Glezer, A. (2006). Pneumatically actuated micromachined synthetic jet modulators. *Sensors and Actuators A*, 132, 689-700.
- Coiffet, F. (2006). *E' tude stochastique tridimensionnelle de la dualite' des pressions en champ proche des jets axisym'etriques turbulents `a haut nombre de Reynolds*, PhD thesis. France: Universit'e de Poitiers.
- Comission, E. (2001). *European Aeronautics: A Vision for 2020*. Luxembourg: Office for Official Publications of the European Communities.
- Commission, E. (2011). *Flight path 2050: Europe's Vision for Aviation*. Luxembourg: Publications Office of the European Union.
- Conibear, J. (2016). *Simulation of Synthetic Jets utilising Noise-reducing Corrugated Orifices*. BEng Dissertation, Brunel University London.
- Cornish, J. J. (1953). *Prevention of turbulent separation by suction through a perforated surface*. Aerophysics Department, Mississippi State College.
- Crispo, C. M., Greco, C. S., Avallone, F., & Cardone, G. (2015). Stereo-PIV Measurements on Circular and Chevron Synthetic Jets. *11th International Symposium on Particle Image Velocimetry*. Santa Barbara, CA.
- Crittenden, T. M., & Raghu, S. (2009). Combustion Powered Actuator with Integrated High Frequency Oscillator. *International Journal of Flow Control*, 1, 87-97.
- Crittenden, T. M., Glezer, A., Funk, R., & Parekh, D. (2001). Combustion-Driven Jet Actuators for Flow. *15th AIAA Computational Fluid Dynamics Conference, AIAA*. Anaheim, CA.
- Crook, A. (2002). *The control of turbulent flows using synthetic jets*. ; PhD thesis, University of Manchester, UK.
- Crowther, W. J., & Gomes, L. T. (2008). An evaluation of the mass and power scaling of synthetic jet actuator flow control technology for civil transport aircraft applications. *IMEchE*, 222.
- (2017). *Current Market Outlook: 2017-2036*. Boeing.
- Dauphinee, T. M. (1957). Acoustic Air Pump. *American Institute of Physics*, 28(6), 452.
- De Giotgi, M., De Luca, C., Ficarella, A., & Marra, F. (2015). Comparison between synthetic jets and continuous jets for active flow control: Application on a NACA 0015 and a compressor stator cascade. *Aerospace Science and Technology*, 43, 256-280.
- De Griorgi, M. G., Ficarella, A., Marra, F., & Pescini, E. (2017). Micro DBD plasma actuators for flow separation control on a low pressure turbine at high altitude flight operating conditions of aircraft engines. *Applied Thermal Engineering*, 114, 511-522.
- De Luca, L., Girfoglio, M., & Coppola, G. (2014). Modeling and Experimental Validation of the Frequency Response of Synthetic Jet Actuators. *AIAA Journal*, 52(8), 1733 - 1748.

- Devenport, W., & Glegg, S. (2008). Aeroacoustics of Flow Control. In *Applications of Modern Flow Control, Progress in Astronautics and Aeronautics* (pp. 353-372). AIAA.
- Didden, N. (1979). On the formation of vortex rings: rolling-up and production of circulation. *Zeitschrift für angewandte Mathematik und Physik ZAMP*, 30(1), 101-116.
- Eckerle, W. A., Sheibani, H., & Awad, J. (1992). Experimental measurement of the vortex development downstream of a lobed forced mixer. *Journal of Engineering for Gas Turbines and Power*, 114(1), 63-71.
- El Hassan, M., & Meslem, A. (2010). Time-resolved stereoscopic particle image velocimetry investigation of entrainment in the near field of circular and daisy-shaped orifice jets. *Physics of Fluids*, 22(3).
- Estruch-Samper, D., Vanstone, L., Hillier, R., & Ganapathisubramani, B. (2015). Micro vortex generator control of axisymmetric high-speed laminar boundary layer separation. *Shock Waves*, 25, 521-533.
- Fischer, D. F., Cobleigh, B. R., Banks, D. W., Hall, R. M., & Wahls, R. A. (1998). Reynolds Number Effects at High Angles of Attack. *20th AIAA Advanced Measurement and Ground Testing Technology Conference, AIAA*. Albuquerque, NM.
- Fugal, S., Smith, B., & Spall, R. (2005). Displacement amplitude scaling of a twodimensional. *Physics of Fluids*, 17(4), 045103.
- Gallas, Q. (2005). *On the modeling and design of zero-net mass flux actuators, Ph.D. Thesis*. University of Florida.
- Gallas, Q., Holman, R., Raju, R., Mittal, R., Sheplak, M., & Cattafesta, L. (2004). Low Dimensional Modeling of Zero-Net Mass-Flux Actuators. *2nd AIAA Flow Control Conference, AIAA*. Portland, OR.
- Gallas, Q., Mathew, J., Kasyap, A., Holman, R., Nishida, T., Carroll, B., . . . Cattafesta, L. (2003). Lumped element modeling of piezoelectric-driven Synthetic Jet Actuators. *AIAA Journal*, 41(2), 240-247.
- Garnier, E. (2015). Flow Control by Pulsed Jet in a Curved S-Duct: A Spectral Analysis. *AIAA Journal*, 53(10), 2813-2827.
- Gibertini, G., Boniface, J. C., Zanotti, A., Droandi, G., Auteri, F., & Gaveriaux, R. (2015). Helicopter drag reduction by vortex generators. *Aerospace Science and Technology*, 47, 324-339.
- Gil, P., & Strzelczyk, P. (2016). Performance and efficiency of loudspeaker driven synthetic jet actuator. *Experimental Thermal and Fluid Science*, 76, 163 -174.
- Glezer, A. (1988). The formation of vortex rings. *Physics of Fluids*, 31(9).
- Glezer, A. (2011). Some aspects of aerodynamic flow control using synthetic-jet actuation . *Philosophical Transactions: Mathematical, Physical and Engineering Sciences*, 369, 1476-1494.

- Glezer, A., & Amitay, M. (2002). Synthetic Jets. *Annual Review of Fluid Mechanics*, 34:503-29.
- Godard, G., & Stanislas, M. (2006). Control of a decelerating boundary layer. Part 1: Optimization of passive vortex generators. *Aerospace Science and Technology*, 10, 181-191.
- Gomes, L. D. (2010). *On the modelling of anisotropic piezoelectric diaphragms for the development of high subsonic synthetic jet actuators*. Manchester, UK: PhD Thesis, University of Manchester.
- Gomes, L., Crowther, W., & Wood, N. (2006). Towards a practical piezoceramic diaphragm based synthetic jet actuator for high subsonic applications - effect of chamber and orifice depth on actuator peak velocity. *3rd AIAA Flow Control Conference*. San Francisco, California: AIAA Flow Control Conference.
- Gomes, L., Crowther, W., & Wood, N. (2006). Towards a practical piezoceramic diaphragm based synthetic jet actuator for high subsonic applications – effect of chamber and orifice depth on actuator peak velocity. *3rd AIAA Flow Control Conference, AIAA*. San Francisco.
- Graham, W. R., Hall, C. A., & Vera Morales, M. (2014). The potential of future aircraft technology for noise and pollutant emissions reduction. *Transport Policy*, 34, 36-51.
- Greco, S. C., Ianiro, A., Astarita, T., & Cardone, G. (2013). On the near field of single and twin circular synthetic air jets. *International Journal of Heat and Fluid Flow*, 44, 41-52.
- Greenblatt, D., & Wygnanski, I. J. (2000). The control of flow separation by periodic excitation. *Progress in Aerospace Sciences*, 36, 487-545.
- Greenblatt, D., & Wygnanski, I. J. (2008). Physical Concepts Underlying the Development and Application of Active Flow Control. In *Fundamentals and Applications of Modern Flow Control* (pp. 21-57). AIAA.
- Greiser, E. (2006). *Risikofaktor nächtlicher Fluglärm - macht Fluglärm krank?* Umweltbundesamt.
- (2017). *Growing Horizons*. Airbus.
- Guoqing, Z., Qijun, Z., Yunsong, G., & Xi, C. (2016). Experimental investigations for parametric effects of dual synthetic jets on delaying stall of a thick airfoil. *Chinese Journal of Aeronautics*, 29(2), 346-357.
- Gutmark, E., & Grinstein, F. (1999). Flow control with noncircular jets. *Annual Review of Fluid Mechanics*, 31, 239-272.
- Henrywood, R., & Agarwal, A. (2013). The aeroacoustics of a steam kettle. *Physics of Fluids*, 25(10).
- Holman, R., Utturkar, Y., Mittal, R., Smith, B., & Cattafesta, L. (2005). Formation criterion for synthetic jets. *AIAA Journal*, 43(10), 2110-2116.
- Howe, M. S. (1998). *Acoustics of Fluid–Structure Interactions*. Cambridge University Press.
- Howe, M. S. (2003). *Theory of Vortex Sound*. Cambridge University Press.

- Howe, M. S. (2008). Rayleigh Lecture 2007: flow–surface interaction noise. *Journal of Sound and Vibration*, 314, 113-146.
- Hu, H., Saga, T., Kobayashi, T., & Taniguchi, N. (2001). A study on a lobed jet mixing flow by using stereoscopic particle image velocimetry technique. *Physics of Fluids*, 13(11).
- Hu, H., Saga, T., Kobayashi, T., & Taniguchi, N. (2000). Research on the vortical and turbulent structures in the lobed jet flow using laser induced fluorescence and particle image velocimetry techniques. *Meas. Sci. Technol.*, 11(6), 698-711.
- Husain, H. S., & Hussain, A. (1999). The elliptic whistler jet. *Journal of Fluid Mechanics*, 397, 23-44.
- IATA. (2016, October 18). *IATA Forecasts Passenger Demand to Double Over 20 Years*. Retrieved from IATA: <http://www.iata.org/pressroom/pr/Pages/2016-10-18-02.aspx>
- ICAO. (2013). Night Flight Restrictions. *Worldwide Air Transport Conference (ATCONF) 6th Meeting*. Montreal.
- Ingard, U., & Labate, S. (1950). Acoustic Circulation Effects and the Nonlinear Impedance of Orifices. *The Journal of the Acoustical Society of America*, 22(2), 211.
- Jabbal, M., & Jeyalingam, J. (2017). Towards the noise reduction of piezoelectrical-driven synthetic jet actuator. *Sensors and Actuators A: Physical*, 266, 273-284.
- Jabbal, M., & Kykkotis, S. (2014). Towards the Noise Reduction of Piezoelectrical-Driven Synthetic Jet Actuators. *32nd AIAA Applied Aerodynamics Conference*. Atlanta, GA: AIAA.
- Jabbal, M., & Zhong, S. (2010). Particle image velocimetry measurements of the interaction of synthetic jets with a zero-pressure gradient laminar boundary layer. *Physics of Fluids*, 22(6).
- Jabbal, M., & Zhong, S. (2010). Particle image velocimetry measurements of the interaction of synthetic jets with a zero-pressure gradient laminar boundary layer. *Physics of Fluids*, 22(6).
- Jabbal, M., Liddle, S., Potts, J., & Crowther, W. (2013). Development of design methodology for a synthetic jet actuator array for flow separation control applications. *Proceedings of the Institution of Mechanical Engineers, Part G: Journal of Aerospace Engineering*, 227(1), 110 - 124.
- Jabbal, M., Liddle, S., Potts, J., & Crowther, W. (2012). Development of design methodology for a synthetic jet actuator array for flow separation control applications. *6th AIAA Flow Control Conference*. New Orleans, Louisiana.
- Jabbal, M., Wu, J., & Zhong, S. (2006). The performance of round synthetic jets in quiescent flow. *The Aeronautical Journal*, 110(1108), 385-393.
- Jain, M., Puranik, B., & Agrawal, A. (2011). A numerical investigation of effects of cavity and orifice parameters on the characteristics of a synthetic jet flow. *Sensors and Actuators A: Physical*, 165(2), 351-366.

- Jain, M., Puranik, B., & Agrawal, A. (2011). A numerical investigation of effects of cavity and orifice parameters on the characteristics of a synthetic jet flow. *Sensors and Actuators A*, 165(2), 351-366.
- Jeyalingam, J., & Jabbal, M. (2016). Optimization of Synthetic Jet Actuator design for noise reduction and velocity enhancement. *AIAA*. Washington D.C.
- Kim, J. H., Al-Sadawi, L., Vathylakis, A., & Chong, T. P. (2014). Trailing Edge Noise Reduction by Passive and Active Flow Controls. *AIAA, 20th AIAA/CEAS Aeroacoustics Conference*. Atlanta: AIAA. doi:2014-3300
- Kinsler, L., Frey, A., Coppens, A., & Sanders, J. (1982). *Fundamentals of Acoustics*. John Wiley & Sons.
- Knight, M., & Bamber, M. J. (1929). *Wind tunnel tests on airfoil boundary control using a backward opening slot*. Washington: NACA-TN-323 .
- Kopiev, V. F., Zaytsev, M. Y., & Ostrikov, N. N. (2013). Subsonic Jet Noise Suppression by a Corrugated Nozzle. *Acoustical Physics*, 59(2), 207-209.
- Kornilov, V. I., & Boiko, A. V. (2012). Efficiency of Air Microblowing Through Microperforated Wall for Flat Plate Drag Reduction. *AIAA Journal*, 50(3), 724-732.
- Kornilov, V. I., & Boiko, A. V. (2014). Flat-Plate Drag Reduction with Streamwise Noncontinuous Microblowing. *AIAA Journal*, 52(1), 93-103.
- Kumar, V., & Alvi, F. S. (2006). Use of High-Speed Microjets for Active Separation Control in Diffusers. *AIAA Journal*, 44(2), 273-281.
- Kwing, S.-C. (2000). European drag-reduction research — recent developments and current status. *Fluid Dynamics Research*, 26(5), 325-335.
- Kykkotis, S. (2014). *Towards the Noise Reduction of Double-Chamber Synthetic Jet Actuators, BEng Dissertation*. Brunel University London.
- Kykkotis, S., & Jabbal, M. (2014). Towards the noise reduction of piezoelectrical-driven synthetic jet actuators. *32nd AIAA Applied Aerodynamics Conference*. Atlanta, GA.
- Lasance, C. J., Aarts, R. M., & Ouweltjes, O. (2008). Synthetic jet cooling part II: Experimental results of an acoustic dipole cooler. *24th Semiconductor Thermal Measurement and Management Symposium*, (pp. 26-31). San Jose, CA.
- Lasance, C. J., Nicole, C., Aarts, R. M., Ouweltjes, O., & Kooijman, G. (2009). Synthetic jet cooling using asymmetric acoustic dipoles. *25th Semiconductor Thermal Measurement and Management Symposium*, (pp. 254-260). San Jose, CA.
- Lee, C. Y., & Goldstein, D. B. (2002). Two-dimensional synthetic jet simulation. *AIAA Journal*, 40(3), 510-516.
- Lee, M., & Reynolds, W. (1985). *Bifurcating and blooming jets*. Dep. Mech. Eng. Thermosci. Div. Rep. TF-22, Stanford Univ.

- Leleu, C., & Marsh, D. (2008). *Dependent on the Dark: Cargo and other Night Flights in European Airspace* (Vol. 5). Eurocontrol.
- Li, L., Song, Y., Chen, F., & Meng, R. (2017). Flow Control on Bowed Compressor Cascades Using Vortex Generator Jet at Different Incidences. *Journal of Aerospace Engineering*, 30(5).
- Lighthill, M. J. (1952). On Sound Generated Aerodynamically I. General Theory. *Royal Society of London. Series A, Mathematical and Physical Sciences*, 211(1107), 564-587.
- Lin, C.-Y., Bai, C.-J., & Hsiao, F.-B. (2014). An Investigation on the Fundamental Characteristics of Excited Synthetic Jet Actuator Under Cavity and Diaphragm Resonances. *Procedia Engineering*, 35-44.
- Lin, J. C. (2002). Review of research on low-profile vortex generators to control boundary-layer separation. *Progress in Aerospace Science*, 38, 389-420.
- Lin, J. C., Howard, F. G., & Selby, G. V. (1990). Small submerged vortex generators for turbulent flow separation control. *Journal of Spacecraft and Rockets*, 27(5), 503-507.
- Lin, Y.-T., Shieh, M.-S., Liou, H.-D., & Hou, C.-S. (1998). Investigation on the mass entrainment of an acoustically controlled elliptic jet. *International Communications in Heat and Mass Transfer*, 25(3), 379-388.
- Lu, F. K., Li, Q., & Liu, C. (2012). Microvortex generators in high-speed flow. *Progress in Aerospace Sciences*, 53, 30-45.
- Mangate, L. D., & Chaudhari, M. B. (2015). Heat transfer and acoustic study of impinging synthetic jet using diamond and oval shape orifice. *International Journal of Thermal Sciences*, 89, 100-109.
- Mangate, L. D., & Chaudhari, M. B. (2015). Heat transfer and acoustic study of impinging synthetic jet using diamond and oval shape orifice. *International Journal of Thermal Sciences*, 89, 100-109.
- Mankbadi, R. R., Golubev, V. V., & Sansone, M. (2015). Effect of a Synthetic Jet Actuator on Airfoil Trailing Edge Noise. *International Journal of Aeroacoustics*, 14(3-4), 553-568.
- Martis, R. R., & Misra, A. (2017). Separation attenuation in swept shock wave–boundary-layer interactions using different microvortex generator geometries. *Shock Waves*, 27(5), 747-760.
- Mathew, J., Sankar, B. V., Sheplak, M., & Cattafesta, L. N. (2006). Optimized Design of Piezoelectric Flap Actuators for Active Flow Control. *AIAA Journal*, 44(12), 2919-2928.
- Matsunuma, T., & Segawa, T. (2012). Effects of Input Voltage on Flow Separation Control for Low-Pressure Turbine at Low Reynolds Number by Plasma Actuators. *International Journal of Rotating Machinery*.
- McCormick, D. C. (2000). Boundary Layer Separation Control with Directed Synthetic Jets. *38th Aerospace Sciences Meeting & Exhibit*. Reno, Nevada.

- McFadden, N. M., Rathert, G. J., & Bray, R. S. (1952). *The effectiveness of Wing Vortex Generators in improving the maneuvering characteristics of a swept-wing*. NACA.
- McVeigh, M., Nagib, H., Wood, T., & Wygnanski, I. (2011). Full-Scale Flight Tests of Active Flow Control to Reduce Tiltrotor Aircraft Download. *Journal of Aircraft*, 48(3), 786-796.
- Mednikov, E., & Novitskii, B. (1975). Experimental study of intense acoustic streaming. *Akusticheskii Zhurnal*, 21(2), 245-249.
- Mele, B., Tognaccini, R., & Catalano, P. (2016). Performance Assessment of a Transonic Wing Configuration with Riblets Installed. *Journal of aircraft*, 53(1), 129-140.
- Meslem, A., Greffet, R., Nastase, I., & Ammar, A. (2014). Experimental investigation of jets from rectangular six-lobed and round orifices at very low Reynolds number. *Meccanica*, 49(10), 2419-2437.
- Michalke, A., & Fuchs, H. (1975). On turbulence and noise of an axisymmetric shear flow. *Journal of Fluid Mechanics*, 70(1), 179-205.
- Milanovic, I., & Zaman, K. (2005). Synthetic jets in crossflow. *AIAA Journal*, 43(5), 929-940.
- Moeser, M. (2009). *Engineering acoustics - An Introduction to Noise Control*. Springer.
- Mominul Islam Mukut, A., Mizunuma, H., & Hiromichi, O. (2014). Flow Separation Control Using Plasma Vortex Generator. *10th International Conference on Mechanical Engineering, ICME 2013, Procedia Engineering*, 90, 232-237.
- Moore, C. J. (1977). The role of shear-layer instability waves in jet exhaust noise. *Journal of Fluid Mechanics*, 80, 321-367.
- Nair, V., & Sujith, R. (2016). Precursors to self-sustained oscillations in aeroacoustic systems. *International Journal of Aeroacoustics*, 15(3), 312-323.
- Narayanaswamy, V., Raja, L. L., & Clemens, N. T. (2010). Characterization of a High-Frequency Pulsed-Plasma Jet Actuator for Supersonic Flow Control. *AIAA Journal*, 48(2), 297-305.
- Nastase, I., & Meslem, A. (2007). Passive control of jet flows using lobed nozzle geometries. *Mechanics & Industry*, 8(2), 101-109.
- Nastase, I., & Meslem, A. (2010). Vortex dynamics and mass entrainment in turbulent lobed jets with and without lobe deflection angles. *Experiments in Fluids*, 48(4), 693-714.
- Nikolic, V. (2005). Movable Tip Strakes and Wing Aerodynamics. *Journal of Aircraft*, 42(6), 1418-1426.
- Nuber, R. J., & Needham, J. R. (1948). *Exploratory Wind-Tunnel Investigation of the Effectiveness of Area Suction in Eliminating Leading-Edge Separation over an NACA 641A212 Airfoil*. Washington: NACA TN-1741.
- Pack, L. G., & Joslin, R. D. (1998). Overview of active flow control at NASA Langley. *SPIE's 5th Annual International Symposium on Smart Structures and Materials*. San Diego.

- Panda, J. (1999). An experimental investigation of screech noise generation. *Journal of Fluid Mechanics*, 378, 71-96.
- Piezo, A. (2014, 08 22). *American Piezo*. Retrieved 05 05, 2017, from https://www.americanpiezo.com/images/stories/content_images/pdf/apc_20-1235.pdf
- Powell, A. (1961). On the edge tone. *The Journal of the Acoustical Society of America*, 33, 395-409.
- Prandtl, L. (1904). Über Flüssigkeitsbewegung bei sehr kleiner Reibung (On the motion of fluid with very small friction). *Proceedings of the 3rd International Mathematical*. Heidelberg, Germany.
- Presz, W. M., Gousy, R., & Morin, B. (1986). Forced mixer lobes in ejector designs. *AIAA Paper No. 86-1614*.
- Presz, W. J., Reynolds, G., & Hunter, C. (1994). Thrust augmentation with mixer ejector diffuser systems. *32nd Aerospace Sciences Meeting and Exhibit, AIAA*. Reno, NV.
- Presz, W., Reynolds, G., & Hunter, C. (2002). Thrust augmentation using mixer/ejector systems. *40th AIAA Aerospace Sciences Meeting & Exhibit, AIAA*. Reno, NV.
- Pullin, D. (1979). Vortex ring formation at tube and orifice openings. *The Physics of Fluids*, 22(3), 401-403.
- PurePower PW1000G Engine*. (2018). Retrieved from Pratt and Whitney: http://www.pw.utc.com/PurePowerPW1000G_Engine
- Raman, G., Rice, E. J., & Reshotko, E. (1991). *An experimental study of natural and forced modes in an axisymmetric jet*. NASA TM 105225.
- Ramasamy, M., Wilson, J. S., & Martin, P. B. (2010). Interaction of Synthetic Jet with Boundary Layer Using Microscopic Particle Image Velocimetry. *Journal of Aircraft*, 47(2), 404-422.
- Raspet, A., Cornish, J. J., & Bryant, G. D. (1956). Delay of the stall by suction through distributed perforations. *Aeronautical Engineering Review*, 15(8), 32 - 39.
- Reynolds, W., Parekh, D. E., Juvet, P. J., & Lee, M. J. (2003). Bifurcating and blooming jets. *Annual Review of Fluid Mechanics*, 35(1), 295-315.
- Riblets and Motor Sports*. (2018). Retrieved from Bionic Surface Technologies: www.bionicsurface.com
- Rockwell, D., & Naudascher, E. (1978). Self-sustaining oscillations of flow past cavities. *Journal of Fluids Engineering*, 100, 152-165.
- Rockwell, D., & Naudascher, E. (1979). Self-sustained oscillations of impinging free shear layers. *Annual Review of Fluid Mechanics*, 11, 67-94.
- Saffman, P. (1978). 78 The number of waves on unstable vortices. *Journal of Fluid Mechanics*, 84, 625-639.

- Salunkhe, P., Tang, H., Zheng, Y., & Yanhua, W. (2016). PIV measurement of mildly controlled flow over a straight-wing model. *International Journal of Heat and Fluid Flow*, 62, 552-559.
- Savas, O., & Coles, D. (1985). Coherence measurements in synthetic turbulent boundary layers. *Journal of Fluid Mechanics*, 160, 421-446.
- Schäfer, A. W., & Waitz, I. A. (2014). Air transportation and the environment. *Transport Policy*, 34, 1-4.
- Schrenk, O. (1928). Tragflügel mit Grenzschichtabsaugung. *Luftfahrtforschung* 2, 49.
- Schrenk, O. (1931). Versuche an einem Aabsaugflügel. *Z. Flugtechnik*, 22, 259 - 264.
- Schubauer, G. B., & Skramstad, H. K. (1948). *Laminar-Boundary-Layer Oscillations and Transition on a Flat Plate*. National Advisory Committee for Aeronautics.
- Seifert, A., Darabi, A., & Wygnanski, I. (1996). Delay of airfoil stall by periodic excitation. *Journal of Aircraft*, 33, 691-698.
- Seifert, A., Darabi, A., Koss, D., Shepshelovich, M., & Wygnanski, I. (1993). Oscillatory blow-ing: a tool to delay boundary-layer separation. *AIAA Journal*, 31(11), 2052-2060.
- Shyy, W., Jayaraman, B., & Andersson, A. (2002). Modeling of glow discharge-induced fluid dynamics. *Journal of Applied Physics*, 92(11), 6434-6443.
- Smith, B. L., & Swift, G. W. (2003). A comparison between synthetic jets and continuous jets. *Experiments in Fluids*, 34(4), 467 - 472.
- Smith, B., & Glezer, A. (1998). The formation and evolution of synthetic jets. *American Institute of Physics*.
- Smith, B. L., & Swift, G. W. (2003). Power dissipation and time-averaged pressure in oscillating. *The Journal of the Acoustical Society of America*, 113(5).
- Smith, B., & Glezer, A. (2005). Vectoring of Adjacent Synthetic Jets. *AIAA Journal*, 43(10), 2117-2124.
- Smith, B., Trautman, M., & Glezer, A. (1999). Controlled interactions of adjacent synthetic jets. *AIAA, 37th Aerospace Sciences Meeting and Exhibit, Aerospace Sciences Meetings*. Reno, Nv, USA.
- Smits, A., & Lim, T. (2000). Dye and smoke visualization . In *Flow Visualisation - Techniques and Examples* (p. 44). London: Imperial College Press.
- Sondhauss, C. (1854). Ueber die beim Ausströmen der Luft entstehenden Töne. *Annalen der Physik*, 167(2), 214-240.
- Suder, K. L. (2012). Overview of the NASA Environmentally Responsible Aviation Project's Propulsion Technology Portfolio. *48th AIAA/ASME/SAE/ASEE Joint Propulsion Conference & Exhibit, AIAA*. Atlanta, Georgia.

- Tam, C. K., Viswanathan, K., Ahuja, K. K., & Panda, J. (2008). The sources of jet noise: experimental evidence. *Journal of Fluid Mechanics*, 615, 253-292.
- Tang, H., Zhong, S., Jabbar, M., Garcillan, L., Guo, F., Wood, N., & Warsop, C. (2007). Towards the Design of Synthetic-jet Actuators for Full-scale Flight Conditions, Part 2: Low-dimensional Performance Prediction Models and Actuator Design Method. *Flow, Turbulence and Combustion*, 78(3-4), 309-329.
- Tang, H., & Zhong, S. (2006). Incompressible flow model of synthetic jet actuators. *AIAA Journal*, 908 - 912.
- Tang, H., & Zhong, S. (2007). A static compressible flow model of synthetic jet actuators. *The Aeronautical Journal*, 111(1121), 421-431.
- Tang, H., Salunkhe, P., Zheng, Y., Du, J., & Wu, Y. (2014). On the use of synthetic jet actuator arrays for active flow separation control. *Experimental Thermal and Fluid Science*, 57, 1-10.
- Taylor, H. D. (1947). *The elimination of diffuser separation by vortex generators*. United Aircraft Corporation Reports No. R-4012-3.
- Tesar, V., & Kordík, J. (2011). Spectral analysis of a synthetic jet. *Sensors and Actuators A: Physical*, 213-225.
- Tide, P. S., & Srinivasan, K. (2010). Effect of chevron count and penetration on the acoustic characteristics of chevron nozzles. *Applied Acoustics*, 71, 201-220.
- Travnicek, Z., Brouckova, Z., & Kordik, T. (2015). Visualization of synthetic jet formation in air. *Journal of Visualization*, 18(4), 595-609.
- (2013). *UK Aviation Forecast*. Department for Transport.
- Van Buren, T., Whalen, E., & Amitay, M. (2016). Achieving a High-Speed and Momentum Synthetic Jet Actuator. *Journal of Aerospace Engineering*, 29(2).
- Van Dyke, M. (1982). *An album of fluid motion*. Stanford, CA: Parabolic Press.
- Vathylakis, A. (2015). *Reduction of broadband trailing edge noise by serrations*, PhD Thesis. Uxbridge: Brunel University London.
- Viswanathan, K. (2006). Instrumentation Considerations for Accurate Jet Noise Measurements. *AIAA*.
- von Gierke, H. (1947). Über die mit dem Mund hervorgebrachten Pfeiftöne. *Pflüger's Archiv für die gesamte Physiologie des Menschen und der Tiere*, 249, 307-312.
- Wahlen, E. A., Shmilovich, A., Spoor, M., John, T., Vijgen, P., Lin, J. C., & Andino, M. (2016). Flight Test of an AFC Enhanced Vertical Tail. *8th AIAA Flow Control Conference*. Washington, D.C.: AIAA.
- Wang, L., Feng, L.-H., Wang, J.-J., & Li, T. (2018). Parameter influence on the evolution of low-aspect ratio rectangular synthetic jets. *Journal of Visualization*, 21(1), 105-115.

- Wang, S., Ma, B., Deng, J., Qu, H., & Luo, J. (2015). Fabrication and characterization of MEMS piezoelectric synthetic jet actuators with bulk-micromachined PZT thick film. *Microsystem Technologies*, 21(5), 1053-1059.
- Ward-Smith, A. J. (1979). Critical Flowmetering: The Characteristics of Cylindrical Nozzles with Sharp Upstream Edges. *International Journal of Heat and Fluid Flow*, 1(3), 123-132.
- Werle, M. J., Paterson, R. W., & Presz, W. M. (1987). Flow structure in a periodic axial vortex array. *25th AIAA Aerospace Sciences Meeting, AIAA*. Reno, NV.
- Williams, D. R., & MacMynowski, D. G. (2008). Brief History of Flow control. In *Fundamentals and Applications of Modern Flow Control* (pp. 1-20). AIAA.
- Xia, Q., & Zhong, S. (2012). An experimental study on the behaviours of circular synthetic jets at low Reynolds numbers. *Proceedings of the Institution of Mechanical Engineers, Part C: Journal of Mechanical Engineering Science*, 226(11), 2686-2700.
- Xiong, D., Zhixun, X., Zhenbing, L., & Lin, W. (2014). A novel optimal design for an application-oriented synthetic jet actuator. *Chinese Journal of Aeronautics*, 27(3), 514-520.
- Yang, Y., Jones, D. L., & Liu, C. (2010). Recovery of rectified signals from hot-wire/film anemometers due to flow reversal in oscillating flows. *American Institute of Physics*, 81(1).
- Zaman, K., & Hussain, A. (1980). Vortex pairing in a circular jet under controlled excitation. PART 1. General Jet response. *Journal of Fluid Mechanics*, 101(3), 449-491.
- Zaman, K. (1994). Axis Switching and Spreading of an Asymmetric Jet - Role of Vorticity Dynamics. *33rd Aerospace Sciences Meeting Exhibit, AIAA*. Reno, NV.
- Zaman, K. (1996). Axis switching and spreading of an asymmetric jet: the role of coherent structure dynamics. *Journal of Fluid Mechanics*, 316, 1-27.
- Zaman, K., Wang, F. Y., & Georgiadis, N. J. (2003). Noise, turbulence and thrust of subsonic free jets from lobed nozzles. *AIAA Journal*, 41(3), 398-407.
- Zhong, S., Jabbal, M., Tang, H., Garcillan, L., Guo, F., Wood, N., & Warsop, C. (2007). Towards the Design of Synthetic-jet Actuators for Full-scale Flight Conditions Part 1: The Fluid Mechanics of Synthetic-jet Actuators. *Flow Turbulence Combustion*, 78(4), 283 - 307.
- Zhou, J., Tang, H., & Zhong, S. (2009). Vortex Roll-Up Criterion for Synthetic Jets. *AIAA Journal*, 47(5), 1252-1262.
- Zong, H.-h., Cui, W., Wu, Y., Zhang, Z.-b., Liang, H., Jia, M., & Li, Y.-h. (2015). Influence of capacitor energy on performance of a three-electrode plasma synthetic jet actuator. *Sensors and Actuators A: Physical*, 222, 114-121.